ADVANCED STEEL CONSTRUCTION

An International Journal

Volume 20 Number 4

December 2024

CONTENTS

Technical Papers

Experimental and Finite Element Investigations of Concrete-Filled Steel Slender Columns with Hexagonal Cross-Section
O. F. Kharoob, M. H. EL-Boghdadi and AZA. M. Elagamey

Study of Mechanical Properties of a Novel Column-Beam-Column Prefabricated Steel Frame Joint
Zhi-Wei Zhang, Dong Li, Hua-Jie Wang, Hong-Liang Qian, Wen-Qi Fang, Xiao-Fei Jing and Feng Fan

Interface Shear Demand and Design of Partially Concrete-Filled Steel Tubular Columns with Transverse Diaphragms
Jian Jiao, Yao-Jun Zhang and Dan Gan

Mechanical Properties of Assembled Wall-Slab Joints Between Thin Double Skin Composite Shear Walls and Precast Floor Slabs Subjected to Pure Bending
Jie Liu, Zhi-Hua Chen, Ting Zhou and Xiao-Feng Wang

A Bayesian-Optimized Neural Network Model for Shear Capacity of a Perfobond Strip Connector in Various Types of Composite Structures
Minh Hai Nguyen and Hoang Nam Phan

Research on Data-Driven Intelligent Design Method for Energy Dissipator of Flexible Protection Systems
Ze-Huan He, Zhi-Xiang Yu, Lin-Xu Liao, Yang-Feng Lyu and Yong-Ding Tian

Numerical Investigation on Seismic Performance of Prefabricated Steel Beam-To-Column Connection with Replaceable U-Shaped Plate
Xun Zhang, Bin Zhou, Jun-Dong Gao, Hui Qian, Lian-Zhi Song and Li-Ming Cai

Experimental and Numerical Analysis on the Mechanical Behavior of a Glulam Suspendome
Chen-Rui Zhang, Jian-Xiong Zhao, Hong-Bo Liu, Shi-Xing Zhao, Jing-Xian Zhao, Shu-Heng Yang and Ting Zhou

Web Crippling Behaviour of Cold-Formed Steel Channels Web Holes under End Two Flange (ETF) Loading
Yakup Bölükbaş

Metal Beams Susceptible to Out-of-Plane Instability Due to Combined Compression and Bending with Geometric Imperfections
Antonio Aguero, Ana Almerich-Chulia, Yvona Kolekova and Pedro Martin-Concepcion

Website: *http://www.hkisc.org*
ISSN 1816-112X
Science Citation Index Expanded, Materials Science Citation Index and ISI Alerting
Cover: Photo@ Yang Yuhua
e-copy of IJASC is free to download at "www.ascjournal.com" in internet and mobile apps.

ADVANCED STEEL CONSTRUCTION

VOL.20, NO.4 (2024)

ADVANCED STEEL CONSTRUCTION

an International Journal

ISSN 1816-112X

Volume 20 Number 4 *December 2024*

ISSN 1816-112X

Science Citation Index Expanded, Materials Science Citation Index and ISI Alerting

Advanced Steel Construction
an international journal

Cover: Photo@ Yang Yuhua
e-copy of IJASC is free to download at "www.ascjournal.com" in internet and mobile apps.

General Information
Advanced Steel Construction, an international journal

Aims and scope

The International Journal of Advanced Steel Construction provides a platform for the publication and rapid dissemination of original and up-to-date research and technological developments in steel construction, design and analysis. Scope of research papers published in this journal includes but is not limited to theoretical and experimental research on elements, assemblages, systems, material, design philosophy and codification, standards, fabrication, projects of innovative nature and computer techniques. The journal is specifically tailored to channel the exchange of technological know-how between researchers and practitioners. Contributions from all aspects related to the recent developments of advanced steel construction are welcome.

Subscription inquiries and change of address. Address all subscription inquiries and correspondence to Member Records, IJASC. Notify an address change as soon as possible. All communications should include both old and new addresses with zip codes and be accompanied by a mailing label from a recent issue. Allow six weeks for all changes to become effective.

The Hong Kong Institute of Steel Construction
HKISC
c/o Prof. SL Chan,
Unit 209B, Photonics Centre, No. 2 Science Park East Avenue,
Hong Kong Science Park, Shatin, N.T., Hong Kong, China.
Tel: 852- 3595 6150 Fax: 852- 3619 7238
Email: ceslchan@connect.polyu.hk Website: *http://www.hkisc.org/*
ISSN 1816-112X
Science Citation Index Expanded, Materials Science Citation Index and ISI Alerting

ISSN 1816-112X

Science Citation Index Expanded, Materials Science Citation Index and ISI Alerting

Advanced Steel Construction
an international journal

VOLUME 20 NUMBER 4 December 2024

Technical Papers

Experimental and Finite Element Investigations of Concrete-Filled Steel Slender Columns with Hexagonal Cross-Section 319
*O. F. Kharoob, M. H. EL-Boghdadi and AZA. M. Elagamey **

Study of Mechanical Properties of a Novel Column-Beam-Column Prefabricated Steel Frame Joint 330
*Zhi-Wei Zhang, Dong Li *, Hua-Jie Wang *, Hong-Liang Qian, Wen-Qi Fang, Xiao-Fei Jing and Feng Fan*

Interface Shear Demand and Design of Partially Concrete-Filled Steel Tubular Columns with Transverse Diaphragms 345
*Jian Jiao, Yao-Jun Zhang and Dan Gan **

Mechanical Properties of Assembled Wall-Slab Joints Between Thin Double Skin Composite Shear Walls and Precast Floor Slabs Subjected to Pure Bending 364
*Jie Liu, Zhi-Hua Chen, Ting Zhou * and Xiao-Feng Wang*

A Bayesian-Optimized Neural Network Model for Shear Capacity of a Perfobond Strip Connector in Various Types of Composite Structures 376
*Minh Hai Nguyen and Hoang Nam Phan **

Research on Data-Driven Intelligent Design Method for Energy Dissipator of Flexible Protection Systems 385
*Ze-Huan He, Zhi-Xiang Yu *, Lin-Xu Liao, Yang-Feng Lyu and Yong-Ding Tian*

Numerical Investigation on Seismic Performance of Prefabricated Steel Beam-To-Column Connection with Replaceable U-Shaped Plate 397
*Xun Zhang, Bin Zhou, Jun-Dong Gao *, Hui Qian, Lian-Zhi Song and Li-Ming Cai*

Experimental and Numerical Analysis on the Mechanical Behavior of a Glulam Suspendome 406
*Chen-Rui Zhang, Jian-Xiong Zhao *, Hong-Bo Liu, Shi-Xing Zhao, Jing-Xian Zhao, Shu-Heng Yang and Ting Zhou*

Web Crippling Behaviour of Cold-Formed Steel Channels Web Holes under End Two Flange (ETF) Loading 413
*Yakup Bölükbaş **

Metal Beams Susceptible to Out-of-Plane Instability Due to Combined Compression and Bending with Geometric Imperfections 424
*Antonio Aguero *, Ana Almerich-Chulia, Yvona Kolekova and Pedro Martin-Concepcion*

Advanced Steel Construction – Vol. 20 No. 4 (2024) 319–329
DOI:10.18057/IJASC.2024.20.4.1

EXPERIMENTAL AND FINITE ELEMENT INVESTIGATIONS OF CONCRETE-FILLED STEEL SLENDER COLUMNS WITH HEXAGONAL CROSS-SECTION

O. F. Kharoob, M. H. EL-Boghdadi and AZA. M. Elagamey *

Department of Structural Engineering, Faculty of Engineering, Tanta University, Tanta, Egypt
** (Corresponding author: E-mail: aza_mohamed@yahoo.com)*

ABSTRACT

This research presents experimental and finite element (FE) investigations of hexagonal concrete-filled steel tubular (HCFST) slender columns. Firstly, a uniform axial load is applied to eight HCFST columns, with four of them being short columns and the others remainder slender. The experiments aim to study the impact of both the cross-section and concrete strength on the strength and behavior of HCFST slender columns. Secondly, HCFST slender columns are analyzed using the FE program (ABAQUS). Validation of the FE analysis in terms of strength and behavior is conducted using the present experimental tests and previous research. The strength and behavior of HCFST slender columns are further explored using a series of parametric studies, including columns' height, concrete strength (f_c), steel cross-section thickness (t), and steel strength (f_y). The results show that increasing the values of t, f_c, and f_y increases the ultimate capacity load of HCFST slender columns. Additionally, the maximum value of λ is identified to be almost equal to 18, indicating the threshold distinguishing short HCFST columns, and after this threshold, the columns are classified as slender. Lastly, a comparison is drawn between the results obtained from the experimental and FE models and the standards obtained in the AISC and EN 1994-1-1 (EC4) codes. The analysis reveals that EN 1994-1-1 (EC4) yields non-conservative results for steel tubes with small thicknesses, whereas AISC tends to give more conservative results across all HCFST slender columns. It is therefore recommended to adhere to the AISC specification for steel tubes with small thicknesses up to 4mm and to use EC4 for other thicknesses exceeding this limit.

ARTICLE HISTORY

Received: 21 August 2023
Revised: 11 February 2024
Accepted: 16 February 2024

KEYWORDS

HCFST slender columns;
Ultimate axial strength;
Experimental study;
Slenderness ratio;
Finite element (FE)

1. Introduction

Generally, composite columns consist of concrete as the compression element, while steel members at the external perimeter are considered the best elements to withstand tension and bending moments. The presence of the concrete component within the steel tube effectively mitigates local buckling by providing resistance compressive loading. Concrete-filled steel tubing (CFST) columns have found extensive application in various structures such as transmission towers, bridges, multi-story buildings, and storerooms. As depicted in Fig. 1, the shapes of CFST columns include rectangular, square, circular, elliptical, and more recently, octagonal and hexagonal shapes. The main advantages of using CFST columns were: economy, increased strength, greater ductility, higher stiffness, higher energy absorption capacity, and reduced construction time and cost [1].

Circular CFST columns perform significantly better than their square or rectangular counterparts due to the more uniform confinement effect experienced by a circular CFST column than on a square or rectangular cross-section [2]. The cross-sections of CFST columns can vary, encompassing shapes such as octagonal [3–6], hexagonal [1, 7–10], round-ended [11–14], and elliptical [15–19] shapes. These shapes have been extensively studied to enhance bearing capacity and simplify connections to neighboring beams.

A new cross-section for CFST columns, termed square concrete-filled double steel tubular (CFDST) columns, has been introduced. This design incorporates an inner circular tube, aiming to combine the advantages of square and circular CFST columns, as described in references [3, 20]. Researchers have tested square CFDST columns under various loads to assess their structural performance [21–25].

Conversely, slender columns have been extensively studied, including circular, square, and oval specimens. Dundu [26] examined the behavior of 29 squares of CFST under concentric axial compression. Overall, buckling was identified as the predominant failure mode for column lengths ranging between 1.5 and 2.7 m. Dai et al. [27] conducted numerical forecasts in conjunction with experimental observations of 18 CFST elliptical columns, verifying the accuracy of the FE. The failure mechanisms observed in the slender CFST columns were global buckling, as established through both experimental and numerical modeling. Ahmed et al. [28] studied numerical models to identify local and global buckling in CFDST columns, proposing a design methodology for calculating the ultimate load. Wang et al. [29] conducted tests on 13 HCFS corner columns under axial or eccentric compression, proposing equations to predict load capacity and providing insights for safe design predictions.

According to the aforementioned, previous studies concentrated on studying the behavior of short CFST columns, with very limited investigation into CFST slender columns with oval, circular, and square cross-sections. However, it is worth noting that there was limited availability of experimental or theoretical investigations regarding the behavior of CFST slender columns with hexagonal cross-sections, except for the findings presented in reference [29].

Recently, only one study has appeared examining slender columns of hexagonal cross-section subjected to eccentric compression [29].

Therefore, the authors believed that this research would complete the study of the behavior of slender columns with a hexagonal cross-section using practical experiments exposed to an axial load. At the end of the experimental study, the ABAQUS program was used to develop the FE model. The FE model was verified by using the results of experiments. Then, the proposed FE model was used in the parametric study, which examined the impacts of column height (H), steel cross-section thickness (t), concrete strength (f_c), steel strength (f_y), and slenderness ratio (λ) on the efficiency of HCFST slender columns. Finally, the results of the FE model study and experimental tests were compared with the guidelines outlined in the AISC and EN 1994-1-1 (EC4) codes.

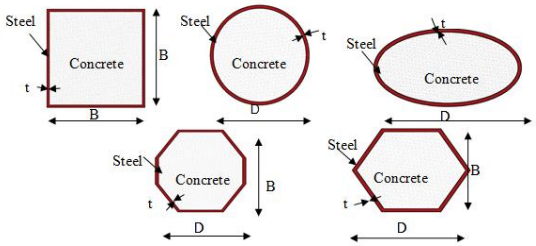

Fig. 1 Shapes of CFST columns

2. Laboratory investigation

2.1. Stage of pre-loading

CFST columns with hexagonal shapes were tested. The experimental program contained eight test specimens of HCFST columns, including four specimens of HCFST short columns (HCSS1, HCSS2, HCSS3, and HCSS4) and four specimens of HCFST slender columns (HCFST1, HCFST2, HCFST3, and HCFST4). The dimensions of tested columns were represented as [$D \times B \times$

t], with the height denoted as [*H*], (θ) of the cross-section 120º, and the calculated value a = *D/2*, with the steel column's thickness [*t*]; please refer to Table 1. Definitions for (*B*, *D*, θ, and a) were provided in Fig. 2. Additionally, Table 1 presents the peak axial strength ($P_{ul,Test}$) of tested columns. The concrete had a strength of 30.25 MPa. Steel plates were bent to create the hexagonal steel tubes, which were then butt-welded at the corners of both ends. Fig. 2 depicts the location of the butt welds along the column length. To monitor the failure mode and prevent rusting of the steel outer surface, the exterior of the steel columns' was treated and painted with gray paint. Initially, the end bearing plate and hexagonal steel tube were welded together. Then, concrete was cast from the other side of the columns. The upper surface of the concrete was leveled to be on the same surface plane as the steel column. Concurrently, the standard concrete cube tests were performed.

After casting, the columns were covered with wet burlap on the upper surfaces to prevent water loss. The top surfaces of the columns were regularly watered. Additionally, the standard concrete cubes were treated in a similar manner as the HCFST columns.

Finally, the other side of the column was covered with plates that were welded to the higher surfaces of the HCFST columns.

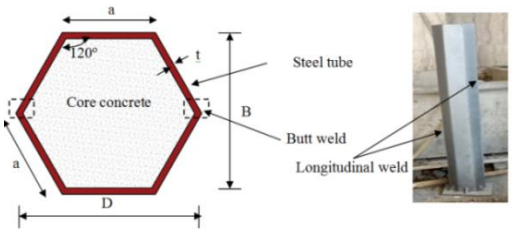

Fig. 2 Definition of symbols and position of butt weld for HCFST columns

Table 1
Tested columns' measurements and ultimate loads

Specimen	*a*[mm]	*H*[mm]	*D*[mm]	*B*[mm]	*t*[mm]	*θ*	P_{uExp}[KN]
HCSS1	80	500	160	138.56	3	120º	894.54
HCSS2	80	500	160	138.56	3	120º	868.53
HCSS3	100	620	200	173.21	3	120º	1178.61
HCSS4	100	620	200	173.21	3	120º	1388.73
HCFST1	80	1494	160	138.56	3	120º	771.63
HCFST2	100	1494	200	173.21	3	120º	1023.57
HCFST3	80	1094	160	138.56	3	120º	879.75
HCFST4	100	1094	200	173.21	3	120º	1100.07

2.2. Stage measurements and loading

The concrete mix specifications are detailed in Table 2. Prior to testing, the mechanical properties of both steel and concrete cubes were examined using standard methods. Concrete cubes measuring 150mm x 150mm x 150mm underwent compression testing according to the procedures outlined in the Egyptian Code [30]. The recorded results of cubic strength [f_{cu}], Young's modulus of the concrete [E_c], and Poison's ratio [v_c] were presented in Table 3. The coupon dimensions of steel plates, corresponding to the Australian Standard AS 1391 [31], were depicted in Figs. 3 and 4. Fig. 5 illustrates the mode of failure observed in the tested plate. The results of the material properties of the steel plates' yield strength [f_y], tensile strengths [f_u], Young's modulus [E_s], and Poison's ratio [v_s] were listed in Table 4 and plotted in Fig. 6. A hydraulic machine applied a 2000 kN axial compression to the test column. The column was stabilized to ensure that the applied load acted uniformly as axial compression. To prevent out-of-plane buckling, a transverse beam was used at mid-height. The two-end boundary conditions of the columns were depicted as hinged supports, as depicted in Fig. 7. To ensure accurate measurement of deformation, four mechanical LVDTs were positioned: two for measuring axial shortening and the others for measuring lateral displacement of the columns', as outlined in Figs. 7 and 8. Additionally, four strain gauges were installed at the midpoint of the two opposing side surfaces of steel tube for the slender columns made of hexagonal concrete-filled steel tubing (HCFST). At the midpoint of the columns' height, strain gauges were positioned: two in tension and two in compression, one vertically and the other horizontally. The axial load was acted upon the upper surface of the rigid steel plate by a hydraulic cylinder in increments of 20 kN up to 30% of the design load and then unloaded. Subsequently, the load was gradually applied until failure was observed. With every increase in load, readings from the strain gauges and LVDTs were recorded.

Table 2
Concrete mix design

Cement[Kg/m^3]	Water[Kg/m^3]	Sand[Kg/m^3]	Aggregate[Kg/m^3]
350	150	650	1300

Table 3
Properties of concrete

f_{cu} [Mpa]	E_c [Mpa]	v_c
30.25	22970.76	0.23

Fig. 3 Tensile coupon test specimen setup

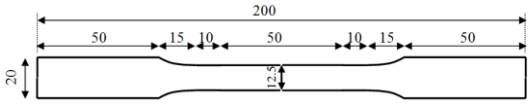

Fig. 4 Dimensions of the test specimen for tensile coupons in mm [31]

Fig. 5 Failure mode of tensile coupon test specimen

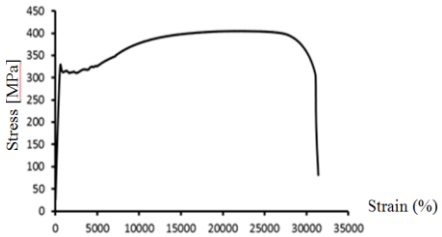

Fig. 6 Steels stress-strain curve

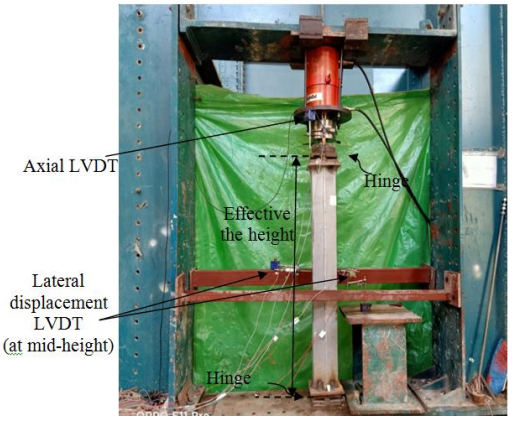

Fig. 7 Test set-up of test specimens

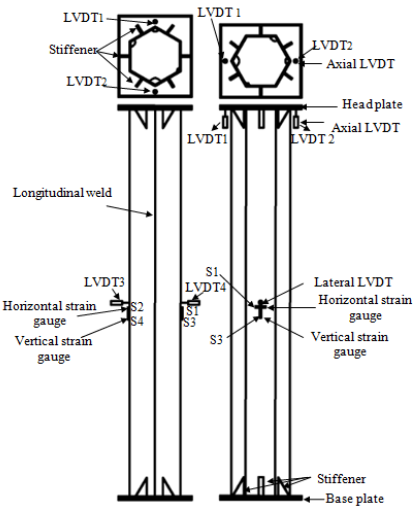

Fig. 8 Strain gauges and LVDTs on the slender columns

Table 4
Measured steel properties

f_y [Mpa]	f_u [Mpa]	E_s	v_s
329.799	405.056	200000	0.29

2.3. Results of the experiments and discussion

The results of specimens HCFST1, HCFST2, HCFST3, and HCFST4 of HCFST slender columns were previously outlined in Table 1. The axial strength (P_{Test}) of each specimen was determined, along with the relationships between the loads and lateral displacement, axial shortening, vertical strain, and horizontal strain. The mode of failure for each column specimen was also discussed. Based on the experimental tests, the peak axial strength ($P_{ul,Test}$) of the tested columns HCFST1, HCFST2, HCFST3, and HCFST4 was 771.63 kN, 1023.57 kN, 879.75 kN, and 1100.07 kN, respectively. Additionally, the axial shortening at the peak strength was recorded as 6.69, 11.86, 10.12, and 10.06 mm, respectively.

The average load-axial shortening relationships of HCFST slender columns are described in Fig. 9. The current results prove that the shortening values increase with increasing load values. Furthermore, an increase in the columns' cross-sectional dimensions results in higher ultimate load values for HCFST-slender columns. However, it was seen that shortening the height of HCFST slender columns also contributes to an escalation in the ultimate load values.

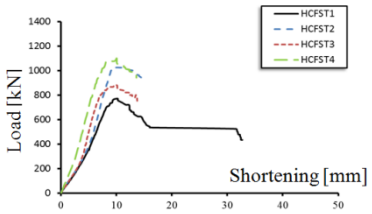

Fig. 9 Load-axial shortening relationships average of LVDT1 and LVDT2 for HCFST

The load- horizontal displacement relationships of the HCFST slender columns are depicted in Fig. 10. It was observed that the load values increased with the lateral displacement values. Additionally, increasing the cross-sectional dimensions of the HCFST slender columns' resulted in higher ultimate load values. Moreover, decreasing the height of the HCFST's slender columns increases the ultimate load. At the middle height of the HCFST slender columns, load-vertical strain and load-horizontal strain were measured and plotted in Fig. 11.

Tension and compression strains were considered positive and negative signs, respectively. The vertical compressive strain and horizontal tension strain of the HCFST slender columns were observed to be greater than the yield strains of their constituent materials ($P_{ul,Test}$). Alternatively, once the vertical strain of the HCFST slender columns (HCFST1, HCFST2, and HCFST3) reversed from compression to tension, the ultimate axial load was determined. Conversely, when attaining the peak load of the HCFST slender columns (HCFST1, HCFST2, and HCFST3), the horizontal strain of the columns was located within the compression zone. Additionally, significant variations in the vertical and horizontal strains of HCFST4 were observed during the initial loading period, due to elastic buckling induced by the slender column. The distorted shapes of the tested columns are depicted in Fig. 12. The failure pattern for the current HCFST slender columns was identified as global buckling, which was typically observed in all columns, particularly in column HCFST1. However, the details of the global buckling behavior of all types of slender columns are illustrated in Fig. 12.

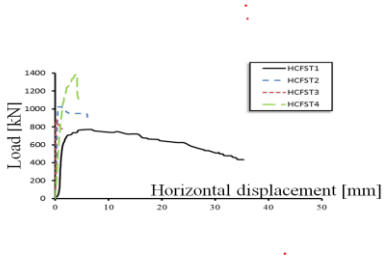

Fig. 10 Load- horizontal displacement relationship average of LVDT3 and LVDT4 for HCFST

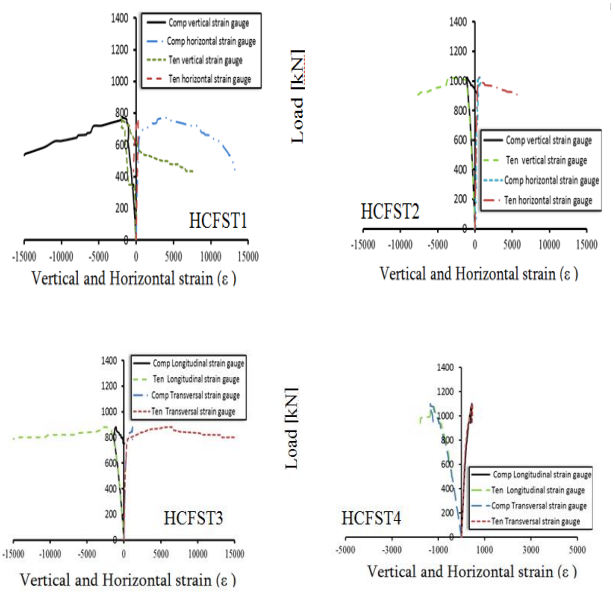

Fig. 11 Load-vertical strain and load-horizontal strain relationships for HCFST slender columns

Fig. 12 Distorted shape of HCFST slender columns

3. Finite element model [FE]

3.1. Overall

The program ABAQUS [32] was utilized to develop the present FE models.

The modeling procedure comprised two steps. Initially, the buckling mode of a perfectly slender column was determined using an elastic buckling analysis referred to as a linear perturbation analysis. In the next stage of the analysis, the HCFST slender columns were loaded through axial compression, determining the peak loads and collapse manner. This analysis incorporated material plasticity strains and geometric imperfections in accordance with the first Eigen mode; RIKS method described in ABAQUS [32]. The model included discrete, rigid upper and lower-end plates, each equipped with a reference point (RP) positioned mid center. These RP's were provided with the boundary conditions, with the vertical load concentrated atop the upper-end plate. Various restrictions were applied at the RPs to simulate pin-ended supports. The lower RP exhibited restraints (u_x= u_y= u_z= θ_z = 0.0), while the top RP exhibited restraints (u_x= u_y= θ_z = 0.0), as shown in Fig. 13 and previously discussed in detail by the first author in [33]. Furthermore, the optimal mesh size was determined through mesh sensitivity analysis, yielding a mesh size of 50mm, as depicted in Fig. 14. The tube was modeled using the shell element with a three-node triangular shape S3 [32]. The concrete was modeled using the three-dimensional solid element C3D4, with a four-node linear tetrahedron shape [32]. Surface-based interactions were used to replicate the interaction between the tube and the concrete. This was achieved using a Coulomb friction model in the tangential orientation on the surface, coupled with a contact pressure-over-closure model in the normal orientation. The steel and concrete surfaces were designated as slave and master surfaces, respectively. As reported by Hassanein et al. [34], the friction coefficient between concrete and steel tube was identified as 0.4. Furthermore, the interaction between the end plates and the concrete was considered to possess the same properties as described above. Additionally, as shown in Fig. 13, all end plates were connected to the tube using the "tie" constraint, as defined in ABAQUS [32]. The stress-strain material of carbon steel was modeled as having bilinear relationships, using the yield and peak strength of steel along with linear strain hardening characterized by a modulus of 2 GPa. Further details on this topic were discussed in the work of the first author [35]. Concrete damage plasticity, available in ABAQUS [32], was selected to simulate the behavior of concrete infill in HCFST slender columns. The full details regarding the stress-strain curve relationships of the infill concrete were provided in [8].

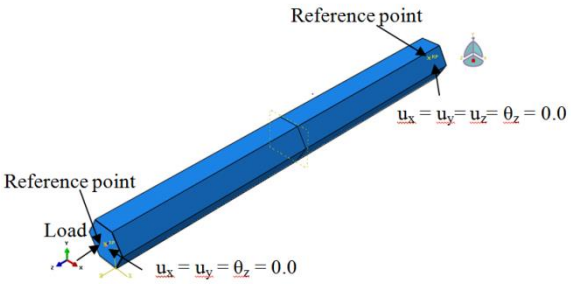

Fig. 13 Load and end conditions on HCFST slender columns

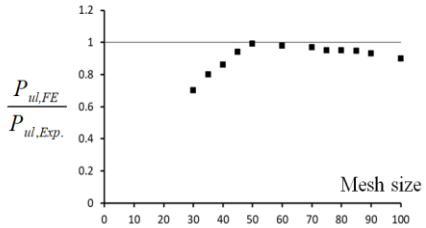

Fig. 14 Mesh sensitivity analysis of HCFST slender columns

3.2. Validation

The FE model was verified using the current HCFST slender columns experimental investigation. Other tests were used to verify the FE from previous research [29, 36].

3.2.1. Validation of the FE model using present tests

The experimental and the FE results were compared concerning ultimate axial load, load-lateral displacement relationships, load-vertical strain relationships, and load-horizontal strain relationships. The ultimate axial strength of the experimental (P_{uExp}) and FE (P_{uEF}) results is compared in Table 5. It is noteworthy that the average value of (P_{uEF}/P_{uExp}) was 0.98, with a standard deviation of (P_{uEF}/P_{uExp}) of 0.038. Therefore, the FE analysis accurately predicted the experimental results for ultimate strength. Additionally, Table 5 compares the strength of FE with the predictions of EC4 (P_{EC4}) and AISC (P_{AISC}), which will be discussed in Section 5.1.3. A comparison of the axial load against horizontal displacement relationships was also made, as shown in Fig. 15. It was observed that the FE model closely aligned with the tested results, accurately including the overall behavior of the axial load-lateral displacement curves, the initial stiffness, and the ultimate axial load. Further comparison was conducted between the axial load against vertical strain and the load against horizontal strain measured at the middle height position on both the tension and compression sides of the column; see Fig. 16. It can be noted that the FE results for vertical and horizontal strain closely matched the tested results; initial stiffness, ultimate load, and overall curve behavior. According to the experimental results, the mode of failure was identified as global buckling; see Fig. 17.

Table 5
Comparison of experimental, FE, and design methods for slender column

S Exp.	P_{uExp}[KN]	P_{uFE}	P_{EC4}[KN]	P_{AISC}[KN]	P_{uFE}	P_{Ec4} /P_{uExp}	P_{AISC}/P_{uExp}
HCFST1	772	774	586	517	1.00	0.76	0.67
HCFST1	1024	1015	917	873	0.99	0.90	0.85
HCFST1	880	862	586	546	0.98	0.67	0.62
HCFST1	1100	1052	917	843	0.96	0.83	0.74
Mean					0.98	0.79	0.72
Deviation from the mean					0.038	0.098	0.099

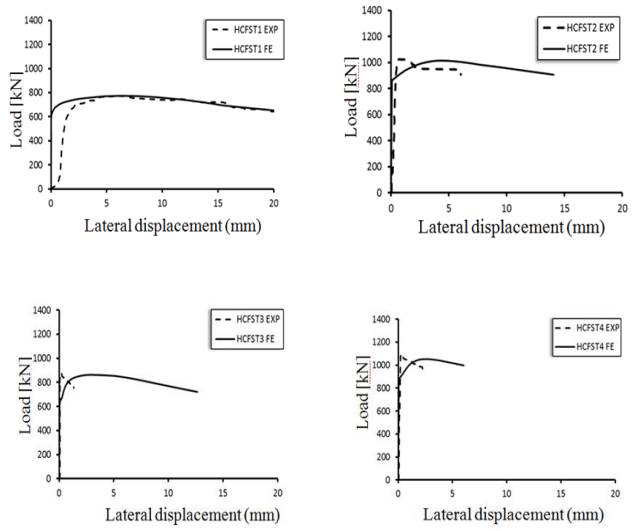

Fig. 15 load-lateral displacement relationship for HCFST slender columns

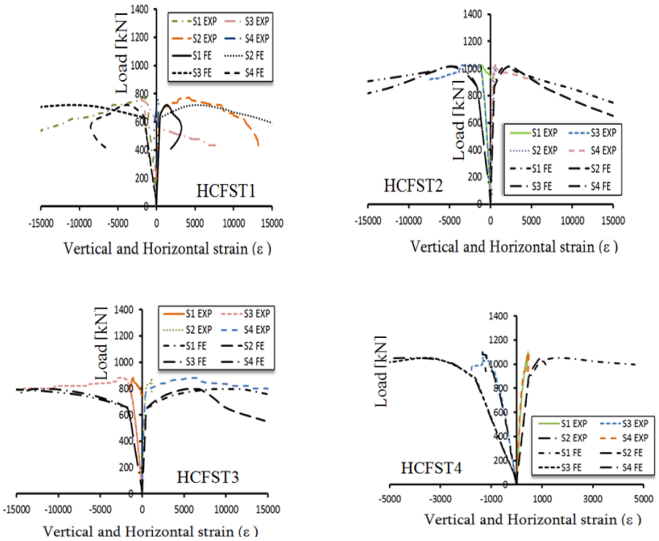

Fig. 16 Load-vertical strain and load-horizontal strain relationships for HCFST

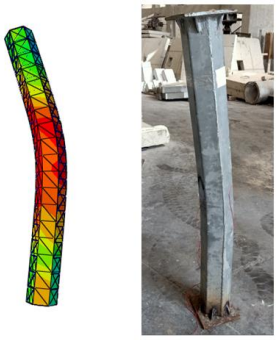

Fig. 17 Mode of failure FE and test results for the HCFST1 slender column specimen

3.2.2. Verification of results: FE and Reference [29]

The FE was validated using the experimental results from reference [29]. Three CFST slender hexagonal column specimens were used in this validation, all sharing sectional dimensions (B = 100 mm and t = 3.95 mm); see Fig. 18. Table 6 presents the geometric properties (B, t, height of column H, θ) and material properties (steel yield strength (f_{y}) and cubic strength of concrete (f_{cu})) listed.

Comparison with the testing results, including experimental axial strength (P_{uExp}), FE axial strength (P_{uFE}), and (P_{uFE}/ P_{uExp}), is depicted in Table 6. The arithmetic mean of (P_{uFE}/ P_{uExp}) was 0.93, with a deviation from the mean of 0.05, indicating a close alignment between the FE experimental axial strengths. Fig. 19 presents another comparison of the axial load against lateral deflection relationships at middle height. Consequently, the FE model accurately predicted the experimental results by accounting for the overall behavior of columns, lateral deflection curves, initial stiffness, and ultimate load.

Table 6
Dimensions and experimental and FE results for HCFST slender columns

S Exp.	*B[mm]*	*t[mm]*	*H*[mm]	f_{cu}[MPa]	f_y	P_{uExp}	P_{uFE}	P_{uFE} /P_{uExp}
HCFT1-0a	100	3.95	1500	89	278.7	2282.8	2004.9	0.88
HCFT1-0b	100	3.95	1500	89	278.7	2052.4	2004.9	0.98
HCFT3-0	100	3.95	2000	89	278.7	2357.6	2158.2	0.92
Mean								0.93
Deviation from the mean								0.05

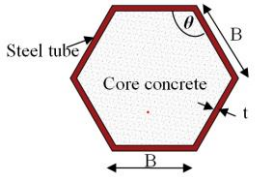

Fig. 18 Dimension of HCFST Ref [29]

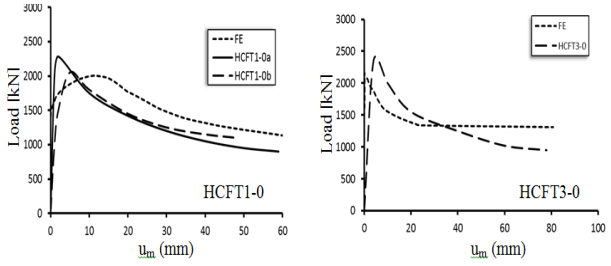

Fig. 19 Axial load–Lateral deflection at mid-height curve for specimens Ref [29]

3.2.3. Validation of the results: FE and Reference [36]

The FE was validated using the experimental results provided in reference [36]. Nine CFST slender circular columns [36] were used, with all specimens having a sectional diameter of (D = 108 mm and t = 4.5 mm), with different values of effective lengths [L_e] and slenderness ratios [λ], as detailed in Table 7. Additionally, the material characteristics (steel yield strength (f_y) and compressive strength of concrete (f_c')) were listed in Table 7. The correspondence between the experimental strength (P_{uExp}) and the FE strength (P_{uFE}) is illustrated in Table 7. The average value of (P_{uFE}/ P_{uExp}) was 0.98, with a deviation from the mean of 0.07, indicating a close match between the FE ultimate load and the experimental results. A comparison of the axial load against lateral displacement relationships at middle height is illustrated in Fig. 20. Consequently, the FE model demonstrated a close correspondence with the experimental results concerning the overall behavior of columns, lateral displacement curves, initial stiffness, and ultimate load.

The FE model yielded satisfactory results concerning the experimental data of the slender concrete-filled columns mentioned above. Consequently, the FE model of HCFST slender columns could be used to simulate the next parametric study.

Table 7
Details and comparison of experimental and FE results Ref. [36]

S Exp.	*D[mm]*	*t[mm]*	L_e[mm]	f_c[MPa]	f_y	P_{uExp}	P_{uFE}	P_{uFE} /P_{uExp}
sc154-3	108	4.5	4158	37.4	348	298	291	0.98
sc154-4	108	4.5	4158	37.4	348	280	291	1.04
sc149-1	108	4.5	4023	37.4	348	318	297	0.94
sc149-2	108	4.5	4023	37.4	348	320	297	0.93
sc141-1	108	4.5	3807	25.4	348	350	377	1.07
sc141-2	108	4.5	3807	25.4	348	370	377	1.02
sc130-1	108	4.5	3510	25.4	348	400	396	0.99
sc130-2	108	4.5	3510	25.4	348	390	396	1.02
sc130-3	108	4.5	3510	37.4	348	440	364	0.83
Mean								0.98
Deviation from the mean								0.07

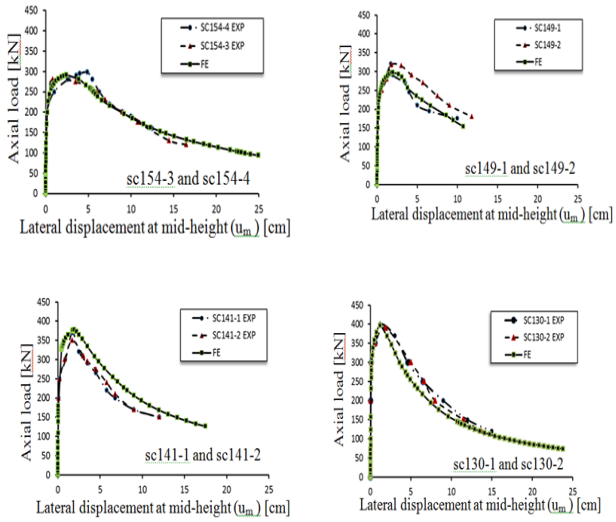

Fig. 20 Axial load–Lateral displacement at mid-height curve for specimens Ref [36]

4. Parametric study

In this part, a parametric study was conducted to simulate the behavior of HCFST slender columns utilizing the model described in the preceding section. The variables of the parametric study were the steel's cross-section (D × B), steel's cross-sectional thickness (t), height of HCFST slender columns (H), (θ of the cross-section 120º), (a = $D/2$) and slenderness ration (λ), as detailed in Tables 8 and 9. Additionally, Tables 8 and 9 presented the details on the steel columns' yield, ultimate (f_y *and* f_u), nominal compression strength of concrete, and the peak load of the FE P_{ulFE}. In this study, an initial imperfection of ($L/1000$) was considered. Young's modulus and Poison's ratio of E_s = 200 GPa and ν_s = 0.3 were respectively adopted and used.

4.1. Slenderness ratio (λ)

The steel cross-section of dimensions D × B × t (600 × 519.62 × 6mm), yield (f_y) and ultimate (f_u) strengths of the steel columns (275 and 430 MPa, respectively), and the nominal compression strength of concrete (f_c = 25

MPa) were examined in this study. Examinations were conducted across various column slenderness ratios (λ) ranging from 7.30 to 182.60, as detailed in Table 8. Therefore, a comprehensive comparison was made between very long columns that failed owing to elastic buckling and short-height columns that failed owing to inelastic buckling. The relationship between peak axial strength (P_{ulFE}) and the cross-sectional strength ($P_{Hassanein}$) [8] for different slenderness ratios (λ) is depicted in Fig. 21.

$$P_{Hassanein}=(\gamma_c f'_c+4.1 f_{rp})A_c+f_y A_s \quad (1)$$

$$f_{rp}=\begin{cases}\left(0.0491703-0.000794\frac{B+D}{2t}\right)f_{sy} & for\ 17\le\frac{B+D}{2t}<63\\ \left(0.0065311-0.0000044\frac{B+D}{2t}\right)f_{sy} & for\ 63\le\frac{B+D}{2t}\le103\end{cases} \quad (2)$$

Where A_s was a steel section area, A_c was a concrete section area, and factor, f_{rp}, was the confinement pressure of regular HCFST.

$$\lambda_{EC4}=\frac{L_e}{\sqrt{I_{DS}/A_{DS}}}\ [37] \quad (3)$$

Where L_e was the length of the effective buckling, I_{DS} was the HCFST column section's moment of inertia, and A_{DS} was the HCFST's cross-sectional area.

Fig. 21 illustrates that as the value of (λ) increased, the peak axial strength of the HCFST column decreased. Additionally, it was observed that the maximum value of λ, which describes the limit for short HCFST columns was, approximately 18. Beyond this limit, the columns were considered slender.

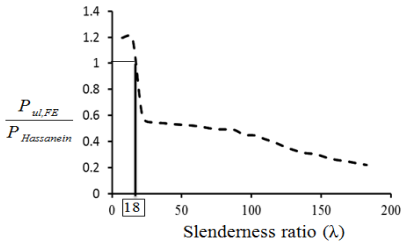

Fig. 21 Variation of the slenderness ratio (λ) with the HCFST's relative capacities

4.2. The thickness (t)

In this part, the effect of steel tube thickness (t) was studied. $D \times B$ (300 × 259.81mm) with f_y = (235, 275, 355 MPa), f_u = (360, 430, 510 MPa), f_c = (30, 40 MPa), and a height of (3000, 4000, 5000, 6000mm) were used.

Fig. 22 illustrates the relationship between lateral displacement and axial load. Generally, the peak axial load decreased as the thickness (t) of the steel tube decreased. It was observed that all curves exhibited the same trend. It is noteworthy that increasing the thickness of the steel cross-section led to an increase in the peak load for HCFST. As shown in Table 9, increasing the height of the HCFST resulted in a reduction of the peak axial load. The effect of increasing the thickness of the steel tube (t) distinctly influenced the enhancement of axial strength for shorter-height columns compared to longer-height columns. Therefore, it is recommended to increase the thickness of the tube section at short and medium heights.

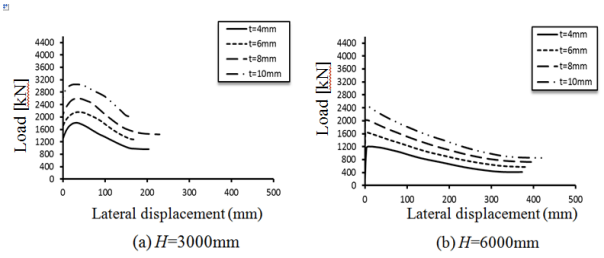

Fig. 22 Load- Lateral displacement relationship for HCFST in case f_y= 235MPa and f_c= 30MPa

4.3. Strength of steel (fy)

In this part, the influence of steel's strength [f_y] was studied. $D \times B$ (300 × 259.81mm) with [t] (4, 6, 8, 10mm), f_c = (30, 40 MPa), and a height of (3000, 4000, 5000, 6000mm) were used.

The peak axial load results for the HCFST slender columns' were presented in Fig. 23. Generally, it was observed that the peak axial load increased with increasing values of [f_y]. As shown in Table 9, increasing the height of the HCFST led to a reduction in the peak load. It was deduced from Table 9 that there was an average increase of approximately 15% in the ultimate axial load with an increase in yield strength.

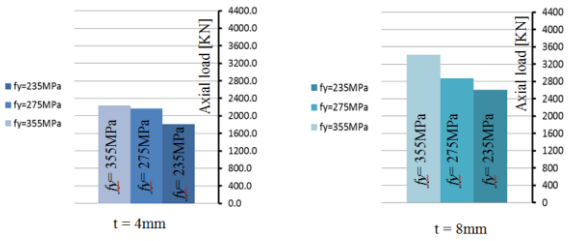

Fig. 23 Comparison of ultimate axial load for HCFST slender columns in case of; (H=3000mm and f_c= 30MPa)

4.4. Concrete strength (f_c)

In this part, the influence of concrete strength (f_c) was studied. $D \times B$ (300 × 259.81mm) with t = (4, 6, 8, 10mm), f_y = (235, 275,355 MPa), f_u = (360, 430,510 MPa) and a height of (3000, 4000, 5000, 6000mm) were used.

Fig. 24 presents the peak axial load results for the HCFST slender columns'. Generally, an increase in the steel cross-section's thickness (t) correlates with an increase in the peak axial load for HCFST slender columns. It is noteworthy that the peak axial load increases with increasing values of f_c, as illustrated in Table 9. Moreover, increasing the height of the HCFST leads to a decrease in the peak load. In reference to Fig. 24 and the results illustrated in Table 9, it is evident that the increase in peak load is clearly observed in the short-height column and could be disregarded in the long-height column regardless of changes in tube thickness. Therefore, it is recommended that in normal concrete, there is no need to increase the concrete strength (f_c).

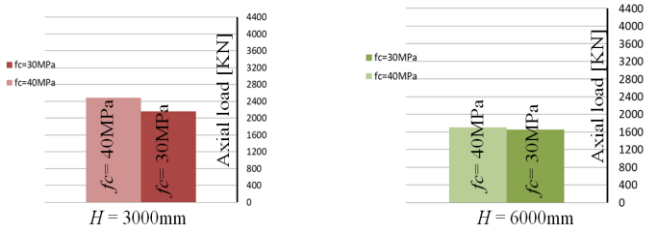

Fig. 24 Comparison of ultimate axial load for HCFST slender columns in case of; (t=6mm and f_y = 235MPa)

4.5. The height (H)

This part studied the impact of height (H). $D \times B$ (300 × 259.81mm) with f_y (235, 275,355 MPa), f_u (360, 430,510 MPa), respectively f_c (30, 40 MPa), and t (4, 6, 8, 10mm) were studied.

Fig. 25 depicts the relationship between axial load and lateral displacement. Generally, the peak load of HCFST slender columns' decreased as the height of HCFST increased. However, the decreases in the short-height column were large compared to the long-height column. The results indicate that the peak load for HCFST increased as the thickness of the steel cross-section increased, as indicated in Table 9.

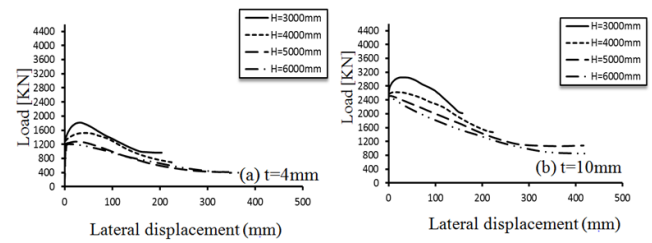

Fig. 25 Load- Lateral displacement relationship for HCFST in case f_y= 235MPa and f_c= 30MPa

Table 8
Slenderness of the HCFST columns

Column	H[mm]	$D[mm]$	$B[mm]$	t[mm]	a [mm]	f_y[MPa]	f_c[MPa]	λ	P_{uFE}[KN]
HC1	1000	600	519.62	6	300	275	25	7.30	7684
HC2	2000	600	519.62	6	300	275	25	14.60	7685
HC3	3000	600	519.62	6	300	275	25	21.90	3777
HC4	4000	600	519.62	6	300	275	25	29.20	3513
HC5	5000	600	519.62	6	300	275	25	36.50	3480
HC6	6000	600	519.62	6	300	275	25	43.80	3426
HC7	7000	600	519.62	6	300	275	25	51.10	3390
HC8	8000	600	519.62	6	300	275	25	58.40	3352
HC9	9000	600	519.62	6	300	275	25	65.70	3280
HC10	10000	600	519.62	6	300	275	25	73.00	3188
HC11	11000	600	519.62	6	300	275	25	80.30	3170
HC12	12000	600	519.62	6	300	275	25	87.60	3148
HC13	13000	600	519.62	6	300	275	25	94.90	2900
HC14	14000	600	519.62	6	300	275	25	102.20	2873
HC15	15000	600	519.62	6	300	275	25	109.50	2690
HC16	16000	600	519.62	6	300	275	25	116.85	2524
HC17	17000	600	519.62	6	300	275	25	124.15	2300
HC18	18000	600	519.62	6	300	275	25	131.45	2128
HC19	19000	600	519.62	6	300	275	25	138.75	2000
HC20	20000	600	519.62	6	300	275	25	146.00	1948
HC21	21000	600	519.62	6	300	275	25	153.35	1789
HC22	22000	600	519.62	6	300	275	25	160.65	1668
HC23	23000	600	519.62	6	300	275	25	168.00	1599
HC24	24000	600	519.62	6	300	275	25	175.30	1501
HC25	25000	600	519.62	6	300	275	25	182.60	1414

Table 9
Comparison between FE results and design methods of slender columns

Column	H[mm]	$t[mm]$	$f_y[MPa]$	$f_c[MPa]$	$P_{uFE}[KN]$	P_{Ec4}KN]	P_{AISC}[KN]	P_{Ec4} / P_{uFE}	P_{AISC} / P_{uFE}
C1	3000	4	235	30	1814	1539	1372	0.85	0.77
C2	3000	6	235	30	2161	1533	1368	0.71	0.63
C3	3000	8	235	30	2603	1528	1364	0.59	0.52
C4	3000	10	235	30	3052	1523	1360	0.50	0.45
C5	4000	4	235	30	1524	1539	1271	1.01	0.83
C6	4000	6	235	30	1887	1533	1267	0.81	0.67
C7	4000	8	235	30	2185	1528	1263	0.70	0.58
C8	4000	10	235	30	2624	1523	1259	0.58	0.48
C9	5000	4	235	30	1277	1538	1152	1.20	0.90
C10	5000	6	235	30	1694	1533	1148	0.91	0.68
C11	5000	8	235	30	2100	1528	1145	0.73	0.55
C12	5000	10	235	30	2515	1523	1141	0.61	0.45
C13	6000	4	235	30	1205	1538	1022	1.28	0.85
C14	6000	6	235	30	1650	1533	1018	0.93	0.62
C15	6000	8	235	30	2023	1528	1015	0.76	0.50
C16	6000	10	235	30	2478	1523	1011	0.61	0.41
C17	3000	4	275	30	2232	1772	1560	0.80	0.70
C18	3000	6	275	30	2484	1767	1556	0.71	0.63
C19	3000	8	275	30	2875	1762	1551	0.61	0.54
C20	3000	10	275	30	3224	1757	1548	0.55	0.48
C21	4000	4	275	30	1686	1772	1428	1.05	0.85
C22	4000	6	275	30	2094	1767	1424	0.84	0.68

C23	4000	8	275	30	2466	1762	1420	0.71	0.58
C24	4000	10	275	30	3021	1757	1416	0.58	0.47
C25	5000	4	275	30	1476	1772	1275	1.20	0.86
C26	5000	6	275	30	1984	1767	1271	0.89	0.64
C27	5000	8	275	30	2463	1762	1267	0.72	0.51
C28	5000	10	275	30	2936	1757	1264	0.60	0.43
C29	6000	4	275	30	1429	1772	1110	1.24	0.78
C30	6000	6	275	30	1899	1767	1106	0.93	0.58
C31	6000	8	275	30	2347	1762	1103	0.75	0.47
C32	6000	10	275	30	2879	1757	1099	0.61	0.38
C33	3000	4	355	30	2468	2240	1918	0.91	0.78
C34	3000	6	355	30	2884	2235	1914	0.77	0.66
C35	3000	8	355	30	3413	2230	1910	0.65	0.56
C36	3000	10	355	30	3747	2225	1905	0.60	0.51
C37	4000	4	355	30	2110	2240	1715	1.06	0.81
C38	4000	6	355	30	2580	2235	1711	0.87	0.66
C39	4000	8	355	30	3201	2230	1707	0.70	0.53
C40	4000	10	355	30	3618	2225	1702	0.61	0.47
C41	5000	4	355	30	1946	2240	1485	1.15	0.76
C42	5000	6	355	30	2437	2235	1481	0.92	0.61
C43	5000	8	355	30	3066	2230	1477	0.73	0.48
C44	5000	10	355	30	3609	2225	1473	0.62	0.41
C45	6000	4	355	30	1697	2240	1246	1.32	0.73
C46	6000	6	355	30	2361	2235	1242	0.95	0.53
C47	6000	8	355	30	2746	2230	1238	0.81	0.45
C48	6000	10	355	30	3175	2225	1234	0.70	0.39
C49	3000	4	235	40	2076	1593	1411	0.77	0.68
C50	3000	6	235	40	2489	1586	1406	0.64	0.56
C51	3000	8	235	40	2990	1580	1400	0.53	0.47
C52	3000	10	235	40	3301	1573	1395	0.48	0.42
C53	4000	4	235	40	1818	1593	1305	0.88	0.72
C54	4000	6	235	40	2016	1586	1300	0.79	0.64
C55	4000	8	235	40	2456	1580	1295	0.65	0.53
C56	4000	10	235	40	2656	1573	1290	0.60	0.49
C57	5000	4	235	40	1410	1593	1180	1.13	0.84
C58	5000	6	235	40	1804	1586	1175	0.88	0.65
C59	5000	8	235	40	2181	1580	1171	0.72	0.54
C60	5000	10	235	40	2577	1573	1166	0.61	0.45
C61	6000	4	235	40	1289	1593	1044	1.24	0.81
C62	6000	6	235	40	1701	1586	1039	0.93	0.61
C63	6000	8	235	40	2080	1580	1035	0.82	0.55
C64	6000	10	235	40	2209	1573	1031	0.71	0.47
C65	3000	4	275	40	2273	1827	1598	0.80	0.70
C66	3000	6	275	40	2648	1820	1593	0.69	0.60
C67	3000	8	275	40	3193	1813	1587	0.57	0.50
C68	3000	10	275	40	3479	1807	1582	0.52	0.45
C69	4000	4	275	40	2023	1827	1461	0.90	0.72
C70	4000	6	275	40	2245	1820	1456	0.81	0.65
C71	4000	8	275	40	2577	1813	1451	0.70	0.56
C72	4000	10	275	40	3115	1807	1446	0.58	0.46
C73	5000	4	275	40	1727	1827	1301	1.06	0.75
C74	5000	6	275	40	2027	1820	1296	0.90	0.64
C75	5000	8	275	40	2489	1813	1292	0.73	0.52

C76	5000	10	275	40	2988	1807	1287	0.60	0.43
C77	6000	4	275	40	1439	1827	1130	1.27	0.79
C78	6000	6	275	40	1963	1820	1125	0.93	0.57
C79	6000	8	275	40	2429	1813	1121	0.75	0.46
C80	6000	10	275	40	2963	1807	1117	0.61	0.38
C81	3000	4	355	40	2543	2295	1955	0.90	0.77
C82	3000	6	355	40	3122	2288	1949	0.90	0.62
C83	3000	8	355	40	3729	2281	1944	0.73	0.52
C84	3000	10	355	40	4222	2274	1938	0.61	0.46
C85	4000	4	355	40	2270	2295	1745	1.01	0.77
C86	4000	6	355	40	2750	2288	1740	0.83	0.63
C87	4000	8	355	40	3312	2281	1735	0.69	0.52
C88	4000	10	355	40	3665	2274	1729	0.62	0.47
C89	5000	4	355	40	1909	2295	1509	1.59	1.05
C90	5000	6	355	40	2575	2288	1503	1.17	0.77
C91	5000	8	355	40	3148	2281	1498	0.94	0.62
C92	5000	10	355	40	3473	2274	1493	0.77	0.50
C93	6000	4	355	40	1746	2295	1262	1.31	0.72
C94	6000	6	355	40	2446	2288	1258	0.94	0.51
C95	6000	8	355	40	2745	2281	1253	0.83	0.46
C96	6000	10	355	40	3210	2274	1249	0.71	0.39
Mean								0.81	0.60
Standard deviation								0.22	0.14

5. Design methods

5.1. Available design methods

In this part, available design strength methods for CFST slender columns were discussed in the case of compact cross-sections.

5.1.1. EN 1994-1-1(EC4) [37]

For a CFST column's ultimate axial capacity, used the EN 1994-1-1 (EC4) [37] equation (P_{EC4}) as known by Eq. (4).

$$P_{Ec4}=\chi P_{pl,Rd} \tag{4}$$

Where $P_{pl,Rd}$ was the plastic strength to axial compression with consideration for the confinement concrete when the ratio of slenderness (λ) did not exceed 0.5, as seen in the following:

$$P_{pl,Rd}=\begin{cases} A_c f'_c(1+\eta_a \frac{t}{D}\frac{f_y}{f'_c})+A_s f_y & : \lambda' \le 0.5 \\ A_c f'_c+A_s f_y & : \lambda' > 0.5 \end{cases} \tag{5}$$

$$\eta_a=0.25(3+2\lambda')\le 1.0 \tag{6}$$

$$\eta_c = 4.9 - 18.5\lambda' + 17\lambda'^2 \ge 0 \tag{7}$$

$$\lambda'=\sqrt{\frac{P_{pl,Rd}(6.30)}{P_{cr}}} \tag{8}$$

$$P_{pl,Rd}(6.30)=0.85 f_c A_c + f_y A_s \tag{9}$$

$$P_{cr}=\frac{\pi^2 (EI_{eff})}{(L_e)^2} \tag{10}$$

$$EI_{eff}=E_s I_s+k_e E_c I_c \tag{11}$$

$k_e = 0.6$

Where (EI_{eff}) was the effective elastic flexural stiffness, L_e was the element's effective height, P_{cr} was the elastic critical buckling, and k_e was a correction factor.The reduction factor (χ) was:

$$\chi=\frac{1}{(\phi+\sqrt{\phi^2-\lambda'^2})}\le 1.0 \tag{12}$$

$$\phi=0.5(1+\alpha(\lambda'-\lambda'_0)+\lambda'^2) \tag{13}$$

$\alpha = 0.34$

$\lambda'_o=0.2$

5.1.2. AISC specification [38]

Provided the equation for a CFST column's ultimate axial capacity (P_{AISC}) by the AISC specification [38] Eq. (14).

$$P_{AISC}=\begin{cases} P_{no}\left[0.658^{(P_{no}/P_e)}\right] & : \frac{P_{no}}{P_e}\le 2.25 \\ 0.877 P_e & : \frac{P_{no}}{P_e}>2.25 \end{cases} \tag{14}$$

$$P_{no}=0.85 A_c f'_c + A_s f_y \tag{15}$$

$$EI_{eff}=E_s I_s+C_1 E_c I_c$$

C1 = 0.7

5.1.3. Comparison and discussion

In this section, an initial comparison was conducted between the peak design strength of square CFST slender columns and the experimentally determined peak strength of HCFST slender columns, as explained in Section 2.3. Table 5 displays a comparison of the experimental results with the peak load calculated by EC4 and AISC. The average peak load ratio of the P_{EC4} [37] to the experimental (P_{Ec4}/P_{uExp}) was 0.79, with a deviation from the mean of 0.098. Additionally, the ratio of P_{AISC} [38] to the experimental (P_{AISC}/P_{uExp}) had mean of 0.72, with a standard deviation of 0.099. Secondly, comparisons were made between the peak design strength of square CFST slender columns and the parametric study conducted using the FE model of HCFST slender columns. Table 9 displays a comparison of the FE results with the ultimate load as determined by EC4 and AISC. The average peak load ratio of the P_{EC4} [37] and FE results (P_{Ec4}/P_{uExp}) was 0.81, with a standard deviation of 0.22. Similarly, the average ultimate load ratio between the P_{AISC} [38] and the FE results (P_{AISC}/P_{uExp}) was 0.60, with a deviation from the mean of 0.14. Based on the results in Tables 5 and 9, it was observed that the design strength derived from the EN 1994-1-1 (EC4) design method gave unconservative results for smaller thicknesses (4mm) of steel tubes, while it provided conservative results for larger thicknesses of steel tubes in HCFST slender columns. Conversely, the AISC specification yielded conservative results across all thicknesses of steel tubes for HCFST slender columns. From the previous comparison, it was concluded that AISC can be used for tubes with small thicknesses up to 4mm, while EC4 is suitable for tubes with thicknesses above 4mm.

6. Conclusions

An experimental and FE model investigation of axially loaded HCFST slender columns has been provided in this paper. The experiments and the FE model aim to study the impact of both the cross-section and concrete strength on the strength and behavior of HCFST slender columns.

Building upon the present experimental results and FE model investigations, the following conclusions could be drawn:

1. It is noted that the ultimate load values for hexagonal slender columns increased with the increase in cross- sectional dimensions. However, it was observed that reducing the height of HCFST slender columns led to an increase in ultimate load values.

2. The mode of failure observed in the present HCFST slender columns was predominantly global buckling, a phenomenon consistently observed for all columns, particularly in column HCFST1.

3. The experimental results provided a reliable prediction of the FE model's peak axial strength. The observed mode of failure, consistent with the experimental results, was global buckling.

4. It was determined that the maximum value of λ, representing the limit of short HCFST columns, was approximately 18. Beyond this limit, the columns were considered slender.

5. The peak axial load for HCFST slender columns increased as the values of (t, f_c, and f_y) increased.

6. Increasing the thickness of the steel tube (t) had a clear effect on enhancing the axial strength of shorter-height columns compared to longer-height columns. Consequently, it is recommended to increase the thickness of the tube section at short and medium heights.

7. It is noted that there was an average increase of approximately 15% in the peak axial load associated with an increase in yield strength.

8. It was observed that the increase in peak axial load was clearly evident in the short-height column and could be disregarded in the long-height column, irrespective of changes in tube thickness. Therefore, it can be recommended that there is no need to increase the concrete's strength (f_c) in normal concrete.

9. It was observed that the design strength based on the EC4 design method yielded unconservative results for smaller thicknesses (4mm) of steel tubes while providing conservative results for larger thicknesses of steel tubes in HCFST slender columns. Conversely, the AISC specification yielded conservative results across all thicknesses of steel tubes for HCFST slender columns.

Recommendations

1- It is recommended to increase the tube thickness for columns of short and medium heights.
2- It is advisable that in normal concrete, there is no need to increase the concrete's strength (f_c).
3- It is recommended to use the design strength specifications of AISC for tubes with thicknesses up to 4mm and EC4 for tubes with other thicknesses.

Finally, it is recommended to conduct additional experimental tests to examine the analysis of HCFST slender columns using high-strength concrete and steel with various cross-sections.

References

[1] Xu W, Han L-H, Li W. " Performance of hexagonal CFST members under axial compression and bending" , J Constr Steel Res Vol. 123, pp. 162–175, 2016.
[2] Sakino K, Nakahara H, Morino S, and Nishiyama I. "Behavior of centrally loaded concrete-filled steel-tube short columns", Journal of Structural Engineering Vol. 130(2), pp. 180-188, 2004.
[3] Ding F-X, Li Z, Cheng S, and Yu Z-W. "Composite action of octagonal concrete-filled steel tubular stub columns under axial loading", Thin-Walled Structures Vol.107, pp.453-461,2016.
[4] Hassanein MF, Patel VI, Elchalakani M, and Thai H-T. "Finite element analysis of large diameter high strength octagonal CFST short columns", Thin-Walled Structures Vol.123, pp.467-482, 2018.
[5] Zhu J-Y and Chan T-M. "Experimental investigation on octagonal concrete filled steel stub columns under uniaxial compression', Journal of constructional steel research. Vol.147, pp.457-467, 2018.
[6] Ahmed M and Liang QQ. "Numerical modeling of octagonal concrete-filled steel tubular short columns accounting for confinement effects", Engineering Structures Vol.226, pp.111405,2020.
[7] Ding F-X, Li Z, Cheng S, and Yu Z-W. "Composite action of hexagonal concrete-filled steel tubular stub columns under axial loading", Thin-Walled Structures Vol.107, pp.502-513,2016.
[8] Hassanein, M.F., Patel, V.I., and Bock, M.," Behaviour and design of hexagonal concrete-filled steel tubular short columns under axial compression ", Engineering Structures, Vol. 153, pp. 732-748, 2017
[9] Liu J, Li Z, and Ding F-X. "Experimental Investigation on the Axially Loaded Performance of Notched Hexagonal Concrete-Filled Steel Tube (CFST) Column" Advances in Civil Engineering; Vol.2612536, 2019.
[10] Ahmed M and Liang QQ. "Numerical analysis of concentrically loaded hexagonal concrete-filled steel tubular short columns incorporating concrete confinement", Advances in Structural Engineering 13694332211004111, 2021.
[11] Wang Z, Chen J, Xie E, and Lin S," Behavior of concrete-filled round-ended steel tubular stub columns under axial compression", Journal of Building Structures Vol. 35(7), pp. 123-130 (Chinese), 2014.
[12] Hassanein MF and Patel VI," Round-ended rectangular concrete-filled steel tubular short columns: FE investigation under axial compression", Journal of Constructional Steel Research Vol.140, pp. 222-236, 2018.
[13] Piquer A, Ibañez C, and Hernández-Figueirido D," Structural response of concrete-filled round-ended stub columns subjected to eccentric loads", Engineering Structures Vol.184, pp. 318-328, 2019.
[14] Ahmed M and Liang QQ. "Numerical analysis of thin-walled round-ended concrete-filled steel tubular short columns including local buckling effects", Structures Vol.28, pp. 181-196, 2020.
[15] Ahmed M, Ci J, Yan X-F, and Chen S. "Nonlinear analysis of elliptical concrete-filled stainless steel tubular short columns under axial compression", Structures Vol.32, pp. 1374-1385, 2021.
[16] Ahmed M and Liang QQ. "Computational simulation of elliptical concrete-filled steel tubular short columns including new confinement model". Journal of Constructional Steel Research, Vol.174, pp. 106294, 2020.
[17] Cai Y, Quach W-M, and Young B. "Experimental and numerical investigation of concrete-filled hot-finished and cold-formed steel elliptical tubular stub columns". Thin-Walled Structures, Vol.145, pp. 106437, 2019.
[18] Hassanein MF, Patel VI, El Hadidy AM, Al Abadi H, and Elchalakani M. " Structural behaviour and design of elliptical high-strength concrete-filled steel tubular short compression members", Engineering Structures, Vol.173, pp. 495-511, 2018.
[19] Lam D, Gardner L, and Burdett M. "Behaviour of axially loaded concrete filled stainless steel elliptical stub columns. Advances in Structural Engineering", Vol.13(3) , pp. 493-500, 2010 .
[20] Ci J, Chen S, Jia H, Yan W, Song T, and Kim K-S. Axial compression performance analysis and bearing capacity calculation on square concrete-filled double-tube short columns. Marine Structures, Vol.72, pp. 102775, 2020.
[21] Pei WJ, Research on mechanical performance of multibarrel tube-confined concrete columns. Chang'an University, Xian, China, ME Thesis, 2005.
[22] Qian J, Zhang Y, Ji X, and Cao W. Test and analysis of axial compressive behavior of short composite-sectioned high strength concrete filled steel tubular columns. Journal of Building Structures, Vol.32(12) , pp.162-169 (in Chinese), 2011.
[23] Qian J, Zhang Y, and Zhang W. Eccentric compressive behavior of high strength concrete filled double-tube short columns. Journal of Tsinghua University (Science and Technology), Vol.55(1) , pp.1-7 (in Chinese), 2015.
[24] Xiong MX, Xiong DX, and Liew JYR. Behaviour of steel tubular members infilled with ultra high strength concrete. Journal of Constructional Steel Research, Vol.138, pp.168-183, 2017 .
[25] Ahmed M, Liang QQ, Patel VI, and Hadi MNS. Experimental and numerical studies of square concrete-filled double steel tubular short columns under eccentric loading. Engineering Structures, Vol.197, pp.109419, 2019.
[26] Dundu, M., " Column buckling tests of hot-rolled concrete filled square hollow sections of mild to high strength steel" Engineering Structures, Vol. 127, pp. 73-85, 2016.
[27] X.H. Dai, D.Lam, N.Jamaluddin, J.Ye " Numerical analysis of slender elliptical concrete filled columns under axial compression ", Thin-Walled Structures, Vol. 77, pp. 26-35, 2014.
[28] Ahmed M, Liang QQ, Patel VI, and Hadi MNS. "Nonlinear analysis of square concrete-filled double steel tubular slender columns incorporating preload effects". Engineering Structures, Vol.207, pp. 110272, 2020.
[29] Wang, Z.B. , Tao, Z., Yu, Q. , GuoJ-T. "Behavior of hexagonal concrete-filled steel corner columns under eccentric compression", Journal of Constructional Steel Research, Vol. 200, pp. 107659, 2023.
[30] ECP 2001: "Egyptian Code of Practice for Reinforced Concrete Construction", Code No. 203, Cairo, Egypt, 2001.
[31] Australian Standard, "Methods for tensile testing of metals", AS 1391. Sydney, Australia,

Standards Association of Australia, 1991.
[32] ABAQUS Standard, User's Manual The Abaqus Software is a product of Dassault Systèmes Simulia Corp., Providence, RI, USA Dassault Systèmes, Version 6.8,USA, 2008.
[33] Hassanein M.F., Kharoob, O.F.," Analysis of circular concrete-filled double skin tubular slender columns with external stainless steel tubes", Thin-Walled Structures, Vol. 79, pp. 23-37, 2014.
[34] Hassanein M.F., Kharoob, O.F.,Liang, Q.Q.,"Behaviour of circular concrete-filled lean duplex stainless steel–carbon steel tubular short columns" Eng. Struct Vol .56 , pp.83–94, 2013.
[35] Hassanein M.F., Kharoob, O.F., Q.Q. Liang"Circular concrete-filled double skin tubular short columns with external stainless steel tubes under axial compression, Thin-Walled Structures, Vol. 73, pp. 252-263, 2013.
[36] Han, LH., "Tests on concrete filled steel tubular columns with high slenderness ratio", Advances in Structural Engineering, Vol. 3(4), pp. 337-344, 2000.
[37] EN 1994-1-1: Eurocode 4. Design of composite steel and concrete structures. Part 1. 1, general rules and rules for buildings. European Committee for Standardization, 2004
[38] AISC, Specification for Structural Steel Buildings, AISC, Chicago, IL, USA, 2016.

Advanced Steel Construction – Vol. 20 No. 4 (2024) 330–344
DOI:10.18057/IJASC.2024.20.4.2

STUDY OF MECHANICAL PROPERTIES OF A NOVEL COLUMN-BEAM-COLUMN PREFABRICATED STEEL FRAME JOINT

Zhi-Wei Zhang [1], Dong Li [2,*], Hua-Jie Wang [1,*], Hong-Liang Qian [1], Wen-Qi Fang [1], Xiao-Fei Jing [3] and Feng Fan [4]

[1] *Department of Civil Engineering, Harbin Institute of Technology at Weihai, Weihai 264209, China*
[2] *Weihai construction group Co., Ltd., Weihaig, China*
[3] *China State Construction first Bureau Co., Ltd., Beijing, China*
[4] *School of Civil Engineering, Harbin Institute of Technology, Harbin, China*
** (Corresponding author: E-mail: 40256724@qq.com; huajie_wang@hit.edu.cn)*

ABSTRACT

Currently, most research on prefabricated steel frame joints focuses on column-column or beam-column connections. However, there has been a lack of effective research on prefabricated column-beam-column joints with higher construction efficiency. In this paper, we present the construction and installation process and technical characteristics of a novel prefabricated column-beam-column joint (NPJ). Initially, we describe the technical specifications of the NPJ. Following this, we examine the mechanical performance of the NPJ using a validated finite element model and conduct a detailed analysis of various parameters affecting its performance. Subsequently, we propose a simplified method for calculating the performance of the NPJ, adhering to existing design codes. Our findings indicate that the NPJ exhibits robust mechanical properties, closely matching those of traditionally welded joints. Notably, the height of the beam emerges as a critical factor influencing the NPJ's load-bearing capacity, more so than the thickness of the lug. This research offers valuable insights and technical guidance for further exploration and practical application of prefabricated steel frame joints.

ARTICLE HISTORY

Received: 19 October 2023
Revised: 27 February 2024
Accepted: 4 March 2024

KEYWORDS

Prefabricated;
Column-beam-column joint;
Mechanical properties;
Finite element analysis;
Simplified calculation method

1. Introduction

Prefabricated steel structures, characterized by their components being manufactured in a factory setting prior to assembly on-site through bolting mechanisms, have garnered considerable interest in recent years. This heightened attention can be attributed to their notable advantages, including enhanced construction efficiency, consistent installation quality, and environmental sustainability [1]. Within these structures, joints play a pivotal role, bearing the brunt of complex forces [2,3]. Given the critical nature of these forces, it becomes imperative to pursue rigorous research focused on the joints within prefabricated steel structures.

Recent explorations into prefabricated steel joints for precast concrete structures have attracted considerable scholarly attention, evidenced by a series of investigations aiming to enhance structural resilience and efficiency [4,5]. Despite these advancements, the field's understanding is still evolving, with several studies identifying critical limitations.

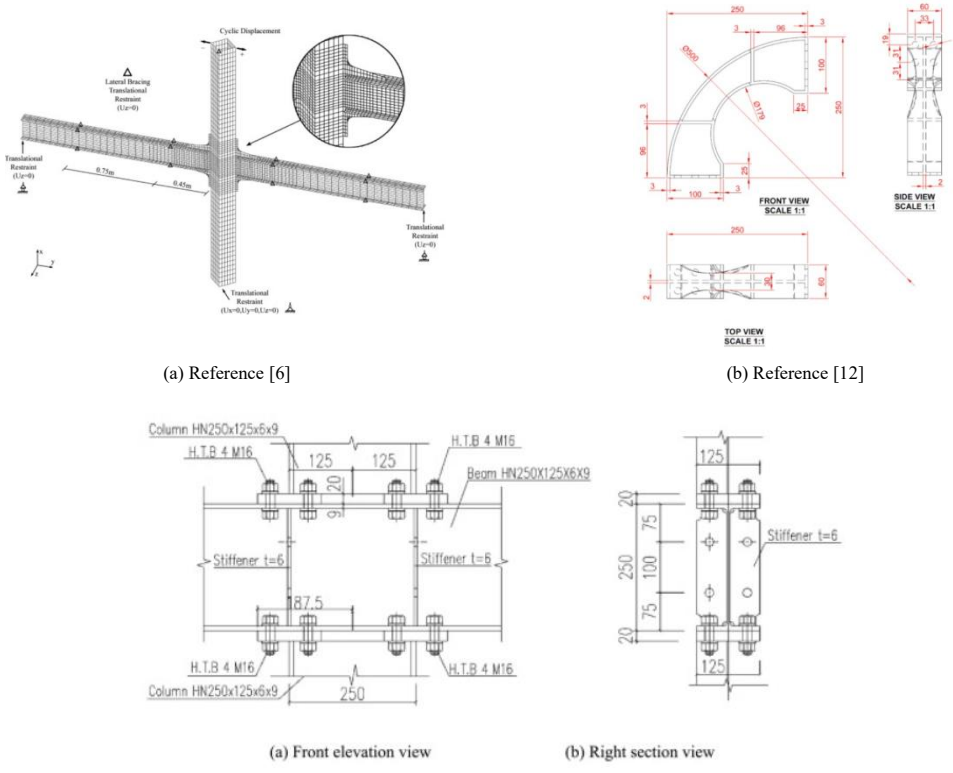

(a) Reference [6] (b) Reference [12]

(a) Front elevation view (b) Right section view

(c) Reference [15]

Fig. 1 Prefabricated beam-column joints

Notably, Torabian et al. [6] introduced an innovative diagonal connection-type joint, which exhibited notable ductility in experimental settings. However, its complex design and unconventional approach to beam and column integration raised questions regarding its feasibility in standard construction practices [7]. Alternatively, Laiyun [8], Xiantie [9], and Zhouhong [10] presented a methodology for attaching the column to an end-plate via a

perforated split bolt, a technique demanding precise alignment of bolt holes, thus complicating its practical application. Further contributions by Jian et al. [11] entailed the development of a vertical connection node utilizing high-strength bolts, which, despite its innovative integration of a steel frame, pre-embedded edge steel frame, and steel casing, revealed that its seismic resilience requires enhancement. The incorporation of dampers into beam-column joints has been proven to significantly improve seismic performance [12-14], yet the high costs associated with this solution limit its widespread adoption. Hongkai et al. [15] proposed a moment-resisting joint designed for H-beam-columns, which demonstrated effective seismic capabilities in testing phases. However, the limited use of H-columns in practical engineering scenarios may restrict its applicability. The discourse has also extended to the replaceability of prefabricated beam-column joints post-earthquake [16-18], suggesting that positioning the connection near the column's end could facilitate easier replacement following seismic events [17, 19]. Regarding simplified calculations, there exists a consensus that most have been formulated in alignment with established design codes [20-22], underscoring a commitment to aligning innovative joint designs with regulatory standards and practical feasibility.

Recent studies on prefabricated frame joints have primarily concentrated on connections between beams and columns or between columns themselves. In contrast, the integrated column-beam-column joint offers a solution that addresses both vertical and horizontal connections within a steel frame structure using a single joint, significantly enhancing construction efficiency. Despite its potential, there has been limited effective research on these integrated joints [23], with existing studies narrowly focusing on specific mechanical properties [24], without a comprehensive overview.

To address these gaps, this research introduces a new type of prefabricated column-beam-column joint, named the novel prefabricated joint (NPJ). We detail the design, construction, and technical features of the NPJ. Following this, we developed and verified a detailed finite element model for the joint. Our investigation covers both static and seismic behaviors of the NPJs, comparing these properties to those of traditional welded joints. We also conducted parametric studies to understand how different geometric factors affect the NPJs' performance. Concluding our study, we propose simplified methods for estimating the load-bearing capacity and initial stiffness of NPJs, based on standard design code formulas. This work aims to serve as a useful resource for future research and practical applications of prefabricated steel frame joints.

2. Novel prefabricated joints

Building on existing prefabricated beam-column joint designs, the authors have made enhancements [24], creating an innovative joint that supports beams of varying heights. This joint is ingeniously constructed from four key prefabricated parts:

(1) **Lower Column**: Includes a flange end plate and a lug, the latter designed with an extension bolt hole for secure attachment.

(2) **Connector**: This piece links the H-shaped steel beam to the lower column's lug, ensuring a stable connection.

(3) **H-shaped Steel Beam**: Features an end plate for easy integration into the joint structure.

(4) **Upper Column**: Comes with a bolt hole and an upper column flange plate to complete the assembly.

The installation process is straightforward and efficient. It begins with attaching the lower connector to the column's lug plate using friction-type high-strength bolts. Next, the H-beam is positioned on top of the lower connector and secured with compression-type high-strength bolts. Finally, the beam is joined to the upper connector and lug plate with similar bolts, ensuring a firm assembly. This process, detailed in Fig. 2, showcases the methodical steps taken to assemble this advanced joint.

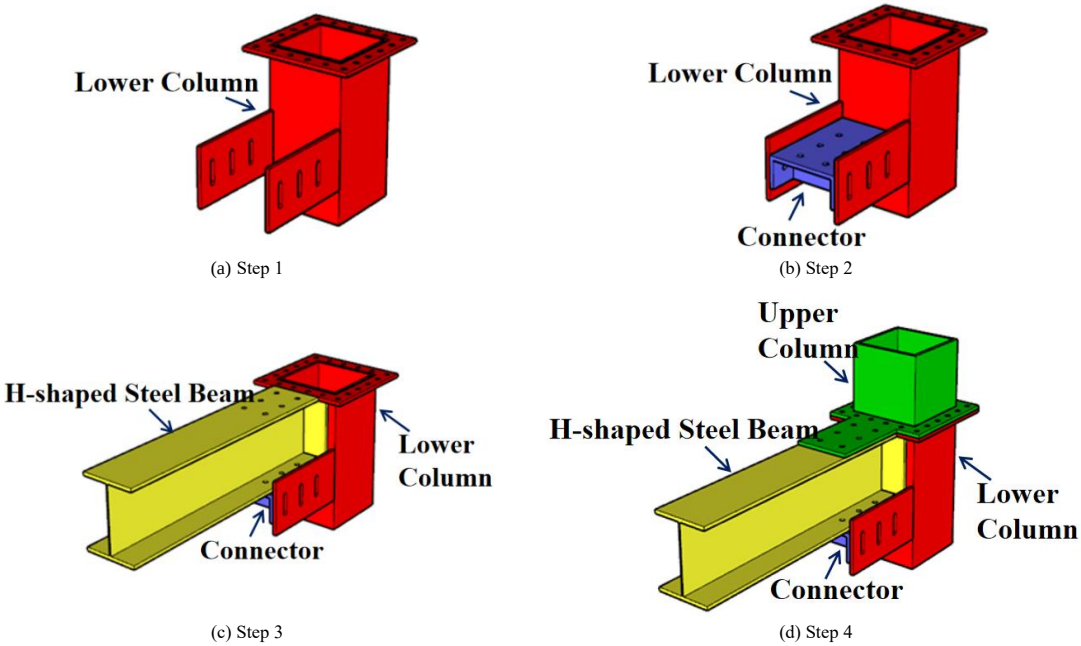

(a) Step 1 (b) Step 2

(c) Step 3 (d) Step 4

Fig. 2 Composition of joints and installation process

The NPJs offer significant technical advantages compared to welded steel frame joints and other prefabricated beam-column joints:

(1) The construction process is straightforward. Both the column-to-column and column-to-beam connections are facilitated by a single joint, leading to a high level of prefabrication. The design also allows for the accommodation of H-shaped steel beams of varying section heights by adjusting the position of the lower connectors.

(2) The quality of construction is dependable. Components are pre-manufactured in a factory setting and assembled on-site using high-strength bolts, eliminating the inconsistencies associated with on-site welding.

(3) The path for force transfer is efficiently designed. The incorporation of lugs and lower connectors on the column enables shear force transfer while preventing the weakening of the column section that can occur with bolt holes. This ensures a reliable load transfer mechanism.

(4) Disassembly and replacement are made easy. Unlike other prefabricated joints, this innovative joint combines the column-to-column and column-to-beam connections at a single floor level. Its high level of prefabrication also allows for the selective replacement of beam and column components during maintenance or service.

3. Establishment and validation of the finite element model

Finite element analysis is a common method of studying the mechanical properties of steel members. In this study, the widely adopted finite element simulation software, ANSYS, was employed.

3.1. Joint dimensions and materials

For a common three-story steel frame structure, one was chosen to numerically analyze the mechanical properties of the edge joints in the middle layer of the outer frame. The joint locations are depicted in Figure 3. Based on a typical joint cross-section, the column's cross-sectional dimensions were chosen to be 400*400*20 mm, and the beam's cross-section was selected as

H400*300*8*20 mm. The lug's connection to the joint employs high-strength friction-type bolts, while the remaining component connections utilize high-strength compression-type bolts. Fig. 4 shows the detailed dimensions of the joints.

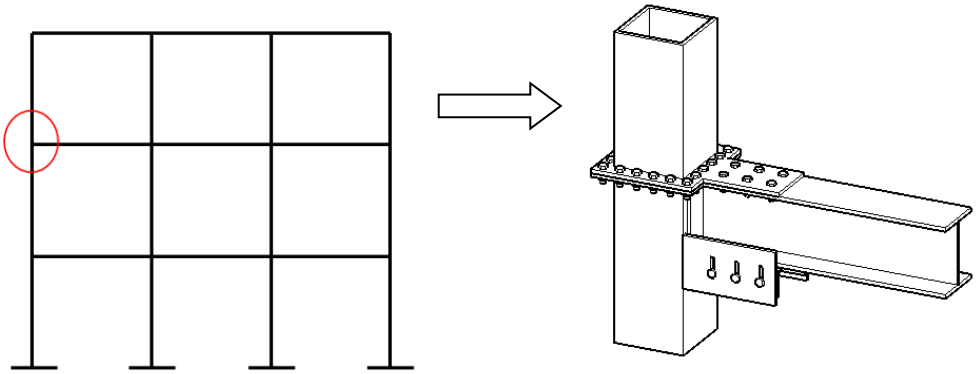

Fig. 3 Location of the joint selection

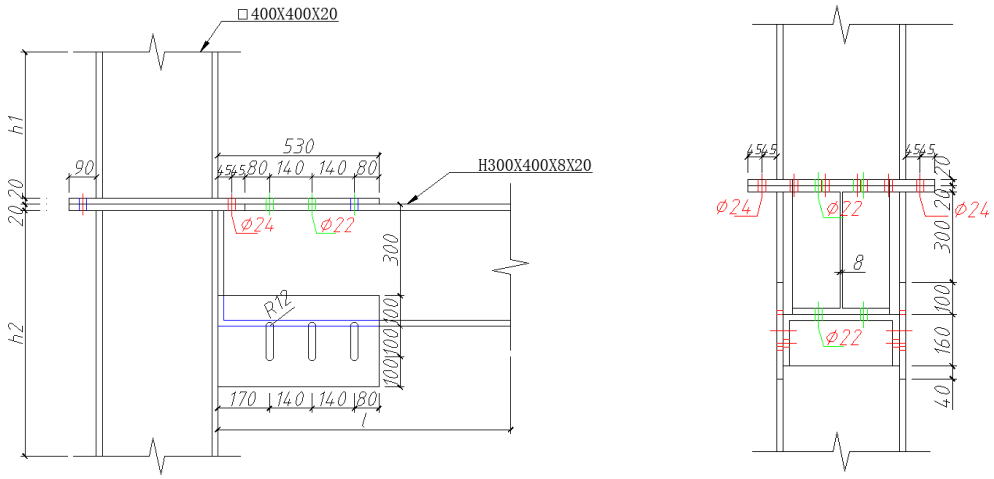

Fig. 4 Dimensions of the joints (in mm)

Table 1
Material properties

Material	Yield strength (MPa)	Ultimate strength(MPa)	Poisson ratio	Yield strain	Modulus of elasticity (GPa)	Tangential modulus (GPa)
Q355 steel	345	500	0.3	0.167	206	4.12
Grade 10.9 Bolt	900	1000	0.3	0.437	206	4.12

The components of the typical joints are made of Q355 steel, and the bolts are all of grade 10.9. The property parameters of both materials are shown in Table 1.

3.2. Finite element models

To incorporate the steel's strengthening effect, the simulation utilized a bilinear follow-through strengthening criterion, with a bilinear model selected for the steel's stress-strain curve, as illustrated in Fig. 5. The joint was modeled using the SOLID 45 element, capable of simulating the plastic stress stiffening of steel. The model's elements were meshed using hexahedral mapping, with denser meshing in areas experiencing high stresses and complex stress patterns, as demonstrated in Fig. 6.

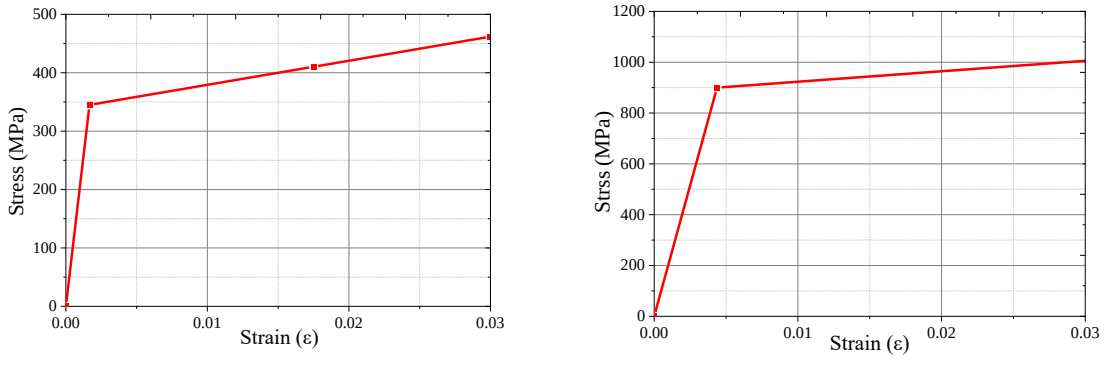

(a) Q345 steel

(b) Grade 10.9 bolt

Fig. 5 Stress–strain curves of the materials

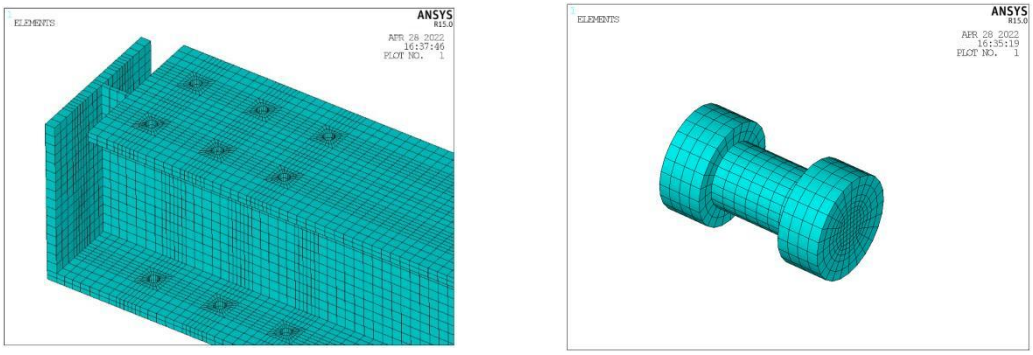

(a) Beam (b) Bolt

Fig. 6 Meshing of the model

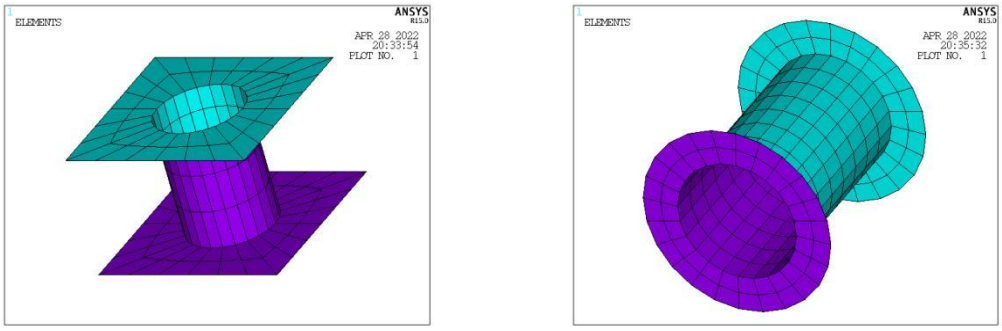

(a) CANTA174 elements (b) TARGE170 elements

Fig. 7 Set-up of the contact elements in the bolt area

To enhance computational efficiency, the bolt shaft is represented as a cylinder, omitting the threads in the bolt modeling process. Given the high strength of the steel frame joints and minimal penetration during contact, CANTA174 and TARGE170 elements were chosen for the contact and target surfaces, respectively, as depicted in Fig.7. The rolled surfaces of each member were not specially processed, and a slip resistance factor of 0.35 was adopted, as referenced in the literature [11,19,25].

High tensile strength bolts are preloaded prior to installation using PRETS179 units. According to the steel design code [26], the preload force is set at 190 kN for M22 class 10.9 high-strength bolts and 225 kN for M24 high-strength bolts. Preload elements are positioned at the slab's contact surface. The joints' top and bottom column ends are fixedly restrained, and a downward displacement load is applied at the beam's end. The model's meshing employs the hexahedral mapping method preset in ANSYS finite element software, with the node model pre-divided to adhere to the hexahedral mapping delineation principle. Fig. 8 displays the comprehensive finite element model of the joint.

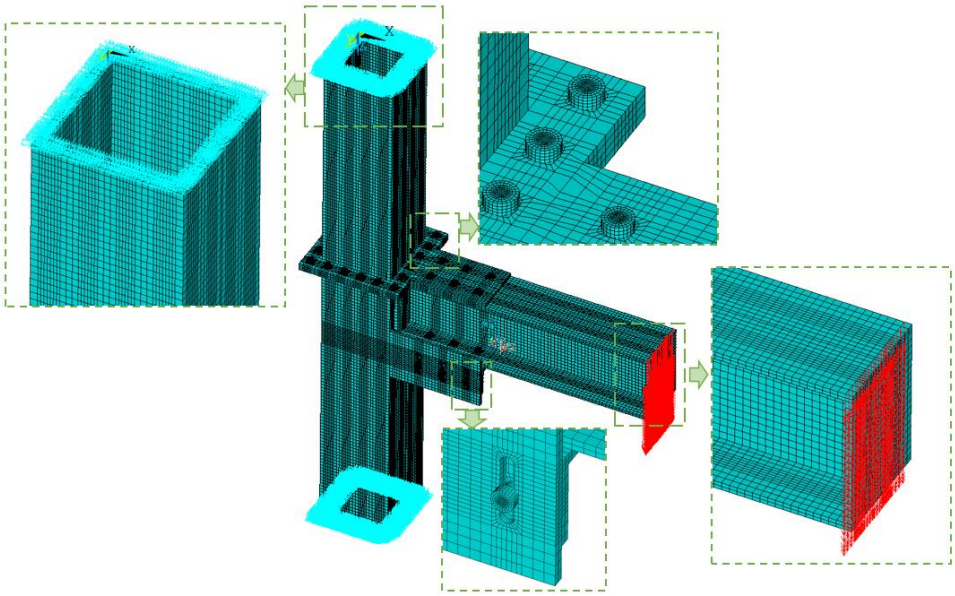

Fig. 8 Overall finite element model

3.3. Model validation

To validate the appropriateness of the chosen setting parameters, a static load test [27] on a prefabricated beam-column joint, similar to the innovative joint introduced in this study, was selected for simulation and subsequent data comparison. Fig. 9 illustrates the experimental setup, where the column's bottom end is attached to a counterframe during the test, and the beam's left side is hinged to this counterframe. A vertical load is then applied to the beam's end using a jack. According to reference [27], the joint underwent detailed finite element modeling, with the established model showcased in Fig. 10.

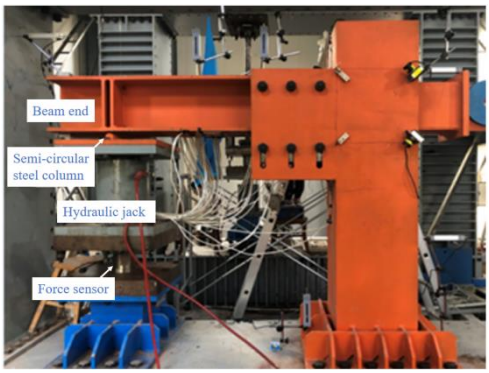

Fig. 9 Test set-up

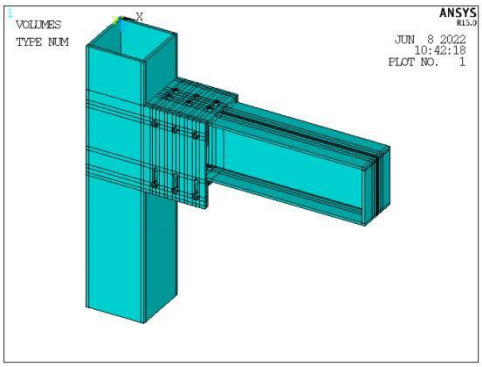

Fig. 10 Finite element model of the joint

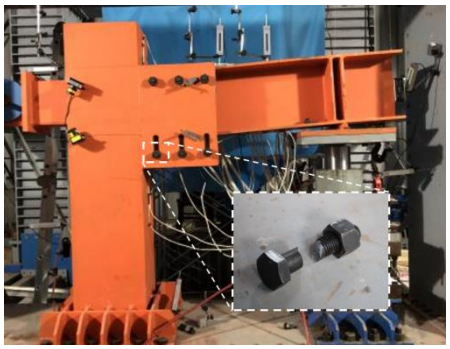

Fig. 11 Ultimate state of the joint

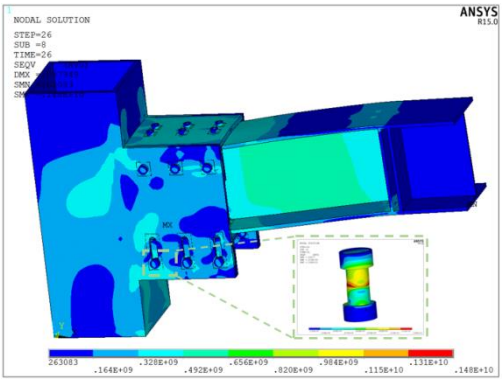

Fig. 12 Stress nephogram

Table 2
Mechanical properties of the joint

	Initial stiffness K_1 (MN·m/rad)	Ultimate bending moment Mu (kN·m)	Ultimate angle θ_u (rad)
FEM	18.7	530.4	0.098
Test[27]	18.5	493.0	0.096

Fig. 11 displays the joint's ultimate state as observed in the experiment. Upon reaching the ultimate load, the beam noticeably displaces upward, with the primary mode of damage being tensile shear failure of the beam's lower flange bolts. The stress distribution, illustrated in Fig. 12 through a stress nephogram from the finite element analysis, closely aligns with the experimental outcomes. Notably, the simulation identified the maximum stress occurring at the lower flange bolt hole of the beam, peaking at 835 MPa, indicating bolt failure. This analysis confirms that the finite element model accurately captures the stress state and damage mode of the joint.

The mechanical properties analyzed for the joints in this study encompass stiffness, yield strength, ultimate strength, among others, as cited in references [27,28]. Table 2 presents a comparison of the mechanical properties derived from finite element simulations against experimental data. The close alignment between the finite element simulation outcomes and the experimental results demonstrates the accuracy of the FEM analysis in evaluating the performance of the joint.

4. Static performance

4.1. Mechanical response of NPJs

The bending moment and rotation curve of the newly designed prefabricated joint (NPJ) under static load is depicted in Fig.13, revealing a distinct nonlinear segment that highlights the NPJ's substantial capacity for plastic deformation. Fig.14 illustrates the joint's stress state at failure, pinpointing high stress concentrations in the beam's web, at the interface between the upper column and the flange plate, and at the lower column's section contacting the beam. During joint failure, the stress in the column remains relatively low, not exceeding the material's yield strength. Significant stresses are noted at the connection between the upper column and the flange plate, and near the bottom edge of the lower column lug plate, though these do not lead to notable changes in the member's shape. The beam experiences high stress levels, with most of the web's stress exceeding the yield strength, leading to beam yielding and failure of some high-strength bolts.

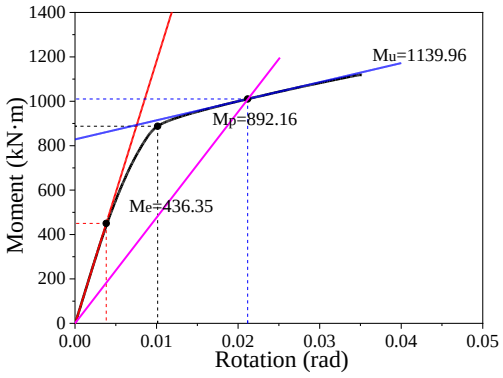

Fig. 13 Bending moment and rotation curve

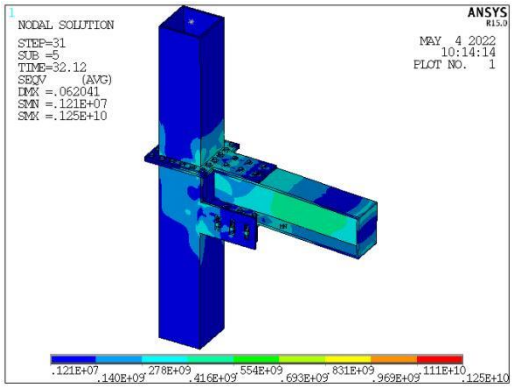

Fig. 14 Stress nephogram at the ultimate condition

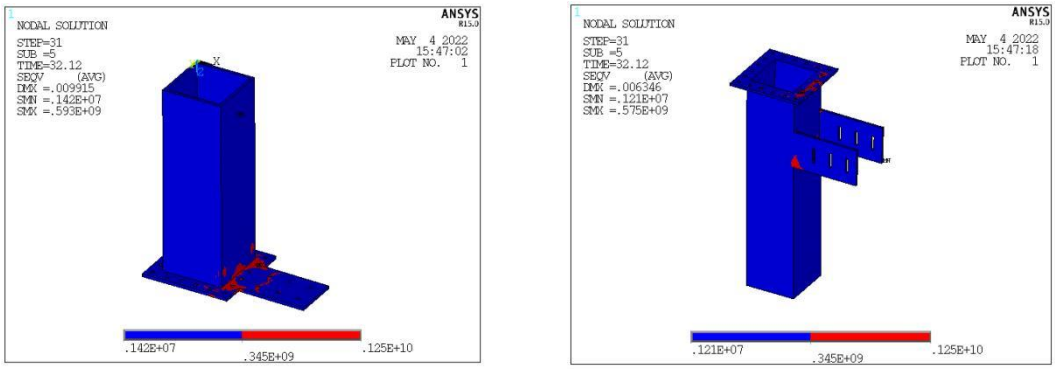

(a) Upper column (b) Lower column

Fig. 15 plastic distribution of the columns at the ultimate condition

The depiction of plastic development in the joint at failure, shown in Fig.15, indicates that plasticity primarily occurs in the area where the flange plate connects to the column and around the first row of bolt holes close to the column. This is largely due to the significant bending moment at the upper column's end. Additionally, plasticity is observed at parts of the lower edge of the lug, mainly attributed to increased bending and shear forces at the edges and corners.

Fig.16 illustrates the stress state of the connector, with the maximum stress occurring at the edge of the beam's lower flange, reaching 417 MPa. The overall stress level of the connector remains within the elastic range. Fig.17 reveals that the high-strength bolts, which connect the column to the column, do not fail upon joint failure and maintain an elastic state. The stress levels in the high-strength bolts connecting the lower column to the connection are generally low, allowing the bolts to continue supporting the load effectively.

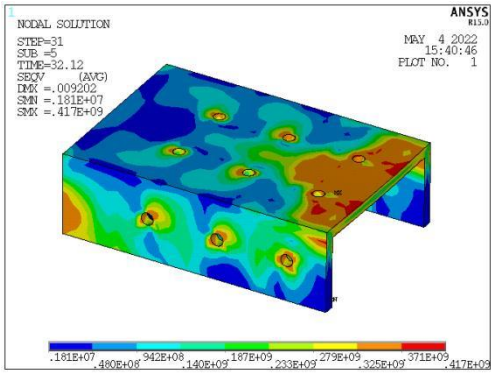

Fig. 16 Stress nephogram of the connection

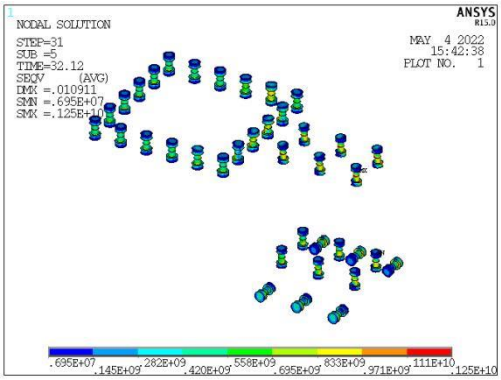

Fig. 17 Stress nephogram of the bolts

Table 3
Mechanical properties of the two joints

Joint	Elastic bending moment (kN·m)	Elastic turning angle (mrad)	Plastic bending moment (kN·m)	Plastic turning angle (mrad)	Ultimate bending moment (kN·m)	Ultimate turning angle (mrad)	Initial stiffness (kN·m/rad)	Strengthen stiffness (kN·m/rad)
Prefabricated	436.4	4.3	892.2	11.4	1140.0	38.6	116757.6	8656.5
Welded	690.8	7.0	900.0	11.4	1312.2	189.6	100581.7	3832.0

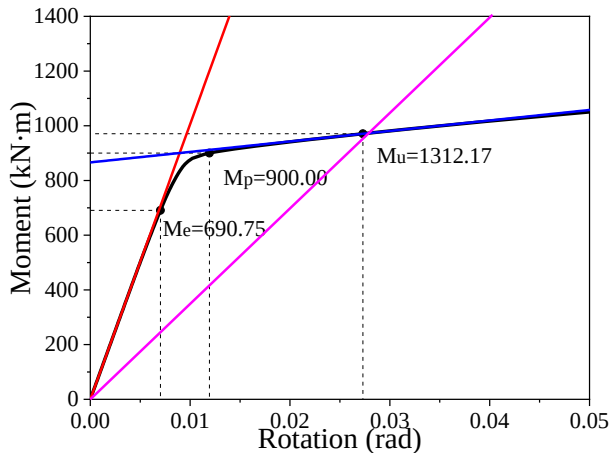

Fig. 18 Bending moment and rotation curve of welded joint

4.2. Comparison with the welded joint

To compare the mechanical properties of the newly designed prefabricated joint (NPJ) with those of the traditional welded joint, a static load simulation was performed on both, using identical beam-column sizes. The comparison (Table 3) reveals that the NPJ's elastic bending moment is 58% higher than that of the welded joint, while the plastic bending moments are nearly identical, and the ultimate bending moment differs by 15.2%. When examining the plastic deformation capabilities of the two joints, it was found that the NPJ's elastic rotation angle is 38.8% smaller than that of the welded joint. However, the difference in ultimate bending moment between the two joints is minor, at approximately 13.2%.

When comparing the moment and rotation curves of the two types of joints, as illustrated in Fig.13 and 18, it becomes apparent that the novel prefabricated joint (NPJ) exhibits differences in deformation capacity primarily due to its larger initial and strengthening stiffness compared to the traditional welded joint. The design of the NPJ, with its connection method, provides increased stiffness at the column ends, resulting in minimal observable deformation.

The displacement nephogram (Fig.19) illustrates that the deformation of the NPJ's beam begins at the section protruding from the flange plate, whereas deformation in the welded joint is more pronounced at the beam-column connection. The damage to the welded joint results from bending and shear buckling of the beam. In contrast, damage to the NPJ primarily occurs through beam yielding, with damage extending to the ultimate state at the section of the beam's upper flange where the high-strength bolt is located. This comparison indicates that the static performance of the NPJ is comparable to that of the traditional welded joint, but with less displacement in the limit state and greater stiffness.

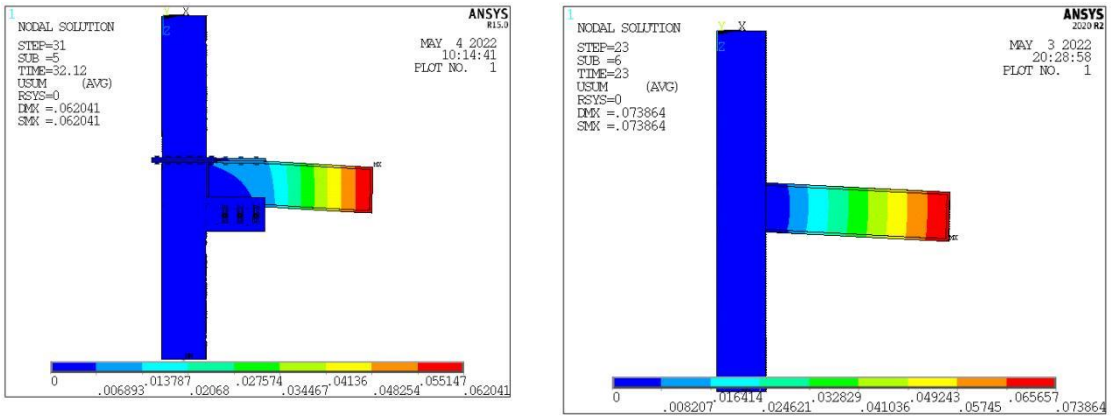

(a) Prefabricated joint (b) Welded joint

Fig. 19 Displacement of the joints

5. Seismic performance

5.1. Hysteresis performance of NPJ

The seismic performance of joints is assessed through displacement-controlled loading [26]. Once the joints achieve plastic displacement, the displacement load is incremented by 0.2 times the plastic displacement at each step, with each displacement level being applied for only one cycle. Upon reaching plastic displacement, the displacement at each subsequent level is doubled, and each level undergoes two cycles. Cyclic loading is discontinued when the member ceases to maintain its load-carrying capacity.

Fig.20 and 21 depict the stress and plastic distribution of the joint in its ultimate condition under hysteresis loading. The stress distribution in the column closely mirrors the results obtained under static loading, with the column predominantly remaining in the elastic phase. The maximum stress, at 343.48 MPa, is observed at the weld between the upper column and the flange plate. The web of the joint beam exhibits bulging and deformation, with both the upper and lower flanges and the web undergoing plastic deformation. The joint's failure mode is characterized by the beam yielding under bending and shear forces, exemplifying the principle of a strong column and weak beam.

The hysteretic and skeleton curves of the joint are presented in Fig.22 and 23. These figures highlight the joint's strong load-bearing capacity under both positive and negative bending moments. Initially, the joint operates within the elastic range, but as displacement increases, there is a noticeable decline in stiffness within a nonlinear segment. This leads to a reduction in the ultimate load capacity of the joint during the elasto-plastic phase, primarily attributed to bolt slippage. The fullness of the hysteretic curve underscores the joint's commendable seismic performance, indicating its resilience and reliability under seismic loading.

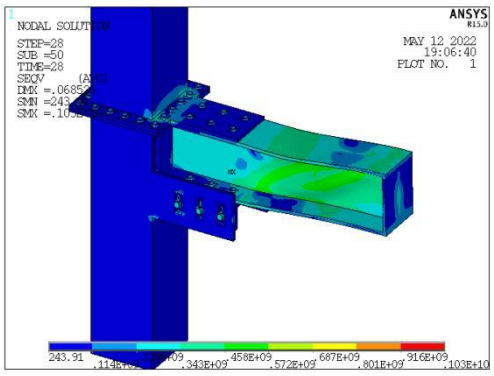

Fig. 20 Stress nephogram under hysteretic loading

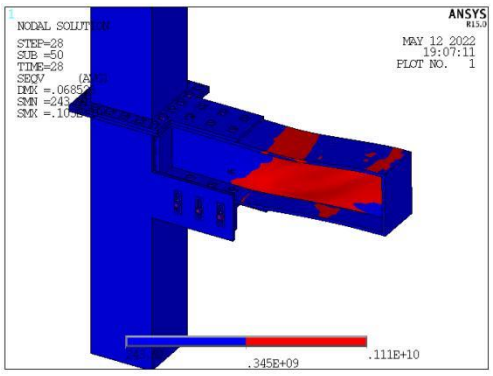

Fig. 21 Plastic distribution under hysteretic loading

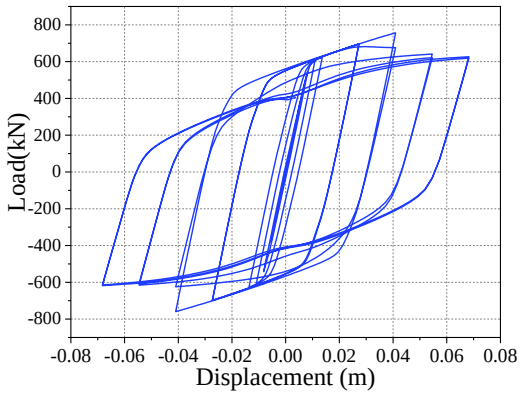

Fig. 22 Hysteretic curve of NPJ

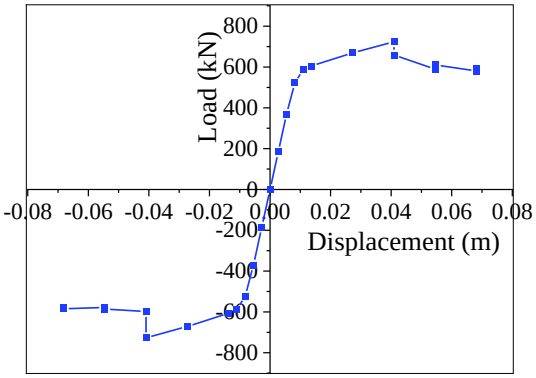

Fig. 23 Skeleton curve of NPJ

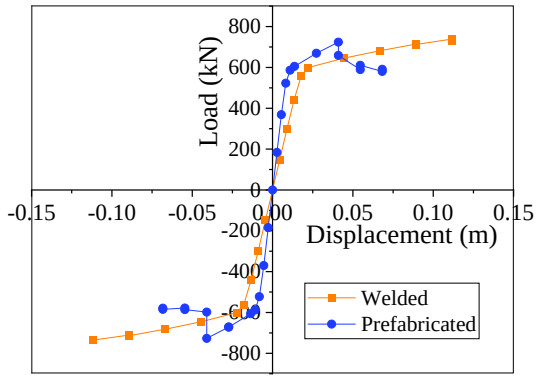

Fig. 24 Comparison of skeleton curves

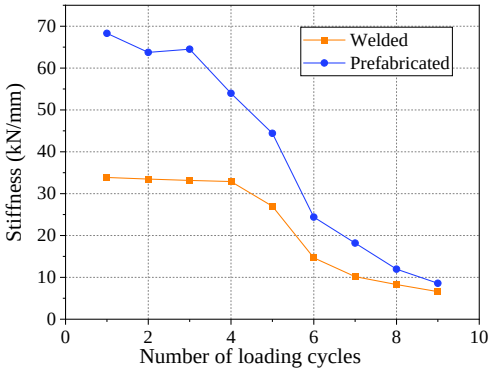

Fig. 25 Comparison of stiffness degradation

5.2. Comparison with the welded joint

Fig.24 and 25 display the comparison of skeleton curves and stiffness degradation curves between different types of joints. The NPJs exhibit a superior maximum load capacity compared to traditional welded joints, albeit with a lesser deformation capability and greater initial stiffness. As loading cycles progress, NPJs experience a faster rate of stiffness reduction, but ultimately, the stiffness levels of both joint types converge to a similar point after undergoing stiffness degradation.

Table 4 presents the ductility coefficients and energy dissipation coefficients for the two types of joints. The ductility coefficient of the NPJs is lower than that of the traditional welded joints, which suggests that the NPJs have a marginally lower capacity for deformation compared to the welded joints. However, both types of joints have ductility coefficients greater than 4, demonstrating good ductility and energy dissipation capabilities. This performance aligns with the requirements of the seismic design code [26], indicating that both joint types are well-suited for seismic applications.

Table 4
Seismic behavior of two kinds of joints

Joint	Ductility coefficient	Energy dissipation coefficient
Prefabricated	8.32	3.72
Welded	6.07	3.46

6. Parametric analysis

6.1. Parameter range in the investigation

In this chapter, we analyze the geometric parameters of components that exhibit high stress levels during the failure of the joint to understand how changes in these parameters affect the static load mechanical properties and failure modes of the NPJs. Utilizing the previously described finite element model, the parameters under investigation include the flange thickness (FT) of the upper column, the number of bolts without altering the overall load-bearing capacity (BN), the lug thickness (LT) of the lower column, and the height of the H-shaped steel beam (BH). The models are named according to the convention FT-N, BN-N, LT-N, and BH-N, where "N" represents the value of the parameter. For instance, FT-16 denotes a model with a flange thickness of 16 mm, with all other geometric parameters remaining as described in Chapter 3. Details of each model are summarized in Table 5.

6.2. The flange thickness (FT) of the upper column

As previously discussed, the upper column's flange plate is subjected to shear and tensile forces resulting from the bending moment load, with its bearing capacity significantly influencing the joint's failure mode and mechanical properties. This section examines upper columns featuring flange thicknesses ranging from 12 mm to 28 mm.

Fig.26 illustrates the plastic nephograms of the joints as the flange thickness varies. When the flange plate's thickness is below 18 mm, the bolt hole area connecting the flange plate to the beam undergoes extensive plastic deformation, leading to a tensile failure mode of the flange plate. As the thickness increases, the extent of plastic deformation in the flange plate diminishes. Beyond a thickness of 22 mm, the flange plate remains in an elastic state under ultimate conditions, with a notable reduction in the plastic area around the bolt holes.

Table 5
Models in parametric analysis

Parameters	Model number	Parameters information
Flange thickness	FT-(12/14/16/18/20/22/24/26/28)	Thickness: 12/14/16/18/20/22/24/26/28 mm
Number of bolts	BN-(10/8/6/4)	Number: 10/8/6/4
Lug thickness	LT-(12/14/16/18/20/22/24/26/28)	Thickness: 12/14/16/18/20/22/24/26/28 mm
Height of the beam	BH-(340/350/360/370/380/400/420/440)	Height: 340/350/360/370/380/400/420/440 mm

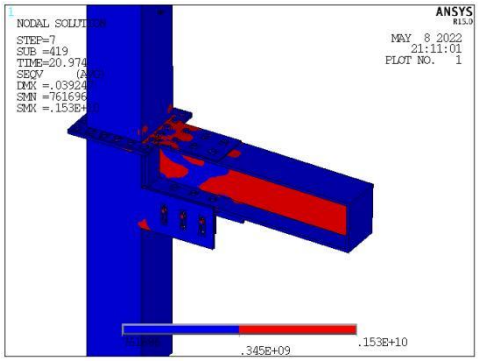

(a) FT-12

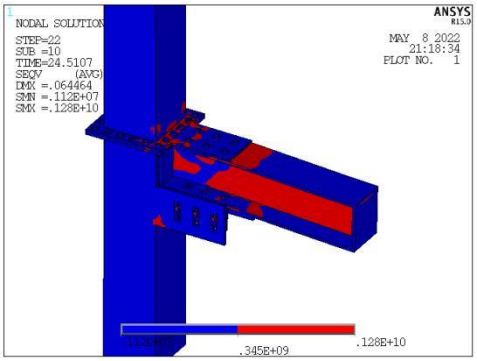

(b) FT-16

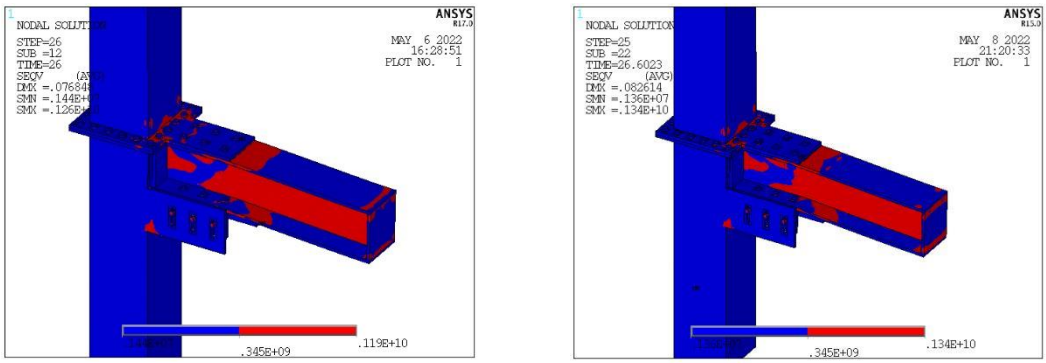

(c) FT-20 (d) FT-24

Fig. 26 Plasticity nephograms with different FT

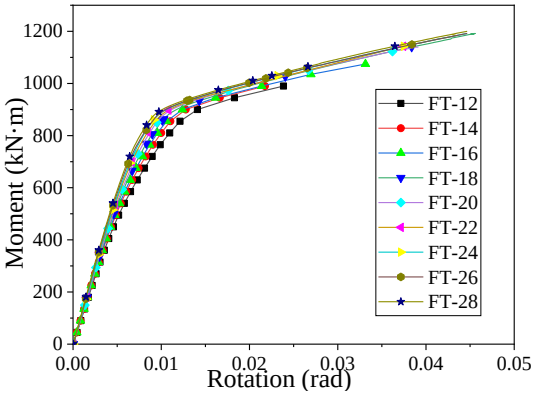

(a) Moment rotation curves

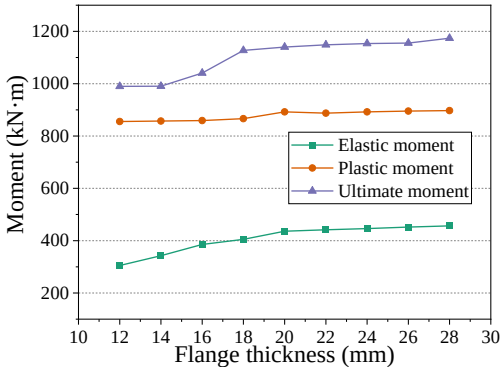

(b) Bearing capacity

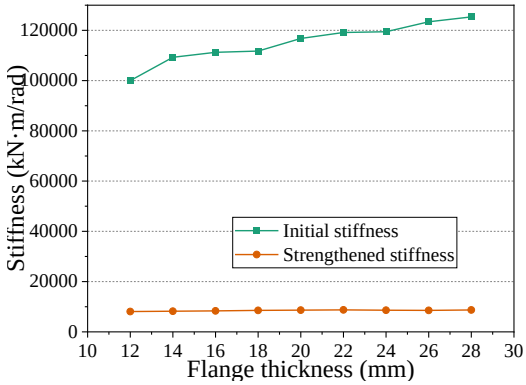

(c) Stiffness

Fig. 27 Joints with different FT

Fig.27 presents the moment-rotation curves and mechanical properties of joints with varying flange thicknesses (FT). For FT values less than 18 mm, both the elastic and ultimate moments of the joints show an increase with the thickness. However, once the FT exceeds 18 mm, further increases in thickness have a minimal impact on the joints' load-bearing capacity. A thicker flange plate results in higher initial stiffness for the joint, though the enhancement in strengthening stiffness is relatively minor. With thinner flange plates, significant plastic deformation is evident in the ultimate condition, and the joint's elastic moment rises with the stiffness of the flange plate. When the flange plate's thickness is above 18 mm, it remains in the elastic phase under ultimate conditions, and failure is primarily governed by the bolt strength and the beam's load-bearing capacity, leading to little variation in the ultimate bending moment.

6.3. Number of bolts (BN)

The examination of different numbers and diameters of bolts on the beam's flange, as presented in the models (4*M27, 6*M22, 8*M20, and 10*M16), reveals a crucial insight into the joint's failure mechanics. Despite variations in the bolt arrangements, with total load capacities ranging from 405.1 kN to 502.2 kN, Fig.28 illustrates that the overall plastic distribution of the joint in its ultimate state remains largely unchanged across different bolt configurations. This consistency suggests that within the tested range, the number of bolts does not significantly influence the stress distribution and the development of plasticity within the joint. Consequently, the failure mode of the joints under ultimate load conditions appears to be relatively insensitive to variations in the number and size of the flange bolts, assuming their total load-bearing capacity is maintained within a comparable range.

Fig.29 reveals that the number of bolts (BN) has minimal impact on joint mechanical properties. However, using 4 × M27 bolts results in lower ultimate bearing capacity due to bending failure from insufficient bolts.

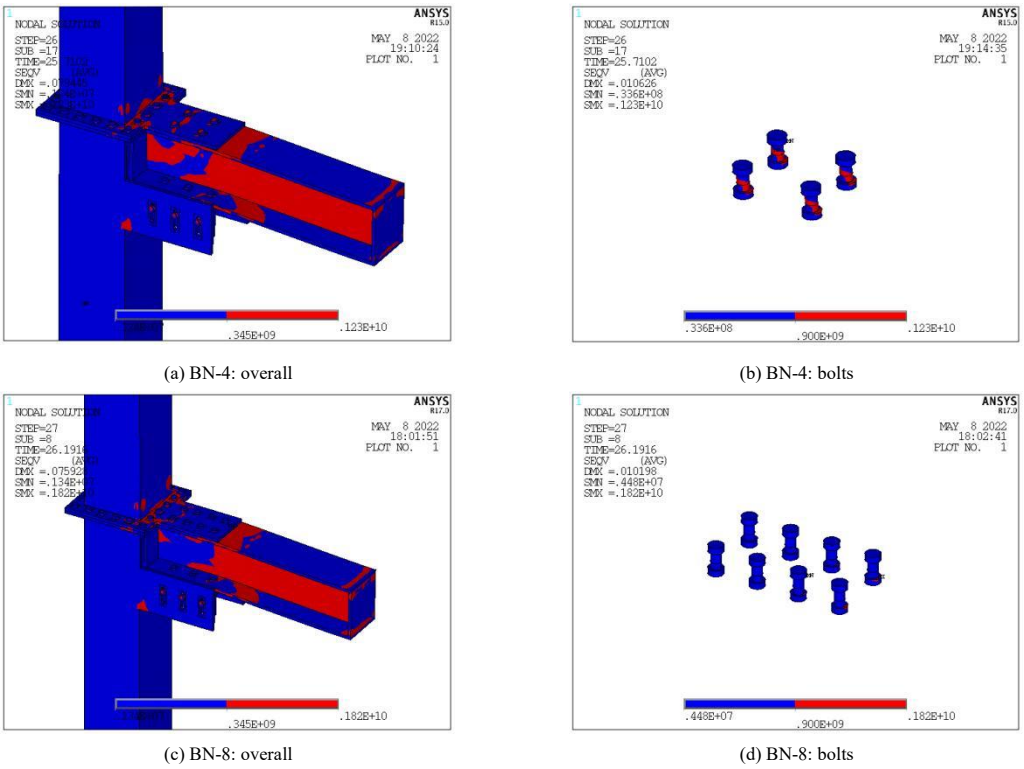

(a) BN-4: overall

(b) BN-4: bolts

(c) BN-8: overall

(d) BN-8: bolts

Fig. 28 Plasticity nephograms with different BN

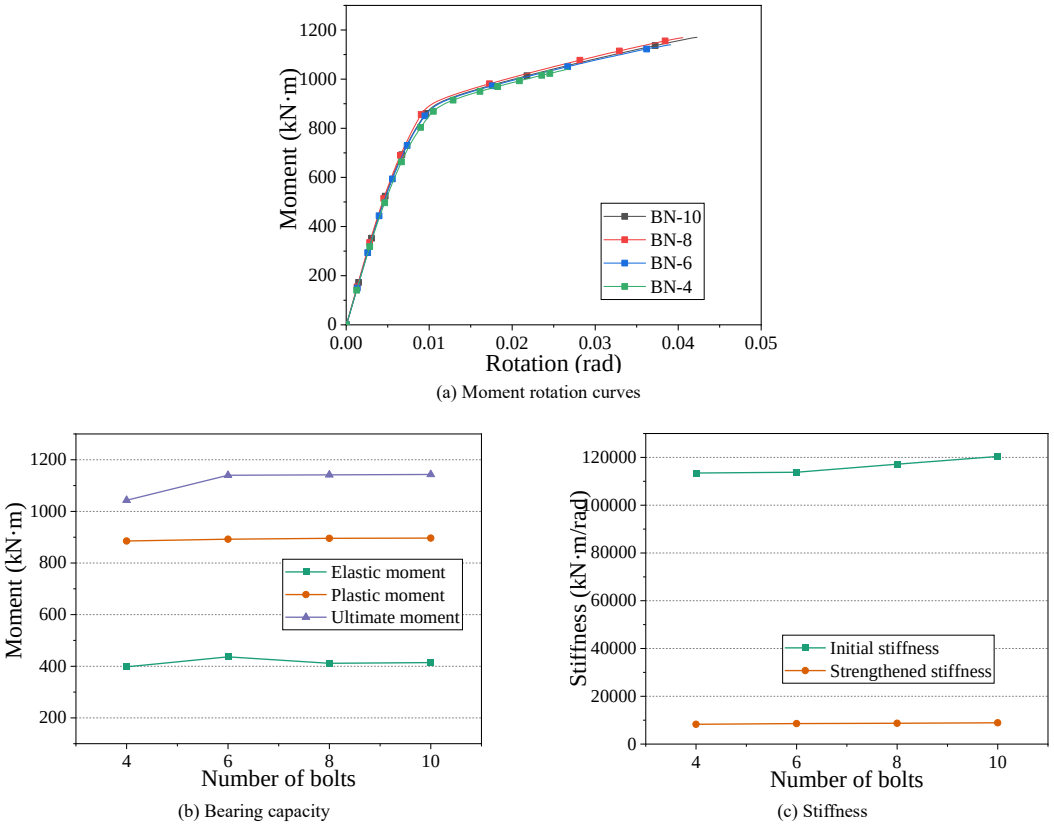

(a) Moment rotation curves

(b) Bearing capacity

(c) Stiffness

Fig. 29 Joints with different BN

6.4. Lug thickness (LT)

The analysis of the lug's thickness (LT) in the lower column, ranging from 12 mm to 28 mm, shows its significant impact on the joint's stiffness and failure mode. Fig.30 illustrates the plastic deformation patterns for joints with varying LTs. With an LT of 12 mm, a noticeable plastic region is observed at the top and bottom edges of the lug near the column end, leading to damage through bending shear yielding of the beam. As the LT increases, the plastic deformation area of the lug steadily decreases. When the LT reaches 28 mm, the lug remains elastic, not undergoing plastic deformation, even when the joint is damaged. This indicates that increasing the LT enhances the lug's resistance to plastic deformation, potentially improving the joint's overall stiffness and altering its failure mode.

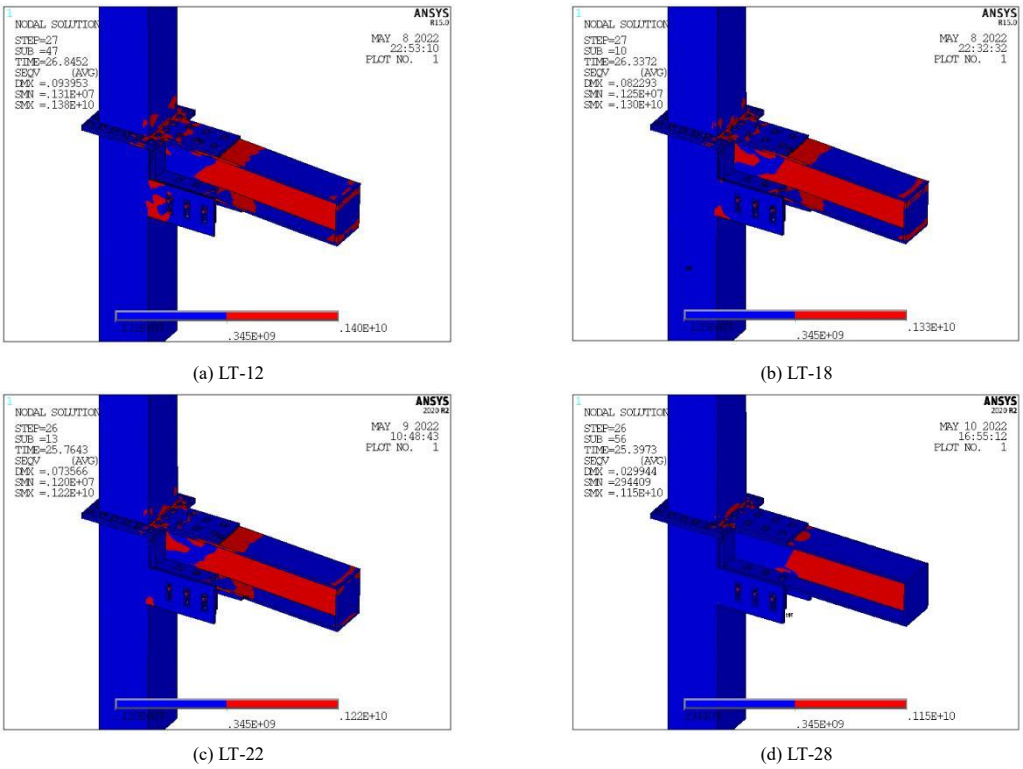

(a) LT-12 (b) LT-18

(c) LT-22 (d) LT-28

Fig. 30 Plasticity nephograms with different LT

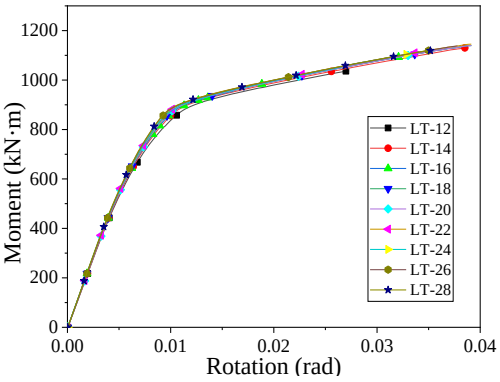

(a) Moment rotation curves

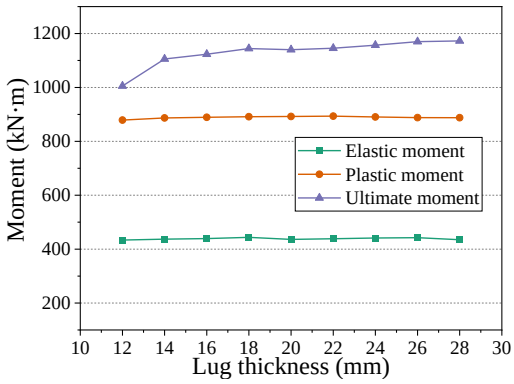

(b) Bearing capacity

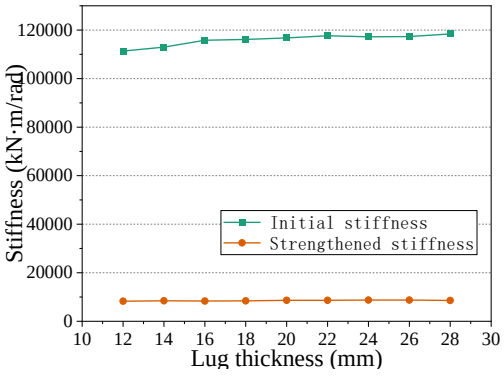

(c) Stiffness

Fig. 31 Joints with different LT

The moment-rotation curves and mechanical properties of joints with varying lug thicknesses (LTs) highlight the influence of LT on joint performance, as depicted in Fig.31. While joints across different LTs maintain commendable plasticity, the augmentation of LT notably enhances the joint's elastic moment capacity, albeit without significantly impacting the plastic or ultimate moment capacities. This slight improvement in initial stiffness attributed to increased LT suggests that while the lug possesses considerable stiffness, its modification has minimal impact on the overall mechanical properties and failure mode of the joint. This observation implies that the advantages gained from increasing the LT are marginal, indicating that other design or reinforcement strategies may be more effective for significantly enhancing joint performance.

6.5. The height of the beam (BH)

The influence of the beam height on the plastic deformation and failure mode of the joint is significant, as illustrated in Fig.32. This variation in beam height from 340 mm to 440 mm notably affects the joint's semi-rigid performance and its failure mechanism. Initially, at a beam height of 340 mm, both the beam flange and the web near the column end undergo extensive plastic deformation, indicating fully developed plasticity within the joint. The primary failure mode here is the yielding of both the beam and flange plate,

suggesting a balanced distribution of plastic zones across critical areas of the joint.

As the beam height increases, there is a consistent reduction in the plastic zones on the upper column flange plate and the connection between the beam and column. This reduction alters the failure mode of the joint. At a beam height of 380 mm, the connection's plastic zone vanishes, shifting the failure mode towards bending and shear yield of the beam, coupled with the failure of some high-strength bolts on the beam. This change indicates a transition from a more distributed plastic deformation towards localized failure points, reflecting the impact of beam height on joint performance.

Upon reaching a beam height of 440 mm, the failure mode further evolves, with only the web area of the beam entering plasticity, leading to the compression failure of high-strength bolts on the beam. This progression demonstrates a significant shift in the joint's failure mechanism, from a more distributed plastic deformation across multiple components to a localized failure primarily within the beam's web and associated bolt failures. This highlights the critical role of beam height in determining the structural behavior and resilience of the joint under load, emphasizing the need for careful consideration of beam dimensions in joint design to optimize performance and failure response.

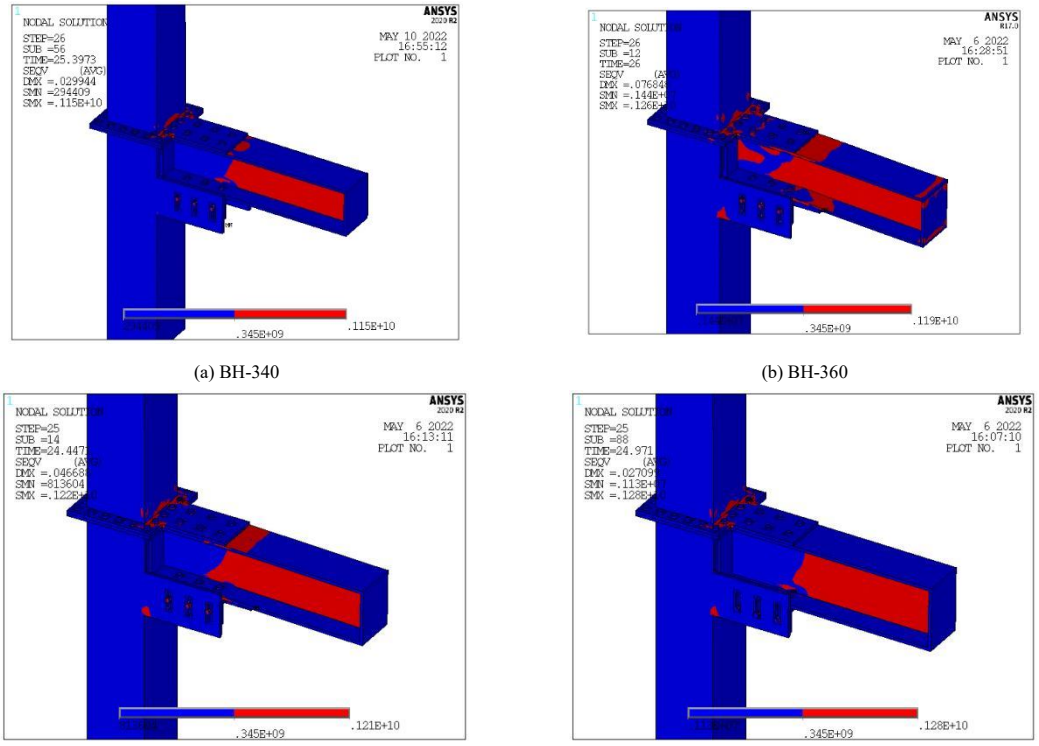

(a) BH-340 (b) BH-360

(c) BH-380 (d) BH-440

Fig. 32 Plasticity nephograms with different BH

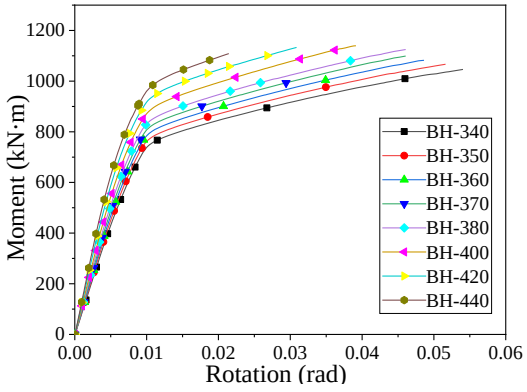

(a) Moment rotation curves

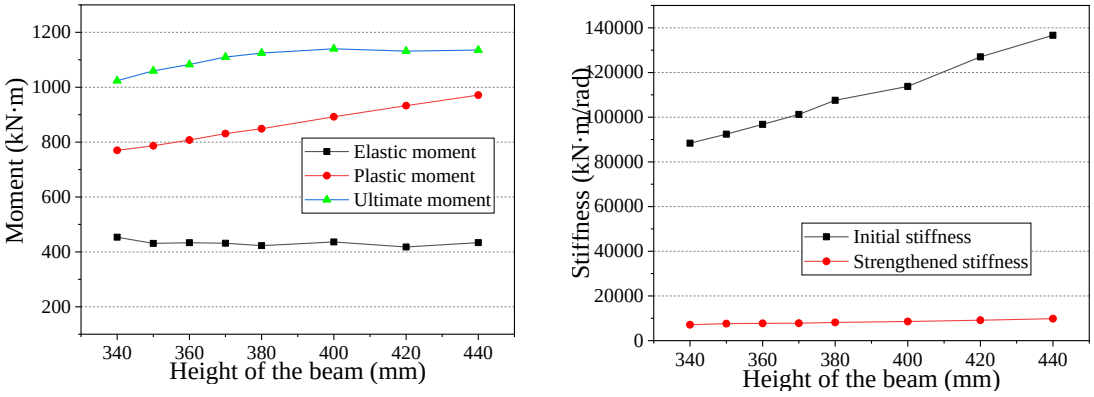

(b) Bearing capacity (c) Stiffness

Fig. 33 Joints with different BH

The analysis of joints with different beam heights (BH) in Fig.33 shows that beam height significantly affects the joint's initial stiffness and deformation capacity. Higher beam heights increase initial stiffness but reduce rotation capacity. This indicates the stiffness of the beam plays a critical role in the joint's overall stiffness, which increases with beam height. Lower beam heights allow for greater beam deformation, influenced by the upper column flange, leading to plastic deformation in both the beam and the flange plate. As beam height increases, the deformation and plastic rotation capacity decrease, altering the failure mode. This suggests lower beam heights optimize the joint's performance by maximizing the plastic capacity of both the upper column flange plate and the beam, highlighting the importance of beam dimensions in joint design for structural integrity and performance.

7. Simplified calculation method

Previous research demonstrated that Nonlinear Plastic Joints (NPJs) exhibit robust load-bearing capacity and stiffness. This section evaluates the NPJs' load-bearing capabilities and stiffness in accordance with two prevalent design standards, GB50017 [26] and Eurocode3 [29]. The aim is to support the design and practical application of NPJs more effectively.

7.1. Calculation of load bearing capacity based on GB50017

Currently, there's no standard calculation method for prefabricated joints. This paper calculates the load capacity of each component based on the joints' force transfer mechanism. As illustrated in Fig. 34, the joint area is subject to the beam's bending moment and shear force. Extensive research [7, 11-13, 19, 22] indicates that adhering to the design philosophy of ensuring joints are stronger than adjoining members, joints fail due to the bending-shear buckling of beams, with other components not reaching their maximum load capacity at failure. The stress distribution in the beam at failure can be simplified to the entire section yielding, with the peak stress reaching the material's tensile strength, as depicted in Fig. 35.

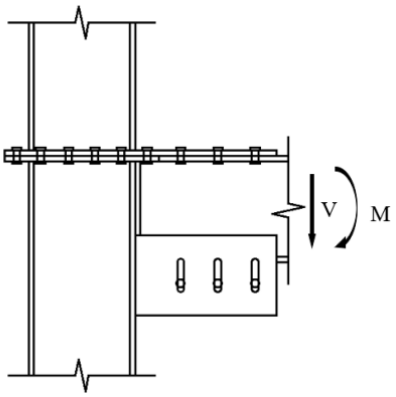

Fig. 34 Force transfer at the end of the beam

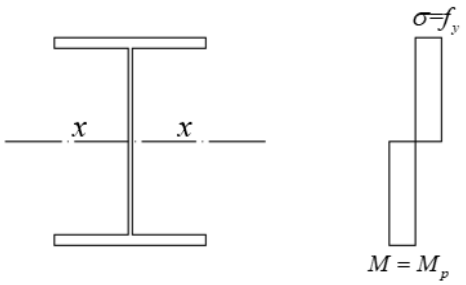

Fig. 35 Maximum stress distribution of beam section

Because the beam section is subjected to the combined action of bending moment and shear, the ultimate bearing capacity of joint beam members can be determined as min {Vum,Vuv,V1}, where Vum is the ultimate bearing capacity under bending moment, Vuv is the ultimate bearing capacity under shear, and V1 is the ultimate bearing capacity under the combined action of bending moment and shear. The calculation methods of the three kinds of bearing capacity are as follows:

(1) Ultimate bearing capacity under bending moment

Considering the plastic capacity of the joint web, the maximum bending moment of the beam member is Meu= Vum*L, so the bearing capacity Vum under the bending moment can be calculated by equation (1):

$$V_{um} = \gamma_x \alpha_e W_x f / L \tag{1}$$

where γx is the plastic development coefficient of the section, Wx is the modulus of the section around the x-axis, f is the design value of the tensile strength of the steel, and αe is the reduction coefficient of the beam considering the effective height of the web.

(2) Ultimate bearing capacity under shear

The general width-thickness ratio λs of joints can be calculated by equation (2):

$$\lambda_s = \frac{h_0 / t_w}{41\sqrt{5.34 + 4\left(h_0 / a\right)^2}} \sqrt{\frac{f_y}{235}} \tag{2}$$

where Ix is the moment of inertia of the web section around the x-axis, hc is the height of the web in compression calculated for the full section, tw is the design value of the tensile strength of the steel and ρ is the effective height factor of the web under compression.

The general width-thickness ratio λs for different beam height joints is found to be less than 0.8. The maximum shear value Vuv, taking into account the plastic capacity of the joint web, can be calculated using equation (3):

$$V_{uv} = h_w t_w f_v \tag{3}$$

where hw is the height of the beam web, fv is the design value of the shear strength of the steel and tw is the thickness of the beam web.

(3) Ultimate bearing capacity under the combined action of bending moment and shear

As mentioned before, the dangerous section of the beam is the edge section of the beam protruding from the flange plate of the upper column. The dangerous section bears a large bending moment and shear force, and the combined action of the bending moment and shear force should be used to calculate the beam when designing the joint. Because the bending moment of the beam does not exceed the bending capacity of the upper and lower flanges Mf, the shear capacity of the beam is still Vuv, and the shear force V1 at the end of the beam should satisfy equation (4):

$$\left(\frac{V_1}{0.5V_{uv}} - 1\right)^2 + \frac{V_1 \bullet L - M_f}{V_{um} \bullet L - M_f} \le 1 \tag{4}$$

The ultimate bearing capacity of joints under different beam heights is calculated by the above equations, as shown in Table 6. The ultimate bearing capacity of joints calculated by the simplified calculation method is 60% and 80% of the finite element simulation results. The above differences are mainly because the design value of the shear strength of the material is considered to be 58% of the tensile strength in the code[26] for safety reasons. Generally, the cross-section size of the NPJs can be designed by design code GB50017, and the designed joint has a large safety reserve.

Table 6
Ultimate bending bearing capacity of joints

Geometrical parameters	Finite element method (kN)	Simplified calculation method (kN)	Result difference (%)
BH340 mm	682.32	432	63.31
BH350 mm	706.36	446.4	63.20
BH360 mm	721.75	460.8	63.84
BH370 mm	739.97	475.2	64.22
BH380 mm	749.70	489.6	65.31
BH400 mm	759.97	518.4	68.21
BH420 mm	754.41	547.2	72.53
BH440 mm	757.02	576	76.09

7.2. Calculation of initial stiffness based on GB50017

To evaluate the deformation capacity of joints, the initial stiffness of joints was calculated by using the code Eurocode3. As shown in Fig. 36, the initial stiffness of a beam-column joint with bolts is a combination of shear column web stiffness k_1, compression column web stiffness k_2, tension column web stiffness k_3, bending flange splint stiffness k_6 and shear bolt stiffness k_{11}. The stiffness of the joints can be calculated by equation (5) as

$$S_j = \frac{Ez^2}{\mu \sum_i \frac{1}{k_i}} \tag{5}$$

Ki is the stiffness of the basic joint components, z is the rotating arm, that is, the beam height of the H-shaped steel beam, E is the elastic modulus of steel, and μ is the joint stiffness ratio, taken as 1.0.

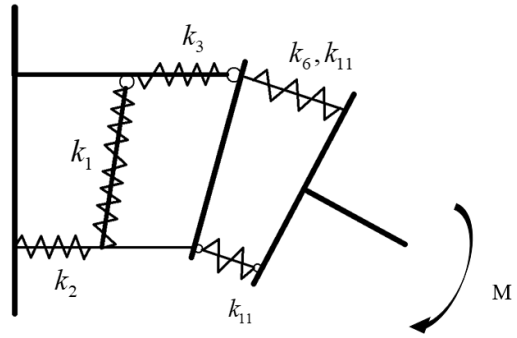

Fig. 36 Calculation of initial stiffness

The shear column web stiffness k_1 can be calculated according to equation (6).

$$k_1 = \frac{0.38 A_{VC}}{\beta z} \tag{6}$$

where A_{vc} is the shear area of the square steel tube column, β is the transformation parameter, taken as 1.0, and z is the shear force arm, taken as the height from the upper flange to the bolt hole in the lug.

The compression column web stiffness k_2 can be calculated according to equation (7).

$$k_2 = \frac{0.7 b_{eff,t,wc} t_{wc}}{d_c} \tag{7}$$

where $b_{eff,t,wc}$ is the effective width of the compressed column web, t_{wc} is the thickness of the compressed column web and dc is the height of the compressed column web.

The tension column web stiffness k_3 can be calculated according to equation (8).

$$k_3 = \frac{0.7 b_{eff,t,wc} t_{wc}}{d_c} \tag{8}$$

where $b_{eff,t,wc}$ is the effective width of the tensioned column web, t_{wc} is the thickness of the tensioned column web and dc is the height of the tensioned column web.

The bending flange splint stiffness k_6 can be calculated according to equation (9).

$$k_6 = \frac{0.9 \ell_{eff} t_a^3}{m^3} \tag{9}$$

where l_{eff} is the effective thickness of the flange, taken as 1/2 of the flange plate width, t_a can be taken as the flange plate thickness, and m is the sum of the joint flange plate thickness and the column flange thickness.

Due to the use of friction-type high-strength bolts, the shear bolt stiffness $k_{11} = \infty$.

To verify the rationality of the simplified calculation method, finite element analysis and theoretical values were calculated for the NPJs with different geometrical dimensions, the results of which are compared in Fig. 37. It can be found that the initial stiffness of the theoretical calculation is slightly higher than the stiffness of the simulation result, and the difference between the two is less than 10%. It is worth mentioning that when the flange thickness is less than 14 mm, the finite element calculation results are slightly larger than the simplified calculation results. The above calculation method provides methodological support for the simplified calculation of engineering design.

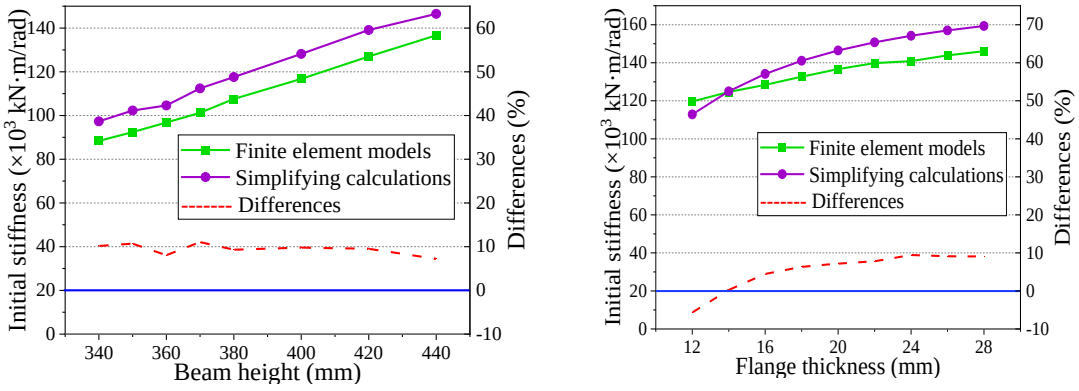

(a) Different beam heights

(b) Different flange thicknesses

Fig. 37 Comparison of initial stiffness of different methods

8. Conclusion

The study delved into the mechanical properties of a novel prefabricated column-beam-column joint using finite element analysis and presented a simplified calculation method. The key conclusions are as follows:

(1) The novel prefabricated joints (NPJs) can accommodate beams of different heights, offering advantages such as convenient construction, controllable quality, reasonable force transfer path, and ease of disassembly and replacement. The validity of the finite element models and simulation parameters was verified through comparison with experimental data.

(2) Under static force at the beam end, the NPJs exhibit a failure mode of beam bending-shear yielding and upper flange bolt failure. In comparison to traditional welded joints, NPJs show slightly smaller plastic moment and ultimate moment by 0.87% and 16.08%, respectively, but possess 16.08% larger initial stiffness. This indicates good static properties and increased construction efficiency.

(3) Hysteresis analysis demonstrates that NPJs have robust load capacity under positive and negative bending moments, with full hysteresis curves. While NPJs exhibit lower ductility coefficient and energy dissipation coefficient than welded joints, both types meet code requirements and demonstrate good seismic performance.

(4) Parametric analysis reveals that the thickness of the flange plate significantly impacts initial stiffness and damage mode, while the number of flange bolts on the beam has a minor effect on static performance. Additionally, an increase in lug plate thickness enhances the joint's mechanical properties during initial loading, and the height of the beam is a crucial factor affecting load carrying capacity.

(5) The study provides and verifies methods for calculating the load carrying capacity and initial stiffness of the novel joint based on design codes GB50017 and Eurocode 3, respectively. These simplified calculation methods empower engineers to design suitable prefabricated steel frame joints effectively.

These conclusions not only contribute to the understanding of the mechanical behavior of novel prefabricated joints but also offer practical insights for designing and implementing such joints in construction projects.

Acknowledgment

This work was financially supported by the General Program of Science Foundation of Shandong Province (ZR2023ME215), the National Natural Science Foundation of China (Grant No. 52308161 and Grant No. 51308154) and Technology research project of CSCEC (CSCEC-2020-Z-35).

References

[1] Peng Z, Wang Y, Zhang M W. Mechanics property analysis of prefabricated rectangular steel tube and H-steel-beam connection joint[J]. Journal of Qingdao University of Technology, 2016.

[2] Li G, Zhang J, Li L, et al. Progressive Collapse Resistance of Steel Framed Buildings Under Extreme Events[J]. Advanced Steel Construction, 2021, 17: 318-330.

[3] Taheripour M, Hatami F, Raoufi R. Numerical Study of Two Novel Connections with Short End I or H Stub in Steel Structures[J]. Advanced Steel Construction, 2022, 18: 495-505.

[4] Ma C, Li G, Wang Z. Experimental Study on Mechanical Performance of Buckling-Restrained Brace on Frames with High-Strength Concrete-Filled Square Steel Tube Columns[J]. Advanced Steel Construction, 2023, 19: 293-307.

[5] Zhang Y, Li D. Development and testing of precast concrete-filled square steel tube column-to-RC beam connections under cyclic loading[J].Construction and Building Materials, 2021, 280:122540.

[6] Torabian S, Mirghaderi S R, Keshavarzi F. Moment-connection between I-beam and built-up square column by a diagonal through plate[J].Journal of Constructional Steel Research,2012,70(2):385-401.

[7] Hassan M K, Tao Z, Katwal U. Behaviour of through plate connections to concrete-filled stainless steel columns[J]. Journal of Constructional Steel Research, 2020, 171.

[8] Lai-Yun W, Lap-Loi C, Sheng-Fu T. Seismic behavior of bolted beam-to-column connections for concrete filled steel tube. Journal of Constructional Steel Research, 2005(61):1387-1410.

[9] Wang X, Hao J, Pan Y, et al. Behavior research of through high strength bolts-end plate connection for concrete filled square steel tube column. Industrial Construction 2008, 38(3): 23-26. (in Chinese)

[10] Zong Z, Lin Y, Lin J. Experimental study on seismic performance of rectangular concrete-filled steel tube column-to-steel beam semi-rigid connections. Journal of Building Structure 2004, 25(6): 29-36. (in Chinese)

[11] Sun J, Qiu H, Xu J. Experimental Verification of Vertical Joints in an Innovative Prefabricated Structural Wall System. Advances in Structural Engineering. 2015, 18(7):1071-1086.

[12] Zaid A, Moussa L, Ahmed F. Experimental validation of a novel curved steel damper for steel frames with flexible beam-column joints[J]. Structures, 2023, 56:105010.

[13] Shakeri J , Abdollahzadeh G .Seismic Rehabilitation of Tall Steel Moment Resisting Frames Damaged by Fire with SMA-Based Hybrid Friction Damper[J]. International journal of steel structures, 2020(1):20.

[14] Reza S, Farhad B.Experimental Studies on a Combined Damper for Repairable Steel Moment Connections[J]. International Journal of Steel Structures, 2018(18): 211-2224.

[15] Hongkai D, Pengfei Z, Yuandong W, et al. Seismic experimental assessment of beam-through beam-column connections for modular prefabricated steel moment frames[J]. Journal of Constructional Steel Research, 2022, 192: 107208.

[16] Ozkula G. High strength steel for seismic resistance of beam-to-column connections： novel metal investigation[Z]. 2011.

[17] Cui Y,Luo Y,Nakashima M. Development of steel beam-to-column connections using SFRCC slabs[J]. Engineering Structures,2013,52：545-557.

[18] Farmani M A,Ghassemieh M. Steel beam-to-column connections equipped with SMA tendons and energy dissipating devices including shear tabs or web hourglass pins.[J]. Journal of Constructional Steel Research, 2017, 135：30-48.

[19] Ataei A, Valipour H R, Bradford M A, et al. Experimental study of steel-timber composite beam-to-column joints with extended end plates[J]. Construction and Building Materials, 2019, 226:636-650.

[20] Chen H, Ke C, Chen C, et al. The Tensile Performance of Inter-Module Connection with a Bolt and Shear Key Fitting for Modular Steel Buildings[J]. Advanced Steel Construction, 2023, 102-111.

[21] Cheng M, Zhang Y, Li Z, et al. Experimental Study of Hysteretic Behavior of Resilient Prefabricated Steel Frames with and without Intermediate Columns[J]. Advanced Steel Construction, 2022, 18: 715-727.

[22] Kristóf I,Novák Z,Hegyi D. A Simplified Method for the Design of Steel Beam-to-column Connections.[J]. Periodica Polytechnica： Architecture, 2017, 48(2): 79-86.

[23] Liu X C, Yang Z W, Wang H X, et al. Seismic performance of H-section beam to HSS column connection in prefabricated structures[J]. Journal of Constructional Steel Research, 2017,138:1-16.

[24] Zhiwei Z, Huajie W, Hongliang Q, et al. Design and Mechanical Performance Analysis of a New Type of Column-Column-Beam Prefabricated Steel Frame Joint[J]. Structural Engineering International, 2021, 31(3).

[25] Wihlborg A, Crafoord R. Steel sheet surface topography and its influence on friction in a bending under tension friction test[J]. International Journal of Machine Tools & Manufacture, 2001, 41(13):1953-1959.

[26] GB50017-2017. Code for Design of Steel structures, 2017. (in Chinese)

[27] Bi Y. Study on mechanical properties of assembled joints between high square steel tube columns and H-shaped steel beams with adjustable beams [D]. Harbin Institute of Technology, 2019. (in Chinese)

[28] Huajie W, Borui Z, Hongliang Q, et al. Experimental and numerical studies of a new prefabricated steel frame joint without field-welding: Design and static performance - ScienceDirect[J]. Thin-Walled Structures, 2020, 159.

[29] EN 1993-4-3:2007, Eurocode 3- Design of steel structure, 2007.

Advanced Steel Construction – Vol. 20 No. 4 (2024) 345–363
DOI:10.18057/IJASC.2024.20.4.3

INTERFACE SHEAR DEMAND AND DESIGN OF PARTIALLY CONCRETE-FILLED STEEL TUBULAR COLUMNS WITH TRANSVERSE DIAPHRAGMS

Jian Jiao [1], Yao-Jun Zhang [2] and Dan Gan [3, *]

[1] *College of Water & Architectural Engineering, Shihezi University, Shihezi 832003, China*
[2] *School of Civil Engineering, Chongqing University, Chongqing 400045, China*
[3] *School of Civil Engineering and Geomatics, Southwest Petroleum University, Chengdu 610500, China*
** (Corresponding author: E-mail: gandan@swpu.edu.cn)*

ABSTRACT

A partially concrete-filled steel tubular (CFST) column is formed by partially filling a steel hollow section (SHS) with concrete, its interface shear demand between the infilled concrete and steel tube is important in design but not usually considered. In this work, a refined finite element (FE) model of circular partially CFST columns with transverse diaphragms was established, followed by parameter analysis of the behavior under the combined axial compression and lateral loads. The main variables included the concrete filling ratio, axial compression ratio, diameter-to-thickness ratio of steel tubes, section size, aspect ratio, and material strength. The results indicate that the optimal filling ratio increases with the axial compression ratio, diameter-to-thickness ratio, and concrete strength, but decreases with the steel strength. Then, calculation methods for the optimal filling ratio, predicting the load capacity of transverse diaphragms, and the interface shear demand between the steel tube and infilled concrete were proposed. Finally, a design procedure for partially CFST columns with transverse diaphragms was proposed.

ARTICLE HISTORY

Received: 26 April 2024
Revised: 3 July 2024
Accepted: 8 July 2024

KEYWORDS

Composite structure;
Finite element analysis;
Optimal filling ratio;
Shear demand;
Transverse diaphragm

1. Introduction

A partially concrete-filled steel tubular (CFST) column is a hollow steel tubular column that is partially filled with concrete. Partially CFST columns developed as a retrofitting measure for piers initially as depicted in Fig. 1[1], which effectively reinforces the potential plastic hinge area at the bottom of the piers in an economical manner. Partially CFST columns exhibit high lateral load capacity, good ductility, and excellent energy dissipation capacity [2-11], making them widely utilized in bridge piers for both post-earthquake repair of existing bridges and construction of new bridges [12-14].

In recent decades, the seismic performance of partially CFST columns have been extensively investigated. Yuan et al. [15-16] illustrated that infilled concrete can enhance the seismic performance of steel piers when subjected to both unidirectional and bidirectional seismic forces. Goto et al. [17-18] introduced a discrete crack model, which aimed at exploring the failure mechanism of partially CFST columns, specifically the development of plastic hinges at the bottom of the column. Lai and Varma [19] performed FE analysis to study how the seismic performance of hollow spiral welded pipes is influenced by the concrete filling ratio. The findings suggested that a higher concrete filling ratio can postpone the local buckling and fracture of steel tubes. Additionally, Xiang et al. [20] indicated that the concrete filling ratio can be used as an optimization design to achieve a balance between structural performance and load capacity.

The concrete filling ratio should be designed as larger than the optimal ratio, which is defined as the minimum concrete filling ratio at which a partially CFST column can achieve the load capacity of a CFST column. Khalifa et al. [21] demonstrated that, circular partially CFST columns (f_y=280MPa, D/t=101) can achieve the load capacity equivalent to 78% of CFST columns under the concrete filling ratio of 39%, with the failure mode being local buckling at the end of the hollow part. However, Wang et al. [22] showed that when the concrete filling ratio of a circular partially CFST pier with a transverse diaphragm with similar parameters (f_y=315MPa, D/t=119) was equal to or greater than 33%, the specimen failed at the bottom of the bridge pier, exhibiting good seismic performance. The difference between the above two researches mainly lies in whether the transverse diaphragm is installed or not. Therefore, it is necessary to take certain measures to effectively transfer the load from the steel tube to infilled concrete, which can affect the optimal filling ratio and structural behavior of partially CFST columns.

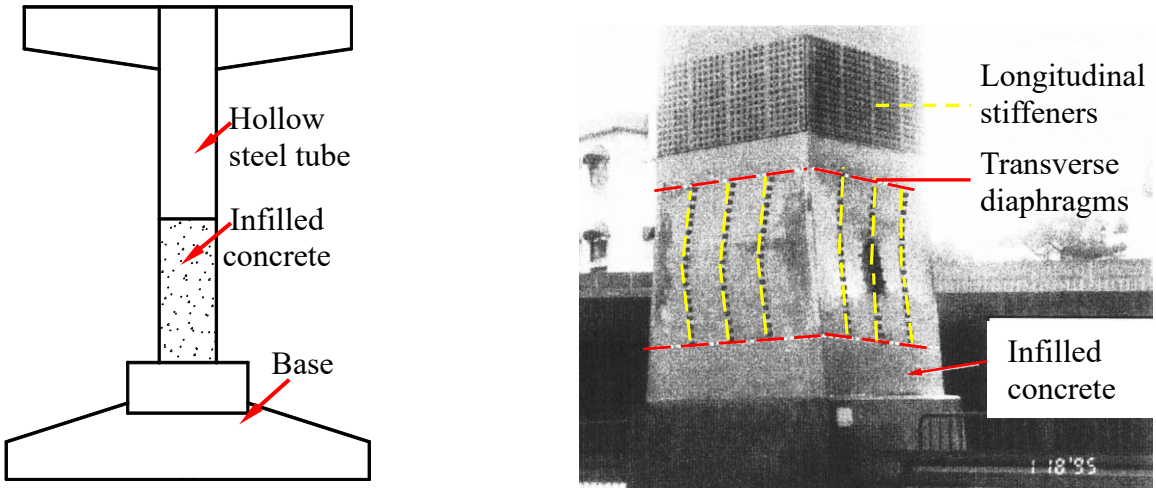

(a) Partially CFST columns pier (b) Partially CFST pier in practice [1]

Fig. 1 Partially CFST columns piers

In order to enhance the interface shear capacity and composite effect of partially CFST columns, transverse diaphragms, longitudinal stiffeners, or a combination of both were deemed essential, as illustrated in Fig. 2. Usami et al. [23-24] conducted seismic test of rectangular partially CFST piers, and the

results indicated that stiffening ribs effectively increased the strength, stiffness, deformation capacity, and energy dissipation performance of the columns. Then, Ge and Usami [25] illustrated that transverse diaphragms were similarly successful in enhancing the seismic performance of the partially CFST piers. Kwon et al. [26] concluded that longitudinal stiffening ribs could increase the load capacity of partially CFST piers beyond the sum of the capacities of the steel tube, stiffening ribs, and concrete, demonstrating a favorable composite effect. However, the design and detailing of transverse diaphragms in partially CFST columns were not discussed or analyzed, such as the mechanism of these diaphragms resists the interface shear and the interface shear demand, which is important for proposing the design methods.

The transverse diaphragm can effectively transfer the load from steel tube to infilled concrete and can be conveniently welded as shown in Fig. 3, so they facilitate utilizing the performance of the infilled concrete and have been widely used in practice. Two fundamental design parameters for the transverse diaphragm include the shear demand in partially CFST columns, as well as the load capacity of the diaphragm. Although both academic researches and practical projects adopt transverse diaphragms in partially CFST columns, the interface shear demand, design of diaphragms, and the selection of the optimal filling ratio needs to be systematically investigated for better guiding the design.

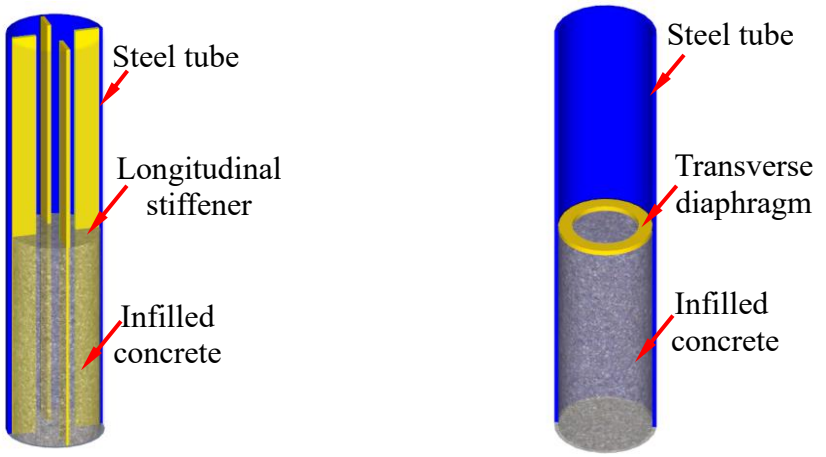

(a) With longitudinal stiffeners (b) With transverse diaphragm

Fig. 2 The stiffening measures of partially CFST columns

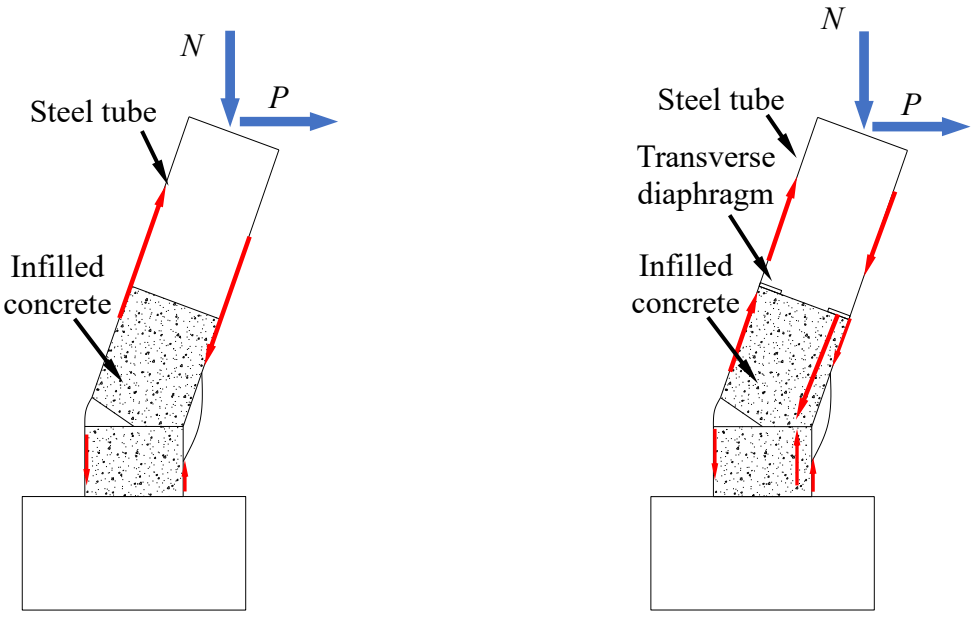

(a) Without transverse diaphragm (b) With transverse diaphragm

Fig. 3 The force transmission effect of the transverse diaphragm

In this study, a FE analysis model of partially CFST columns was established and verified, followed by parameter analysis of the behavior under the combined axial compression and lateral loads. The main parameters contained the concrete filling ratio, axial compression ratio, diameter-to-thickness ratio of steel tubes, section size, aspect ratio, and material strength. Then, a calculation method for the optimal filling ratio, predicting the load capacity of transverse diaphragms. and the shear demand between the steel tube and infilled concrete were proposed. Finally, a design procedure was proposed.

2. Nonlinear analysis

2.1. Model description

The model was established by using the software ABAQUS. The eight-node linear hexahedral element (C3D8R) was used for the steel tubes, concrete, and transverse diaphragms. Through sensitivity analysis of the mesh size, the element division size was set to one-tenth of the cross-sectional width [27]. Surface-to-surface contact interactions were established between the steel tube and infilled concrete, as well as between the transverse diaphragms and concrete. Finite sliding was used in the contacts, with its normal behavior being modeled as hard contact and its tangential behavior being represented by penalty functions incorporating a friction coefficient of 0.6 [28]. The transverse diaphragms were connected using “tie” constraints. The FE model and boundary conditions are shown in Fig. 4. The top surface of the column was coupled to point RP-1, where the load was applied; the bottom surface of the partially CFST column was fixed and coupled to point RP-2.

A steel model followed an elastic-perfectly plastic model, as shown in Eq. (1), featuring an elastic modulus (E_s) of 2.06×105 MPa and a Poisson’s ratio of 0.3. The concrete was characterized by an elastic modulus (E_c) of 4700fc0.5 [29] and a Poisson’s ratio of 0.2, as shown in Eq. (2). A plastic damage model [30] was implemented for the concrete, incorporating the specific parameters detailed in Table 1. To characterize the tensile behavior of concrete, a fracture energy

model was employed, defining the tensile stress f_t by the Ref. [31] and tensile fracture energy Gf as suggested in the CEB-FIP MC90 [32], as defined in Eq. (3) and Eq. (4).

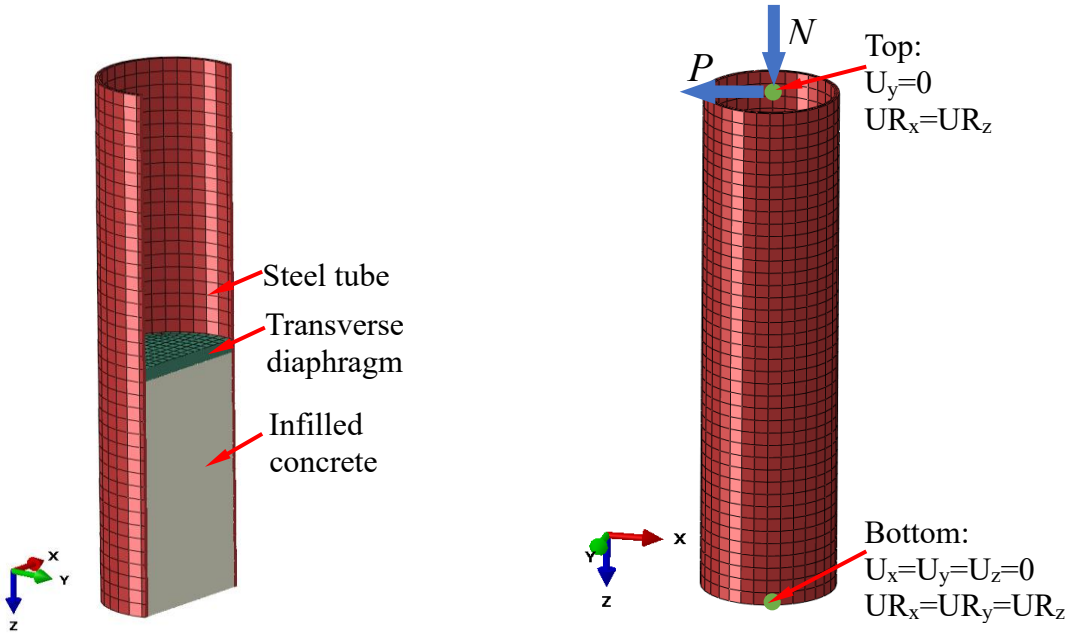

Fig. 4 FE model and boundary conditions

$$\sigma = \begin{cases} E_s\varepsilon, & (\varepsilon \le \varepsilon_y) \\ f_y, & (\varepsilon > \varepsilon_y) \end{cases} \quad (1)$$

where E_s is the elastic modulus of steel; f_y and ε are the yield stress and strain of steel, respectively.

$$y = \begin{cases} 2x - x^2, & (x \le 1) \\ \dfrac{x}{\beta_0(x-1)^\eta + x}, & (x > 1) \end{cases} \quad (2)$$

where $x = \varepsilon/\varepsilon_0$; $y = \sigma/\sigma_0$; $\sigma_0 = f_c'$; $\beta_0 = (f_c')/1.2\sqrt{1+\xi}$; $\xi = A_s f_y/A_c f_{ck}$; $\eta = 1.6 + 1.5/x$; $f_{ck} = 0.642 f_{cu}$; $f_c' = 0.833 f_{cu}$; $\varepsilon_0 = \varepsilon_c + 800\xi^{0.2} \times 10^{-6}$; $\varepsilon_c = (1300 + 12.5 f_c') \times 10^{-6}$.

Table 1
Concrete parameter values

ψ	e	f_{b0}/f_{c0}	K_c	μ
38°	0.1	1.16	0.667	0.0001

$$f_t = 0.375 f_{cu}^{0.55} \quad (3)$$

$$G_f = \alpha(0.1 f_c)^{0.7} \quad (4)$$

where α is related to the size of concrete aggregates, taken as 0.03.

2.2. Model verification

To verify the accuracy of the FE analysis models, the experimental results of partially CFST columns under bending load [21] were selected and compared. The comparison of the failure modes is depicted in Fig. 5. The circular partially CFST column displayed plastic hinge formation at the end of the hollow section, with the simulated failure mode aligning closely with the experimental results. Meanwhile, the load-displacement curves depicted in Fig. 6 illustrated a good agreement between the FE analysis results and the experimental results.

(a) The failure mode of T160-16

(b) The FE result

Fig. 5 Comparison of failure mode

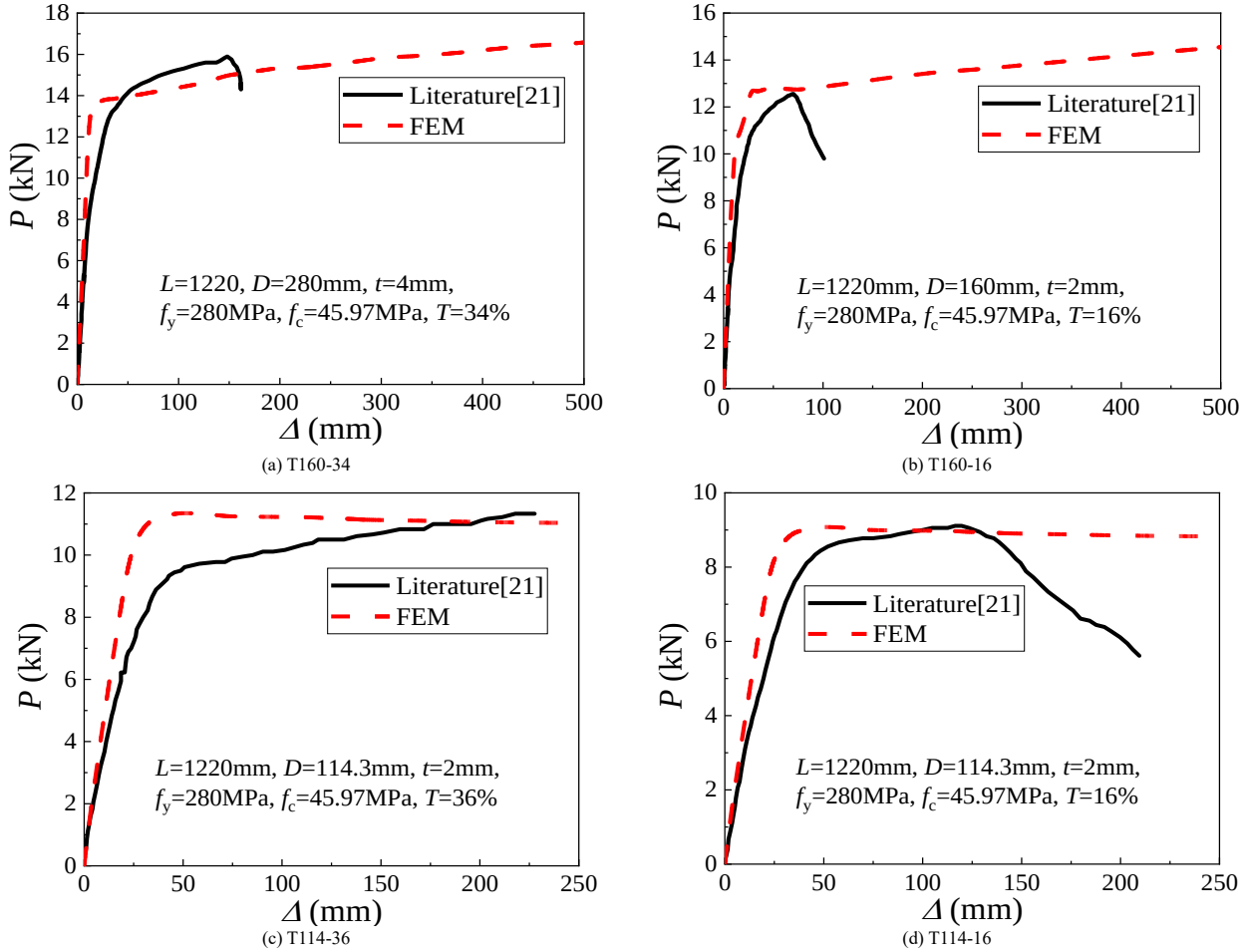

Fig. 6 Comparison of load-displacement curves between FE analysis and experiments

2.3. Parameter analysis

2.3.1. Parameter matrix

The models were subjected to combined axial compression and lateral loading. 440 FE models were designed, and the analysis parameters are listed in Table 2. Model designation conventions are explained using "n2-q235-4-33-40-30%" as an example: "n2" signifies an axial compression ratio of n=0.2 (where $n=N/(f_yA_s)$, A_s is the cross-sectional area of the steel tube), "q235" indicates a steel yield strength of 235 MPa, "4" represents an aspect ratio of L/D = 4, "33" represents a steel tube diameter-to-thickness ratio of D/t = 33, "40" denotes a cubic compressive strength of f_{cu}=40 MPa, and "30%" indicates a concrete filling ratio (T) of 30%.

The concrete filling ratio (T) ranged from 0% to 95%, with models established at 5% intervals. Using a binary search method, the optimal filling ratio, i.e., the minimum concrete filling ratio at which a partially CFST column basically reaches the load capacity of a CFST column, is determined with a precision of one hundredth of a percent.

In order to ensure that the transverse diaphragm is sufficient to transfer the load to the concrete, the diaphragm was set as a solid plate, and the thickness of the transverse diaphragm was calculated based on the axial compressive load capacity of the steel tube as the shear resistance. The material properties were the same as the steel tube.

Table 2
Main design parameters of the partially CFST models

Model Number	Main design parameters					
	Steel tube outer diameter D (mm)	Steel tube thickness t (mm)	Aspect ratio L/D	Concrete strength f_{cu}（MPa）	Steel strength f_y（MPa）	Axial compression ratio n
n1-q235-200-4-33-40-(0–95)	200	6	4	40	235	0.1
n2-q235-200-4-33-40-(0–95)	200	6	4	40	235	0.2
n3-q235-200-4-33-40-(0–95)	200	6	4	40	235	0.3
n4-q235-200-4-33-40-(0–95)	200	6	4	40	235	0.4
n5-q235-200-4-33-40-(0–95)	200	6	4	40	235	0.5
n6-q235-200-4-33-40-(0–95)	200	6	4	40	235	0.6
n2-q235-400-4-33-40-(0–95)	400	12	4	40	235	0.2
n2-q235-600-4-33-40-(0–95)	600	18	4	40	235	0.2
n2-q235-800-4-33-40-(0–95)	800	24	4	40	235	0.2
n2-q235-200-4-20-40-(0–95)	200	10	4	40	235	0.2
n2-q235-200-4-25-40-(0–95)	200	8	4	40	235	0.2
n2-q235-200-4-50-40-(0–95)	200	4	4	40	235	0.2
n2-q235-200-8-33-40-(0–95)	200	6	8	40	235	0.2

n2-q235-200-12-33-40-(0–95)	200	6	12	40	235	0.2
n2-q235-200-16-33-40-(0–95)	200	6	16	40	235	0.2
n2-q355-200-4-33-40-(0–95)	200	6	4	40	355	0.2
n2-q460-200-4-33-40-(0–95)	200	6	4	40	460	0.2
n2-q690-200-4-33-40-(0–95)	200	6	4	40	690	0.2
n2-q235-200-4-33-20-(0–95)	200	6	4	20	235	0.2
n2-q235-200-4-33-30-(0–95)	200	6	4	30	235	0.2
n2-q235-200-4-33-50-(0–95)	200	6	4	50	235	0.2
n2-q235-200-4-33-60-(0–95)	200	6	4	60	235	0.2

2.3.2. Failure modes

The influence of the concrete filling ratio on the failure modes follows a similar pattern in different models, represented by models n2-q235-4-33-40-(0–95%).

As shown Fig. 7(a), at a concrete filling ratio of 0 (i.e., steel hollow tube), the failure mode is characterized by plastic buckling at the bottom of the steel tube. With increasing concrete filling ratio (0% to 10%), the failure mode changes to plastic buckling of the steel hollow section (SHS) above the steel-concrete interface, resulting in increased load capacity and ductility, as shown in Fig. 7(b). When the concrete filling ratio increased to the range of 10% to 28%, as depicted in Fig. 7(c), the failure mode changes from buckling of the SHS to plastic hinge formation at the bottom of the column. This indicates that the optimal filling ratio is 28%. Beyond the optimal filling ratio, the failure mode is the same as shown in Fig. 7(d). As the concrete filling ratio further increases, the stiffness slightly improves, while the load capacity and ductility barely change, as shown in Fig. 8.

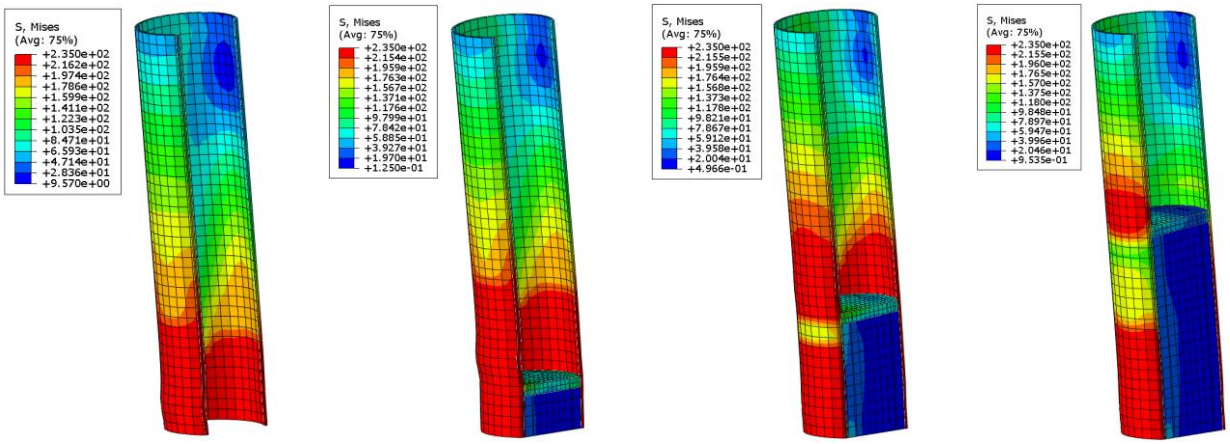

(a) T =0% (b) T=10% (c) T=28% (d) T=50%

Fig. 7 Failure modes of partially CFST columns under different concrete filling ratios

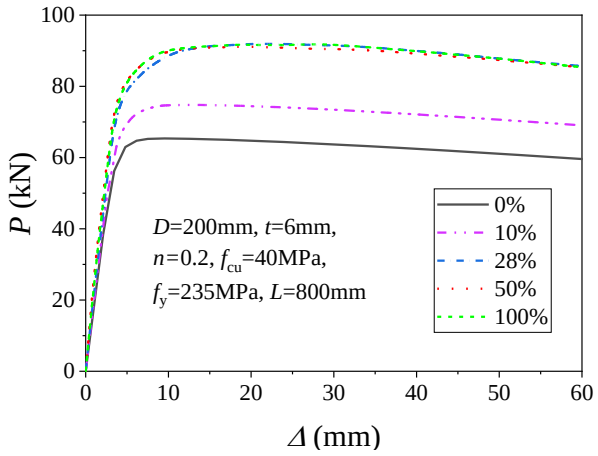

Fig. 8 Load-displacement curves of partially CFST columns with different concrete filling ratios

2.3.3. Parametric analysis

Before analyzing the impact of various parameters on the optimal filling ratio, it is necessary to clarify that, as explained in Section 2.3.2, when the optimal filling ratio is achieved, the failure mode of the partially CFST column is characterized by the formation of plastic hinges at both the base of the column and the SHS above the steel-concrete interface. Both sections reach their combined compressive and bending load capacity.

At this point, if the strength of the composite section enhances, the lateral load will also increase, while the strength of SHS remains unchanged, which will cause the failure of the hollow steel tube. To ensure the failure mode mentioned earlier, the concrete filling height will increase, so the optimal filling ratio will increase, as shown in Fig. 9(a). Conversely, if the strength of the SHS increases, the SHS will not fail. To achieve the desired failure mode, the height of concrete filling should be reduced, resulting in a decrease in the optimal filling ratio, as shown in Fig. 9(b), in which M_s and M_{sc} represent the compression-bending capacity of the SHS and the composite section, respectively. In addition, M_{s1} and M_{sc1} represent the compression-bending capacity of the strengthened SHS and composite section, respectively. From this analysis, it can be concluded that the optimal filling ratio is related to the relative strength of the SHS and the composite section. When the load capacity of the composite section increases more significantly compared to the SHS, the optimal filling ratio decreases, and vice versa.

(1) Axial compression ratio

When the axial compression ratio ranges from 0.1 to 0.6, the lateral load capacity decreases with an increase in the axial compression ratio (Fig. 10(a)). Once the optimal filling ratio is reached, the load capacity basically un-changes,

at the optimal filling ratio, the differences in the load capacity among the columns decrease. This is because before reaching the optimal filling ratio, the failure occurs in the SHS above the concrete interface, and the influence of axial compression ratio on the steel tube is obvious; when the optimal filling ratio is reached, the composite section of the column base fails, while the influence of axial force is relatively small.

The optimal filling ratio increases with the axial compression ratio as depicted in Fig. 10(b). This is also because when the axial force increases, the compressive and bending load capacity of the composite section decreases less than the SHS. The relationship between the axial compression ratio and the compression-bending capacity of the sections can be determined based on the *N-M* curve, as shown in Fig. 11(a), and the load capacity ratios of the two sections under different axial compression ratios are shown in Fig. 11(b). It can be observed that as the axial compression ratio increases, the compression-bending capacity of the composite section becomes relatively stronger compared to the unfilled steel tube section, resulting in an increase in the optimal filling ratio.

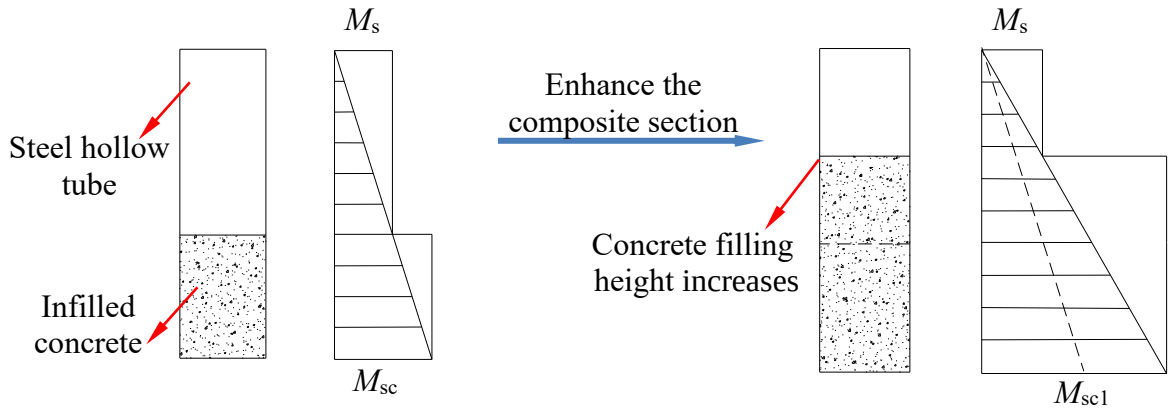

(a) Optimal filling ratio increases with a stronger composite section

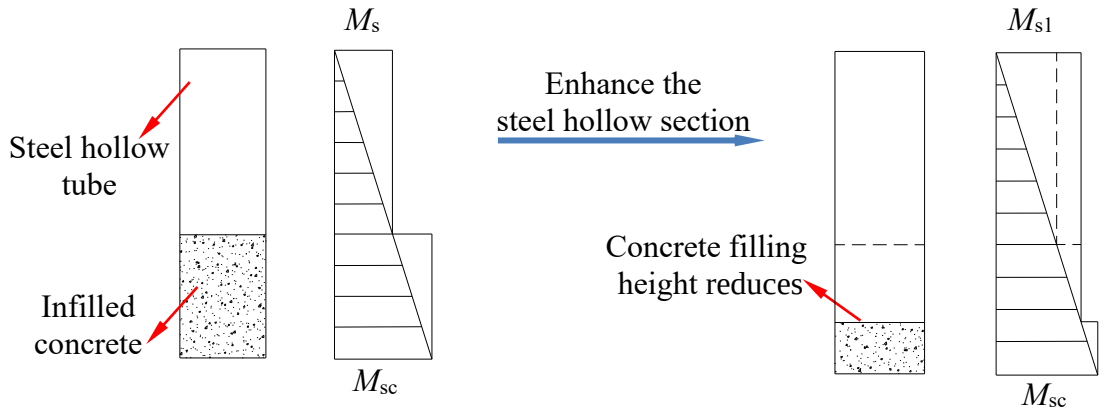

(b) Optimal filling ratio decreases with a stronger steel hollow section

Fig. 9 The influence of two types of sections strength on the optimal filling ratio

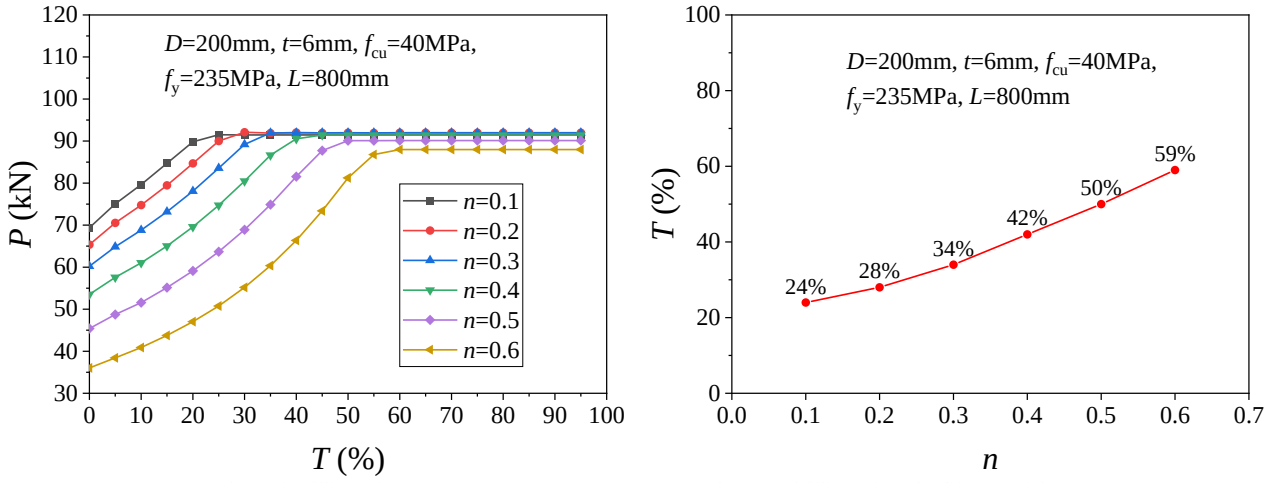

(a) Load capacity-filling ratio curves

(b) Optimal filling ratio under different axial compression ratios

Fig. 10 Effect of axial compression ratio on the load capacity and optimal filling ratio

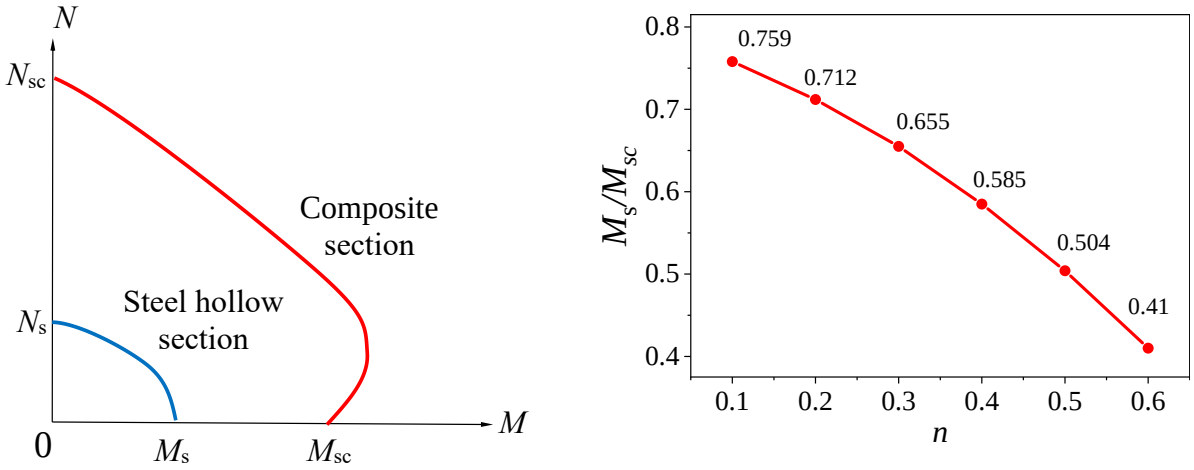

(a) Comparison of *N-M* curves for two sections (b) The ratio of load capacity decreases with axial compression ratios

Fig. 11 Effect of vertical load on the load capacity of SHS and composite section

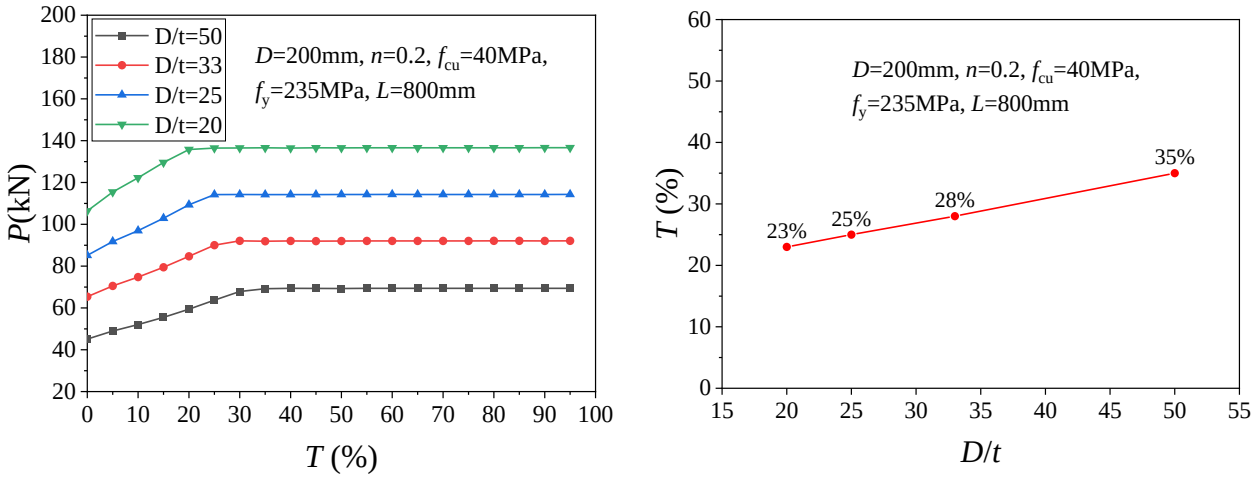

(a) Load capacity-concrete filling ratio curves (b) Optimal filling ratio under different diameter-to-thickness ratios

Fig. 12 Effect of diameter-to-thickness ratio on the load capacity and optimal filling ratio

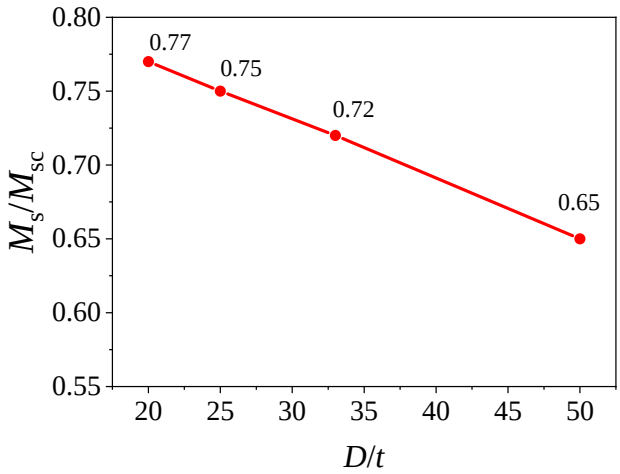

Fig. 13 The ratio of load capacity decreases with diameter-to-thickness ratios

(2) Diameter-to-thickness ratio

When the diameter-to-thickness ratio ranges from 20 to 50, the lateral load capacity decreases with an increase in the diameter-to-thickness ratio (Fig. 12(a)). This is because as the ratio of diameter-to-thickness increases, the strength of the composite section decreases, resulting in a corresponding decrease in load capacity of columns at every concrete filling ratio.

The optimal filling ratio increases with the diameter-to-thickness ratio (Fig. 12(b)). This is because when the steel tube thickness reduces, the compression-bending capacity of the SHS reduced more, as shown in Fig. 13.

(3) Steel strength

Fig. 14 (a) depicts that the lateral load capacity of steel tubes increases with the increase of steel strength in the range of 235MPa to 690MPa. This is because the increase of steel tube strength enhances the compressive-bending load capacity of the composite section.

Fig. 14(b) illustrates the optimal filling ratio increases with increasing steel strength. This is attributed to the fact that as the steel strength increases, the compression-bending capacity of the composite section increases relatively smaller than that of the SHS, as shown in Fig. 15.

(4) Concrete strength

When the concrete strength ranges from 20MPa to 60MPa, there is no difference in lateral load capacity before reaching the optimal filling ratio (Fig. 16(a)). However, once the optimal filling ratio is achieved, the load capacity increases with higher concrete strength. This is because the concrete strength is only related to the load capacity of the composite section. Therefore, when the SHS is damaged, the load capacity of every CFST column is consistent. When the composite section is damaged, the load capacity of the section increases with the increase of concrete strength.

The optimal filling ratio increases with increasing concrete strength (Fig.

16(b)). This is attributed to the fact that as the concrete strength increases, the load capacity of the composite section is enhanced.

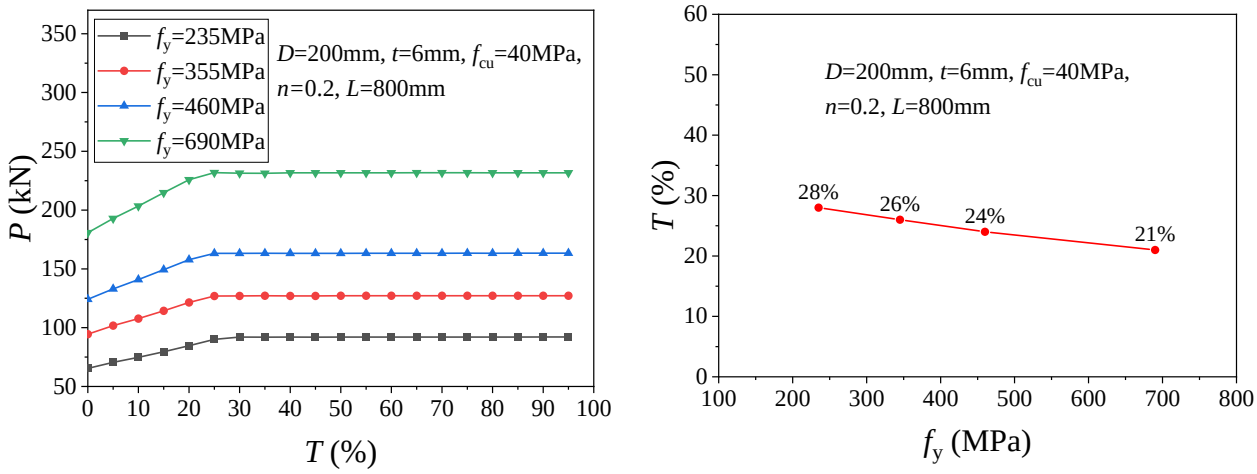

(a) Load capacity-concrete filling ratio curves (b) Optimal filling ratio under different steel strengths

Fig. 14 Effect of steel strength on the load capacity and optimal filling ratio

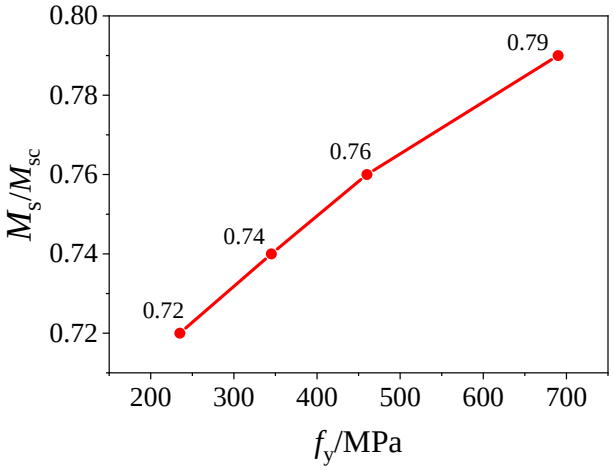

Fig. 15 The ratio of load capacity increases with steel strengths

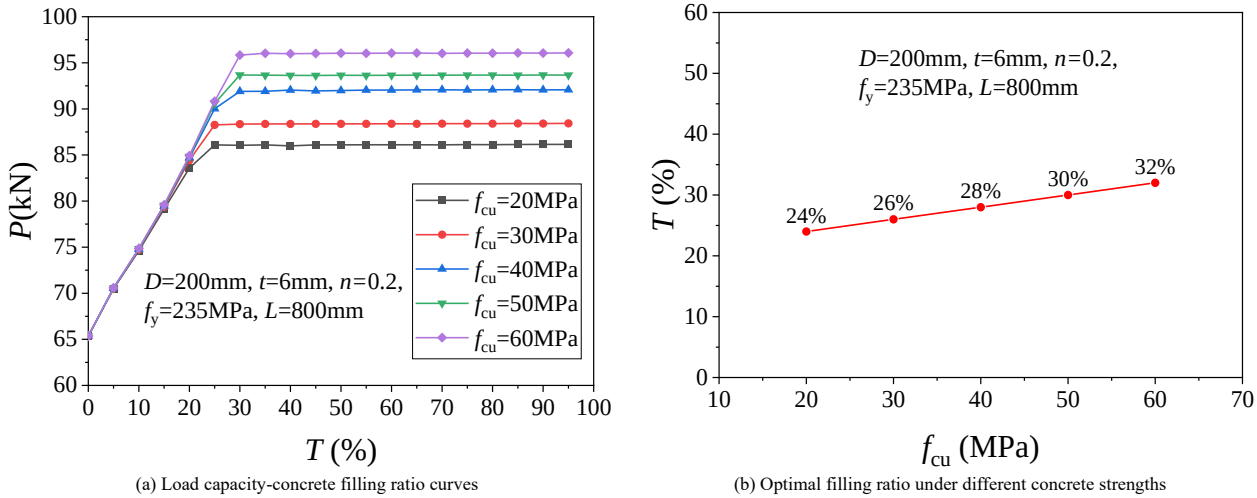

(a) Load capacity-concrete filling ratio curves (b) Optimal filling ratio under different concrete strengths

Fig. 16 Effect of concrete strength on the load capacity and optimal filling ratio

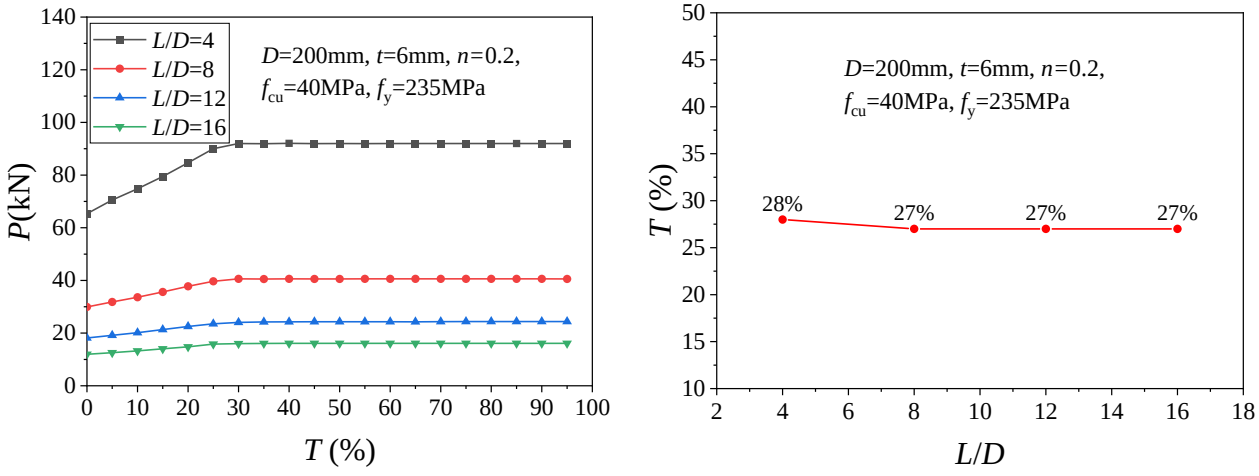

(a) Load capacity-concrete filling ratio curves (b) Optimal filling ratio under different aspect ratios

Fig. 17 Effect of aspect ratio on the load capacity and optimal filling ratio

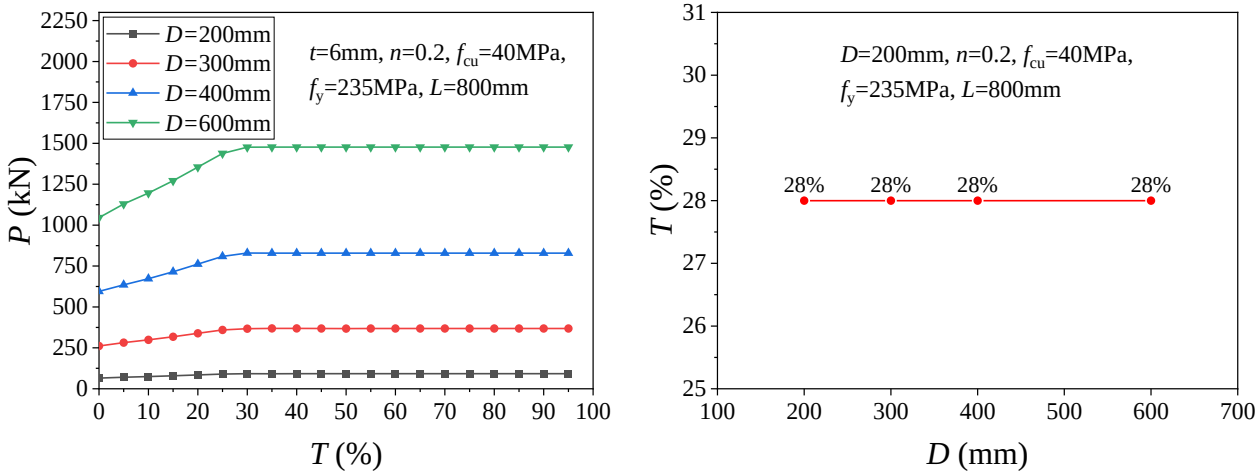

(a) Load capacity-concrete filling ratio curves (b) Optimal filling ratio under different section sizes

Fig. 18 Effect of section size on the load capacity and optimal filling ratio

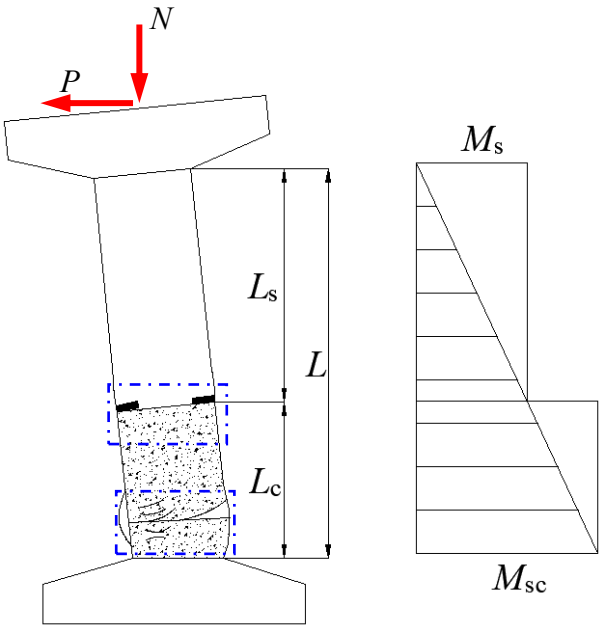

Fig. 19 Critical failure mechanism of partially CFST columns

(5) Aspect ratio

When the aspect ratio ranges from 4 to 16, the lateral load capacity is independent of the aspect ratios (Fig. 17(a)). Meanwhile, the aspect ratio has little effect on the optimal filling (Fig. 17(b)). This is because, within the considered parameter range, the change in aspect ratio has no effect on the strength of the two sections.

(6) Section size

Fig. 18(a) shows that when the section size ranges from 200mm to 600mm, the lateral load capacity increases with an increase in the section size. Fig. 18(b) illustrates the section size has no impact on the optimal filling ratio. This is because only changing the section dimension will lead to a proportional increase in the load capacity of both the SHS and the composite section.

3. Calculation method for the optimal filling ratio

3.1. Simplified mechanical model

When the aspect ratio of the column is greater than or equal to 4, the influence of cantilever shear deformation on structural performance can be ignored [32]. Therefore, compression-bending-shear components can be simplified as compression-bending components.

3.2. Calculation formulas for the optimal ratio

As mentioned before, the failure mode of partially CFST columns is characterized by a gradual transition from external buckling of the SHS to the formation of plastic hinges at the bottom of columns with increasing concrete filling ratio. At the critical point corresponding to the optimal filling ratio, as shown in Fig. 19, the SHS at the interface with the infilled concrete and the composite section at the bottom of column both reach their ultimate compression-bending capacity limits (i.e. M_1=M_s, and M_2=M_{sc}, where M_1 and M_2 correspond to the compression-bending capacity at the two respective sections in Fig. 19, M_s and M_{sc} represent the ultimate compression-bending capacity of the SHS and the composite section, respectively), which is also applicable to columns subjected to cyclic loading. Thus, the following equation can be obtained:

$$\frac{M_s}{L_s} = \frac{M_{sc}}{L} \tag{5}$$

where L_s is the length of the unfilled concrete within the steel tube, L_c is the

height of the infilled concrete, and L is the total length of the steel tube.

Based on the Eq. (5), the formula of optimal filling ratio can be further obtained in Eq. (6).

$$T_0 = 1 - \frac{M_s}{M_{sc}} \tag{6}$$

The compression-bending capacity of the composite section M_{sc} and the SHS M_s can be calculated according to Refs. [33] and [34], respectively.

3.3. Theoretical verification

3.3.1. Comparison between theoretical and FE results of section capacity

Comparisons between the theoretical values (M_s and M_{sc}) with the FE results (M_{sf} and M_{scf}) of the compression-bending capacity of the SHS and the CFST section are shown in Fig. 20. The average values of M_{sf}/M_s and M_{scf}/M_{sc} are 1.0583 and 1.0302, respectively, with variances of 0.0041 and 0.0050, respectively.

3.3.2. Comparison between theoretical and FE results of optimal filling ratio

The comparisons of optimal filling ratios between the theoretical calculation and FE analysis results under different parameters are shown in Fig. 21. It can be seen that they are in good agreement, indicating the theoretical formulas have a certain degree of good accuracy.

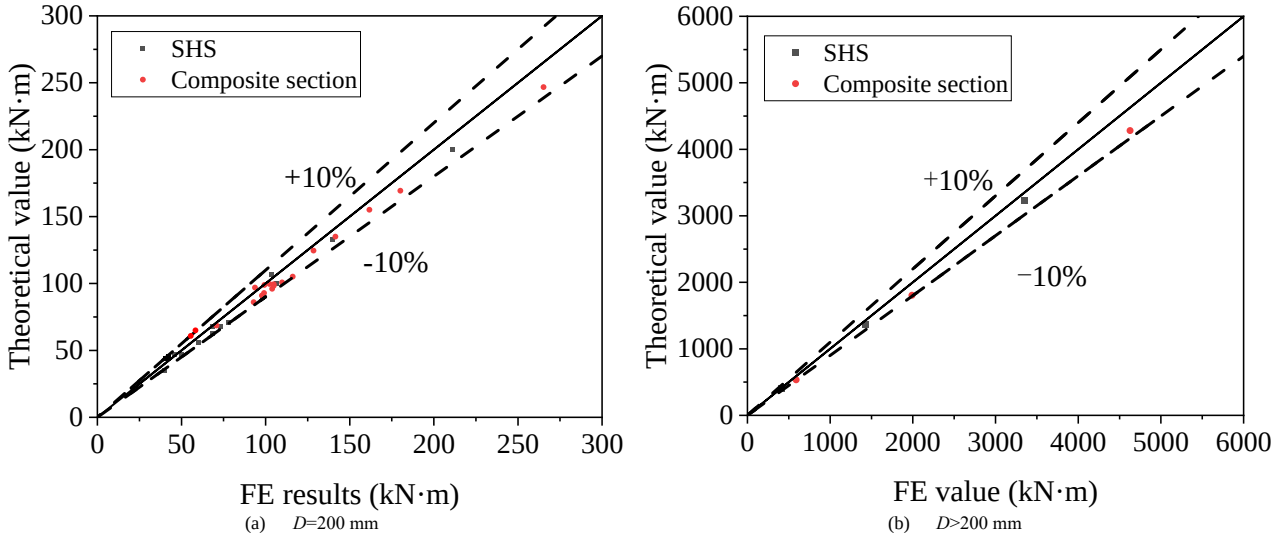

(a) D=200 mm (b) D>200 mm

Fig. 20 Comparison between theoretical and FE results

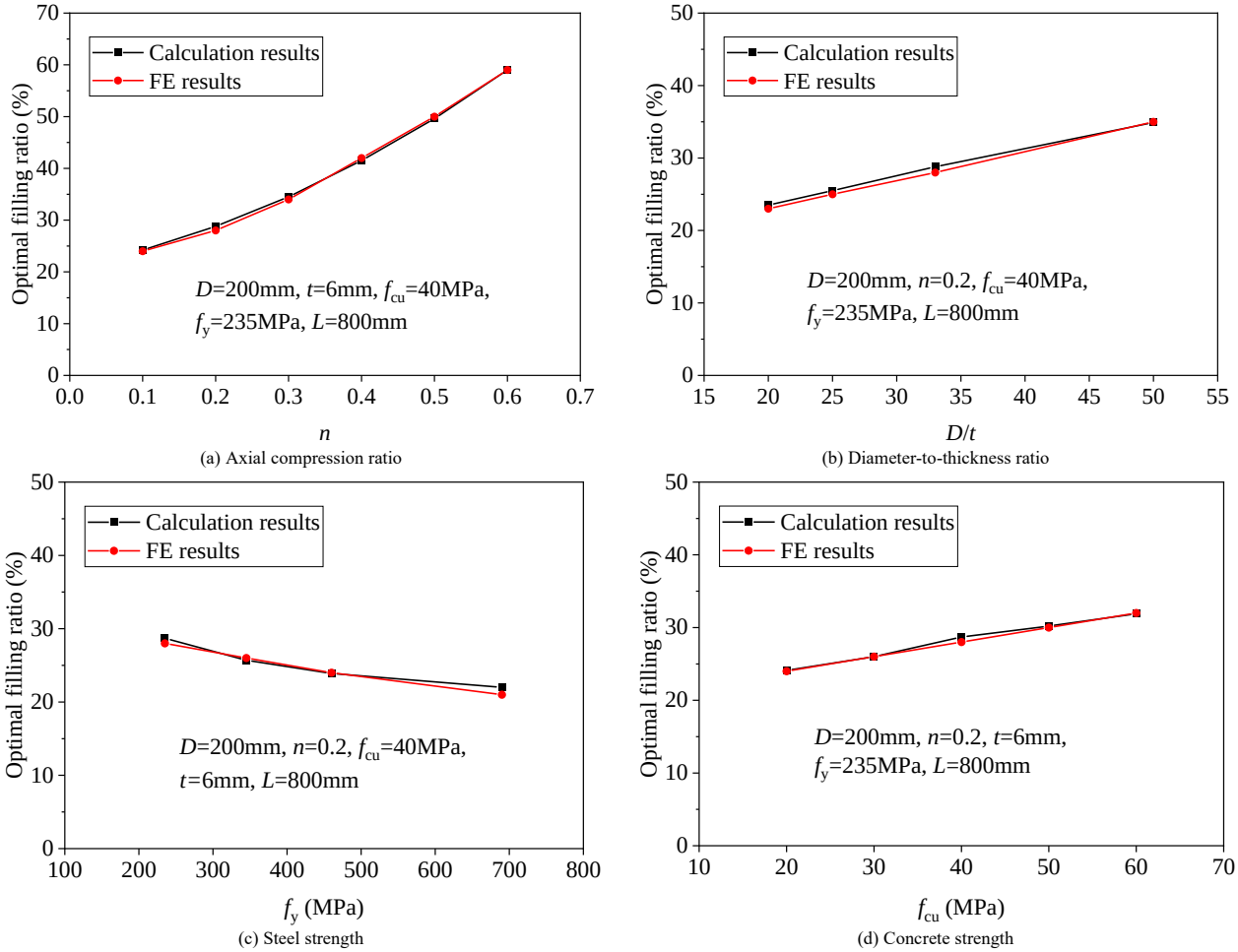

(a) Axial compression ratio (b) Diameter-to-thickness ratio

(c) Steel strength (d) Concrete strength

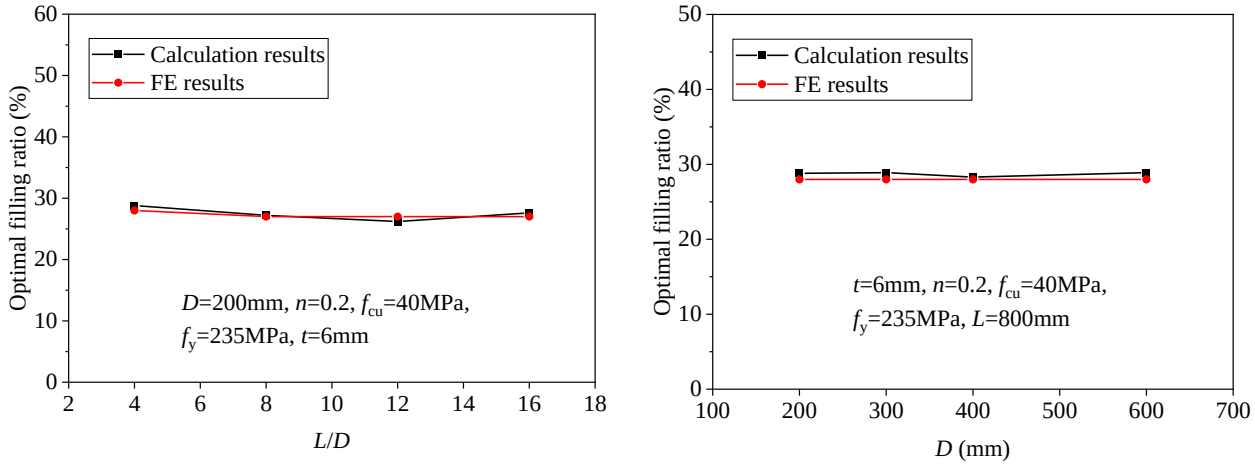

(e) Aspect ratio (f) Section size

Fig. 21 Optimal filling ratios of partially CFST columns between theoretical calculation and FE analysis result under different parameters

Table 3
Comparison between theory and experimental results in reference [34]

Specimen	*R* (mm)	*t* (mm)	*L* (mm)	Concretefilling ratio	Test results (kN)	Calcul-ation results(kN)	ratio	Optimal filling ratio (%)
SC34-66-00	140	4	1527	0	60.3	59.4	1.02	/
SC34-66-24	140	4	1527	24%	72.7	78.4	0.93	24.2%
SC34-66-28	140	4	1527	28%	71.7		0.92	
SC34-66-35	140	4	1527	35%	75.6		0.96	
SC26-85-00	180	4	1527	0	96.4	99.4	0.97	/
SC26-85-26	180	4	1527	26%	116.7	124.8	0.94	20.4%
SC26-85-35	180	4	1527	35%	116.1		0.93	
SC26-85-38	180	4	1527	38%	121.8		0.98	

3.3.3. Comparison between theoretical and experimental results of optimal filling ratio

The calculation results of the test specimens from Ref. [34] are presented in Table 3, and the failure mode is shown in Fig. 22. Using the calculation formula proposed in this paper, the optimal filling ratios of the partially CFST columns in Ref. [34] at two diameter-to-thickness ratios are listed in Table 3. This suggests that the failure mode after reaching the optimal filling ratio is the formation of plastic hinges at the bottom of column, which is consistent with the failure mode explained earlier.

4. Shear resistance of the transverse diaphragm

When a partially CFST column is subjected to combined axial compression and lateral loading, the interface shear needs to be transmitted from the steel tube to infilled concrete. Due to the reduced bond length of partially CFST columns, the natural bond strength between the steel tube and infilled concrete is significantly reduced, and necessary structural measures are required. Transverse diaphragms are critical structural elements to facilitate the composite effect between the steel tube and concrete in partially CFST columns. Therefore, it is necessary to analyze its transmission effect and load capacity.

4.1. FE model of columns with transverse diaphragms

4.1.1. Model description

The shear resistance of the transverse diaphragm was simulated through a push-out experimental model. In this model, an additional rigid loading plate was introduced, with a diameter 2mm smaller than the inner diameter of the steel tube and the point load was applied at the loading plate. All other settings are the same as Section 2. The FE model and boundary conditions are shown in Fig. 23.

4.1.2. Model verification

The shear resistance of the transverse diaphragm was simulated according to the Ref. [35], and the failure mode is shown in Fig. 24, where outward buckling occurred at the bottom of column. The comparison of load-displacement curves between the test results and the FE result is shown in Fig. 25. It can be seen that the FE model coincide effectively with the test.

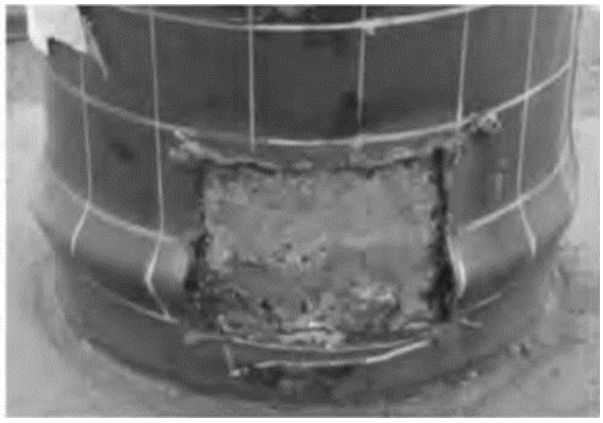

Fig. 22 Failure mode of SC-34-66-28

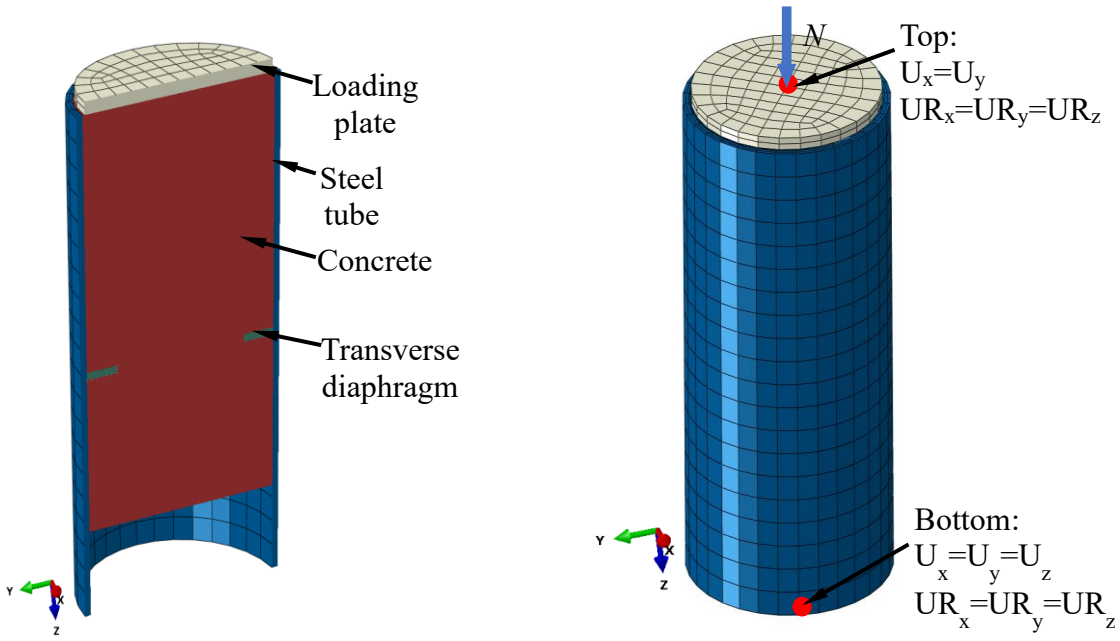

Fig. 23 FE model and boundary conditions

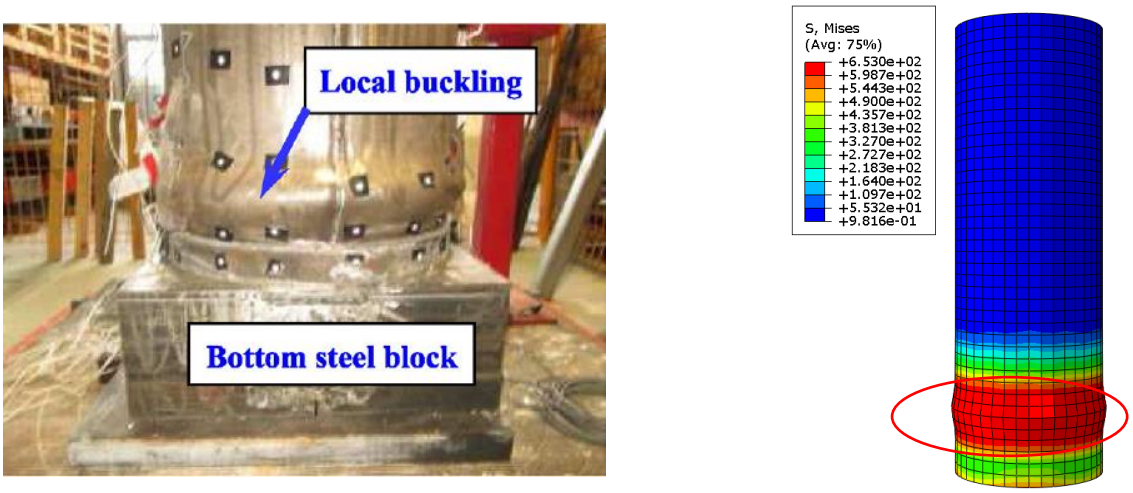

(a) Damage mode of CS400NR[35] (b)FE result

Fig. 24 Comparison of damage mode

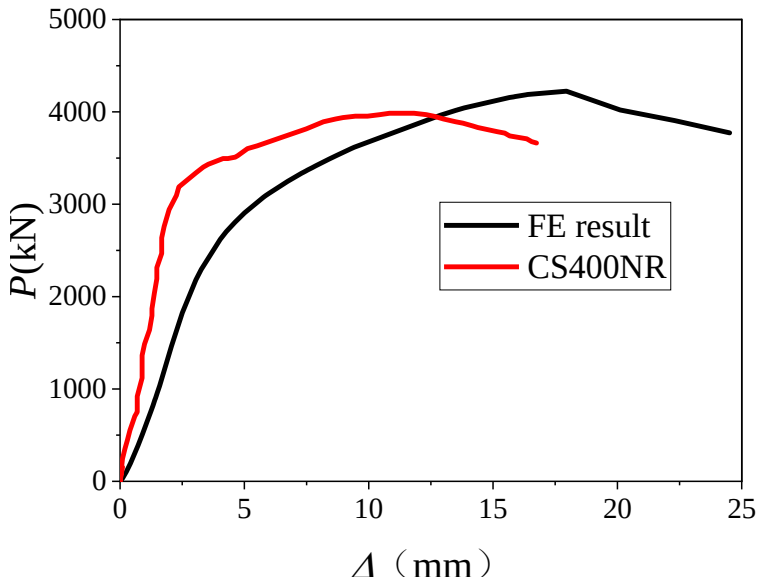

Fig. 25 Comparison of load-displacement curves

4.2. Parameter analysis

Akihiko Kono et al. [36] proposed a formula to calculate the shear strength P_d of a circular transverse diaphragm, as shown in Eq. (7). From the force analysis (Fig. 26), it can be seen that under axial load, the transverse diaphragm transfers the force from the concrete to the steel tube, and at this time, the

diaphragm is subjected to both pressure and reaction force.

$$P_{\mathrm{d}} = \varphi t_{\mathrm{d}} \frac{\sigma_y}{\sqrt{3}} \quad (7)$$

where φ is the inner circumference of the steel tube, t_{d} is the thickness of the circular transverse diaphragm, and σ_{y} is the yield strength of the circular transverse diaphragm.

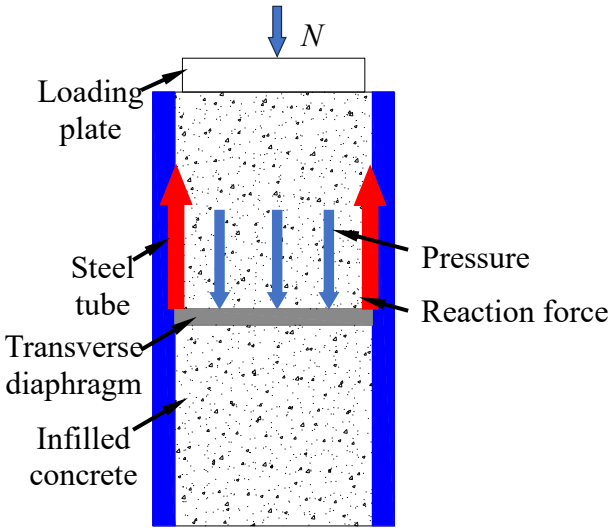

Fig. 26 Schematic diagram of the force acting on the transverse diaphragm

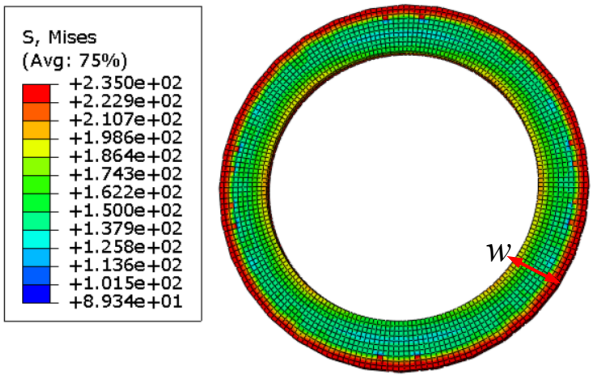

Fig. 27 The failure of transverse diaphragm

Table 4
Main parameters of the transverse diaphragms

Model Number	f_y (MPa)	t (mm)	d (mm)	w (mm)
q200-w30-t6-188	200	6	188	30
q235-w30-t6-188	235	6	188	30
q300-w30-t6-188	300	6	188	30
q355-w30-t6-188	355	6	188	30
q400-w30-t6-188	400	6	188	30
q460-w30-t6-188	460	6	188	30
q235-w30-t4-188	235	4	188	30
q235-w30-t5-188	235	5	188	30
q235-w30-t7-188	235	7	188	30
q235-w30-t8-188	235	8	188	30
q235-w30-t6-94	235	6	94	15
q235-w30-t6-282	235	6	282	45
q235-w15-t6-188	235	6	188	15
q235-w20-t6-188	235	6	188	20
q235-w25-t6-188	235	6	188	25
q235-w35-t6-188	235	6	188	35
q235-w40-t6-188	235	6	188	40
q235-w45-t6-188	235	6	188	45
q235-w50-t6-188	235	6	188	50

A preliminary simulation was conducted on the model, as shown in Fig. 27. It was inferred that the failure mode of the transverse diaphragm was shear failure at the edge. Therefore, when the transverse diaphragm fails, its shear load capacity is related to the strength of the weld seam or the strength of the welded part. Therefore, four parameters, namely, the strength, thickness, outer diameter and width of the transverse diaphragm, were selected for analysis.

Thus, 19 FE models were established as shown in the table 4, model designation conventions are explained using "q200-w30-t6-188" as an example: "q200" indicates a steel yield strength f_y =200 MPa, "w30" indicates that the width of the transverse diaphragm w=30 mm, "t6" denotes that the thickness of the steel tube t=6 mm, and "188" represents that the outer diameter of the transverse diaphragm d=188 mm. It should be noted that in order to achieve the failure of the transverse diaphragm, the cubic compressive strength f_{cu}=50MPa, the steel tube strength f_y=690MPa, and the diameter-to- thickness ratio (D/t) is set to 33.3, the length of the steel tube was taken as 400mm, the length of the concrete is 350mm, the transverse diaphragm was located in the middle of the steel tube. In order to obtain the load capacity of the transverse diaphragm, the contact between the concrete and steel tube interface and the concrete and transverse diaphragm interface was set to be frictionless.

4.2.1. Thickness

The load capacity of transverse diaphragm linearly increases with the thickness of transverse diaphragm as depicted in Fig. 28.

4.2.2. Strength

Fig. 29 depicts that the load capacity of transverse diaphragm linearly increases with yield strength (f_{y}).

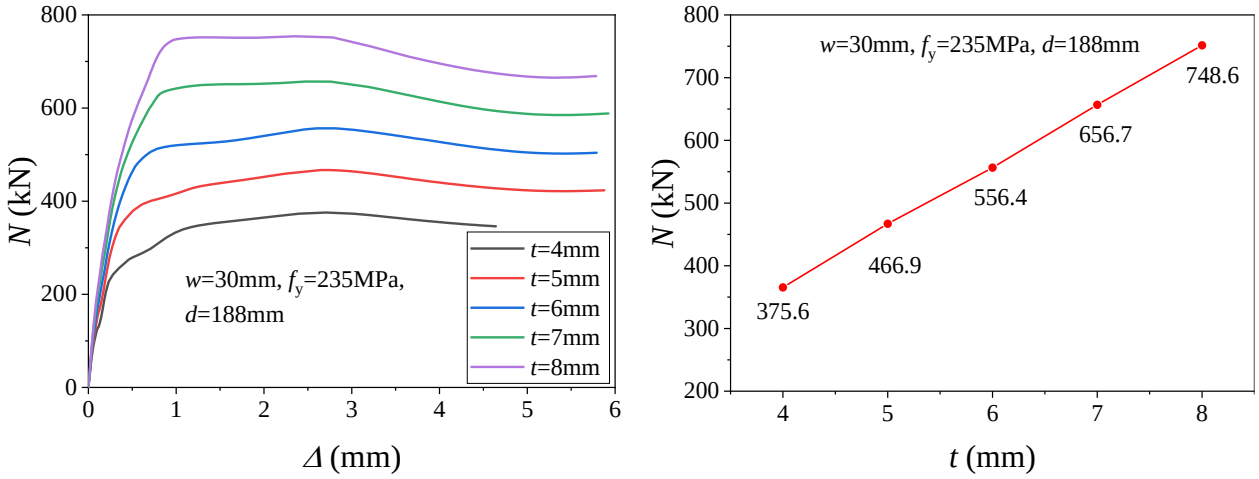

(a) Load-displacement curves of transverse diaphragms with different thicknesses (b) Load capacity of transverse diaphragms with different thicknesses

Fig. 28 The effect of thickness on the load capacity of transverse diaphragms

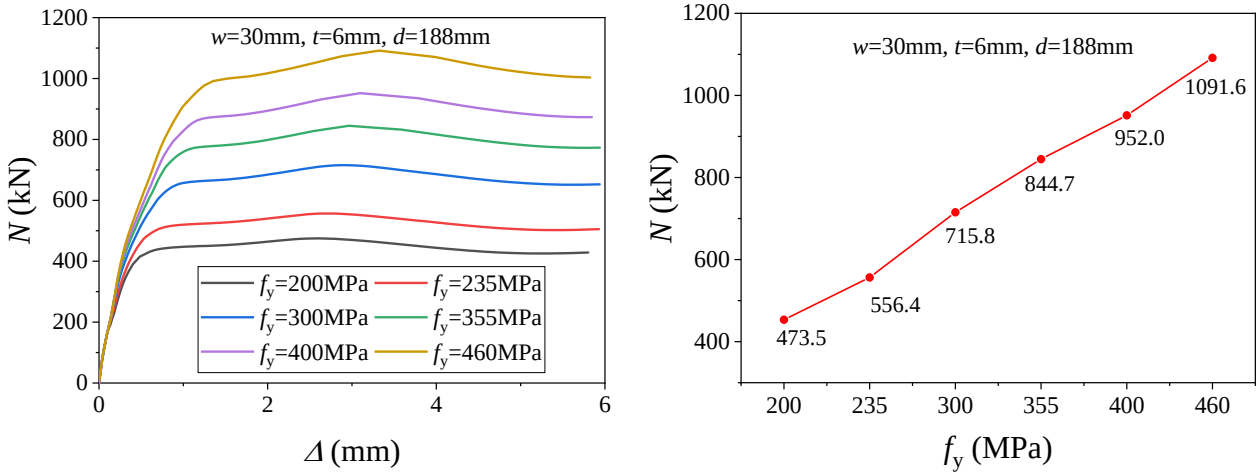

(a)Load-displacement curves of diaphragm under different strengths (b) Load capacity of transverse diaphragms with different strengths

Fig. 29 Effect of strength on the load capacity of transverse diaphragms

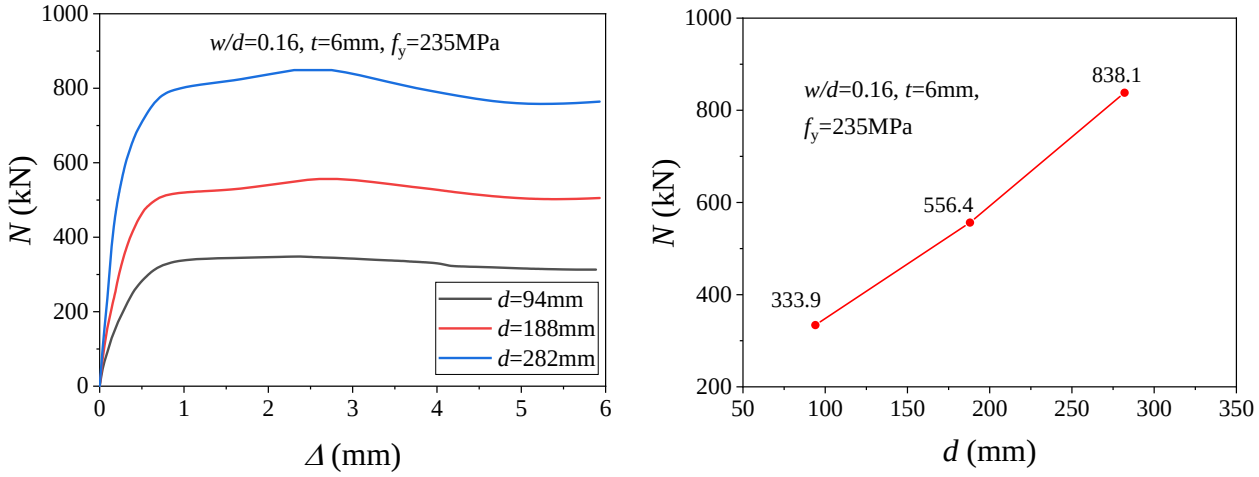

(a) Load-displacement curves of diaphragm under different outer diameters (b) Load capacity of transverse diaphragms with different outer diameters

Fig. 30 Effect of outer diameter on the load capacity of transverse diaphragms

4.2.3. Outer diameter of the diaphragm

Fig. 30 depicts when the outer diameter of the transverse diaphragm ranges from 94mm to 282mm, the transverse diaphragm load capacity almost linearly increases with transverse diaphragm strength.

4.2.4. Width

The load capacity suddenly increases when the width of the transverse diaphragm increases from 15mm to 20mm (The corresponding ratio of diaphragm area to concrete area ranges from 0.38 to 0.29), while further increasing the width does not significantly improve the load capacity (Fig. 31). The reason is that the compressed concrete area is too small, its load capacity is insufficient, and the concrete is crushed. Therefore, in order to prevent concrete from being crushed, the width of the diaphragm must be controlled. Ref. [37] reported that the annular compression area in steel tube concrete shall not be less than 1/3 of the concrete section, which is consistent with the FE results. In summary, the width of the transverse diaphragm is not considered as the main influencing factor, but it should not be too small, it is recommended to set the area of the transverse diaphragm to 1/3 of the concrete cross-sectional area, conservatively taking, w=0.1d.

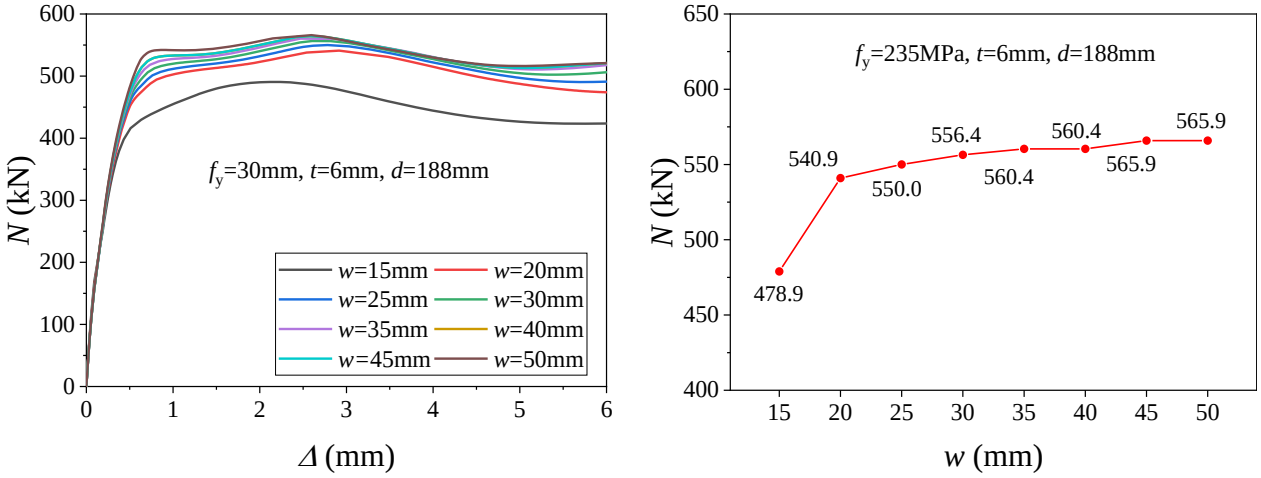

(a) Load-displacement curves of transverse diaphragms with different widths (b) Load capacity of transverse diaphragms with different widths

Fig. 31 Effect of width on the load capacity of transverse diaphragms

4.3. Design method for transverse diaphragms

4.3.1. Transverse diaphragm load capacity

The load capacity of the transverse diaphragm is primarily proportional to thickness, strength, and perimeter length of the transverse diaphragm. The FE results were compared with the formula calculation results, as shown in Fig. 32. It can be seen that Eq. (7) is relatively conservative and can be used to predict the load capacity of the diaphragm.

4.3.2. Load capacity reduction factor ω

When the partially CFST column is subjected to the combined lateral and axial loads, the equivalent plastic strain nephogram of concrete under peak load is shown in Fig. 33, and it can be seen that the failure of concrete is mainly concentrated in the compression zone, indicating that the concrete here loads a large force, while the concrete in the tension zone is almost not subjected to force. Additionally, as shown in Fig. 34, the transverse diaphragm reaches yield in the compression zone, but the stress in the tension zone is basically small. Therefore, the force acting on the transverse diaphragm decreases uniformly along the negative y-axis direction, as shown in Fig. 35, and the reduction factor is defined as ω. ω can be calculated as Eq. (8), and the calculated reduction factor of transverse diaphragm is 0.5.

$$\omega = \left(\frac{2\int_0^{\frac{\pi}{2}} R\cos\theta d\theta}{R} + \frac{2\int_{-\frac{\pi}{2}}^{0} 1-R\cos\theta d\theta}{-R}\right)/2\pi \quad (8)$$

Therefore, the load capacity of the transverse diaphragm in partially CFST column under combined lateral and axial loads can be obtained from Eq. (9).

$$P_{c1} = 0.5\varphi t_d \frac{\sigma_y}{\sqrt{3}} \quad (9)$$

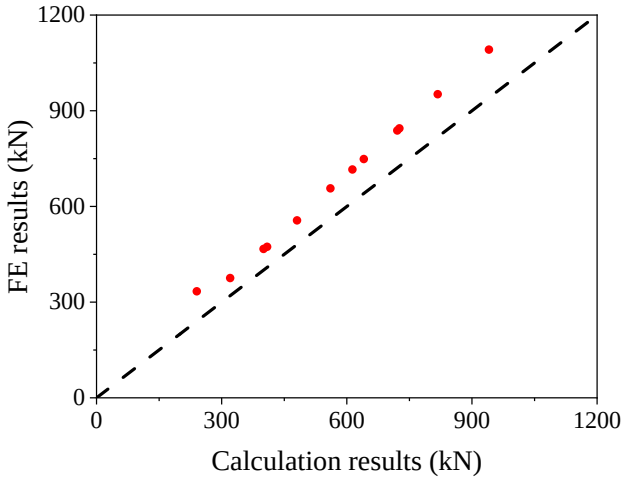

Fig. 32 Comparison between theory results and FE results

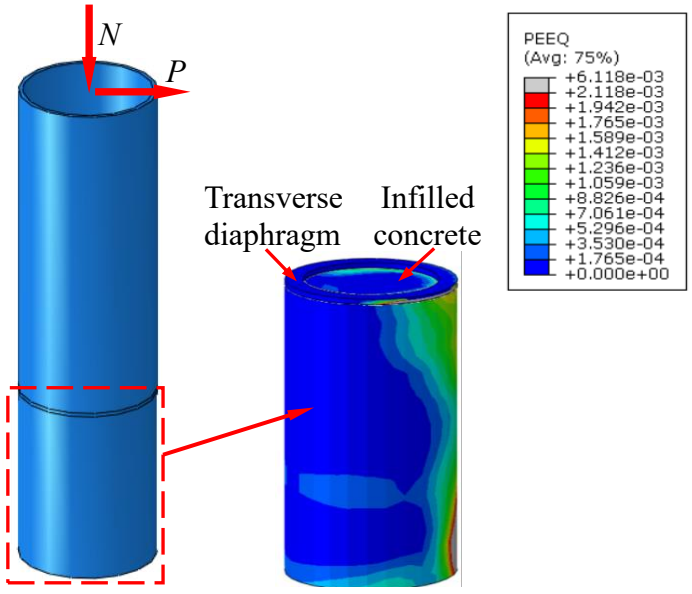

Fig. 33 Equivalent plastic strain nephogram of concrete under peak load

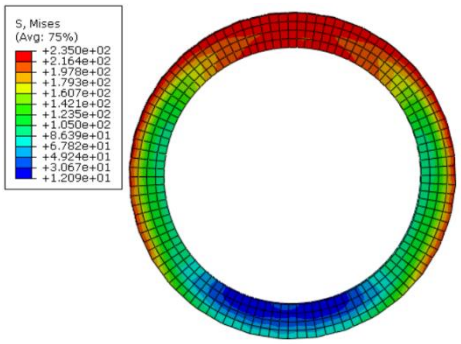

Fig. 34 Stress nephogram of the transverse diaphragm

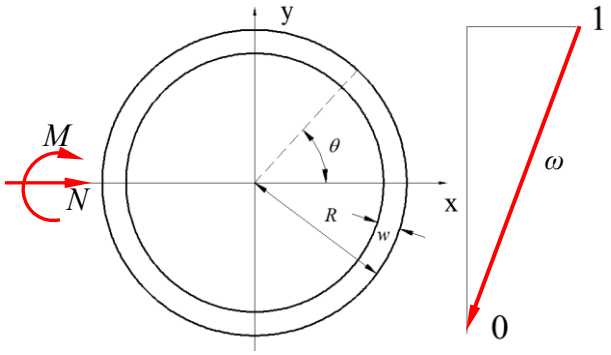

Fig. 35 Schematic diagram of reduction factor ω

5. Interface shear demand and design procedure

5.1. Shear demand in partially CFST columns

From the force analysis shown in Fig. 36, it is evident that under combined lateral and axial loads, the interface shear force exists between the inner wall of the steel tube and the surface of the infilled concrete. The interface shear resistance should be greater than the shear demand, so the transverse diaphragms are sufficient to transfer the load to the infilled concrete, allowing the infilled concrete to be fully utilized. Note that the contribution of friction is ignored and used as a strength reserve.

The calculation of the plastic load capacity of the composite section is based on the following assumptions:

(1) At the ultimate limit state, transverse diaphragms can effectively transfer the shear force between the steel tube and infilled concrete.

(2) The tensile resistance of the concrete is neglected.

(3) The plane remains plane.

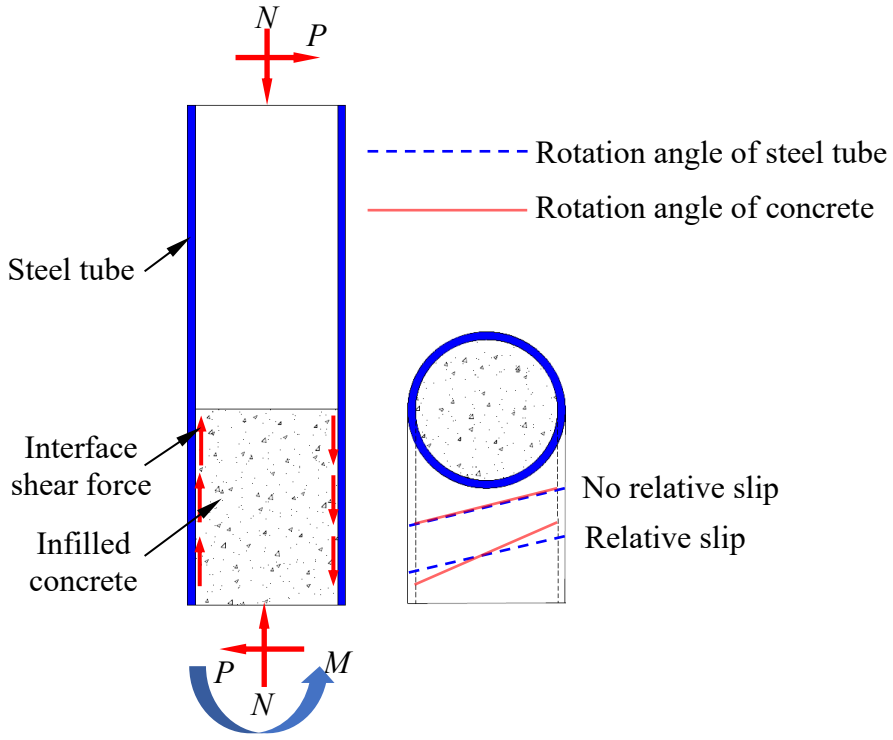

Fig. 36 Schematic diagram of mechanism analysis under lateral and compression loads

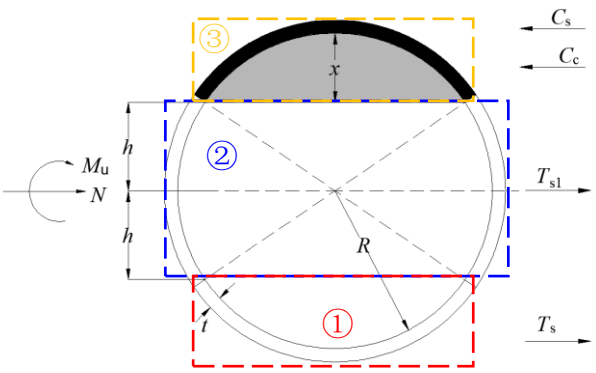

Fig. 37 Force conditions of circular composite section under compression-bending state

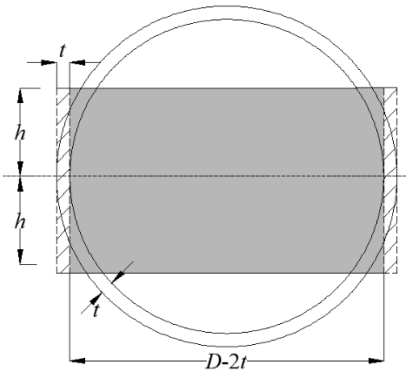

Fig. 38 Simplified calculation diagram

5.2. Calculation of shear demand for circular composite sections

Fig. 37 shows the force diagram of a circular composite section under compression and bending, for ease of explanation, the section is divided into three zones: ①, ②, ③. And the equilibrium equation of the force ($\sum F$=0) is obtained:

$$C_s + C_c - T_s - T_{s1} - N = 0 \tag{10}$$

where C_c is the axial compressive resistance of the compressed concrete, C_s is the axial compressive resistance of the steel tube in zone ③, T_s is the tensile force of the steel tube in zone ①, T_{s1} is the tensile force of the steel tube in zone ②.

As shown in Fig. 37, zone ① and zone ③ are completely symmetrical, therefore, Eq. (11) can be obtained:

$$C_s = T_s \tag{11}$$

Simultaneous Eq. (10) and (11)

$$N = C_c - T_{s1} \tag{12}$$

As shown in Fig. 38, simplify the concrete area within the 2h range to the gray area and simplify the steel tube area within the 2h range to the shaded area (h is the distance from neutral axis to central axis). Therefore, C_c and T_{s1} can be expressed as

$$C_c = (\frac{\pi D^2}{8} - hD) f_c' \tag{13}$$

$$T_{s1} = 4thf_y \tag{14}$$

where, f_c' is the cylinder compressive strength of concrete, t is the thickness of the steel tube, D is the inner diameter of the steel tube, R is the inner radius of the steel tube.

Eq. (12), Eq. (13) and Eq. (14) are combined to calculate h, as shown in Eq. (15).

$$h = \frac{\frac{\pi D^2}{8} f_c' - N}{f_c' D + 4tf_y} \tag{15}$$

The above calculations are based on the compression zone being above the centerline of the section. At this point, the height of the compression concrete zone is

$$x = R - h \tag{16}$$

Then, substitute Eq. (15) into Eq. (16):

$$x = R + \frac{N - \frac{\pi D^2}{8} f_c'}{f_c' D + 4tf_y} \tag{17}$$

when the height of the compression zone x is greater than the radius R, the result remains unchanged.

The shear demand for composite sections is

$$N_v = A_c' f_c' \tag{18}$$

where A_c' is the concrete area in compression zone, and A_c' can be determined by Eqs. (19) and (20).

$$A_c' = (\beta R^2 - R\sin\beta)/2 \tag{19}$$

$$\beta = \arcsin\frac{h}{R} \tag{20}$$

5.3. Calculation verification

Fig. 39 shows a schematic diagram of the composite section under combined axial and lateral loads. The calculation of the compression-bending capacity for circular composite section corresponding to the shear demand is as follows:

$$M_c = A_c' f_c' y_{st} + 4f_y \int_{\alpha}^{\frac{\pi}{2}} R_0^2 t \sin\theta d\theta = \frac{2}{3}\left(\frac{h}{\tan\alpha}\right)^3 f_c' + 4\cos\alpha R_0^2 t f_y \tag{21}$$

where y_{st} is the distance from the central axis for C_c, R_0 is the radius of the center surface of the steel tube, α is the angle in radians between the edge of the compression zone and the positive direction of the x-axis.

The comparison between the calculated results (M_c) based on shear demand and the theoretical values (M_{ch}) are shown in Table 5. The average ratio of M_c/M_{ch} is 0.9453, with a variance of 0.00089. The results indicate that the calculated results agree well with the theoretical values.

Table 5
Comparison of calculated values with theoretical values

Model Number	Composite section		
	M_c (kN·m)	M_{ch} (kN·m)	M_c/M_{ch}
C235-n1-200-4-33-32	64.92	70.19	0.9249
C235-n2-200-4-33-32	67.98	71.59	0.9496
C235-n3-200-4-33-32-	70.35	73.58	0.9561
C235-n4-200-4-33-32	71.89	73.13	0.9830
C235-n5-200-4-33-32	72.52	72.09	1.0060
C235-n6-200-4-33-32	72.21	70.38	1.0260
C235-n2-400-4-33-32	538.70	588.77	0.9150
C235-n2-600-4-33-32	1811.47	1989.22	0.9106
C235-n2-800-4-33-32	4285.51	4626.42	0.9263
C235-n2-200-4-20-32	102.05	109.17	0.9348
C235-n2-200-4-25-32	85.64	91.37	0.9373
C235-n2-200-4-50-32	49.15	53.44	0.9197
C355-n2-200-4-33-32	97.76	101.51	0.9631
C460-n2-200-4-33-32	122.77	130.57	0.9403
C690-n2-200-4-33-32	175.14	185.36	0.9449
C235-n2-200-4-33-20	62.55	67.79	0.9227
C235-n2-200-4-33-30	65.68	70.70	0.9290
C235-n2-200-4-33-50	69.90	74.91	0.9331
C235-n2-200-4-33-60	72.01	76.80	0.9376
	Average value		0.9453
	Variance		0.00089

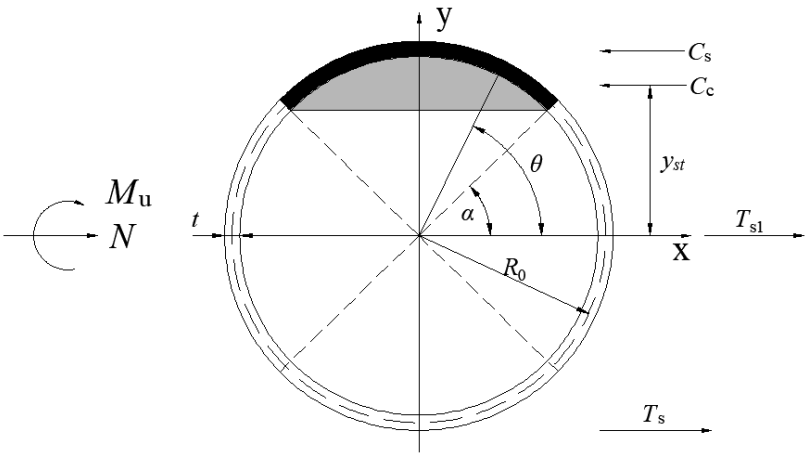

Fig. 39 Schematic diagram for calculating compression-bending capacity of circular composite section

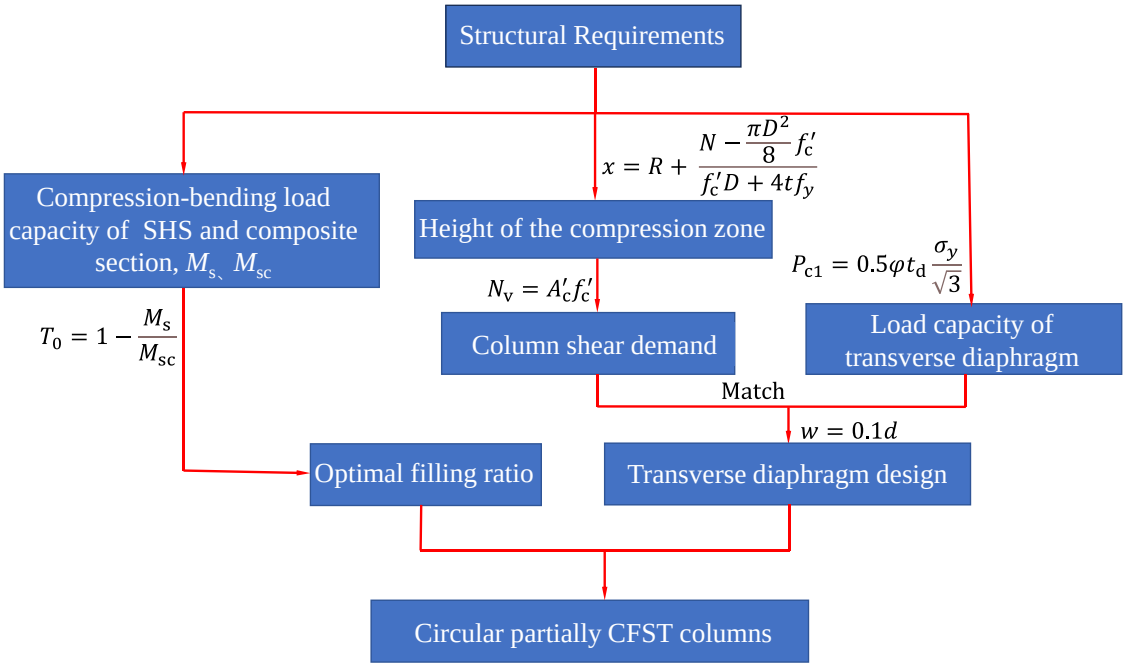

Fig. 40 Design procedure for partially CFST columns

5.4. Design procedure

Base on the comprehensive analysis of the mechanism of partially CFST columns, the main process is shown in Fig. 40. Firstly, based on the known engineering conditions and structural requirements, specific parameters for the partially CFST columns can be designed. Secondly, the optimal filling ratio can be calculated from the compression-bending capacity of the SHS and composite section using Eq. (6). Then, the shear demand of the partially CFST columns can be computed from the column dimensions, materials, and load conditions using Eq. (17) and Eq. (18). Finally, With Eq. (9), design recommendations for w=0.1d, considering the dimensions, and shear demand of the partially CFST columns, the design parameters for the transverse diaphragms can be determined. The design process concludes with the establishment of the concrete filling ratio and transverse diaphragm design, completing the design procedure for the partially CFST columns.

6. Conclusions

This study comprehensively discusses the influence of various parameters on the load capacity and optimal filling ratio of partially CFST columns. Based on the extensive FE and theoretical analysis of partially CFST column, the following observations and conclusions can be drawn:

(1) The concrete filling ratio can alter the failure mode of circular partially CFST columns subjected to combined constant axial compression and lateral loading. With an increase in the concrete filling ratio, the failure position shifts from the SHS above the filling interface to the bottom composite section.

(2) Prior to reaching the optimal concrete filling ratio, the load capacity, ductility, and stiffness of partially CFST columns increase with increasing concrete filling ratio. After reaching the optimal filling ratio, the load capacity and ductility remain relatively constant, but the stiffness increases.

(3) The optimal filling ratio of partially CFST columns under combined compression and lateral loads increases with increasing axial compression ratio, diameter-to-thickness ratio and concrete strength but decreases with increasing steel material strength. However, it is largely unaffected by the aspect ratio and section size.

(4) Transverse diaphragms transfer interface shear force, and the load capacity of transverse diaphragms is linearly related to the thickness, strength, and outer diameter of the transverse diaphragms. The calculation formulas for the load capacity of the transverse diaphragm in partially CFST columns was proposed. Additionally, it is recommended to use 0.1 times the outer diameter of the transverse diaphragm as the width of the transverse diaphragm.

(5) The interface shear demand in partially CFST columns was theoretically derived. By matching the shear demand with the load capacity of the transverse diaphragm, the design of the transverse diaphragm can be determined.

(6) The design procedure that can facilitate their wider applications for partially CFST columns was summarized and proposed, in which the optimal filling ratio and transverse diaphragm dimensions are main parameters.

Future research should focus on the application and optimized design of partially CFST columns in frame structures.

Acknowledgments

The authors greatly appreciate the financial support provided by the National Natural Science Foundation of China (No. 52378133) and Chongqing Natural Science Foundation of China (No. CSTB2023NSCQ-MSX0758). However, the opinions expressed in this work are solely the authors' own.

References

[1] Report on the Hanshin-Awaji earthquake disaster-damage to civil engineering. Tokyo: Maruzen Co, Ltd, 1996 [in Japanese].
[2] Li GC, Chen BW, Zhu BW, Yang ZJ, Ge HB, Liu YP. Axially loaded square concrete-filled steel tubular long columns made of high-strength materials: Experimental investigation, analytical behavior and design. J Build Eng 2022;58:104994.
[3] Du ZL, Liu YP, He JW, Chan SL. Direct analysis method for noncompact and slender concrete-filled steel tube members.Thin Wall Struct 2019;135:173-184.
[4] Li GC, Yang Y, Yang ZJ, Fang C, Ge HB, Liu YP. Mechanical behavior of high-strength concrete filled high-strength steel tubular stub columns stiffened with encased I-shaped CFRP profile under axial compression. Compos Struct 2021;275: 114504.
[5] Chan SL, Liu YP, Liu SW, A New Codified Design Theory of Second-order Direct Analysis for Steel and Composite Structures – From Research to Practice. Structures 2017; 9: 105-111.
[6] Li GQ, Chen BW, Yang ZJ, Ge HB and Li X. Axial behavior of high-strength concrete-filled high-strength square steel tubular stub columns. Adv Steel Constr 2021;17(2):158-168.
[7] Li GC, Qiu ZM, Yang ZJ, Chen BW and Feng YH. Seismic performance of high strength concrete filled high strength square steel tubes under cyclic pure bending. Adv Steel Constr 2020;16(2):112-123.
[8] Zhou XH, Gan D, Liu JP and Chen YF. Composite effect of stub square steel tubed columns under axial compression. Adv Steel Constr 2018;14(2):274-290.
[9] Li GC, Liu XH, Yang ZJ, Fang C, Ge HB, Liu YP. Testing, modeling, and design of square CFST columns internally reinforced by pultruded CFRP profile under axial compression. Eng Struct 2022;273: 115110.
[10] Li GC, Sun X, Yang ZJ, Fang C, Chen BW, Ge HB, Liu YP. Structural performance of concrete-filled square steel tubular columns encased with I-shaped CFRP under eccentric compression. Eng Struct 2021;248: 113254.
[11] Kang WH, Uy B, Tao Z and Hicks S. Design strength of concrete-filled steel columns. Adv Steel Constr 2015;11(2):165-184.
[12] Kitadt T. Ultimate strength and ductility of state-of-the-art concrete-filled steel bridge piers in Japan. Eng Struct 1998; 20(4-6): 347-354.
[13] Gan D, Zhang YJ, Zhou XH, Zhang XJ. Investigation of cyclic behavior of partially concrete-filled steel tubular columns, Eng Struct 2024; 300: 117175.
[14] Goto Y, Ebisawa T, Lu XL. Local Buckling Restraining Behavior of Thin-Walled Circular CFT Columns under Seismic Loads. J Struct Eng 2012; 140(5): 04013105.
[15] Yuan H, Dang J, Aoki T. Experimental study of the seismic behavior of partially concrete-filled steel bridge piers under bidirectional dynamic loading. Earthq Eng Struct D 2013; 42: 2197-2216.
[16] Yuan H, Dang J, Aoki T. Behavior of partially concrete-filled steel tube bridge piers under bidirectional seismic excitations. J Constr Steel Res 2014; 93(2): 44-54.
[17] Goto Y, Ghosh P, Kawanishi N. Nonlinear Finite Element Analysis for Hysteretic Behavior of Thin-Walled Circular Steel Columns with In-Filled Concrete. J Struct Eng, 2010; 136(11): 1413-1422.
[18] Goto Y, Mizuno K, Ghosh P. Nonlinear finite element analysis for cyclic behavior of thin-walled stiffened rectangular steel columns with in-filled concrete. J Struct Eng 2012; 138(5): 571-584.
[19] Lai ZC, Varma AH. Seismic behavior and modeling of concrete partially filled spirally welded

pipes. Thin Wall Struct 2017; 113: 240-252.
[20] Xiang NL, Yang F, Xu C. Novel fiber-based seismic response modeling and design method of partially CFST bridge piers considering local buckling effect. Soil Dyn Earthq Eng 2023; 170: 107911.
[21] Khalifa M, Shaat A, Ibrahim S. Optimum concrete filling ratio for partially filled noncompact steel tubes. Thin Wall Struct 2019; 134: 159-173.
[22] Wang ZF, Sui WN, Zhao ZH Pang H, Liao J. Study on seismic performance of partially concrete-filled steel circular bridge piers with transverse diaphragm. J Build Struct 2013; 34(S1): 233-239(in Chinese).
[23] Usami T, Ge HB, Saizuka K. Behavior of partially concrete-filled steel bridge piers under cyclic and dynamic loading. J Constr Steel Res 1997; 41(2-3): 121-136.
[24] Usami T, Ge HB. Ductility of concrete-filled steel box columns under cyclic loading. J Struct Eng 1994; 120(7): 2021-2040.
[25] Ge HB, Usami T. Cyclic tests of concrete-filled steel box columns. J Struct Eng 1996; 122(122): 1169-1177.
[26] Kwon YB, Song JY, Kon KS. The structural behavior of concrete filled steel piers. Proceedings of 16th Congress of IABSE. Iucerne, Switzerland: University of Applied Sciences Fribourg,2000; 16(18): 115-154.
[27] Zhou XH, Cheng GZ, Liu JP, Gan D, Chen YF. Behavior of circular tubed-RC column to RC beam connections under axial compression. J Constr Steel Res 2017; 130: 96-108.
[28] Li GC, Chen BW, Yang ZJ, Liu YP, Feng YH. Experimental and numerical behavior of eccentrically loaded square concrete-filled steel tubular long columns made of high-strength steel and concrete. Thin Wall Struct 2021;159: 107289.
[29] Zhou XH, Zhou Z, Gan D. Analysis and design of axially loaded square CFST columns with diagonal ribs. J Constr Steel Res 2020; 167: 105-848.
[30] Han LH, Yao GH, Tao Z. Performance of concrete-filled thin-walled steel tubes under pure torsion. Thin Wall Struct 2007; 45(1):24-36.
[31] Han LH. Concrete filled steel tubular structures: Theory and Practice. 3rd ed. Beijing：Science Press, 2016: 253-261 [in Chinese].
[32] 'International Federation for Structure Concrete. Model Code for Concrete Structures 2010: CEB-FIP MC90. Lausanne: International Federation for Structure Concrete, 2013.
[33] Tong GS. In-plane Stability of Steel Structures [M]. Beijing: China Construction Industry Press, 2015 [in Chinese].
[34] Wang ZF, Sui WN, Li GC, Wu Q, Ge L. Mechanical behavior of partially concrete-filled steel circular bridge piers under cyclic lateral load. China J High Transp 2015; 28(1): 62 - 70 [in Chinese].
[35] Tao Z, Song TY, Uy B, Han LH. Bond behavior in concrete-filled steel tubes. J Constr Steel Res 2016; 120:81-93.
[36] Akihiko K, Kenji S, Yuki O, et al. A quantitative evaluation of the stress transfer effect between steel tube and infill concrete by horizontal diaphragms in a CFST column. Architec Inst Jpn 2005; 598: 163-167 [in Japanese].
[37] Xue LH, Cai SH. Experimental study on bearing strength of concrete near the interface of steel tube and concrete core. Build Sci 1998; 04: 9-13+18 [in Chinese].

Advanced Steel Construction – Vol. 20 No. 4 (2024) 364–375
DOI:10.18057/IJASC.2024.20.4.4

MECHANICAL PROPERTIES OF ASSEMBLED WALL-SLAB JOINTS BETWEEN THIN DOUBLE SKIN COMPOSITE SHEAR WALLS AND PRECAST FLOOR SLABS SUBJECTED TO PURE BENDING

Jie Liu [1, 2], Zhi-Hua Chen [1], Ting Zhou [3, *] and Xiao-Feng Wang [2, 4]

[1] *School of Civil Engineering, Tianjin University, Tianjin, 300072, China*
[2] *Central Research Institute of Building and Construction Co., Ltd, MCC Group, Beijing 100088, China*
[3] *School of Architecture, Tianjin University, Tianjin, 300072, China*
[4] *National Steel Structure Engineering Technology Research Center, Beijing 100088, China*
** (Corresponding author: E-mail: zhouting1126@126.com)*

ABSTRACT

Two new types of assembled wall-slab joints are proposed for thin double skin composite shear walls and steel truss floor slabs, which are commonly used in construction. Pure bending tests were performed to investigate the failure modes and mechanical performance of these newly devised wall-slab joints. The results demonstrated that the new assembled wall-slab joints offer superior flexural bearing capacity and ductility. When subjected to pure bending load, the steel truss floor slabs failed before the joints, adhering to the design principle of "strong joints and weak members". Finite element models for the new assembled wall-slab joints were established and compared with test results. Furthermore, recognizing the prefabricated floor slab's failure section as the weakest, a new formula to calculate the bending capacity of these wall-slab joints was proposed, based on the principle of sectional force balance. Notably, these calculated results were more conservative than the test results.

ARTICLE HISTORY

Received: 27 October 2023
Revised: 30 August 2024
Accepted: 5 September 2024

KEYWORDS

Assembled wall-slab joints;
Thin double skin composite shear wall;
Pure bending test;
Finite element model;
Calculation method

1. Introduction

Owing to high population density and limited land resources, many urban areas in China have experienced an increase in the height of residential buildings to conserve urban land and accommodate large populations. As the height of these buildings increases, their structural sensitivity to lateral loads, such as seismic and wind forces, becomes more pronounced. Shear wall systems, which comprise rigidly connected shear walls and floor slabs, effectively counteract these lateral loads and are commonly employed in high-rise construction[1]. Previous studies have identified that the highest stress concentrations occur at the joints between shear walls and slabs under seismic loads. The primary failure mode in these joints is often attributed to inadequate ductility, resulting from improper arrangement in the joint zones, which can lead to potential global structural failures[2]. Consequently, numerous scholars have conducted extensive experimental research on traditional shear wall-to-slab joints and proposed more detailed reinforcement strategies[3-7]. These strategies include dual-layer reinforcement within the wall, additional transverse reinforcement, external FRP grid reinforcement, cross bracing, and X-type reinforcements, among others. These methods have been demonstrated to significantly enhance the load-bearing performance of these joints.

In the realm of prefabricated construction, the safety of joints between precast shear walls and floor slabs becomes paramount. Precast reinforced concrete shear walls are typically manufactured in factories and assembled on-site using wet joints at wall-to-slab interfaces. To enhance the bond characteristics in the core areas of these joints, reinforcing bars from the slabs are anchored within the shear walls. The entire assembly is made to work as a unit once the cast-in-place concrete reaches the desired strength[8]. Comparative studies between precast and cast-in-place joints have confirmed the structural integrity of prefabricated wall-to-slab joints[9-12].

Additionally, double skin composite (DSC) shear walls, a prevalent structural form in prefabricated construction, are widely used in nuclear facilities and high-rise buildings due to their high load-bearing capacity, superior seismic performance, and construction ease[13-15]. Per the Chinese code "Technical Specification for Steel Plate Shear Walls" [16], steel plates in commonly used shear walls are recommended to be at least 10 mm thick, with an optimal thickness ratio between the wall body and steel plates ranging from 25 and 100. Therefore, the minimum thickness of commonly used DSC shear wall is 250mm. However, in an effort to maximize indoor space, developers are increasingly reducing the thickness of shear walls, prompting researchers to develop innovative forms of thin DSC shear walls[17-20]. Studies indicate that, even with reduced wall thickness, these walls maintain a high load-bearing capacity and stiffness, and their seismic performance remains robust[18]. The interior of the thin DSC shear walls is segmented into channels with smaller cross-sectional areas, facilitating the integration of transverse reinforcements within the specimens, significantly enhancing their strength[17].

Common connection techniques for DSC shear walls with cast-in-place floor slabs involve reserving anchoring steel bars and shear connectors at the wall ends, followed by welding floor slab rebars to these anchors before pouring concrete[21]. Assembly methods for precast composite floor slabs and shear walls may similarly follow these procedures. However, installing precast composite floor slabs requires reliable support from below, which complicates construction. Despite numerous patents filed on the connections between steel plate shear walls and precast composite floor slabs, mechanical performance tests remain scarce, leaving the reliability of these connections unverified. Consequently, this study introduces two new types of assembly connection connections between thin DSC shear walls and prefabricated floor slabs. Compared to existing connection types, these improvements directly support the composite floor slabs on the lower flanges of angle or H-shaped steel, thereby simplifying construction and enhancing convenience.

To investigate the connection performance of thin DSC shear walls and prefabricated floor slabs, the steel truss floor slab is utilized, as shown in Fig. 1. The steel truss comprises upper rebars, lower rebars and web rebars, assembled through spot welding. Comprising the steel truss and the composite plate, together with the cast-in-place concrete above, forms a complete steel truss floor slab. The composite plate can be used as the formwork for pouring concrete and can bear the weight of concrete and certain construction loads during the construction stage. The steel truss floor slab is widely used in China towing to its standardization, high load-bearing capacity, and ease of construction.

In this study, we introduce two new types of assembled wall-slab joints for thin double skin composite shear walls and steel truss floor slabs. A pure bending test of these two types of new assembled wall-slab joints is conducted. The failure modes and mechanical properties of these newly assembled wall-slab joints across various joint forms and slab thicknesses were investigated. Using the ABAQUS finite element platform, finite element models of the new assembled wall-slab joints is established and compared the simulation results with the test outcomes to evaluate the modeling method's feasibility. A method for calculating the pure flexural bearing capacity of the joints, based on the stress balance of the broken section of the specimen is proposed. The finding of this research may serve as a reference for applying the new assembled wall-slab joints in engineering practices and for predicting the joints' bearing capacity.

Fig. 1 Steel truss floor slab

2. Experimental study

Two types of assembled wall-slab joints, Type I and Type II, were tested. In the construction of the Type I, an angle steel is affixed to the shear wall, with the prefabricated floor slabs subsequently placed atop the angle steel. Anchorage steel bars are threaded through both the shear wall and floor slab. The process concludes with the pouring of the floor concrete. For the Type II joint, an H-shaped steel with unequal upper and lower flanges is welded to the shear walls, and the lower flange of the H-shaped steel supports the prefabricated floor slabs. Similarly, the anchorage steel bars are threaded through the shear wall, H-shaped steel and the floor slab. This assembly concludes with the pouring of the floor concrete. These two types of joints obviate the need for traditional bottom formwork and support frame in concrete floor slabs, thereby optimizing process flow and accelerating assembly speed. Anchored steel bars are strategically positioned in the tension area of the joints to counteract the tensile stresses induced by bending moment. Due to structural design considerations, the anchoring reinforcement bars in the Type I joint may be positioned either above (Fig. 2a) or below (Fig. 2b) the upper rebars of the slab, leading to variable floor thickness. Consequently, this study produced three joint specimens: two angle-steel joints (Type I), namely CWSA140 (Fig. 2a) and CWSA120 (Fig. 2b), and one H-steel joint (Type II), labeled CWH130 (Fig. 2c).

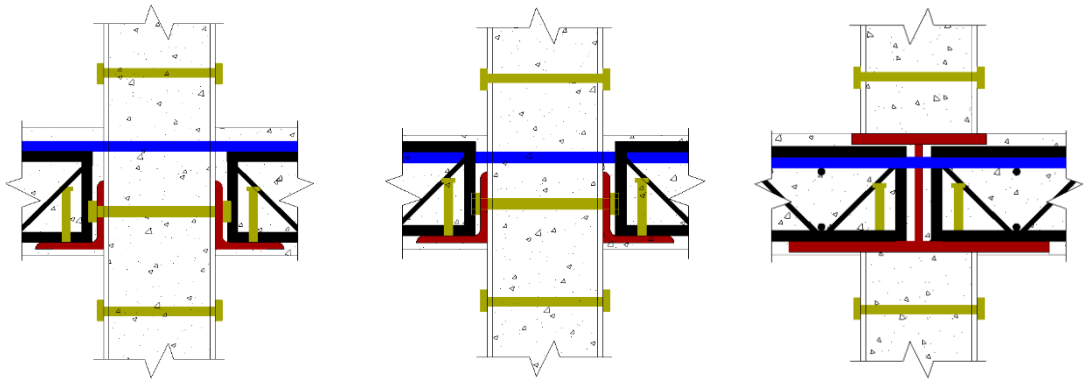

(a) CWSA140 (b) CWSA120 (c) CWH130

Fig. 2 Structure of joints of DSC shear wall and stee truss floor slab

2.1. Specimen design

Three assembled wall-slab joints have been designed for thin DSC shear walls and steel truss floor slabs. The DSC shear wall features a width of 130 mm, steel plate thickness of 6 mm on both sides, and is infilled with C30 concrete. The composite floor slab comprises a steel bar truss deck, model TD7-90, produced by Duowei Union Group Co., Ltd. The floor slab incorporates three trusses, each 90 mm high and 100 mm wide, spaced 100 mm apart. The upper and lower rebars of the steel truss have a diameter of 12 mm, while the web rebars measure 5.5 mm in diameter. The steel plate, angle steels, and H-steel are composed of Q345B steel, whereas the steel bar utilizes HRB400. The shear bolt specification is M16×80. The anchoring reinforcement bars measure 10 mm in diameter and 400 mm in length, extending into the floor slab. Each specimen contains three anchorage bars, spot-welded with the upper rebars of the steel truss. The tension bolts on the shear walls are spaced300 mm apart and have a diameter of 10 mm. Detailed sizes of the specimens are provided in Table 1, and their structure is illustrated in Fig. 3. The thickness of the concrete protective layer is 15mm. Distance between the hinged support and both ends of the specimen is 200 mm.

2.2. Material properties

Six cubic concrete test blocks (150 mm × 150 mm × 150 mm) were prepared, and a cube compression test was performed after 28 days of curing. The measured compressive strength of the concrete cubes was 35.65 MPa. According to the “Metal Materials tensile test method at room temperature” guidelines, the yield strength, tensile strength, and elastic modulus of various steels were measured (Table 2). The material testing results for the steel and concrete are presented in Figs. 4 and 5.

Table 1
Statistics of pure bending specimens

Group	Specimen number	Shear wall size T × B × H/mm	Single slab length L/mm	Slab thickness t/mm	SA/HB size/mm	Total length L/mm
Type I	CWSA140	130×500×600	1600	140	60×80×8×8	3330
	CWSA120	130×500×600	1600	120	60×80×8×8	3330
Type II	CWH130	130×500×600	1600	130	124×290（150）×10×12	3330

Table 2
Properties of steel and concrete materials

Name	Thickness t/mm	Yield strength f_y (MPa)	Ultimate strength f_u (MPa)	Modulus of elasticity E
Steel plate	5.8	389.58	569.42	205045.82
Steel angle	8.2	390.43	541.36	205292.88
Upper rebar /Lower rebar/ anchorage rebar	12	425.49	599.38	183110.96
Web rebar	10	254.07	523.43	181384.68
Compressive strength of concrete	f_c=35.65Mpa			

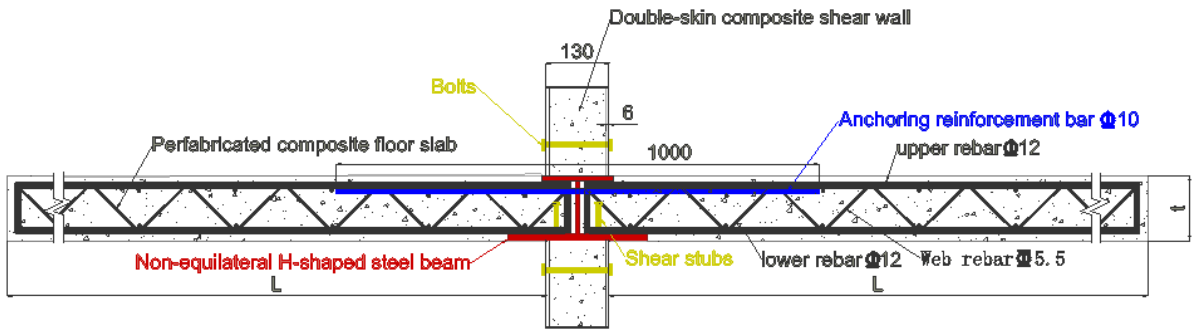

(a) Front view of the overall structure

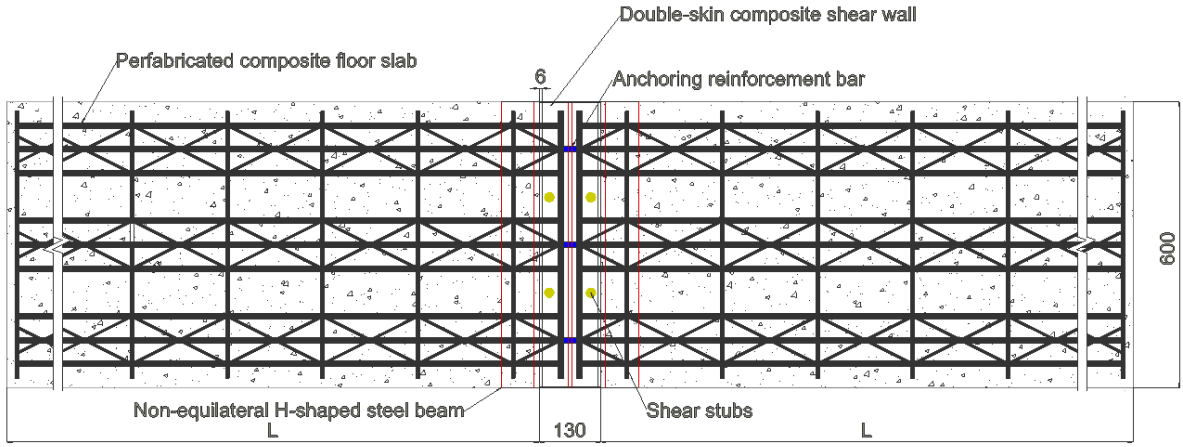

(b) Vertical view of the overall structure

Fig. 3 Specimen size and overall structure (taking Type II joint as an example)

(a) Loading device

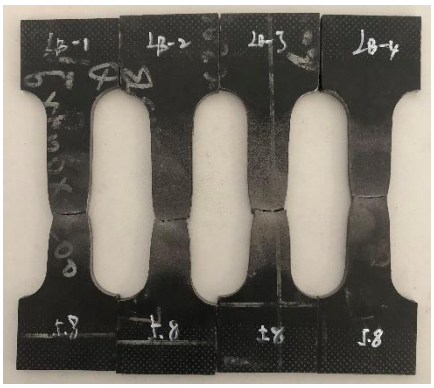

(b) Steel plate and SA specimens

(c) Reinforcement bar specimens

Fig. 4 Properties test of steel materials

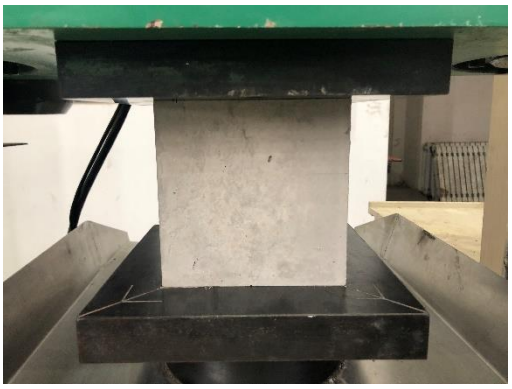

(a) Loading device

(b) Concrete specimens

Fig. 5 Properties test of concrete materials

2.3. Test device and measurement

In the Civil Structures Laboratory of Tianjin University, a laboratory reaction frame, sensors, and an MTS electro-hydraulic servo loading device (Fig. 6) were utilized to conduct the pure bending tests on newly assembled wall-slab joints. The orientation of the joint specimens, depicted in Fig. 2, was initially set in a regular placement direction. Under bending moment load, the lower part of the joint experiences compressive stress while the upper part undergoes tensile stress. During testing, to simulate the actual stress conditions experienced in practical applications, the specimens were rotated 180 degrees (Fig. 6). A vertical load was applied downward along the length direction of the specimen at two points, one-quarter of the way from each end, to mirror the load distribution typical in engineering application. For descriptive supposes, the directions of the specimen were labelled as N- and S-directions. Side A represented the compression surface, side B faced the tension surface, side D faced the tester, and side C was oriented opposite to the tester.

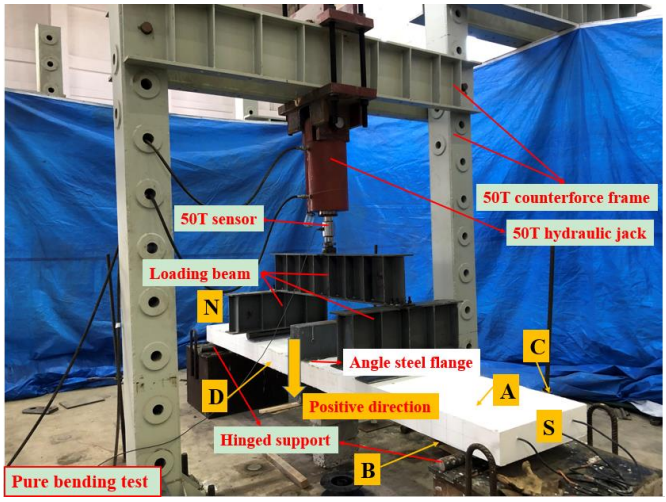

Fig. 6 Loading device of pure bending test

2.4. Measuring arrangement and loading system

Principal positions were identified for measuring strain and deformation in the specimens. Fig.7 and Fig.8 illustrate the arrangement of the strain gauge and linear variable displacement transducers (LVDTs) on the specimens. The pure bending test was a unidirectional static loading test. In the preloading stage, 10% of the initial calculated cracking load was applied in five incremental stages, with each stage maintained for one min. This stage was followed by verifying the working status and connection of the instrument, and the familiarity of the operators. It was then unloaded to zero. A grading loading system was adopted during formal loading, and 10% of the calculated yield load was loaded at each stage, and 5% of the yield load was controlled when it was close to the ultimate load. The test was stopped when the load was directly loaded to 80% of the ultimate load or the peak load or the crack width of the concrete reached 10 mm.

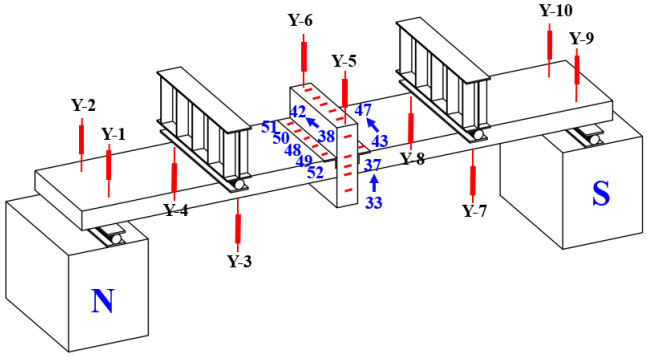

Fig. 7 Strain gauge and LVDTs of pure bending test

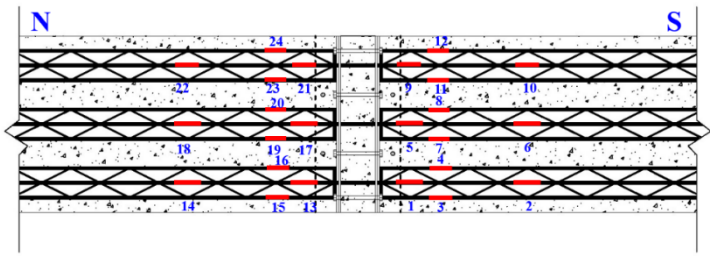

Fig. 8 Reinforcement strain gauge arrangement

3. Results and analysis

3.1. Test phenomenon

The test procedure was divided into three stages.

(1) Elastic Working Stage to Tensile Zone Concrete Cracking Stage. Initially, all sections exhibited minimal bending moments, and the specimens remained in an elastic working state. As the load escalated, the first crack appeared approximately 150 mm from the loading point within the slab's tension zone. Comparing the cracking load of different specimens, it can be found that specimen CWSA140 was the first to crack, while specimen CWH130 demonstrated the greatest resistance, cracking last.

(2) Tensile Zone Concrete Cracking Stage to Longitudinal Tension Reinforcement Yield Stage. As the load increased, cracks in the slabs proliferated and propagated from the tension zone to the compression zone along the slab height. Crack began to propagate at 45-degree angle on both sides, and the rate of crack width expansion accelerated. Significant deflection was observed as the specimens reached the yield load. Cracks within the tensile zone were evenly distributed across the bending zone along the slab length.

(3) Longitudinal Tension Reinforcement Yield Stage to Failure Stage. Subsequent to the longitudinal tension reinforcement yielding, a noticeable inflection point was observed in the load-displacement curve of the specimens, with specimen deflections increasing rapidly. Specimens CWSA140, CWSA120 and CWH130 failed upon reaching vertical displacements of 99, 173, and 110 mm, respectively. The failure points were all located within the concrete's compression zone, 150 mm away from the loading point in the S-direction. Despite the increase in load, the number of cracks stabilized, but their width expanded significantly. As specimen CWSA140 reached the ultimate load, the bearing capacity declined abruptly, accompanied by the audible snap of the reinforcing bar. The bearing capacity of specimen CWSA140 initially increased with continuous loading due to stress redistribution within the force section, before eventually declining. A significant cracking sound was noted as the vertical displacement of specimen CWSA140 reached 155 mm, which was immediately followed by the emergence of a substantial crack at the loading end in the S direction and a sharp decline in bearing capacity, signalling the conclusion of the test. For specimen CWSA120, the slab cracked and the bearing capacity plummeted when the vertical displacement reached 183 mm. The slab of specimen CWH130 fractured with a loud noise upon reaching the ultimate load of 49.31 kN, reducing its bearing capacity to zero.

After the test, all specimens demonstrated significant deflections, with a extensive crack in the S-direction of the three slabs (Fig. 9). The maximum crack widths at the final failure stage for specimens CWSA140, CWSA120, and CWH130 were recorded as 5 mm, 10 mm, and 2 mm, respectively. Notably, the deformation resistance of the H-steel joint (CWH130) exceeded that of the angle-steel joints (CWSA140 and CWSA120). Damage within the mid-span joint region of all three specimens was depicted in Fig. 9. In specimen CWSA140, cracks originated at the interface between the shear wall and the floor slab at the base, ascending along the interface. These cracks ascended along the contact surface, halting at the angle flange (Fig. 10a). Simultaneously, the concrete floor slab near the specimen's loading point sustained crushing and damage. The crack development in the joint area of specimen CWSA120 was mirrored that of specimen CWSA140. After the tensile zone's concrete cracking, anchored rebars underwent tensile stress. Since the anchoring reinforcement bars of the angle-steel joints (CWSA120 and CWSA140) were positioned differently, the anchoring reinforcement bars of CWSA120 were only activated when the concrete cracks were substantial. Consequently, the deformation capacity of CWSA120 was inferior to that of CWSA140, resulting in more extensive crack development in the joint area (Fig. 10b). The anchorage bars in the joint area of specimen CWH130 extended into the H-shaped steel's interior, thereby preserving the joint area's integrity. Cracks that appeared in CWH130 during the initial loading stage did not expand in the subsequent stages (Fig. 10c).

(a) Deformation and bottom cracks (b) Deformation and concrete fracture

Fig. 9 Overall deformation of the three specimens

(a) CWSA140 (b) CWSA120 (c) CWH130

Fig. 10 Local failure of the three specimens

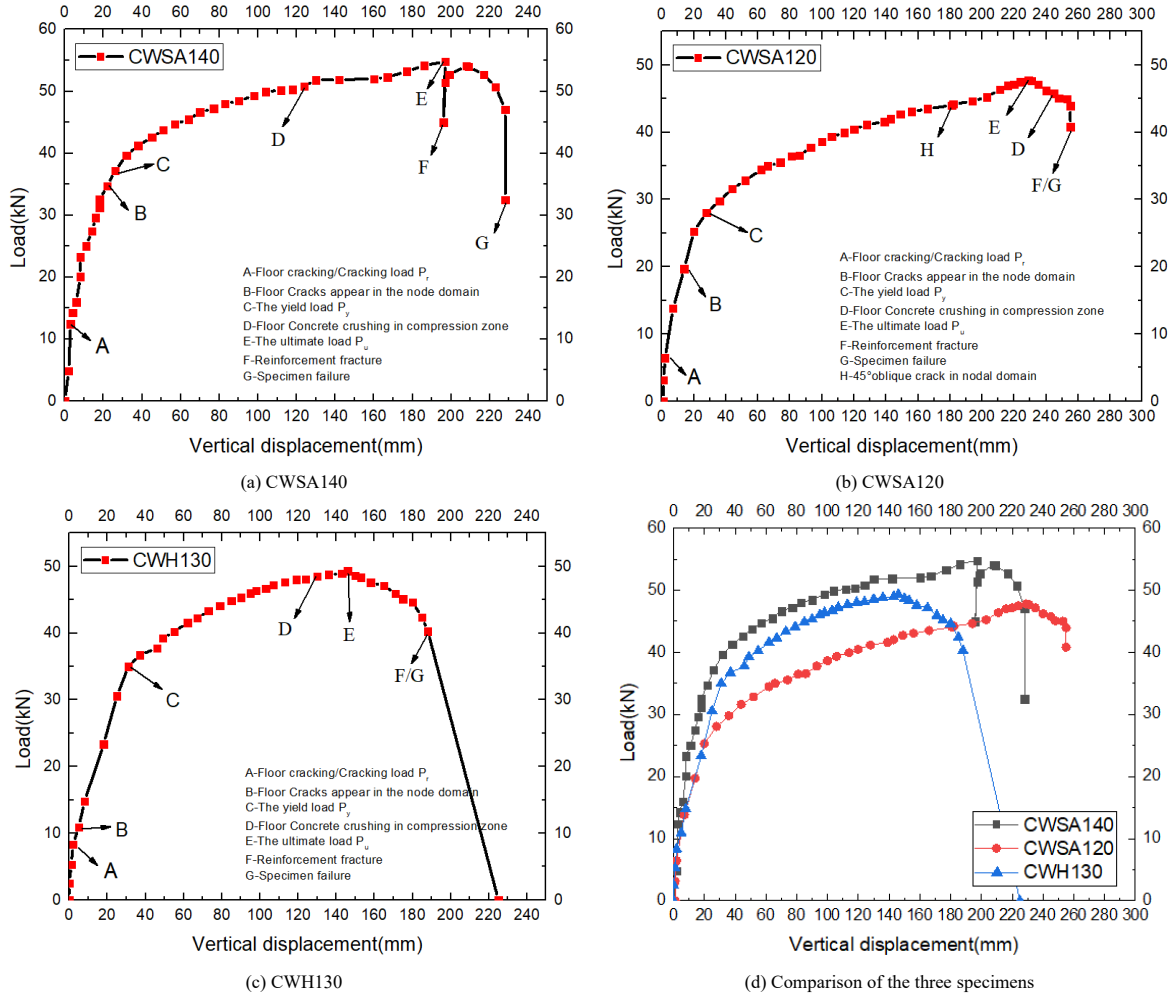

(a) CWSA140 (b) CWSA120

(c) CWH130 (d) Comparison of the three specimens

Fig. 11 Load–displacement curves

3.2. Load–displacement curve

Fig.11 presents a comparison of the load–displacement curves for the three specimens. The load was measured using a 50 T sensor coupled with a static acquisition instrument. The vertical displacement was calculated by averaging the readings from of LVDTs Y-5 and Y-6. Key points on each load–displacement curve was highlighted to emphasize specific characteristics.

The specimen CWSA140 exhibited the greatest initial stiffness and ultimate load. Upon achieving its ultimate load, the bearing capacity of specimen CWSA140 experience a significant reduction. This abrupt decrease can be primarily attributed to the breakage of the slab tensile rebars at the loading beam in the S-direction. Despite additional load increments, the concrete in the slab's tensile area continued to disengage from the applied load, culminating in the steel rebars at the crack reaching their capacity limit. As the crack width expanded, the bearing capacity of specimen CWSA140 declined rapidly. When specimens CWSA120 and CWH130 reached their ultimate bearing capacity, there was a continuous increase in the crack width in the slab's tensile zone at the loading end in S direction. Following the fracture of the tensile rebars, the bearing capacity of the two specimens decreased rapidly and could no longer sustain additional load. Due to safety concerns, the tests were terminated at this juncture.

Compared to specimen CWSA120, the ultimate load of specimen CWSA140 increased by 14.72%, and the ultimate displacement decreased by 13.93%. This variationist primarily attributed to the different placements of the anchorage rebars. In specimen CWSA140, the arrangement of anchorage rebars not only increased the section height of the sla but also enhanced its flexural stiffness. In comparison to specimen CWSA120, the initial stiffness of specimen CWH130 improved, the ultimate load increased by 3.27%, and the ultimate displacement decreased by 36.02%. Although specimen CWH130 exhibited earlier cracking compared to the SA connection specimens, the progression of these cracks was more gradual. The angle-steel joints specimens developed cracks at a later stage, yet these exhibited larger final crack widths compared to those in the H-steel joint specimen.

The ductility and deformation capacity of the test specimens were evaluated by analysing the ductility coefficient and the rotation capability. All three specimens demonstrated ductility coefficients exceeding 5, indicative of superior ductility in the connections between the DSC shear wall and the steel truss floor slab. Notably, specimen CWSA120 exhibited the lowest bearing capacity yet excelled remarkable ductility. The ratio of the ultimate bearing capacity to the yield bearing capacity (P_p/P_y) of all three specimens ranged between 1.47-1.89. This data suggests that the flexural bearing capacity of these assembled wall-slab joints possesses a substantial safety margin. Additionally, the peak angle θ_p of all specimens exceeded 1/10, demonstrating the robust deformation ability of these assembled wall-slab joints.

Here, P_y and Δ_y represent the yield load and yield displacement, respectively, P_p and Δ_p represent the peak load and peak displacement, respectively, θ_y and and θ_p represent the floor rotation under yield load and peak load, respectively, μ represents the ductility coefficient.

Table 3
Characteristics of each specimen

Specimens	P_y/kN	Δ_y/mm	θ_y	P_p/kN	Δ_p/mm	θ_p	μ	P_p/P_y
CWSA140	37.16	26.64	1/52	54.78	197.12	1/5.5	7.4	1.47
CWSA120	25.26	20.33	1/62	47.75	229.01	1/4	11.26	1.89
CWH130	30.56	24.87	1/34.4	49.31	146.52	1/13.5	5.89	1.61

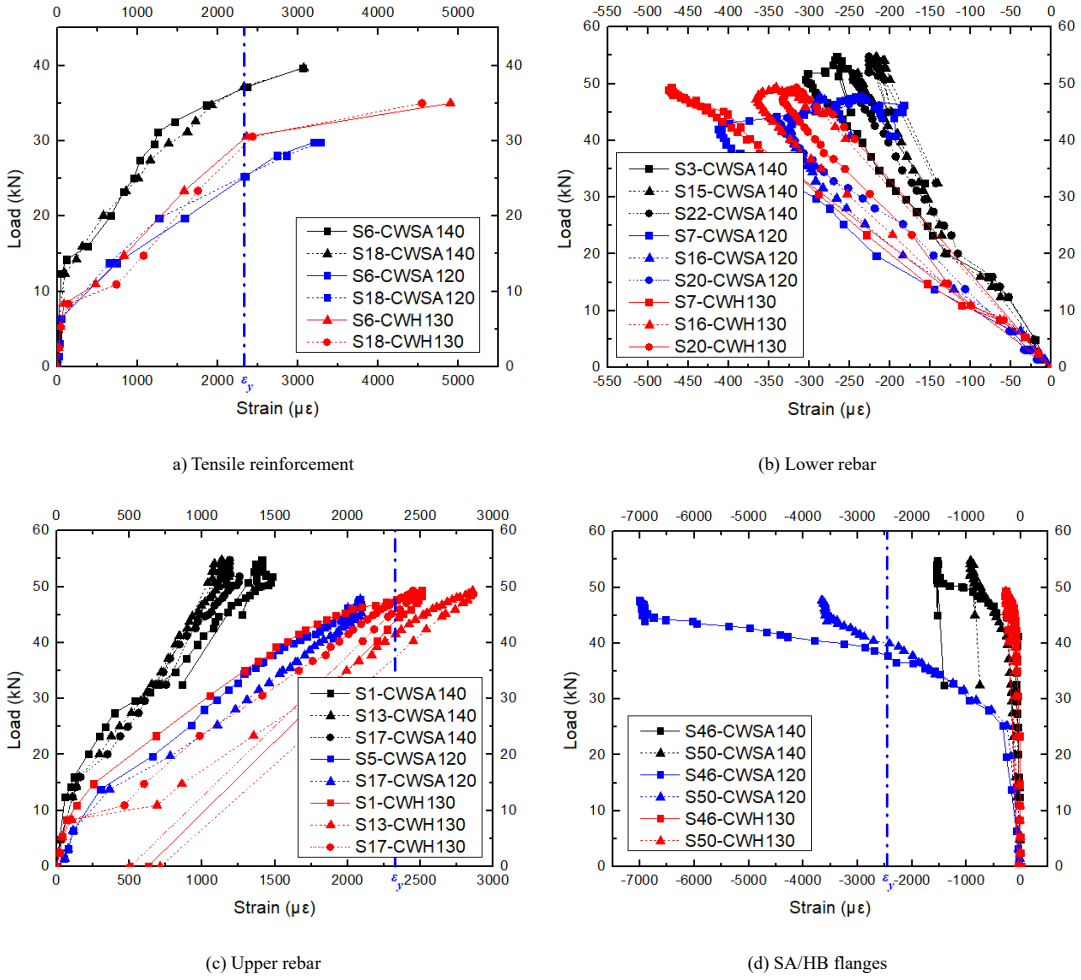

a) Tensile reinforcement (b) Lower rebar

(c) Upper rebar (d) SA/HB flanges

Fig. 12 Strain analysis of specimens

3.3. Strain analysis

Fig. 12 illustrates the load-strain curves for the three specimens. The upper rebars of the steel truss at the loading point reached the yield stress in all specimens, which is consistent with the observed fracture positions. Conversely, the lower rebars of the steel truss, which were subjected to compressive stress, did not yield at the ultimate load. Notably, strain development in the upper rebars within the tensile zone near the joint area was significantly slower than at the loading point. Upon reaching the ultimate load, the tensile rebars in the joint zone of specimens CWSA140 and CWSA120 did not yield, while those in the joint tension zone of specimen CWH130 reached the yield stress. This behavior, coupled with the failure phenomena observed in the joint areas (Fig. 10), demonstrates that the joint structure of the CWH130 specimen is more logical and effective. The anchoring rebars in specimen CWH130 proved effectively anchoring the two prefabricated floor slabs and shear walls, thereby efficiently transmitting the negative bending moment of the floor slab.

4. Finite element analysis

4.1. Finite element modeling

Finite element models for the newly assembled wall-slab joints of thin double skin composite shear walls and steel truss floor slabs were developed using the ABAQUS finite element platform. Based on tensile test results of steel plates and rebars, the constitutive models of all steel components were simplified. The simplified constitutive model of steel plate and rebars adopted the elastoplastic stress-strain relation model proposed by Han et al, as indicated in Fig. 13(a). The stress-strain relation model of concrete adopted the constitutive relation proposed by in Appendix C of the Code for Design of Concrete Structures[22], as indicated in Fig. 13(b). Additionally, the damage plasticity model defined in ABAQUS was used to simulate the three-way force relationship in the concrete of shear wall and slabs. Key material parameters were determined according to previous studies[23-25].

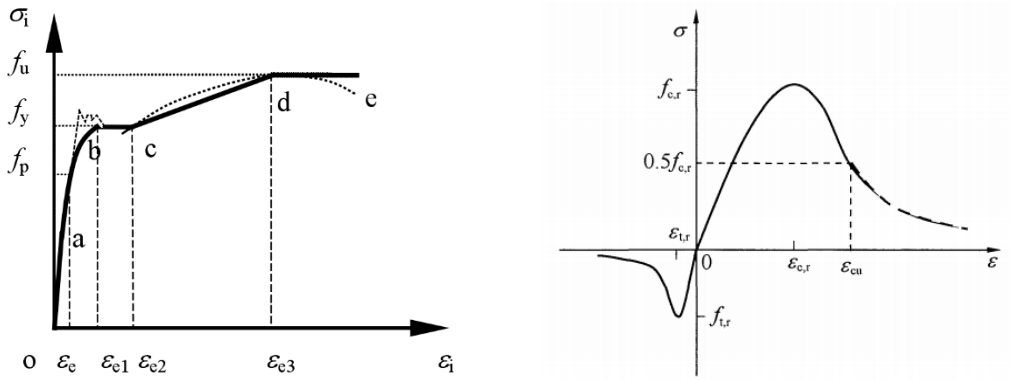

(a) Stress-strain relation model of steel

(b) Stress-strain relation model of concrete

Fig. 13 Stress-strain relation models of steel and concrete

Each component of the joint model is meticulously constructed to match the dimensions of the test specimens. Concrete, steel plates, angle steel, H-shaped steel, studs, and bolts are all simulated using ABAQUS's three-dimensional eight-node reduced integration unit (C3D8R). Steel rebars are simulated using the three-dimensional two-node truss unit (T3D2). To optimize the balance between computational accuracy and efficiency, the mesh size for the steel truss is set at 20mm, while the mesh for other components is set at 30mm.

The steel rebar is first built with line unit, then all rebars are combined into a steel rebar skeleton using the "merge" option of the "Assembly" module of ABAQUS. This steel rebar skeleton is then assigned as a "truss" unit in the "Grid" module of ABAQUS. The steel rebar skeleton is embedded into the concrete slab using the "embedded" command. A detailed contact model is established at the interface of each component to simulate the contact behavior. The main contact interfaces are between: the shear wall steel plate and internal concrete, the shear wall steel plate and concrete slab, the angle steel and concrete slab, the H-shaped steel and concrete slab, the bolt hole and its contact plane, and the support and concrete slab. These contact relationships are defined as "face to face" contact. The tangential behavior between contact surfaces is simulated using a frictional contact, with a friction coefficient of 0.4. The normal behavior between the contact surfaces is simulated using "hard contact". The "Tie" command is used to simplify the welding connections between the shear wall outer steel plate and angle steel, the shear wall steel plates and H-beam steel, the angle steel and bolts, and the H-beam steel and bolts.

To simulate the test's hinged boundary conditions and loading modes, supports and loading beams are positioned at the corresponding positions. Reference points (RP-3 and RP-4) are established on the support plane, constraining the 3-direction translation (U_x, U_y and U_z) and horizontal rotation (R_x). Reference points (RP-1 and RP-2) are established on the plane of the loading beam, and a vertical downward displacement load (U_z) is applied. Given the similarity in the models of the two angle-steel joints (CWSA140 and CWSA120), the specimen CWSA120 is taken as an example. The details of finite element model for specimen CWSA120 are shown in Fig. 14. The details of finite element model of CWH130 are shown in Fig. 15.

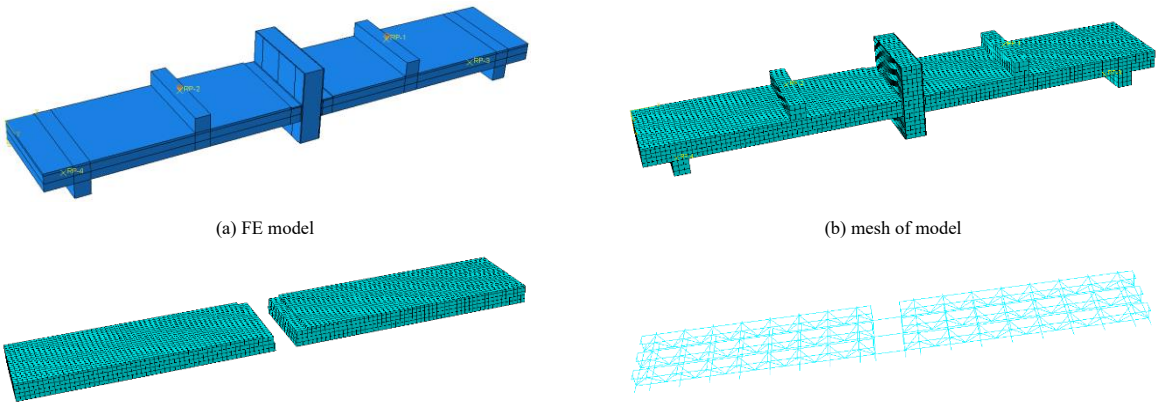

(a) FE model

(b) mesh of model

(c) concrete slab

(d) steel rebar skeleton

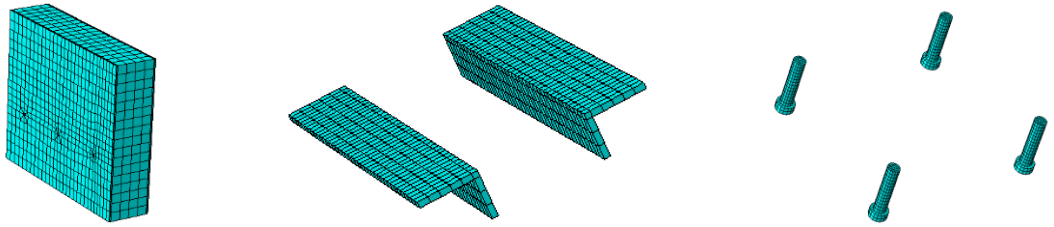

(e) DSC shear wall (f) angle steels (g) shear bolts

Fig. 14 Boundary condition and mesh generation of specimen CWSA120

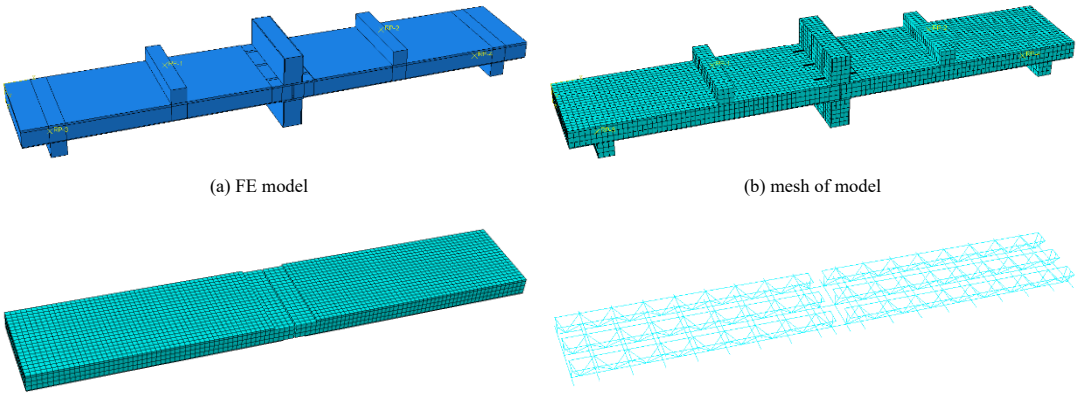

(a) FE model (b) mesh of model

(c) concrete slab (d) steel rebar skeleton

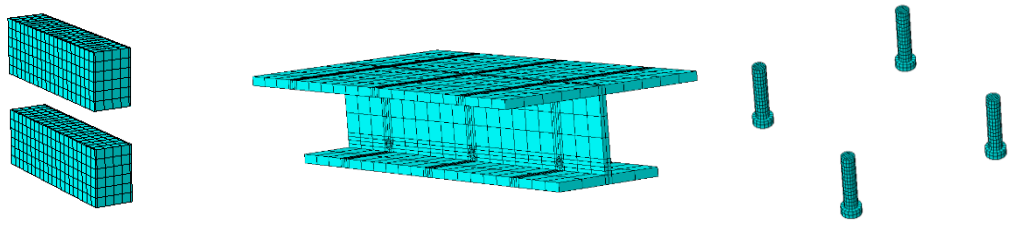

(e) DSC shear wall (f) H-steel (g) shear bolts

Fig. 15 Boundary condition and mesh generation of specimen CWH130

4.2. Results analysis

The bending failure images obtained from the tests of the three specimens were compared to the outcomes of the finite element simulation results (Fig. 16). The three-dimensional finite element models effectively simulated the overall bending failure mode for each specimen. Notably, observations from models CWSA140 andCWSA120 indicate that the highest stresses occur at the angle steel flange in the compression zone of the connection, where cracks also develop between the concrete and the external steel plate of the shear wall in the tension zone. These failure patterns in the joint core area are consistent with experimental observations. Future analysis focused exclusively on the failure of the floor slab' failure reveals that the points of maximum concrete stress in the compression zones of model CWSA140 and specimen CWSA120 are located approximately 100 mm and 150 mm from the load points, respectively, aligning closely with the locations of concrete crushing observed in the experiments. Further examination of model CWH130 shows that the maximum stress occurs at the flange of the H-shaped steel in the compression zone of the joint, with no cracks observed in the concrete of the tension zone—a finding that corroborates the experimental results. The position of maximum compressive stress in the concrete of model CWH130 is observed to be approximately 200 mm from the loading point, which closely matches the concrete crushing locations noted in the experiments. The slab's flexural zone stress could indicate the range of crack development, but the finite element results were unable to accurately predict the location and width of cracks or the crushing phenomenon of the concrete in the top surface of the slab's compression zone. This discrepancy arises primarily attributed to the limitations of the adopted concrete constitutive model, which does not account for the development of concrete cracks and shear transfer.

The load-displacement curves obtained from the finite element analysis (FEA) of the three specimens were compared with the test results, as illustrated in Fig. 17. For specimen CWSA140, the finite element model effectively simulated the specimen's stiffness during the initial loading stage and the bearing capacity at the yield stage but failed to simulate the increase in bearing capacity observed during the later loading stage of loading. For specimens CWSA120 and CWH130, the finite element model effectively simulated the specimens' stiffness at the initial loading stage but was unable to simulate the load decline observed in the tests. The bearing capacities obtained from the FEA for specimens CWSA140, CWSA120, and CWH130 were 49.59kN, 44.86kN, and 48.49kN, respectively. These values represent a decrease of 9.47%, 6.05%, and 1.66% compared to the test results. The discrepancies between the FEA results and the test results is within an acceptable range, supports that the modeling method used in this study accurately reflects the failure mode and bearing capacity of the new assembled wall-slab joints.

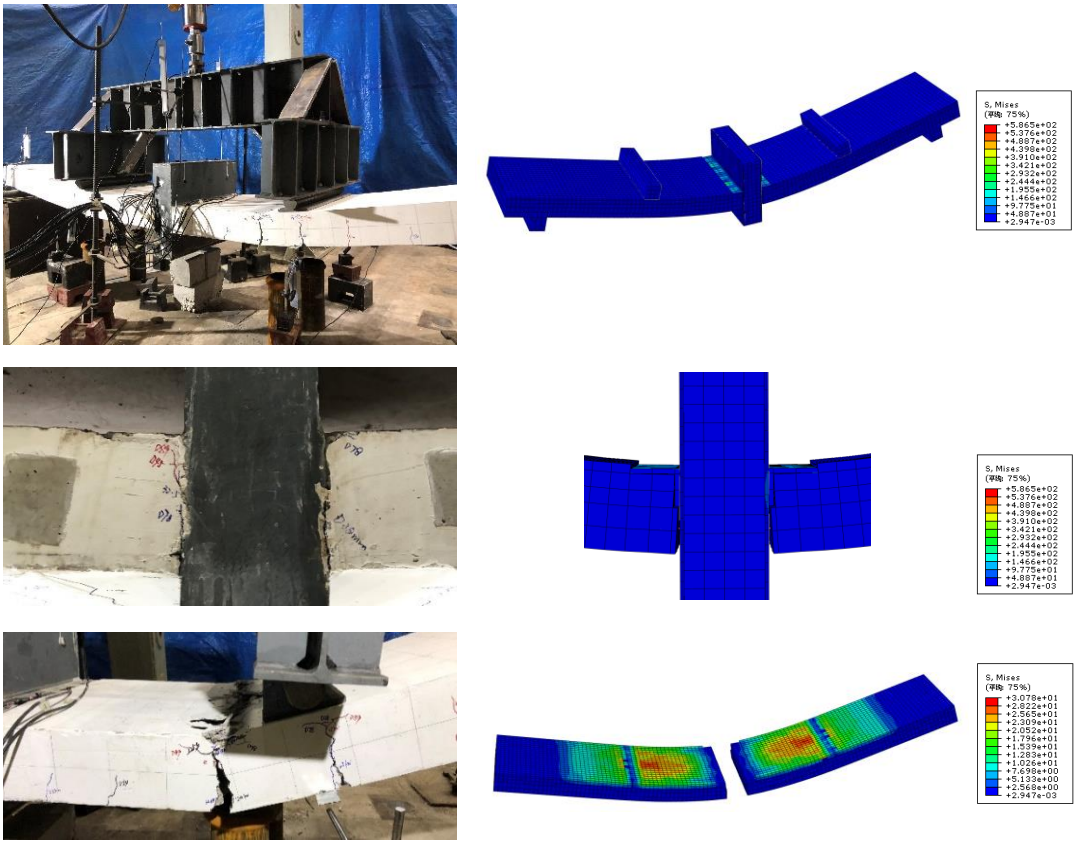

(a) CWSA140

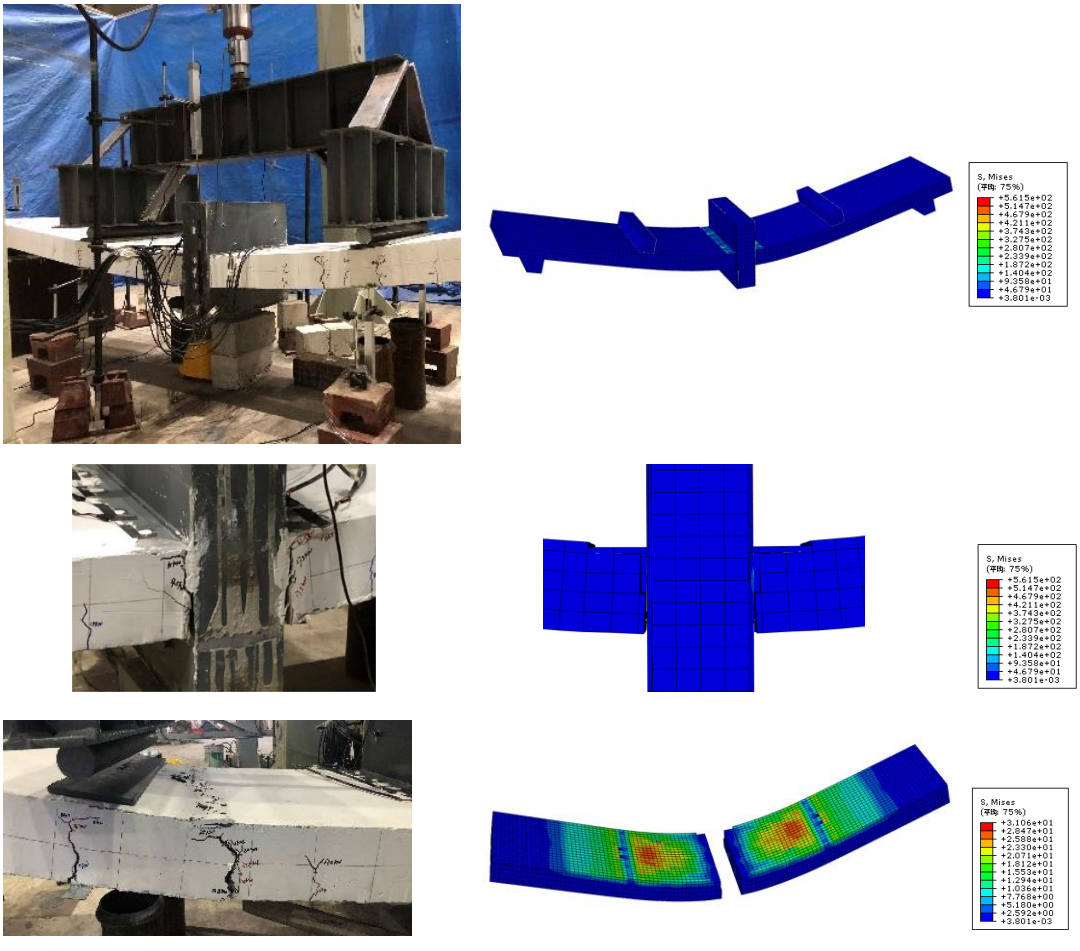

(b) CWSA120

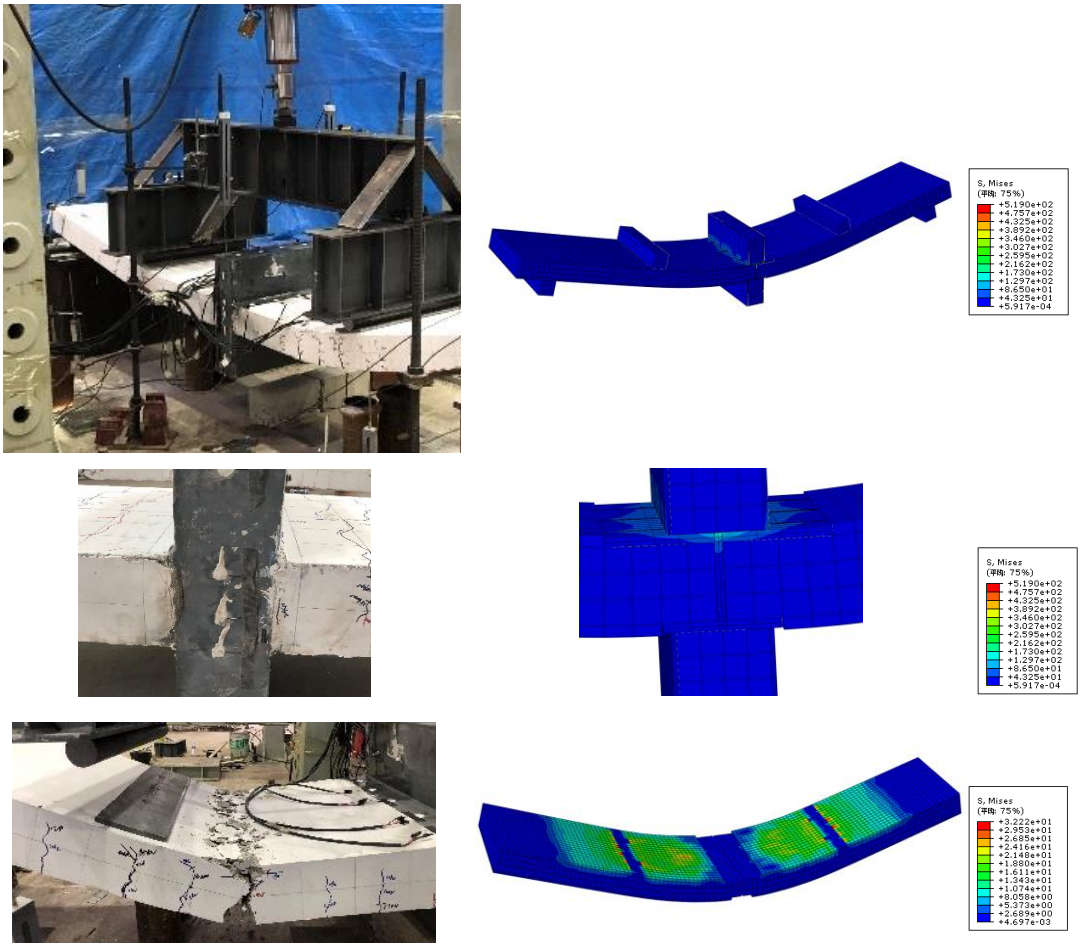

(c) CWH130

Fig. 16 Comparison of the overall deformation of test results and finite element results

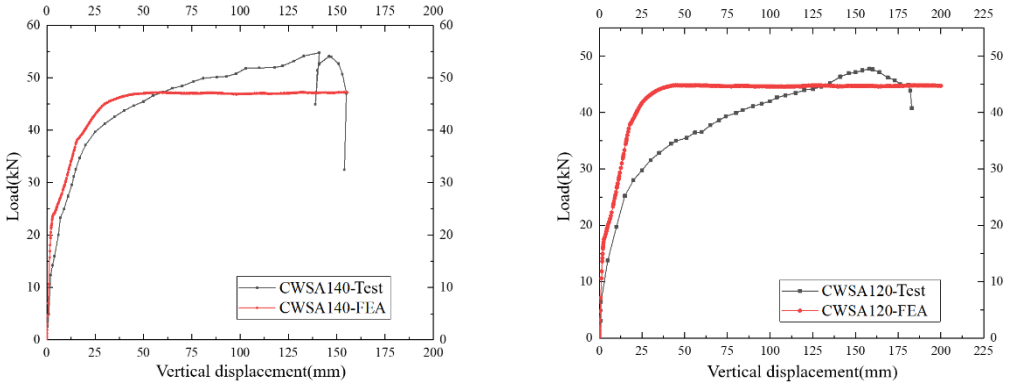

(a) CWSA140 (b) CWSA120

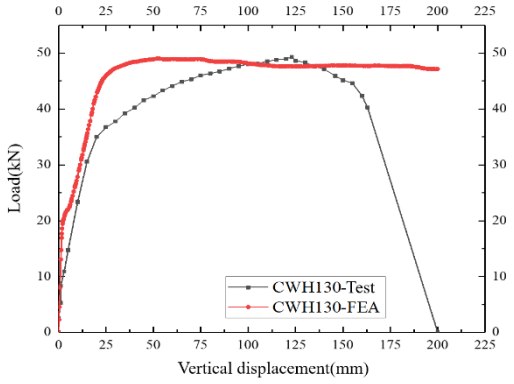

(c) CWH130

Fig. 17 Comparison of load-displacement curves between test specimens and finite element results

5. Calculation of bending capacity

Structural integrity is critically dependent on the performance of connections. A compromised connection can lead to the collapse of an entire structure. The Technical Requirements for Steel Plate Shear Walls [16] and the Code for Seismic Design of Buildings[26], both emphasize the principle of "strong connections and weak members" at shear wall joints. In light of these requirements, the pure bending capacities of two newly assembled wall-slab joints were calculated, adhering to these existing codes. These calculations were conducted to assess the applicability of the current formula to the two newly assembled wall-slab joints. The results serve as a crucial reference for the design of such connections in future projects.

To accurately simulate the stress states of the joint specimens under normal operating conditions, the specimens were inverted during the testing phase. The configuration of the force application is illustrated in Fig. 18. The specimen's bottom supports are hinged, and the vertical load is applied at two quartile points along the specimen. This setup ensures that the section for the specimen between these two loading points is subjected exclusively to a pure bending state.

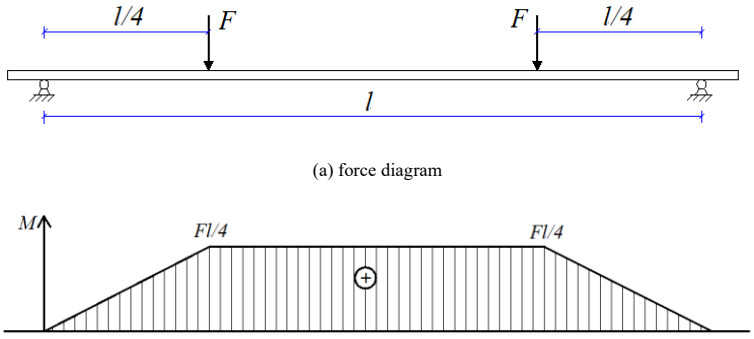

(a) force diagram

(b) bending moment distribution

Fig. 18 The force diagram and bending moment distribution

The relationship between the vertical load (F) and the bending moment (M) of the specimen is expressed as follows:

$$M_{\max} = Fl/4 \quad (4\text{-}1)$$

Failure in specimens typically occurs at the connection positions on the floor slab adjacet to either side of the loading point. As a result, cross-section of the floor slab at these locations is the weakest section when subjected to bending moment loads. To calculate bending moment bearing capacity of these joint specimens, the calculation incorporates the maximum bending moment that the floor slab's cross-section is capable of bearing the bending capacity of the specimens. Fig. 19 illustrates the stress distribution across the floor section when it is subjected to a bending load.

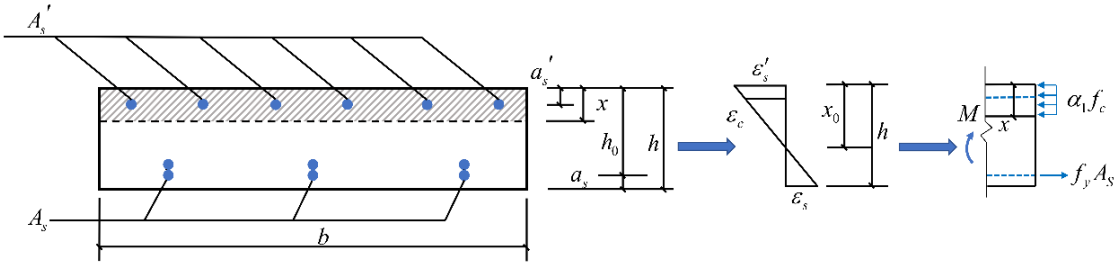

Fig. 19 Calculation diagram of floor cross section under bending moment

According to the cross-section stress balance:

$$\sigma_s A_s = \sigma_s' A_s' + f_c b x \quad (4\text{-}2)$$

The ultimate bending capacity under bending load is obtained as follows:

$$M = \sigma_s A_s (h_0 - a_s') \quad (4\text{-}3)$$

where σ_s and σ_s' are the stresses of longitudinally stressed steel bars in the tension zone and the compression zone, respectively; A_s and A_s' are the section areas of the longitudinal reinforced bars in the tension zone and compression zone, respectively; x is the distance between the edge of compression zone and the point at which the resultant force of the longitudinal reinforcement is applied; h_0 is the effective height of the section; and a_s' is the distance between the application point of longitudinally stressed reinforcement in the compression zone and the edge of the compression zone.

Strain analysis (Fig. 12) demonstrates the longitudinal stressed steel bars (lower rebars of the steel truss) located in the compression zone of the three specimens do not attain the yield strain when subjected to the ultimate load. Consequently, the concrete range of the compression zone cannot be calculated using Eq. (4-2). Conversely, the rebars situated in the joint tension zone do reach the yield stress under the conditions of the yield load. Thus, the specimen's bearing capacity at yield moment and ultimate bending moment can be calculated using the subsequent formula:

Bearing capacity at yield bending moment:

$$M_y = f_y A_s (h_0 - a_s') \quad (4\text{-}4)$$

Bearing capacity at ultimate bending moment:

$$M_p = f_u A_s (h_0 - a_s') \quad (4\text{-}5)$$

A comparison analysis of the calculated and test values is presented in Table. 4. After the vertical bearing capacity (P_y, P_p in Table. 3) is obtained, the yield bending moment (M_y)and ultimate bending moment (M_p) for the test specimens are calculated using Eq. (4-1). This comparison indicates that the error range for the predicted bending capacity of specimens CWSA140 and CWH130 using this calculation method is between 3%-8%. For specimen CWSA120, however, the error ranges from 11% to 20%. Notably, the predicted values for the ultimate bending capacities of all three specimens consistently fall below their test corresponding values. Consequently, it is safe to conclude that the calculation method proposed in this study is a reliable approach for predicting the ultimate bending capacity of the new assembled wall-slab joints for thin double skin composite shear walls and steel truss floor slabs.

Table 4
Bend bearing capacity comparison between the calculated results and test results

Specimens	M_y/(kN·m)	$M_{y,c}$/(kN·m)	M_p/(kN·m)	$M_{p,c}$/(kN·m)	$M_y/M_{y,c}$	$M_p/M_{p,c}$
CWSA140	27.22	26.54	40.13	37.39	1.03	1.07
CWSA120	18.50	20.77	34.98	29.26	0.89	1.20
CWH130	22.59	23.66	36.12	33.32	0.95	1.08

6. Conclusions

This study introduced two newly assembled wall-slab joints f aimed at enhancing the safety of connection between thin double skin composite shear walls and steel truss floor slabs. The mechanical behavior of these joints was evaluated through pure bending tests conducted on three specimens with different connection structures., This evaluation involved test analysis, finite element simulation, and theoretical analyses. The following conclusions were reached:

(1) The two newly assembled wall-slab joints exhibited superior mechanical properties under pure bending load. These joints exhibit reliable structure and excellent force transfer capabilities. The prefabricated floor slabs were identified as the primary failure points under pure bending load, while the joint region remained intact, adhering to the design principle of “strong joint and weak member”. All three specimens developed significant cracking at the loading points of the floor slabs, thus reaching the ultimate load. As a result, the bending capacity of these newly assembled wall-slab joints is predominantly dependent on the flexural performance of the floor slabs. Specifically, the specimens equipped with H-steel joint (CWH130) cracked the latest, exhibiting greater deformation resistance than the other two specimens.

(2) The ABAQUS finite element model proposed in this study effectively simulated the mechanical behavior of the newly assembled wall-slab joints under pure bending loads. The three-dimensional finite element models effectively simulated the entire failure modes for each specimen. Despite the model’s limitation in precisely capturing the crack locations and the concrete crushing phenomena in the compression zones, it accurately predicted the overall bending failure modes.

(3) Considering the failure section of prefabricated floor slab as the weakest section, this study introduces a method to calculate the bending capacity of these joints based on the principle of force balance. The deviations between the calculation results from this formula and the test results were under 20%. The formula's predicted ultimate bending capacities for the three joint specimens were conservative compared to the test values. The calculation method presented in this article provides a dependable foundation for the future engineering design and application of these newly assembled wall-slab joints.

Acknowledgements

The study was sponsored by National Natural Science Foundation of China (No 52278202). The authors acknowledge the financial support and express their gratitude for the support provided by China Construction Science and Industry Corporation Ltd.

References

[1] R.S. Surumi, K.P. Jaya, S. Greeshma. Modelling and Assessment of Shear Wall–Flat Slab Joint Region in Tall Structures. *Arab J Sci Eng*. 40 (2015), 2201–2217.
[2] Y.Q. Shang, W. Ma, X. Li er al. Seismic performance of superposed shear wall- superposed floor slab joints. *Structures*. 60 (2024), 105900.
[3] M.A. Masrom, H.M. Yee, M.E. Mohamed, et al. Seismic performance on stiffness and hysteresis loop of interior wall-slab joint for tunnel form building designs to British standard. *J Fundam Appl Sci*. 9(5S) (2018),75-87.
[4] A. Chalot, N. Roy, L. Michel, et al. Mechanical behavior of a full-scale RC wall-slab connection reinforced with frp under cyclic loading. *Eng Struct*. 239(2021), 112146.
[5] S.R. Salim, J.K. Prabhakaran. Effectiveness of a novel ductile detailing of reinforced concrete wall-flat slab joint. *Aust J Struct Eng*.21(1) (2019), 7–20.
[6] S.C. Chun, T. Ha. Cyclic behavior of wall-slab joints with lap splices of cold-straightened rebars and mechanical splices. *J Struct Eng*.141(2) (2014), 04014101.
[7] A.A.N. Al-aghbari, S.H. Hamid; N.H.A. Hamid, et al. Structural performance of two types of wall slab connection under out-of-plane lateral cyclic loading. *J. Eng. Sci. Technol*. 7(2) (2012), 177–194.
[8] Y.Q. Wang, X. Wang, Y.N. Zhang, et al. Analysis of loading capacity of steel bar truss and concrete superimposed two-way slab. *Journal of Shenyang Jianzhu University (Natural Science)*. 30(3) (2014), 385-391. [in Chinese].
[9] H.J. Wang, H.L. Qian, H.S. Guo, et al. Seismic performance of precast shear wall–slab joint with and without outer longitudinal reinforcement. *Struct Des Tall Special Build*. 30(7) (2021),1-24.
[10] Z.F. Zhu, Z.X. Guo. Seismic test and analysis of joints of new precast concrete shear wall structures. *China Civil Engineering Journal*. 45(1) (2012), 69-76. [in Chinese].
[11] Z.Z. Zhao, J.H. Ke, J.R. Qian, et al. Seismic behavior of cast-in-place reinforced concrete hollow slab-shear wall joints. *Build Struct*.9 (2009), 49-54. [in Chinese].
[12] D. Zenunovic, R. Folic. Models for behaviour analysis of monolithic wall and precast or monolithic floor slab connections. *Eng Struct*. 40 (2012), 466–78.
[13] H.S. Hu, J.G. Nie, M.R. Eatherton. Deformation capacity of concrete-filled steel plate composite shear walls. *Journal of Constructional Steel Research*. 103 (2014) 148–158.
[14] A.H. Varma, S.R. Malushte, K.C. Sener, Z.C. Lai. Steel-plate composite (SC) walls for safety related nuclear facilities: design for in-plane force and out-of-plane moments. *Nuclear Engineering and Design*. 46 (8) (2014), 240–249.
[15] J. Shi, S.Gao, L.H. Guo. Compressive behaviour of double skin composite shear walls stiffened with steel-bars trusses. *Journal of Constructional Steel Research*. 180 (2021),106581.
[16] JGJ/T380-2015: Technical specification for steel plate shear walls. *Ministry of Housing and Urban-Rural Development of the People's Republic of China (MOHURD)*, 2015. [in Chinese].
[17] X. Zhang, Y. Qin, Z. Chen. Experimental seismic behavior of innovative composite shear walls. *Journal of Constructional Steel Research*. 116 (2016), 218–232.
[18] Y. Qin, G.P. Shu, G.G. Zhou, J.H. Han. Compressive behavior of double skin composite wall with different plate thicknesses. *Journal of Constructional Steel Research.* 157 (2019), 297–313.
[19] Y.J. Yu, Y.Q. Luo, S.W. Lin, et al. Experimental seismic behaviors of different connections to CFST end-columns in shear walls. *Journal of Constructional Steel Research.* 196 (2022), 107385.
[20] Z.h. Chen, Z.Y. Zi, T. Zhou, et al. Axial compression stability of thin double-steel-plate and concrete composite shear wall. *Structures*.34 (2021) 3866-3881.
[21] DBJ33/T 1273-2022: Technical specification for double-skin truss-reinforced composite sheer walls. *Zhejiang Provincial Department of Housing and Urban Rural Development,* 2022. [in Chinese].
[22] GB 50010-2010: Code for design of concrete structures. *Ministry of Housing and Urban-Rural Development of the People's Republic of China (MOHURD)*, 2010. [in Chinese].
[23] Z.H. Chen, J. Liu, Ting Zhou, et al. Uniaxial Eccentric-Compression Performance Analysis for Double-Plate Connected Concrete-Filled Steel-Tube Composite Columns. *J. Struct. Eng*.146(8) (2020), 04020161.
[24] Z. Tao, Z.B. Wang, Q. Yu. Finite element modelling of concrete-filled steel stub columns under axial compression. *J. Constr. Steel Res.* 89 (10) (2013),121–131.
[25] A. P. C. Duarte, B. A. Silva, N. Silvestre, et al. Finite element modelling of short steel tubes filled with rubberized concrete. *Compos. Struct.* 150 (8) (2016), 28–40.
[26] GB 50011-2010: code for seismic design of buildings. *Ministry of Housing and Urban-Rural Development of the People's Republic of China (MOHURD)*, 2010. [in Chinese].

Advanced Steel Construction – Vol. 20 No. 4 (2024) 376–384
DOI:10.18057/IJASC.2024.20.4.5

A BAYESIAN-OPTIMIZED NEURAL NETWORK MODEL FOR SHEAR CAPACITY OF A PERFOBOND STRIP CONNECTOR IN VARIOUS TYPES OF COMPOSITE STRUCTURES

Minh Hai Nguyen and Hoang Nam Phan *

Faculty of Road and Bridge Engineering, The University of Danang - University of Science and Technology, Da Nang, Viet Nam
** (Corresponding author: E-mail: phnam@dut.udn.vn)*

ABSTRACT

Perfobond strips are integral to composite steel-concrete structures or joints between precast concrete elements. However, the diverse boundary conditions and design parameters in various applications have led to numerous empirical and analytical methods to investigate their shear behavior. Existing empirical formulas often fail to accurately assess the shear capacity of perfobond strip connectors under different conditions. This study addresses this issue by developing a comprehensive prediction model for the shear capacity of perfobond strip connectors using a Bayesian-optimized artificial neural network (ANN). The proposed model evaluates shear capacity under various conditions, including the presence or absence of penetrating rebar in perforations, the use of normal or fiber-reinforced concrete, and various experimental specimen shapes applied in different composite structures. By utilizing an extensive dataset of 253 specimens, including 136 previously tested by the authors, the model is trained and optimized with a Bayesian optimization algorithm using a Gaussian process prior. This approach explores a wide range of hyperparameters to achieve optimal performance. The results show that the model excels in predicting the shear capacity of perfobond strip connectors across different design parameters and experimental conditions. A subsequent parametric study confirms the model's consistency with the shear-resisting mechanism of perfobond strips, underscoring the reliability and effectiveness of the ANN-based model. This model serves as a valuable tool for accurately predicting shear capacity in perfobond strip connectors across diverse design scenarios.

ARTICLE HISTORY

Received: 17 February 2024
Revised: 21 August 2024
Accepted: 5 September 2024

KEYWORDS

Perfobond strip;
Bayesian optimization;
Artificial neural network;
Shear capacity;
Sensitivity analysis;
A technical paper

1. Introduction

To ensure stress transfer between the steel and concrete components in composite structures, it is common to use shear connectors [1]. While headed studs have been the most used shear connectors [2, 3], the perfobond strip (called Perfobond Lestein in German, abbreviated as PBL) proposed by Leonhardt, et al. [4] has been increasingly utilized for various types of composite structures due to its unique advantages, such as high stiffness, good fatigue resistance [5], simple shape and flexible construction methods. Originally developed as a shear connector for composite girders, the PBL involves welding a steel plate with multiple perforations onto the top flange of the steel girder, as shown in Fig. 1(a). Concrete is then poured onto the concrete slab to fill the perforations, providing shear capacity that integrates the steel girder and concrete slab.

Since its development for the first application in composite girder bridge, many types of applications of the PBL have been developed. Among them, in the corrugated steel web of composite bridges, a PBL is used as shown in Fig. 1(b) [6-8]. In truss steel web composite bridges, PBL connectors are used at the joint between truss steel and concrete members, as shown in Fig. 1(c) [9]. Furthermore, in a composite deck designed to reduce the thickness of the bridge slabs and improve its fatigue durability, PBL connectors are also commonly used, as shown in Fig. 1(d) [10-12]. In these applications, the penetrating rebars are often placed in the perforations of the PBL to enhance the shear capacity and the stiffness of the shear connectors. In addition, Fig. 1(e) and Fig. 1(f) show examples of the PBL application in the rigid connection of the steel girder-concrete pier [13], and the steel-concrete hybrid pier [14], respectively. Furthermore, Fig. 1(g) shows an example of the application of the PBL to the joint of a prestressed concrete girder and steel girder in hybrid girder bridges with a proven application record in multi-span continuous girder bridges [15, 16]. Note that, in structures such as those shown in Fig. 1(e)-(g), the PBL is in concrete enclosed by a steel shell, so the PBL resists shear forces in the condition with the very highly confined condition.

With the advancements in manufacturing and construction technologies for precast concrete components in recent years, developing joints between these components has become increasingly important. One perspective-joining method that has gained prevalence in recent studies is the utilization of PBL connectors. These have been applied to joints between precast reinforced concrete slabs [17, 18], precast concrete barriers in bridges [19], and steel columns and precast concrete walls in buildings [20], as shown in Fig. 1(h) to Fig. 1(k). However, narrow joints are often preferred in these cases, making it difficult to arrange the surrounding reinforcement. To address this issue, PBLs are often used in conjunction with high-strength steel fiber concrete to ensure concrete workability in narrow spaces and prevent brittle joint failure in the absence of surrounding reinforcement [21].

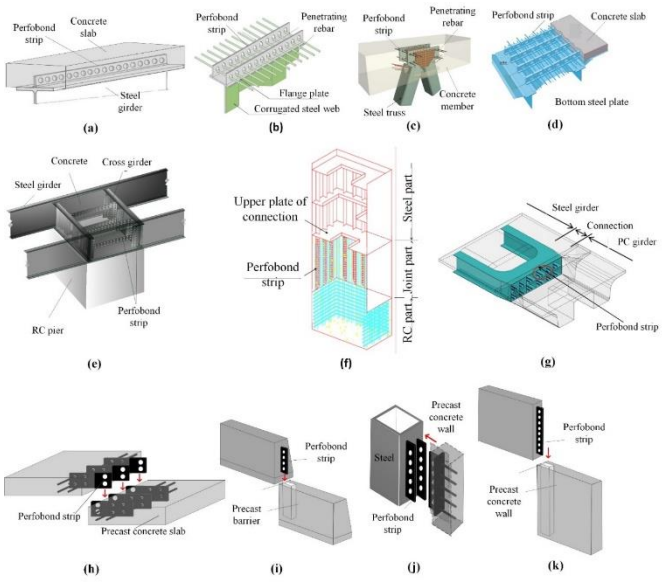

Fig. 1 Various applications of the PBLs: (a) Composite girder bridge; (b) Steel web PC bridge, (c) Steel truss web composite bridge; (d) Composite deck, (e) Rigid connection between pier and concrete slab, (f) Hybrid pier, (g) Hybrid girder bridge, (h) Joint of precast concrete slabs, (i) Joint of precast concrete barriers, (j) Joint between steel columns and precast concrete walls, and (k) Joint of precast concrete walls

As previously mentioned, PBL connectors have been utilized in a variety of applications, each with different usage conditions. Previous studies [22-28] have revealed that the shear capacity of PBL connectors is affected by several parameters, including the diameter and the number of perforations, the dimensions of perfobond steel plate, the diameter and the yield strength of penetrating rebar, the concrete strength, and particularly the confined conditions surrounding the PBL. In addition, the confined effect on the connector shear capacity depends on various factors, such as the specimen's concrete block dimension, specimen shape, support conditions during the loading test, and the arrangement of steel hoops or steel shells around the perfobond plate [29, 30]. Moreover, using high-strength fiber-reinforced concrete significantly increases confined effects in the absence of steel hoops [21]. However, most previous

studies offer empirical formulas to assess the shear capacity of PBL connectors based on a specific condition, without considering all the above parameters [4, 22, 23, 30-36]. As a result, these formulas only predict the shear capacity of PBL connectors in specific usage cases. Consequently, engineers may find it challenging to develop or design new and diverse uses of the PBL, as depicted in Fig. 1, using these formulas. Therefore, a more comprehensive prediction method is needed that accounts for the influence of a broader range of design parameters.

When a predicted value is influenced by multiple parameters, machine learning emerges as a promising method [37]. Recent studies have employed this technique to predict the shear capacity of PBL connectors. Allahyari, et al. [38] used an artificial neural network (ANN) to construct a prediction model based on the results of 90 collected test specimens. Sun, et al. [39] combined the backpropagation ANN model, the Genetic algorithm method, and the GSA method to develop a prediction model for the shear capacity of PBL connectors based on 107 specimens. However, most of the test specimens in these studies had a shape that corresponded to the use of the PBL in composite beams (Fig. 1(a)). This means that two perfobond steel plates were welded on both sides of the H-shaped steel, and the concrete slabs were symmetrically poured on both sides. As a result, these models fail to account for the shear capacity of PBL connectors in scenarios where the surrounding concrete experiences high confinement or when PBL is combined with high-strength fiber-reinforced concrete. This is because the parameters concerning the shape of the test specimens are not readily quantifiable, making it difficult to incorporate them into the machine learning models.

Therefore, this study aims to develop a comprehensive prediction model for the shear capacity of PBL connectors using an optimized neural network. While most previous studies have only proposed prediction models for the shear capacity under specific experimental conditions, including certain shapes and sizes of specimens, the novelty of this study lies in developing a model that can predict the shear capacity of PBL connectors under extensive experimental conditions, such as with or without penetrating rebar in the perforations, using normal or fiber-reinforced concrete, and especially for different shapes and dimensions of specimens. This allows engineers to use a single model to design the perfobond strip under various working conditions, thereby shortening the time needed to consider the correlation of each current design formula with the working conditions of the designed structure, requiring specialized knowledge to avoid errors when selecting inappropriate formulas.

Initially, a dataset comprising 253 specimens from various studies with diverse experimental conditions, including 136 from the authors' tests, was compiled, making it the largest dataset used in any study. This dataset was then utilized to systematize the shear-resisting mechanisms of perfobond strips, providing readers with a more comprehensive understanding of these mechanisms across different working conditions. Then, these results are also compared with the calculated values of eight existing empirical formulas to clarify the correlation between the calculated and experimental values as well as the limitations of each formula. To overcome the limitation of the existing models, an ANN model is then developed for the prediction of the shear capacity of PBL connectors, where a total of 12 input variables are considered in the training data. The model is also optimized based on a Gaussian process prior through a Bayesian optimization algorithm considering a large range of hyperparameters. Since the ANN model has been trained, a comprehensive parametric study is finally carried out, where the effectiveness of some primary parameters on the shear capacity of PBL connectors is evaluated and discussed in detail.

2. Collection of experimental data from the push-out and pull-out tests

Fig. 1 showcases the versatility of PBLs, widely employed in diverse applications. To investigate their shear capacity, researchers have proposed various test specimen shapes, as illustrated in Fig. 2. The five commonly used types, labeled A, B, C, D, and E, exhibit distinct configurations. While parameters like perforation diameter, number, steel plate dimensions, rebar diameter and yield strength, and concrete strength are variables across all specimens, there are also unique considerations for each type. Differences in the effects of confined surrounding concrete and the contribution of the bond between the steel plate and concrete contribute to varying shear capacities among the different PBL connector specimen types.

In A and D specimens, the concrete surrounding the PBL is located at the center. In contrast, in B and C specimens, the perfobond plate is welded onto a base steel plate and positioned at the edge of the concrete block. As a result, the confined effect of the surrounding concrete on the connector shear capacity is greater in A and D specimens than in B and C specimens, particularly when the concrete block is enclosed in a steel shell, as in D specimens [40]. Furthermore, the support conditions during the loading test differ across specimens. For A and D specimens, the reaction forces appear over the entire bottom surface of the concrete block, with the total vector of the reaction force coinciding with the loading direction. Conversely, the total reaction force vector of B, C, and E specimens is eccentric to the loading direction, inducing a moment on the concrete block that may affect the connector shear capacity in these cases [36]. Additionally, the interface between the steel plate and concrete is more extensive in B, C, and D specimens than in A and E specimens, leading to differences in the contribution of the bond between steel plates and concrete to the shear capacity of the PBL connector among these specimen types.

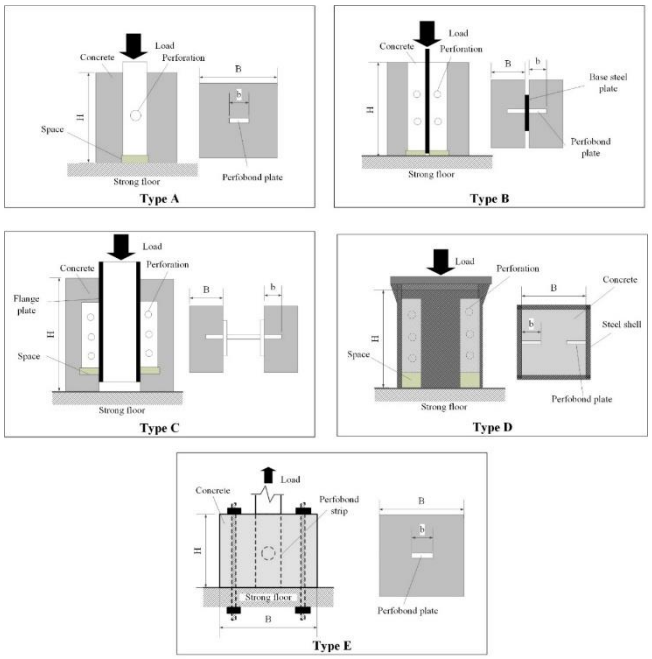

Fig. 2 Various types of test specimens for the PBL

Due to the variety of factors that affect the shear capacity of PBL connectors, most studies have only investigated its capacity within a certain range of usage. To construct a comprehensive prediction model that considers most of the necessary design parameters, this study collected and constructed a dataset of 253 experimental specimens, with a wide range of parameters as shown in Table 1 [21, 29, 32, 34-36, 41-53].

Among these specimens, 136 specimens were collected from the previous studies of the authors [21, 29, 34-36], with types A, B, and E, while the remaining specimens were collected from other studies. Twelve experimental parameters were considered, which is more than any previous model predicting the shear capacity of PBL connectors.

Table 1
Range of experimental parameters

No.	Parameters	Notation	Range
1	Specimen type	Shape	5 types (A – E)
2	Perfobond plate thickness	T (mm)	8-25
3	Perfobond plate width	a (mm)	60-300
4	Perfobond plate length	L (mm)	100-655
5	Number of perforations	n	1-5
6	Perforation diameter	D (mm)	30-90
7	Rebar diameter	d (mm)	0, 10-25
8	Concrete compressive strength	f_c (MPa)	14-105
9	Volumetric content of steel fibers in concrete	V_f (%)	0-2.3
10	Yield strength of penetrating rebar	f_y (MPa)	0, 329-410
11	Concrete block height	H (mm)	150-1000
12	Concrete block width	B (mm)	150-500

The dataset included 82 specimens that used penetrating rebars in the perforations and 172 specimens that did not. In addition, the dataset is composed of 5 different specimen shapes, with varying dimensions of the perfobond steel

plate, penetrating rebars, and concrete blocks. Notably, the compressive strength of the concrete ranged from 14-105 MPa, demonstrating that the dataset includes cases where the PBL is used in combination with high-strength concrete.

Fig. 3 displays the distribution of key parameters. It can be observed that the data is focused on the range of design parameters commonly used for the PBL. Specifically, the data for specimens with perforation diameters is uniformly distributed between 30-70mm, while only a few specimens have diameters larger than 70mm (Fig. 3(a)). This is because the PBL is typically used within the width limit of perfobond steel plates under 150mm, and the diameter of the perforation is usually limited to half the width of the perfobond steel plate. The diameter of the penetrating rebar is evenly distributed between 10-25mm in Fig. 3(b), while smaller diameter rebars are not used because they do not contribute much to the connector shear capacity.

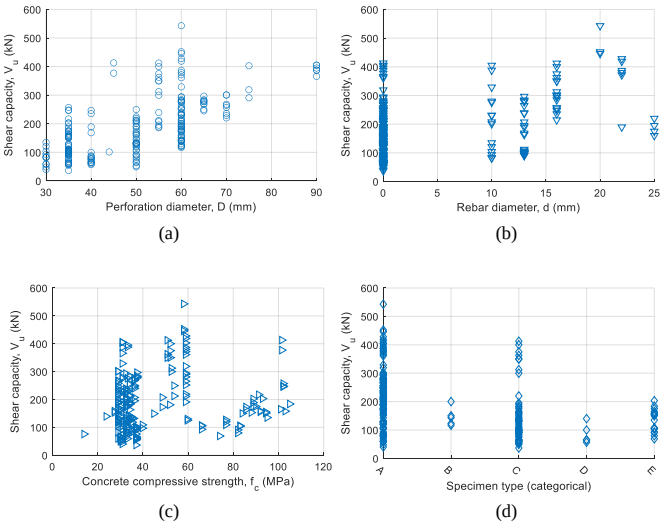

Fig. 3 Data distribution of main parameters related to shear capacity: (a) Perforation diameter, (b) Penetrating rebar diameter, (c) Concrete compressive strength, (d) Specimen types

Furthermore, the compressive strength data for concrete is mainly concentrated within the range of ordinary concrete, which is 25-60 MPa (Fig. 3(c)). However, there are also quite a few test specimens using high-strength concrete over 60MPa. On the other hand, the amount of data for specimen types A, C, and E is higher than that for types B and D. For type D specimens, the PBL is enclosed by a steel shell, which corresponds to a scenario where the concrete area around it has a very high confined condition, and this is rare in practical applications. Type B specimens are also rarely used because the stress transmission mechanism of this specimen is relatively similar to that of type C specimens. The effects of these parameters on the connector shear capacity, as well as the effect of the data distribution on the results of machine learning models, will be discussed in subsequent sections of the paper.

3. Shear resisting mechanism of the PBLs based on previous results

3.1. *Affecting mechanism of penetrating rebars*

Fig. 4(a), extracted from the authors' previous push-out tests [34, 35], presents examples of the relationship between shear force and slip for perfobond strips with a perforation diameter of 60 mm, both in cases without penetrating rebar (black lines) and with penetrating rebar of 13 mm diameter (red lines). It is noticed that other experimental parameters, such as concrete strength and the shape and size of the specimens, were kept consistent. The results indicate that the presence of penetrating rebar does not significantly influence the behavior in the initial stage of shear force, where the slip is below 3 mm; however, it does impact the subsequent stages of shear force. Based on this behavior, Fig. 4(b) idealizes the typical relationships between shear force and slip for both cases, with and without penetrating rebar.

For a case without penetrating rebar, the shear-resisting mechanism of the PBL can be divided into three stages: (1) the linear region, (2) the nonlinear region, and (3) the softening region. Fig. 4(c) visually presents stress components, revealing key observations:

In the linear region, PBL force is resisted by the bond at the steel plate-concrete interface and concrete shear force in the perforation. Initial stiffness is high but diminishes in stage (2) when the interface stress exceeds bond strength. Variations in specimen behavior arise from the steel plate-concrete interface, influencing both initial stiffness and the linear region's endpoint.

In the nonlinear region, PBL force is chiefly resisted by shear force on two concrete surfaces in the perforation. The maximum shear force, defining connector shear capacity, occurs upon shear fracture at these surfaces. Factors influencing capacity include perforation diameter, concrete strength, steel plate thickness, and confined conditions. The shape, size, support conditions, and the use of reinforcements or fiber-reinforced concrete also significantly impact shear capacity.

Post-shear fracture in stage (2), concrete confinement around the PBL prevents abrupt shear force decline. Greater confinement leads to a gradual decrease in shear force. This region's characteristics, often dependent on coarse aggregate dispersion in the perforation, are typically modeled as a straight line with a negative slope in shear force-slip models.

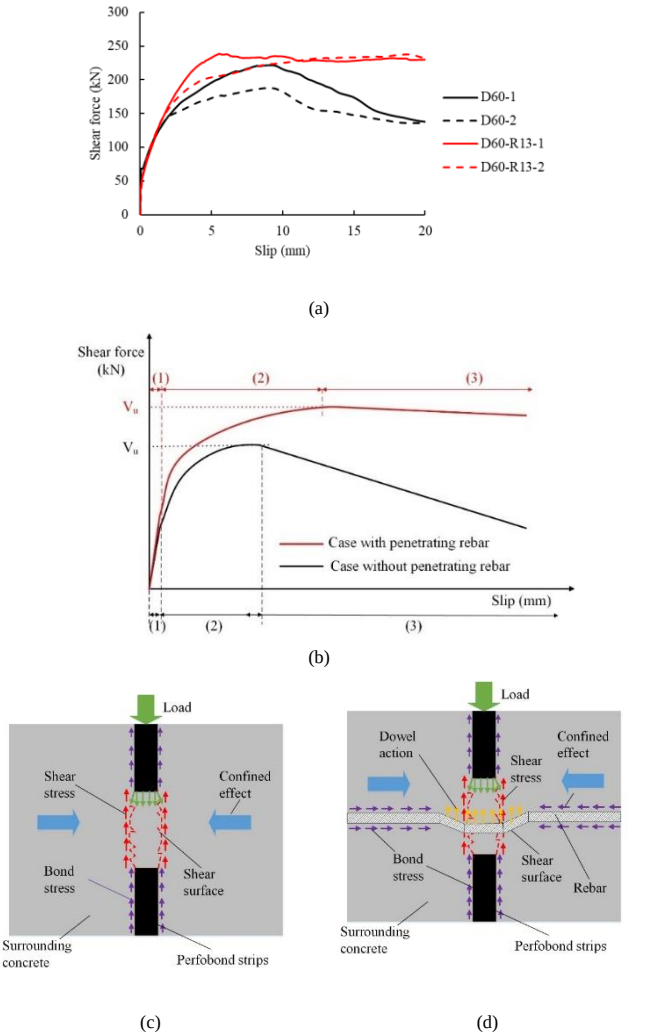

Fig. 4 Shear force–slip relationship of the PBLs: (a) Examples of the experimental shear force–slip relationships of the PBLs, (b) Model for shear force-slip relationship of the PBLs, (c) Shear resisting mechanism in the case without penetrating rebar, (d) Shear resisting mechanism in the case with penetrating rebar

In the presence of a penetrating rebar in the perforation, the mechanism remains similar during stage (1) as previously explained. However, the rebar significantly enhances shear capacity in stage (2) and prevents sudden shear force reduction after reaching capacity in stage (3). Fig. 4(c) illustrates the rebar's action, encompassing the dowel effect from rebar flexural deformation and the confined effect in the concrete around the PBL due to the rebar-concrete bond. The penetrating rebar's diameter notably impacts shear capacity, while the steel plate thickness influences stress distribution and, consequently, the rebar's flexural deformation range. Concrete strength also affects this deformation. The shear-resisting mechanism with penetrating rebar is more intricate than without, with parameters influencing shear capacity mutually. Despite this complexity, the rebar arrangement aids in averting brittle failure of the shear connector, making it prevalent in PBL applications with low confined concrete conditions and convenient rebar arrangement.

3.2. *Affecting mechanism of specimen types and block dimensions*

Most previous studies have conducted experiments using basic parameters,

such as concrete strength, perforation diameter, perfobond steel plate thickness, and the diameter of penetrating rebar, on specimens with fixed shapes and dimensions. However, even when these experimental parameters are identical, the shear capacity of the perfobond strip can still vary. To clarify this, Fig. 5(a) [34, 45, 46] illustrates the impact of specimen shape, corresponding to types A, B, and C in Fig. 2, while Fig. 5(b) [29] demonstrates the influence of the dimensions of the concrete block surrounding the perfobond strip in type A specimens. All test samples in these figures were derived from the authors' previous tests, with a perforation diameter of 60 mm, perfobond steel plate thickness of 12 mm, concrete compressive strength of approximately 30 MPa, and no penetrating rebar. It is evident that both the specimen shape and the concrete block dimensions significantly affect the shear capacity of the perfobond strip. This effect can be explained by the different confinement effects exerted by the concrete region surrounding the perfobond strip in the various test specimens, as shown in Fig. 5(c).

When shear force is transmitted to the concrete shear surface within the perforation, the uneven surface, caused by randomly distributed aggregates, generates a push-out force perpendicular to the perforation shear surface. This push-out force causes cracks to propagate into the surrounding concrete around the perfobond strip, ultimately reducing the shear capacity. In type A specimens, where the perfobond steel plate is centrally located within the concrete region, the confinement effect is generated from both sides of the strip, which is stronger than the effect generated from one side, as in type B and C specimens. This increased confinement effect restricts crack propagation into the surrounding concrete caused by the push-out force. Consequently, even with identical design parameters for the perfobond strip and concrete strength, the shear capacity of type A specimens remains higher than that of types B and C, as shown in Fig. 5(a).

Additionally, the confinement effect increases when the distance from the edge of the perfobond steel plate to the outer surface of the concrete block is larger. This explains why increasing the width of the concrete block significantly enhances the shear capacity of the perfobond strip, as demonstrated by the results in Fig. 5(b).

In summary, in addition to the basic design parameters, such as concrete strength, penetrating rebar, and perfobond strip dimensions, the boundary conditions and size of the concrete block surrounding the strip also significantly impact its shear capacity. This influence mechanism becomes more complex when multiple design parameters are varied simultaneously for different specimen types. Consequently, most current design formulas can assess the shear capacity of the perfobond strip under specific experimental conditions but show a low correlation with data when those conditions change, as will be discussed in Section 4 of this study.

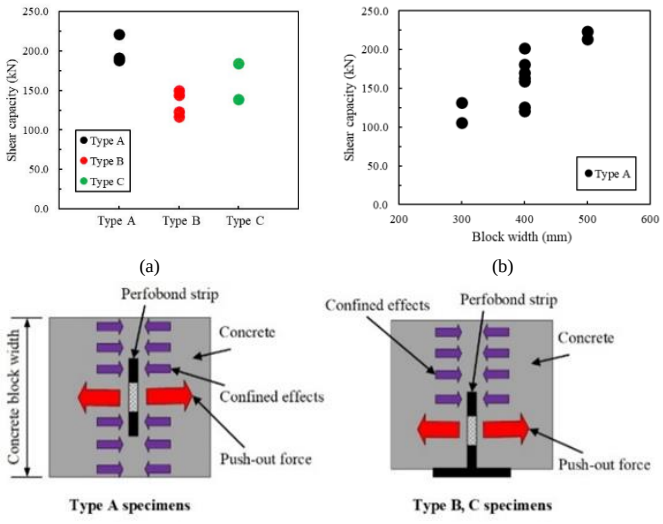

Fig. 5 Affecting mechanism of specimen types and block dimensions: (a) Effects of the specimen types on the shear capacity, (b) Effects of concrete block width on the shear capacity, (c) Schematics of the affecting mechanism

4. Evaluation of the existing shear capacity formulas of PBL connectors

4.1. Existing models for predicting the shear capacity of PBL connectors

Accurately predicting the shear capacity of PBL connectors is essential for designing shear connectors in composite steel-concrete structures and joints between precast concrete components. Consequently, multiple studies have focused on developing empirical formulas to predict the shear capacity of PBL connectors. Table 2 presents eight formulas proposed in previous studies [4, 22, 23, 30-36], arranged in chronological order of publication. Most of these formulas are based on statistical methods for experimental results, with experimental conditions and parameters varying within a specific range. Therefore, the range of applicability for each formula is determined based on the database used to construct it. However, to assess the applicability of these formulas over a broader range, the calculated values are compared with experimental results from a wide range of collected datasets, as described in a later section.

Table 2
Existing formulas for predicting the shear capacity of PBL connectors

1	Leonhardt, et al. [4]	For a case without penetrating rebar: $V_u = 2.553D^2 f_c$
2	Oguejiofor and Hosain [22]	$V_u = 4.5h_{sp}Tf_c + 0.91A_r f_y + 3.31D^2\sqrt{f_c}$
3	Ahn, et al. [23]	$V_u = 3.14h_{sp}Tf_c + 1.21A_r f_y + 1.895\pi D^2\sqrt{f_c}$
4	Chen [30]	$V_u = 1.38(D^2 - d_r^2)f_c + 1.24d_r^2 f_y$
5	JSCE [31]	For a case without penetrating rebar: $V_u = 1.6D^2 f_c$ For a case with penetrating rebar: $V_u = 1.85A - 26.1 \times 10^3$ In which, $A = \frac{\pi(D^2 - d_r^2)}{4}f_c + \frac{\pi d_r^2}{4}f_t$
6	He, et al. [32]	$V_u = \tau_b A_b + 1.06A_c f_c + 2.09A_r f_y$ In which, $\tau_b = -0.022f_c + 0.306\sqrt{f_c} - 0.573$
7	Zheng, et al. [33]	$V_u = 1.76(A - A_r)f_c + 1.58A_r f_y$
8	Nakajima and Nguyen [34-36]	For a case without penetrating rebar and using normal concrete: $V_u = 0.15\kappa_1 A f_c^{0.65} A_{sb}^{0.43} T^{-0.5}$ For the case without penetrating rebar and using high-strength steel fiber concrete: $V_u = \kappa_1\kappa_2\kappa_3 A f_c^{0.65}$ In which, κ_1 = 1.0 or 0.78, $\kappa_2 = 22V_f + 0.48$, $\kappa_3 = 0.22V_b^{0.24}$ for push-out force, and $\kappa_3 = 0.17V_b^{0.24}$ for pull-out force For a case with penetrating rebar and using normal concrete: $V_u = V_c + V_r$ In which, $V_c = 0.15\eta\kappa_1(A - A_r)f_c^{0.65}A_{sb}^{0.43}T^{-0.5}$ $V_r = 0.84d_r f_y D^{0.1}T^{0.8}$ $\eta = 6.9d_r^{0.4}D^{-0.7}$

Notes: V_u: Shear capacity per one perforation (N); D: Perforation diameter (mm); f_c: Concrete compressive strength (MPa); h_{sp}: Width of perfobond steel plate (mm); T: Thickness of perfobond steel plate (mm); A_r: Cross section of penetrating rebar (mm^2); f_y: Yield strength of penetrating rebar (MPa); d_r: Penetrating rebar diameter (mm); τ_b: Bond strength between steel plate and concrete (MPa); A_b: Steel plate-concrete interface area (mm^2); A_c: Area of concrete part in perforation (mm^2); A_{sb}: Side area of the concrete block surrounding the PBL (mm^2); κ_1: Influence coefficient of the test specimen's shape; κ_2: Influence coefficient of the volume content inside the concrete mixture; κ_3: Influence coefficient of the concrete block size; η: Interaction coefficient between concrete and penetrating rebar

Table 2 reveals that the coefficients in the formulas vary, but most formulas share a relatively similar form. The formula of Leonhardt, et al. [4], which introduced the PBL concept, has the simplest form as it only considers the effects of concrete strength and perforation diameter. This is because Leonhardt et al. initially developed the PBL concept for composite beams and penetrating rebar was not arranged in the perforation. Their formula is based on the results of the type C specimen test. However, due to its simplicity and ease of use for engineers, the committee on hybrid structures of the Japan Society of Civil Engineers [31] has adjusted the coefficients based on this form and incorporated them into the corresponding standard to predict the shear capacity of PBL connectors without penetrating rebar.

Oguejiofor and Hosain [22] proposed a method of using PBLs with penetrating rebar and intermittently welded perfobond steel plates on the steel girder flange, leading to three components that contribute to the connector shear capacity. These components include the bearing force at the perfobond steel plate's edge, the axial action of the penetrating rebar, and the concrete's shear force in the perforation. The contribution of each component is indicated by corresponding coefficients. Ahn, et al. [23] also developed a formula based on this concept but with coefficients adjusted based on expanded experimental data. It should be noted that the bearing force at the PBL edge is not considered in the calculation of the connector shear capacity for the specimens collected in this study. This is because a gap is established under the perfobond steel plate in all test specimens. Chen [30], He, et al. [32], and Zheng, et al. [33] also have similar forms but do not account for the end-bearing force at the perfobond plate's edge. Among them, the formula developed by He, et al. [32] considers the bond stress between the perfobond steel plate and concrete. Nakajima and Nguyen's formulas [34-36] have a basic structure that includes the concrete shear force in the perforation and the penetrating rebar's contribution. However, each component is more complex and considers more parameters than the other formulas, which are formulated based on an exponential function to assess the mutual influences of the parameters.

4.2. Statistical analysis of the correlation between empirical formulas and experimental data

Figs. 6(a)-(h) depict the correlation between the experimental shear capacity (target value) and the calculated values (output value) for each of the eight formulas presented in Table 2. The regression line is represented by the blue line in each figure, while the line $y = x$ is indicated by the black dotted line, signifying the point at which the calculated value equals the experimental value. The vertical axis of each figure displays the formula of the regression line. Fig. 7 presents the statistical analysis results for the data in Fig. 6, with the Min, Max, and Mean ratios indicated by the minus sign for each formula. The standard deviation of the data is represented by the height of the blue rectangle, while the red plus sign denotes whiskers, signifying the data points that fall outside the trend determined by the regression analysis.

Figs. 6(a)-(c) and Fig. 7 demonstrate that the formula of Leonhardt, et al. [4] overestimates the experimental shear capacity, whereas the formulas of Oguejiofor and Hosain [22] and Ahn, et al. [23] tend to underestimate the experimental values. The formula of Leonhardt, et al. [4] considers only the effects of perforation diameter and concrete strength and is based on a limited experimental dataset, which explains the discrepancy with the results of a more extensive dataset. In contrast, the formulas of Oguejiofor and Hosain [22], as well as Ahn, et al. [23], were developed based on specimens that include the end bearing force at the perfobond steel plate's edge. However, the calculated values in Figs. 6(b) and 6(c) do not account for this contribution since the test specimens used in this study have a gap established under the perfobond steel plate. Consequently, the resisting mechanism of the specimens in the database used to formulate the formulas of Oguejiofor and Hosain [22], as well as Ahn, et al. [23], differs from that of the specimens collected in this study, leading to a significant difference between the calculated and experimental values.

Fig. 7 indicates that the remaining formulas have average values in the range of 0.75 to 1.1, while Figs. 6(d) to 6(h) reveal that the correlation coefficients differ among the formulas. The formula proposed by Chen [30] exhibits the lowest average ratio due to the limited dataset used to develop their formula. Conversely, the formula proposed by JSCE demonstrates a high average ratio and the most skewed data, as it only considers the basic parameters and reference structure of the Leonhardt et al. formula, leading to a low correlation with the large experimental dataset that accounts for many complex influencing factors. The average values corresponding to the recently proposed formulas by He, et al. [32], Zheng, et al. [33], and Nakajima and Nguyen range from 0.8 to 1.0, as they are based on larger experimental datasets than previous formulas. However, the standard deviation of the data using He et al.'s formula is relatively high because of the bond strength between the steel plate and concrete, which has a large experimental error.

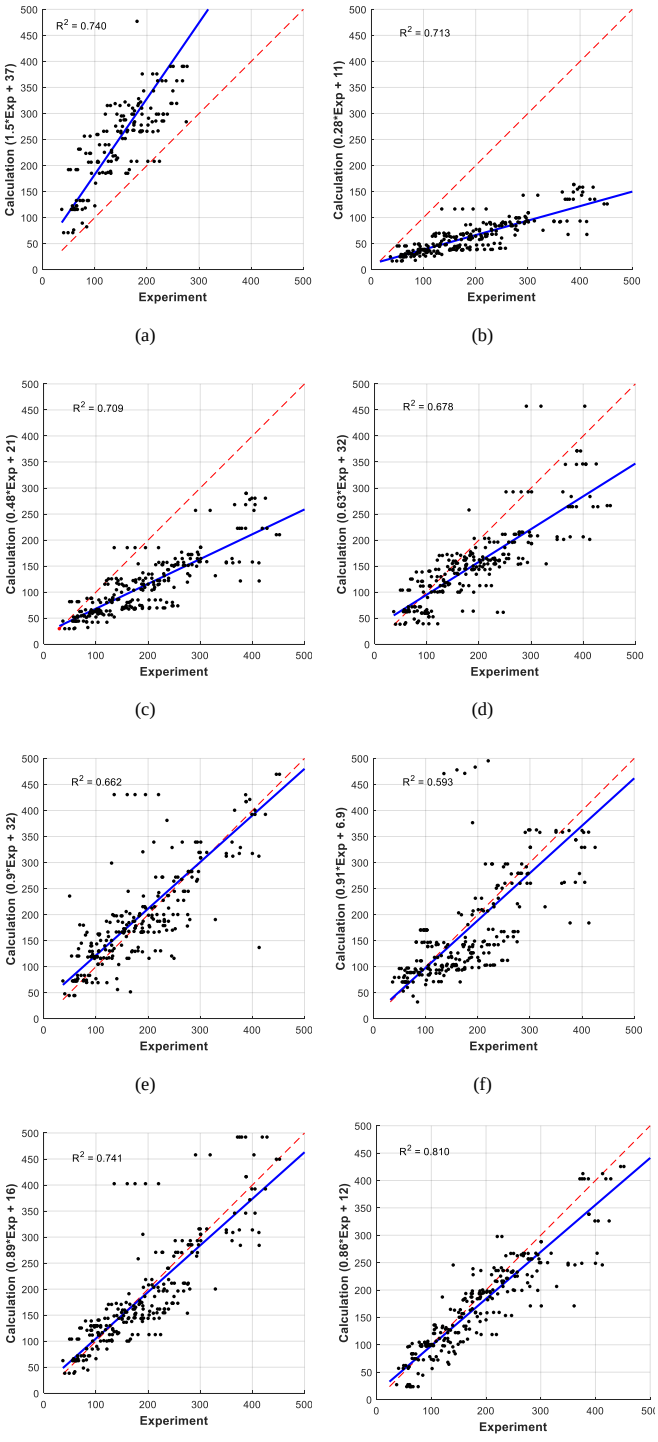

Fig. 6 Statistical analysis of the shear capacity ratio from existing formulas and experimental data: (a) Leonhardt et al., (b) Oguejiofor and Hosain, (c) Ahn et al., (d) Chen, (e) JSCE, (f) He et al., (g) Zheng et al., and (h) Nakajima and Nguyen.

On the other hand, Nakajima and Nguyen's formula indicates the best correlation with the experimental data based on all statistical parameters, such as the average value, correlation coefficient, standard deviation, and the number of skewed specimens, as it is based on a large database, considers many influencing factors by analyzing the PBL connector mechanism, and is suitable for the parameters of the connector within the common range. Nevertheless, the correlation coefficient in Fig. 6(h) is only 0.900, and there are still many skewed data points, especially those in the experimental shear capacity range above 300 kN and below 80 kN. This may be attributed to the fact that Nakajima and Nguyen's formula focuses only on the parameters of the connector within the common range, without considering cases where the perforation is too small or too large.

In conclusion, the correlation of most current experimental formulas with the experimental dataset is not high, primarily due to (i) the limited dataset used in the statistical analysis to develop the formulas and (ii) the difficulty in

considering all the influencing factors based on conventional statistical methods. Hence, machine learning may provide a feasible solution when the influencing factors are complex, and the experimental dataset is large enough.

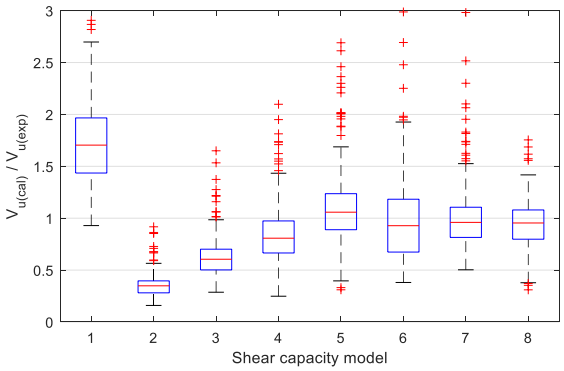

Fig. 7 Descriptive statistics of the ratio between the existing models and experimental data

5. Optimization of neural network model

5.1. ANN training data and feature selection

In the literature, various machine-learning models have been employed to tackle regression problems [40]. In this study, an ANN model is utilized for prediction purposes. The ANN architecture, as illustrated in Fig. 8, includes an input layer, one or more hidden layers, and an output layer, with fully connected neurons. The input layer is comprised of n neurons, which correspond to the input variables of the training data. The hidden layers can contain one or multiple layers, and each layer consists of several neurons. The selection of the number of hidden layers and neurons per layer is based on the complexity of the problem and performance evaluation. The output layer is made up of one or more neurons, with each neuron representing a predicted output. During the training process, the ANN adjusts the weights of the connections between neurons to minimize the difference between the predicted outputs and actual outputs of the training data.

The ANN model excels in capturing complex and nonlinear relationships between input variables and outputs. Prediction accuracy depends on the quality and quantity of training data, as well as model parameter selection. A well-trained and optimized ANN model can offer precise and robust predictions for regression problems.

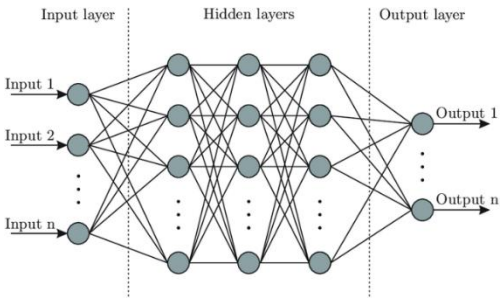

Fig. 8 Example of ANN architecture

This study uses 253 test results as training data, with 12 input variables and connector shear capacity as the output. Table 1 details the parameters and their ranges, with only specimen type labeled; other parameters are numeric. The data is split into a training set (85% or 215 data) and a test set (15% or 38 data). While the parameters in Table 1 are more comprehensive than in prior studies, some are not included. The yield or tensile strength of the steel plate is omitted, as failures primarily involve concrete shear or rebar fracture. Additionally, the reinforcement arrangement in the concrete block, a crucial parameter, varies widely in applications, complicating data collection. Furthermore, prior research by the authors has shown that this factor primarily contributes to preventing brittle failure rather than directly enhancing shear resistance [29, 34]. Hence, this parameter has been omitted. The influence of frictional force between the perfobond steel plate and concrete can be represented by parameters such as perfobond plate width and length. However, since the effect of frictional force between the base steel plate and concrete only appears in type B, C, and D specimens, and not in type A and E specimens, thereby it is not included. For type D specimens, this effect can be indirectly considered through the width and height of the concrete block. For type B and C specimens, as the width of the base plate varies minimally among specimens with the same type, the differences in the frictional force between the base steel plate and concrete among the specimens can also be indirectly assessed through the height of the concrete block. Therefore, the parameters related to the dimensions of the base steel plate are not listed.

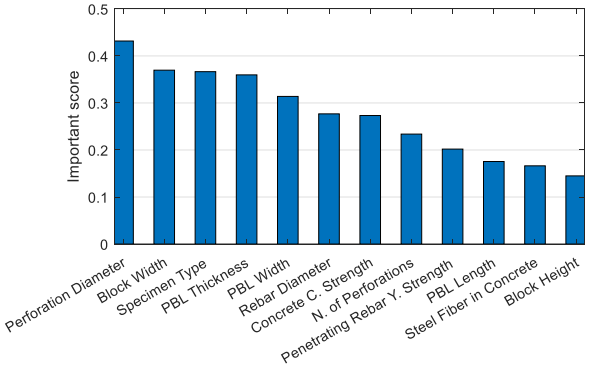

Fig. 9 Feature important scores sorted by the MRMR algorithm

The feature selection is first performed to identify the important score of each input feature on the response variable. The MRMR algorithm is used [54]. This algorithm seeks to identify an optimal feature set that is both maximally dissimilar and mutually exclusive, and that can effectively represent the response variable. The primary objective of the MRMR algorithm is to identify an optimal feature set S that maximizes the relevance of S to the response variable y while minimizing the redundancy of S. These two objectives are quantified using mutual information I. The optimal set S can be obtained by considering all $2^{|\Omega|}$ possible feature combinations, where Ω is the entire set of available features. However, the MRMR algorithm uses a forward addition scheme to rank features, which reduces the computation cost to $O(|\Omega| \cdot |S|)$ by utilizing mutual information quotient (MIQ) values,

$$MIQ_x = \frac{I(x,y)}{\frac{1}{|S|}\sum_{z \in S} I(x,z)}, \quad (1)$$

where the numerator and denominator are the relevance and redundancy of a feature, respectively, and $|S|$ is the number of features in S.

The function can be used to rank all features in Ω. The computation cost for this function is $O(|\Omega|2)$, and it uses a heuristic algorithm to quantify the importance of each feature, returning a score that indicates the significance of each predictor.

MRMR analysis findings in Fig. 9 reveal the influence of 12 input parameters on connector shear capacity. Beyond parameters like perforation diameter and concrete strength, those linked to the confined condition around the PBL (e.g., block width or specimen type) significantly affect shear capacity. Neglecting this can lead to deviations in calculated values. Dimensions of the perfobond steel plate, like thickness and width, exert substantial influence due to the bond with concrete. Steel plate thickness impacts stress distribution and shear surface formation, influencing capacity. Parameters related to specimen height have a lower impact, suggesting that multiple perforations on the steel plate minimally affect shear capacity per perforation.

5.2. Optimizable neural network

During the process of training a machine learning model or neural network, a crucial step is selecting values for parameters such as learning rate, epochs, number of layers, and hidden units. The selection of reasonable parameters often relies on experience, and for each set of parameters, we must train the model, observe the results achieved, evaluate the results, adjust the parameters, and repeat the process. To automate this process, search algorithms such as Grid Search or Random Search are used [55]. However, these algorithms are only effective with a small number of parameters because the search space increases rapidly with many parameters, making the search time-consuming. Bayesian optimization is an algorithm that optimizes effectively for objective functions with large evaluation costs (such as training a neural network) based on the Bayesian theorem [56]. Bayesian optimization significantly reduces the number of trials compared to Grid Search or Random Search [56]. The following is an algorithm for Bayesian optimization with a Gaussian process prior:

Define the objective function $f(x)$ and specify the prior distribution over the objective function. This is typically done by assuming a Gaussian process prior over $f(x)$.

Define an acquisition function $\alpha(x)$ that measures the utility of sampling x. Popular acquisition functions include upper confidence bound, expected improvement, and probability of improvement.

For $t = 1, 2, \ldots, t_{max}$ (t_{max} is the maximum number of iterations):

Fit a Gaussian process model to the available data (x, y), where $y = f(x) + noise$. The model provides a posterior distribution over $f(x)$ given the observed data.

Select the next point to sample by maximizing the acquisition function: $x_t = argmax\, \alpha(x|D_{t-1})$, where D_{t-1} is the data up to time $t-1$.

Sample the objective function at x_t: $y_t = f(x_t) + noise$.

Add the new data point (x_t, y_t) to the observed data.

Finally, return the best-observed value of $f(x)$.

Table 3
Optimization analysis result

Hyperparameter	Value
Number of hidden layers	2
Activation function	Relu
Layer biases initializer	Ones
Layer weights initializer	He
Regularization strength	2.549
Number of neurons per hidden layers 1-2	210, 58

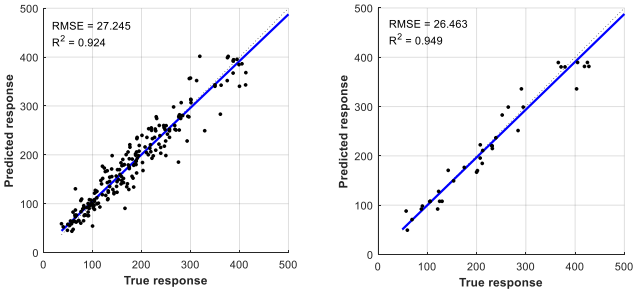

(a) (b)

Fig. 10 Regression plot of the calculated and actual values

To optimize the ANN model, a range of hyperparameters needs to be defined. In this study, the range of hyperparameters for the ANN model is introduced including the number of hidden layers (1, 2, and 3), the first, second-, and third-layer size (1-253 neurons), the activation function (ReLU, Tanh, Sigmoid), the layer biases initializer (Zeros, Ones), layer weights initializer (Glorot, He) [57, 58] and the regulation strength $(1e^{-5}/n, 1e^{5}/n)$, n is the number of observations. The iteration limit is fixed to 1000, and the train neural network regression model is adopted; this model is used to train a feedforward, fully connected neural network. The number of iterations of the Bayesian optimization is set as 100, and the acquisition function is selected as the expected improvement. For the validation, 5-fold cross-validation is used [59]. The result of the Bayesian optimization as the optimal hyperparameter for the ANN model is shown in Table 3, which comprises an optimal ANN model for the prediction.

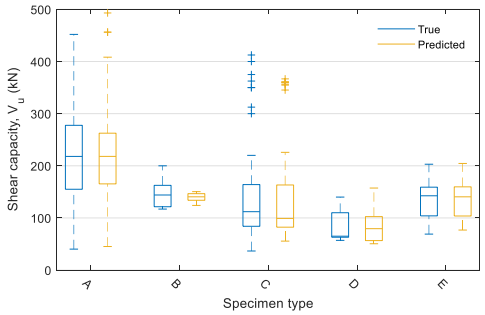

Fig. 11 Descriptive statistics of true and predicted values for specimen types

In addition to the validation using the 5-fold cross-validation on the training set, a separate test set of 15% data is used to test the model performance. The regression plots of the predicted and actual values from the 5-fold cross-validation and the test set are shown in Fig. 10 and an example of descriptive statistics of true and predicted values for specimen types is shown in Fig. 11. As observed from the figures, R^2 values are 0.924 and 0.948 for both the cross-validation and the separate test set, respectively, remarkably higher than that of the existing models previously mentioned. This demonstrates the high performance of the ANN model in predicting the shear capacity of PBL connectors in steel-concrete composite structures.

6. Effectiveness of primarily design parameters on shear capacity

The influence of key parameters on connector shear capacity was investigated using the developed model in Section 4. Figs. 12(a) to 12(e) present the impact of perforation diameter, penetrating rebar diameter, concrete compressive strength, perfobond plate thickness, and concrete block width. Type D specimens were excluded due to their limited quantity.

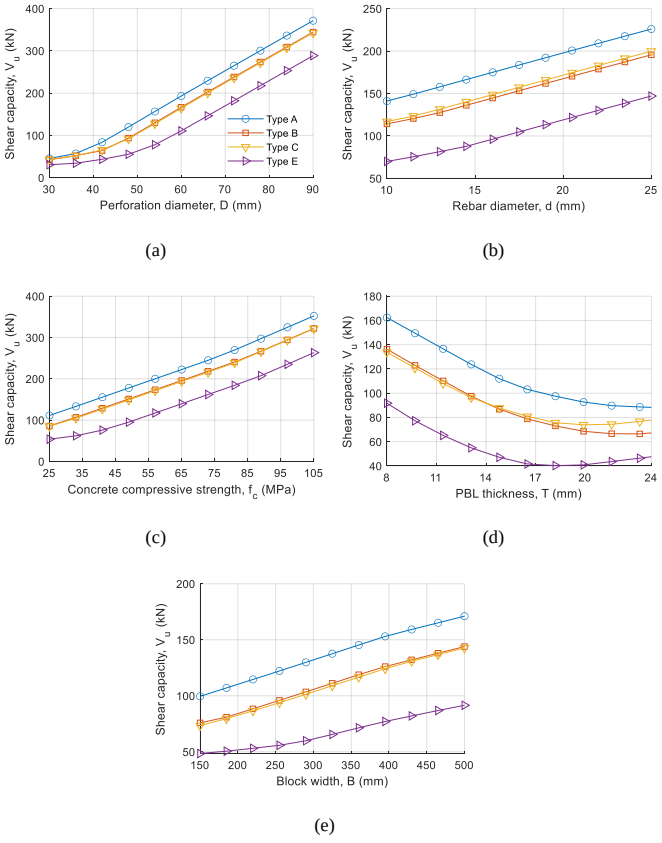

(a) (b) (c) (d) (e)

Fig. 12 ANN model-based parametric study results in terms of (a) Perforation diameter (b) Rebar diameter, (c) Concrete compressive strength, (d) PBL thickness, and (e) Block width

Results in Fig. 12 show that, with identical design parameters, type A has the highest shear capacity, followed by types B and C, with type E having the lowest. This aligns with load-bearing mechanisms discussed in Sections 2 and 3.1, emphasizing the importance of selecting an appropriate specimen type matching real conditions for accurate shear capacity calculations in design.

Observations in Fig. 12(a) indicate a non-linear increase in shear capacity with perforation diameter, suggesting expression in terms of the perforation area or square of the diameter, common in empirical formulas (Table 2). Conversely, the relationship between shear capacity and penetrating rebar diameter is nearly linear across all specimen types. Thus, it's recommended to express this relationship in terms of the diameter, reflecting the dowel action's dependence on rebar flexural deformation and diameter, as demonstrated in Nakajima and Nguyen's proposed formula.

Fig. 12(c) shows a nearly linear relationship between shear capacity and concrete compressive strength, consistent across normal-strength and high-strength concrete. Empirical formulas in Table 2 use various approaches to represent this effect, such as square root or exponential functions. However, the combined influence of concrete compressive strength on shear strength in the perforation and the confined effect on surrounding concrete is evaluated through its actual value.

Equations (1) to (7) in Table 2 overlook the impact of perfobond steel plate thickness on the shear force in the perforation and the contribution of the penetrating rebar. Conversely, Nakajima and Nguyen's formula highlights that increasing steel plate thickness reduces shear force but enhances the dowel effect. The observed trend in Fig. 12(d) aligns with Nakajima and Nguyen's study and emphasizes the importance of steel plate thickness.

Concrete block width consistently influences confined effects around the PBL, enhancing shear stress on two shear surfaces. This effect is neglected in Equations (1) to (7) but considered in Equation (8), making Nakajima and Nguyen's formula more correlated with the experimental data.

In summary, the parametric study aligns with the shear-resisting mechanism explained in Sections 2 and 3.1, confirming the reliability of the proposed machine learning-based model for a large experimental dataset, both statistically and in terms of the PBL's shear-resisting mechanism.

7. Conclusions

This study aims to develop a comprehensive prediction model for the shear capacity of PBL connectors using an optimized neural network. The research conducted a thorough investigation and meticulous data collection to create a dataset of 253 specimens from various sources, including 136 contributed by the authors, which is more than any other previous study. Based on this extensive dataset, the research systematically examined the shear-resisting mechanism of the perfobond strip and critically analyzed eight existing empirical formulas. This helps engineers gain a more comprehensive and deeper understanding of the shear resistance mechanism of the perfobond strip, as well as the strengths and limitations of the existing design formulas. The comparative analysis revealed inherent limitations in existing formulas, attributing their diminished correlation with experimental values to the challenges posed by a limited dataset and the complexity of incorporating all influencing factors through conventional statistical methods.

While most previous studies have only proposed prediction models for the shear capacity under specific experimental conditions, including certain shapes and sizes of the specimens, the novelty of this study lies in developing a model that can predict the shear capacity of PBL connectors under more comprehensive working conditions, such as with or without penetrating rebar in the perforations, using normal or fiber-reinforced concrete, and especially for different shapes and dimensions of test specimens. To achieve this objective, a feature selection analysis identified 12 input parameters and found that perforation diameter, block width, specimen type, and PBL thickness are significant contributors to the shear capacity of PBL connectors. Employing the Bayesian optimization algorithm, an optimized ANN model with a two-layer architecture demonstrated exceptional predictive performance, attaining an impressive R^2 value of 0.949 on a separate test set. This result demonstrates superiority over most existing prediction models, especially since this model can also predict the shear capacity of the perfobond strip with a more comprehensive range of applications.

The parametric study results consistently aligned with the shear-resisting mechanism of PBL, reinforcing the credibility and applicability of the proposed machine learning-based model across a broad experimental dataset. In light of these findings, this study not only advances the understanding of PBL connector behavior but also contributes a comprehensive prediction model with practical implications. This model stands poised for integration into engineering practices, offering a valuable tool for optimizing the design and analysis of concrete structures.

References

[1] X. Zeng, S.-F. Jiang, and D. Zhou, "Effect of shear connector layout on the behavior of steel-concrete composite beams with interface slip," *Applied Sciences*, vol. 9, no. 1, p. 207, 2019.

[2] Z. Fang, H. Fang, J. Huang, H. Jiang, and G. Chen, "Static behavior of grouped stud shear connectors in steel–precast UHPC composite structures containing thin full-depth slabs," *Engineering Structures*, vol. 252, p. 113484, 2022.

[3] A. El-Zohairy, H. Salim, and H. Shaaban, "Experimental investigation on fatigue behavior of composite beams with different studs arrangements," in *Structures*, 2022, vol. 35: Elsevier, pp. 146-159.

[4] F. Leonhardt, W. Andrä, H. P. Andrä, and W. Harre, "Neues, vorteilhaftes Verbundmittel für Stahlverbund-Tragwerke mit hoher Dauerfestigkeit," *Beton-und Stahlbetonbau,* vol. 82, no. 12, pp. 325-331, 1987.

[5] Y. Xu, X. Liu, B. Wang, and X. Yi, "Residual mechanical properties of composite beams with PBL connectors under fatigue loads," in *Structures*, 2023, vol. 51: Elsevier, pp. 185-195.

[6] J. He *et al.*, "The development of composite bridges with corrugated steel webs in China," in *Proceedings of the Institution of Civil Engineers-Bridge Engineering*, 2021, vol. 174, no. 1: Thomas Telford Ltd, pp. 28-44.

[7] W. Changyu, Y. Shiping, W. Boxue, D. Jianhua, R. Xiaoping, and Z. Xiaoliang, "Research on the transverse flexural performance of T-PBL joints between corrugated steel webs and concrete slabs," in *Structures*, 2022, vol. 44: Elsevier, pp. 1057-1069.

[8] G. Németh, B. Jáger, B. Kövesdi, and N. Kovács, "Experimental investigation of steel-concrete composite push-out tests with embedded corrugated web," *Advances in Structural Engineering*, vol. 25, no. 11, pp. 2332-2347, 2022.

[9] J. Machacek and M. Cudejko, "Composite steel and concrete bridge trusses," *Engineering Structures*, vol. 33, no. 12, pp. 3136-3142, 2011.

[10] H.-Y. Kim and Y.-J. Jeong, "Experimental investigation on behaviour of steel–concrete composite bridge decks with perfobond ribs," *Journal of Constructional Steel Research*, vol. 62, no. 5, pp. 463-471, 2006.

[11] R. Xiao, C. Song, B. Sun, R. Guo, and H. Chen, "Design and experimental study of a replaceable steel-UHPC composite bridge deck," in *Structures*, 2022, vol. 40: Elsevier, pp. 1107-1120.

[12] Y. Shan, Y. Chen, Z. Zong, L. Liu, J. Li, and Z. Li, "Flexural behavior of different types of steel-concrete composite decks with perfobond rib or head stud shear connectors," *Advances in Structural Engineering*, vol. 26, no. 7, pp. 1187-1208, 2023.

[13] C. Liang, Y. Liu, and Y. Liu, "An orthogonal component method for steel girder-concrete abutment connections in integral abutment bridges," *Journal of Constructional Steel Research*, vol. 180, p. 106604, 2021.

[14] S. Liu, X. Ding, X. Li, Y. Liu, and S. Zhao, "Behavior of rectangular-sectional steel tubular columns filled with high-strength steel fiber reinforced concrete under axial compression," *Materials*, vol. 12, no. 17, p. 2716, 2019.

[15] B. Shangguan, Q. Su, J. R. Casas, H. Su, S. Wang, and R. Zhao, "Modeling and Testing of a Composite Steel–Concrete Joint for Hybrid Girder Bridges," *Materials*, vol. 16, no. 8, p. 3265, 2023.

[16] J. Leng, J. Yang, Z. Zhang, Y. Zou, J. Chen, and J. Zhou, "Experimental and numerical investigations on force transfer mechanism of steel-concrete joint in hybrid girder bridges," in *Structures*, 2023, vol. 54: Elsevier, pp. 153-170.

[17] M. H. Nguyen, A. Nakajima, S. Fujiwara, R. Obata, S. Fujikura, and Y. Hirano, "Bending Test of Joint Structure of Precast PC Slab Using Perfobond Strip and its Corresponding Element Test," *Journal of Japan Society of Civil Engineers, Ser. A1 (Structural Engineering & Earthquake Engineering (SE/EE))*, vol. 76, no. 5, pp. II_17-II_28, 2020.

[18] N. M. Hai, S. Fujikura, A. Nakajima, and H. N. Phan, "Experimental investigation on flexural behavior of a precast slab joint with perfobond strips and steel fiber-reinforced mortars," in *Structures*, 2022, vol. 39: Elsevier, pp. 278-292.

[19] K. Aoki, K. Uehira, Y. Tanaka, and K. Takagi, "Development of new joint method for precast railing," in *Proc 9th Symp Res Appl Hybrid Comp Struct*, 2011, pp. 1-8.

[20] Y. Sato and Y. Nishimura, "Shear failure behavior of perfobond rib under shear force at single fracture surface," *Proc Jap Concrete Inst*, vol. 31, pp. 1171-1176, 2009.

[21] N. M. Hai, A. Nakajima, S. Fujikura, T. Murayama, and M. Mori, "Shear behavior of a perfobond strip with steel fiber-reinforced mortar in a condition without surrounding reinforcements," *Materials and Structures*, vol. 53, pp. 1-15, 2020.

[22] E. Oguejiofor and M. Hosain, "Numerical analysis of push-out specimens with perfobond rib connectors," *Computers & structures*, vol. 62, no. 4, pp. 617-624, 1997.

[23] J.-H. Ahn, C.-G. Lee, J.-H. Won, and S.-H. Kim, "Shear resistance of the perfobond-rib shear connector depending on concrete strength and rib arrangement," *Journal of Constructional Steel Research*, vol. 66, no. 10, pp. 1295-1307, 2010.

[24] S. He, Z. Fang, and A. S. Mosallam, "Push-out tests for perfobond strip connectors with UHPC grout in the joints of steel-concrete hybrid bridge girders," *Engineering Structures*, vol. 135, pp. 177-190, 2017.

[25] X. Tan, Z. Fang, and X. Xiong, "Experimental study on group effect of perfobond strip connectors encased in UHPC," *Engineering Structures*, vol. 250, p. 113424, 2022.

[26] G. Ji, E. Zhu, B. Wang, C. Zhu, and S. Li, "Bearing capacity analysis of perfobond rib shear connectors in steel-concrete composite structures," in *Structures*, 2023, vol. 57: Elsevier, p. 105292.

[27] Z. Wang, Q. Li, and C. Zhao, "Ultimate shear resistance of perfobond rib shear connectors based on a modified push-out test," *Advances in Structural Engineering*, vol. 16, no. 4, pp. 667-680, 2013.

[28] S.-H. Kim, J.-H. Ahn, K.-T. Choi, and C.-Y. Jung, "Experimental evaluation of the shear resistance of corrugated perfobond rib shear connections," *Advances in Structural Engineering*, vol. 14, no. 2, pp. 249-263, 2011.

[29] A. Nakajima, S. Koseki, M. Hashimoto, Y. Suzuki, and M. H. Nguyen, "Evaluation of shear resistance of perfobond strip based on simple push-out test," *Journal of Japan Society of Civil Engineers, Ser. A1 (Structural Engineering & Earthquake Engineering (SE/EE))*, vol. 68, no. 2, pp. 495-508, 2012.

[30] Z. Chen, "Experimental study of shear capacity of perfobond connector," *Engineering Meachnics*, vol. 29, no. 12, pp. 349-354, 2012.

[31] *Standard specifications for hybrid structures*, JSCE, 2015.

[32] S. He, Z. Fang, Y. Fang, M. Liu, L. Liu, and A. S. Mosallam, "Experimental study on perfobond strip connector in steel–concrete joints of hybrid bridges," *Journal of Constructional Steel Research*, vol. 118, pp. 169-179, 2016.

[33] S. Zheng, Y. Liu, T. Yoda, and W. Lin, "Parametric study on shear capacity of circular-hole and long-hole perfobond shear connector," *Journal of Constructional Steel Research*, vol. 117, pp. 64-80, 2016.

[34] A. Nakajima, M. Hashimoto, M. Nguyen, and Y. Suzuki, "Shear resisting mechanism and shear resistance evaluation of perfobond strip without penetrating rebar," *Journal of Japan Society of Civil Engineers, Ser. A1 (Structural Engineering)*, 2014.

[35] A. NAKAJIMA and M. H. NGUYEN, "Strain behavior of penetrating rebar in perfobond strip and its evaluation of shear resistance," *Journal of JSCE*, vol. 4, no. 1, pp. 1-18, 2016.

[36] M. H. Nguyen, Y. Hirano, A. Nakajima, S. Fujikura, and R. Niimura, "Experimental evaluation of the shear capacity of perfobond strips with steel fiber-reinforced mortar in narrow joint structures," in *Structures*, 2020, vol. 28: Elsevier, pp. 1173-1186.

[37] H.-T. Thai, "Machine learning for structural engineering: A state-of-the-art review," in *Structures*, 2022, vol. 38: Elsevier, pp. 448-491.

[38] H. Allahyari, I. M. Nikbin, S. Rahimi, and A. Heidarpour, "A new approach to determine strength of Perfobond rib shear connector in steel-concrete composite structures by employing neural network," *Engineering Structures*, vol. 157, pp. 235-249, 2018.

[39] G. Sun, J. Shi, and Y. Deng, "Predicting the capacity of perfobond rib shear connector using an ANN model and GSA method," *Frontiers of Structural and Civil Engineering*, vol. 16, no. 10, pp. 1233-1248, 2022.

[40] M. Nguyen, A. Nakajima, N. Takahashi, M. Mizutori, M. Ono, and S. Fujikura, "Revaluation of shear resistance of perfobond strip considering difference of rib plate and concrete block arrangement," ed: J Jap Soc Civil Eng Ser. A1 (Struct Eng Earthquake Eng (SE/EE)), 2018, pp. 22-27.

[41] K. Nishiumi and M. Okimoto, "Shear strength of perfobond rib shear connector under the confinement," *Doboku Gakkai Ronbunshu*, vol. 1999, no. 633, pp. 193-203, 1999.

[42] U. Yoshitaka, H. Tetsuya, and M. Kaoru, "An experimental study on shear characteristics of perfobond strip and its rational strength equations," in *International symposium on*

connections between steel and concrete, 2001: RILEM Publications SARL, pp. 1066-1075.
[43] T. Hosaka, K. Mitsuki, H. Hiragi, Y. Ushijima, Y. Tachibana, and H. Watanabe, "An experimental study on shear characteristics of perfobond strip and its rational strength equations," *J. Struct. Eng. JSCE*, vol. 46A, pp. 1593–1604, 2000.
[44] H. Furuuchi, T. Ueda, O. Suzuki, and H. Taguchi, "A study on shear transfer capacity of perfobond strip," in *Proceedings of the 6th Symposium on Research and Application of Hybrid and Composite Structure*, 2005, no. 26, pp. 1-8.
[45] K. Fujii, H. Iwasaki, K. Fukada, T. Toyota, and N. Fujimura, "Crack restraint factors in ultimate slip behavior of perfobond strip," *Journal of Japan Society of Civil Engineers, Ser. A*, vol. 64, no. 2, pp. 502-512, 2008.
[46] K. Fujii, Y. Dokan, H. Iwasaki, M. Himukai, K. Mori, and S. Yamaguchi, "Ultimate shear strength of perfobond strip," *J. Jpn. Soc. Civ. Eng. Ser A*, vol. 1, p. 2014, 2014.
[47] Q.-T. Su, W. Wang, H.-W. Luan, and G.-T. Yang, "Experimental research on bearing mechanism of perfobond rib shear connectors," *Journal of Constructional Steel Research*, vol. 95, pp. 22-31, 2014.
[48] S. Guo, S. Hino, K. Yamaguchi, J. Choi, and T. Sonoda, "Bending behavior of steel-concrete composite girder with perfobond shear connector using super-light weight concrete with steel fiber reinforcement," 2008.
[49] R. Yamaguchi, "The push-out test of perfobond strip using high performance concrete," presented at the 8th Symp. Res. Appl. Hybrid Comp. Struct., 2009, 54.
[50] T. Yamada *et al.*, "Experimental study on the mechanical behavior of perfobond rib shear connectors in the rigid connection of a steel-concrete composite portal rigid frame bridge," presented at the 10th Symp. Res. Appl. Hybrid Comp. Struct. , 2013, 59.
[51] I. Norimatsu, T. Tanaka, J. Sakai, and A. Kawano, "Experimental study on mechanical behavior of various kind of shear connectors under constant axial force," presented at the 10th Symp. Res. Appl. Hybrid Comp. Struct., 2013, 20.
[52] T. Ebina, Y. Kutsuna, H. Tategami, and K. Sonoda, "Experimental study on the pull-out resistance of the perfobond rib with flask-shaped steel plate," presented at the Jap. Concr. Ins., 2004.
[53] Y. Taira, K. Furuichi, M. Yamamura, and T. Tominaga, "Experimental Study on Characteristics of Shear Connector using Perforated Plate," presented at the Jap. Concr. Ins., 1998.
[54] C. Ding and H. Peng, "Minimum redundancy feature selection from microarray gene expression data," *Journal of bioinformatics and computational biology*, vol. 3, no. 02, pp. 185-205, 2005.
[55] P. Liashchynskyi and P. Liashchynskyi, "Grid search, random search, genetic algorithm: a big comparison for NAS," *arXiv preprint arXiv:1912.06059*, 2019.
[56] J. Snoek, H. Larochelle, and R. P. Adams, "Practical bayesian optimization of machine learning algorithms," *Advances in neural information processing systems*, vol. 25, 2012.
[57] X. Glorot and Y. Bengio, "Understanding the difficulty of training deep feedforward neural networks," in *Proceedings of the thirteenth international conference on artificial intelligence and statistics*, 2010: JMLR Workshop and Conference Proceedings, pp. 249-256.
[58] K. He, X. Zhang, S. Ren, and J. Sun, "Delving deep into rectifiers: Surpassing human-level performance on imagenet classification," in *Proceedings of the IEEE international conference on computer vision*, 2015, pp. 1026-1034.
[59] T. Fushiki, "Estimation of prediction error by using K-fold cross-validation," *Statistics and Computing*, vol. 21, pp. 137-146, 2011.

Advanced Steel Construction – Vol. 20 No. 4 (2024) 385–396
DOI: 10.18057/IJASC.2024.20.4.6

RESEARCH ON DATA-DRIVEN INTELLIGENT DESIGN METHOD FOR ENERGY DISSIPATOR OF FLEXIBLE PROTECTION SYSTEMS

Ze-Huan He [1], Zhi-Xiang Yu [1, 2, *], Lin-Xu Liao [1] , Yang-Feng Lyu [1] and Yong-Ding Tian [1]

[1] *School of Civil Engineering, Southwest Jiaotong University, Chengdu, China*
[2] *National Engineering Laboratory for Prevention and Control of Geological Disasters in Land Transportation, Chengdu, China*
** (Corresponding author: E-mail: yzxswjtu@163.com)*

ABSTRACT

The brake ring, an essential buffer and energy dissipator within flexible protection systems for mitigating dynamic impacts from rockfall collapses, presents notable design challenges due to its significant deformation and strain characteristics. This study introduces a highly efficient and precise neural network model tailored for the design of brake rings, utilizing BP neural networks in conjunction with Particle Swarm Optimization (PSO) algorithms. The paper studies the key geometric parameters, including ring diameter, tube diameter, wall thickness, and aluminum sleeve length, with performance objectives centered on starting load, maximum load, and energy dissipation. A comprehensive dataset comprising 576 samples was generated through the integration of full-scale tests and simulations, which facilitated the training of the neural network for accurate forward predictions linking physical parameters to performance outcomes. Furthermore, a PSO-based reverse design model was developed to enable effective back-calculation from desired performance outcomes to specific geometric configurations. The BP neural network exhibited high accuracy, evidenced by a fit of 0.991, and the mechanical performance of the designed products aligned with target values in over 90% of cases, with all engineering errors remaining within acceptable limits. The proposed method significantly reduces the design time to under 5 seconds, thereby vastly improving efficiency in comparison to traditional approaches. This advancement offers a rapid and reliable reference for the design of critical components in flexible protection systems.

ARTICLE HISTORY

Received: 10 March 2024
Revised: 9 August 2024
Accepted: 5 September 2024

KEYWORDS

Flexible protective systems;
Energy dissipator;
Brake ring;
Data-driven;
Intelligent design

1. Introduction

Flexible protection systems are widely used in rockfall protection projects along transportation routes [1-3], with the energy dissipator serving as a critical component. When subjected to dynamic impacts, the energy dissipator is activated by the high tension in the ropes, functioning similarly to the hydraulic buffering devices in aircraft carrier arresting systems. Its simplicity and efficiency make it an indispensable part of flexible protection systems. Muraishi et al.[4] demonstrated that energy dissipators could enhance the protective performance of flexible protection systems by more than threefold, with the contribution ratio of energy dissipators to the performance of flexible protection systems exceeding 60%. Therefore, energy dissipators are essential for flexible protection systems under strong impacts, making their proper design crucial for protection success. Currently, brake rings are commonly used as energy dissipators in flexible protection systems. They consist mainly of circular steel tubes and aluminum sleeves (see Fig. 1). When the wire ropes pass through these tubes and are pulled tight, they cause them to bend and deform, creating an energy-absorbing mechanism that enhances the system's protective performance (see Fig. 2).

Numerous scholars have extensively researched various forms to advance the scientific design of energy dissipators. Fresno et al.[5] performed mechanical experiments on double U-shaped energy dissipators, exploring their energy absorption capabilities and conducting finite element analysis. Their findings suggest that these energy dissipators exhibit enhanced energy absorption under asymmetric tensile loads at a 2/3 ratio. Lamber et al.[6] investigated a novel tubular buckling energy dissipator through model tests and numerical simulations. They discovered this new dissipator type is more effective and exhibits greater energy absorption than friction-type dissipators. J.J.Del Coz Díaz et al.[7] used numerical simulations and model experiments to study the mechanical behavior of U-shaped ring energy dissipators. They identified that the failure mode was due to the compression damage of the aluminum sleeves. Castanon-Jano et al.[8] systematically analyzed the roles and mechanical behaviors of various energy dissipators in flexible protection systems. Qi Xin et al.[9] conducted drop-weight impact dynamic tests on brake rings and proposed a four-stage mechanical model under dynamic loads. The aforementioned studies have revealed the quasi-static and dynamic mechanisms of various energy dissipators. They have identified key parameters affecting mechanical performance and addressed challenges in simulating large deformations, geometric nonlinearity, and material nonlinearity. These insights provide a solid foundation for designing energy dissipators. However, existing design methods are limited by high experimental costs and complex theoretical calculations, hindering the practical application of energy dissipators. A fast and precise design method has long been lacking in engineering.

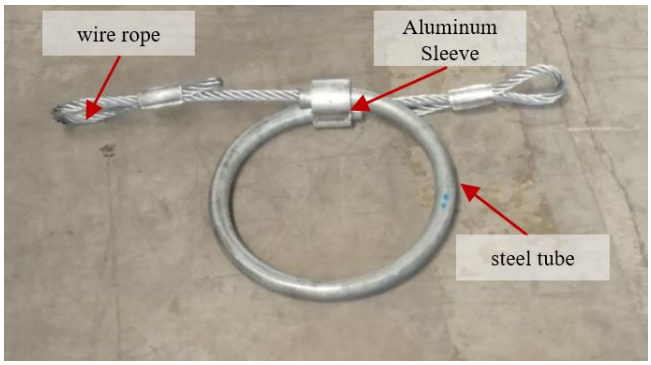

Fig. 1 The brake ring

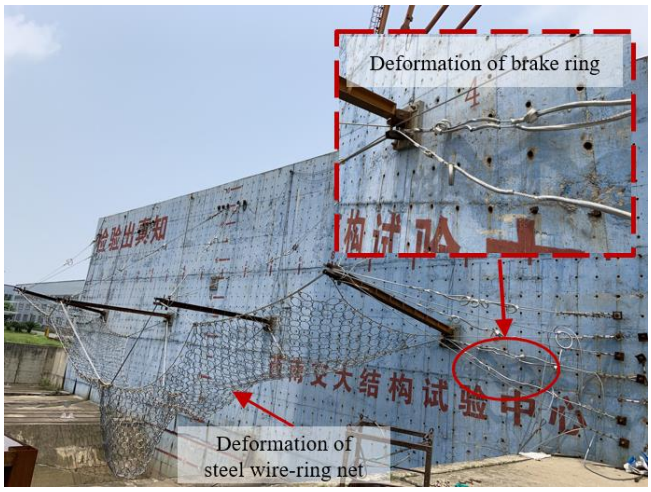

Fig. 2 Deformation of flexible protection systems by impact

The application of artificial intelligence (AI) technology in structural engineering design has witnessed a significant surge in recent years, thus emerging as a prominent area of research focus[10-15]. The AI algorithms, with their self-learning and parallel processing capabilities, effectively establish mathematical models linking complex input parameters to design outcomes.

This approach circumvents the decoupled calculations of complex engineering mechanics [16-18], freeing engineers from intricate computations and enabling efficient, accurate designs. Among various AI algorithms, the backpropagation (BP) neural network stands out for its ability to automatically optimize models through the backpropagation algorithm, requiring only the forward process to be differentiable. Ma Gao et al.[19] used a BP neural network to predict the compressive strength of CFRP-confined concrete. The number of data points with an error within 15% was increased by 20% compared to traditional statistical regression. Zhou Zhong et al.[20] successfully used a BP neural network optimized with Particle Swarm Optimization (PSO) to predict the turbidity levels of wastewater from tunnel construction processes.

In the field of flexible protection engineering, LIAO et al.[21] have pioneered the application of neural networks, developing an intelligent computational method that achieves complex nonlinear mapping between system performance and structural components. Given the strong non-linear characteristics of flexible protection engineering, neural networks offer a more efficient and comprehensible means to map the intricate relationships between protection performance and various structural parameters [22,23]. Despite these advancements, intelligent design methods for both individual components and entire flexible protection systems remain largely unexplored. Therefore, researching intelligent design methods for flexible protection engineering is crucial for developing precise and efficient protection solutions.

Consequently, this paper centers on energy dissipators in flexible protection systems, providing a theoretical analysis of their contribution to the system and the influence of their structural parameters on protection performance. In practical application, this study integrates finite element analysis with intelligent algorithms, employing LS-DYNA software for simulations and analyzing data using BP neural networks and particle swarm optimization (PSO) algorithms. A novel data-driven energy dissipator design method was developed, validated through physical testing to enhance design precision and efficiency. Compared to traditional methods, the proposed approach offers high efficiency and automation. The comprehensive process comparison illustrated in Fig. 3.

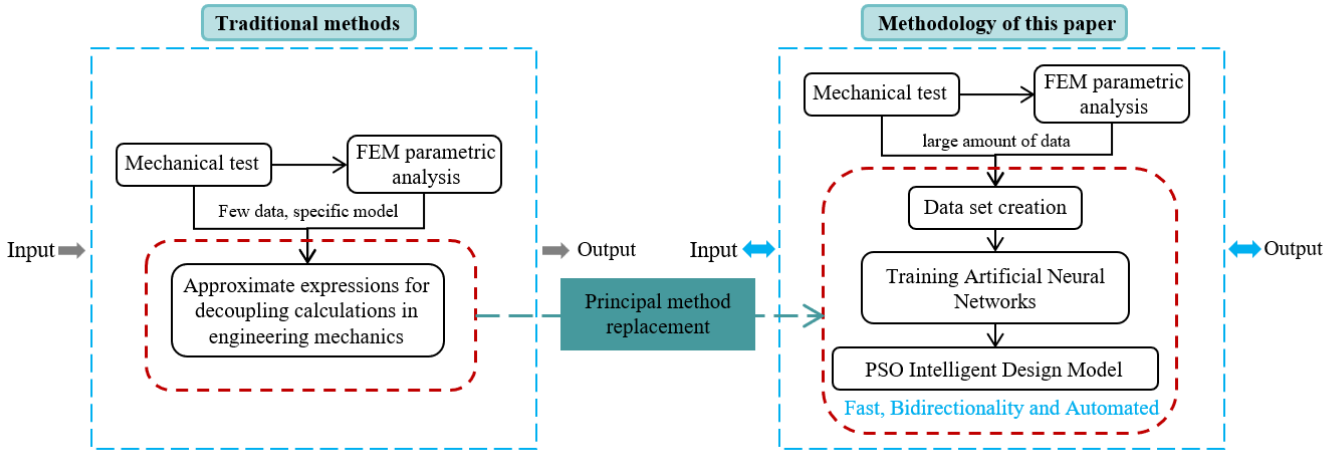

Fig. 3 Comparison of technical approaches

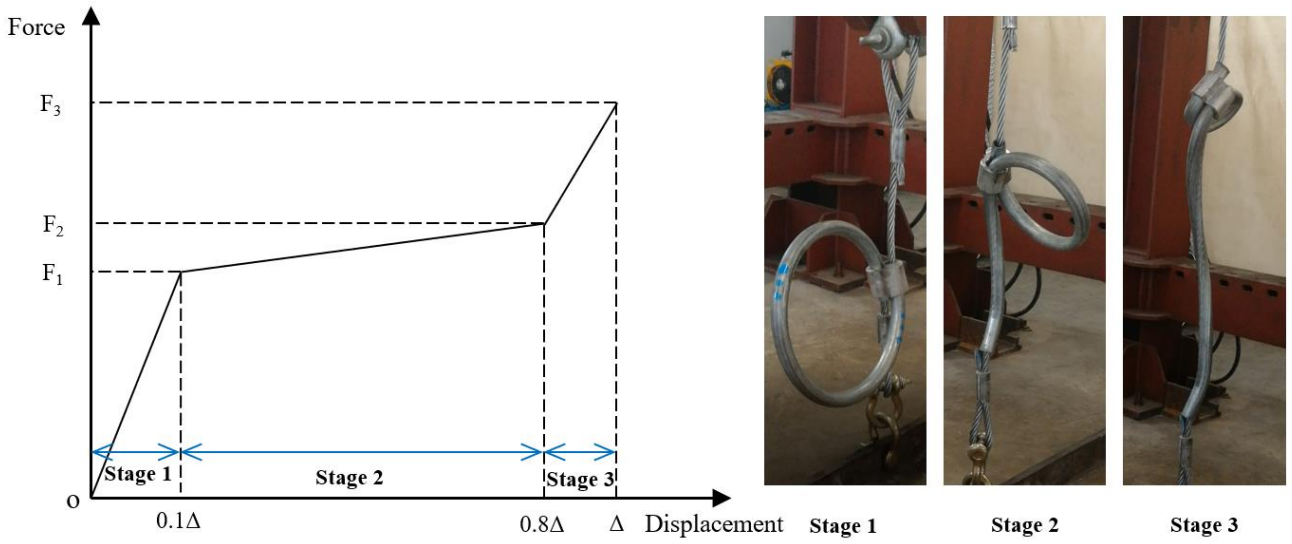

Fig. 4 The Trilinear model of the load-displacement curve and its corresponding stage deformation of brake ring

2. Data set creation

2.1. Principle of brake ring operation

When the system impacts, the rope experiences high tension, which activates the brake ring. Despite variations in construction, different types of energy dissipators generally absorb energy through friction and plastic deformation. For instance, the brake ring's working phase primarily involves the bending-straightening deformation of the steel tube and the sliding friction deformation through the aluminum sleeve, collectively forming a pseudo-plastic P-D mechanism. When the steel tube stretches to its maximum length, the brake ring will strengthen and eventually break. In practical engineering, the effective sliding distance Δ is typically considered to be 0.7 times the circumference of the brake ring. The energy absorption process of the brake ring can be divided into three distinct stages. Phase One: The tensile force of the steel wire rope rapidly increases, overcoming the friction between the aluminum sleeve and the steel tube. During this phase, minimal displacement occurs as static friction is overcome, with corresponding displacement at 0-0.1Δ. Phase Two: The tensile force of the steel wire rope overcomes static friction, causing relative displacement between the steel tube and the aluminum sleeve. Overcoming static friction results in a sudden drop in the load. As the relative displacement progresses, the diameter of the brake ring gradually decreases,

while the stiffness and constraining ability of the aluminum sleeve increase, causing a slow increase in load, with corresponding displacement at 0.1-0.8Δ. Phase Three: When the brake ring contracts to a certain extent, the steel tube undergoes torsional deformation, increasing the contact force between the aluminum sleeve and the steel tube. This leads to a significant increase in load during the final phase, with displacement increasing slowly until failure occurs, corresponding to a displacement of 0.8-1Δ (see Fig. 4).

The main factors influencing friction energy dissipation include the compression force P_t during deformation, the dynamic friction coefficient μ, the length of the aluminum sleeve L, the diameter of the steel tube ring D, and the diameter of the steel tube d. The specific geometric parameters are depicted in Fig. 5.

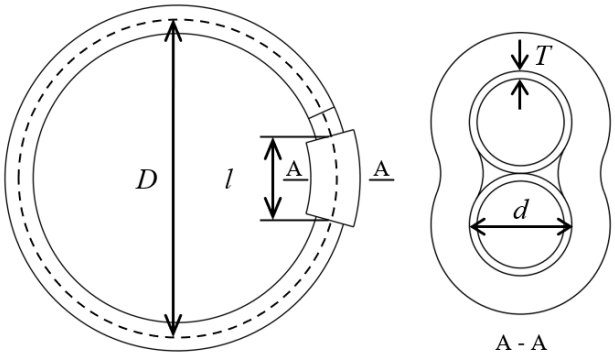

Fig. 5 Structural parameters of the brake ring

As the dynamic friction coefficient μ remains constant, the compressive force during deformation is primarily determined by the dimensions of the steel tube and the aluminum sleeve. Therefore, the friction energy dissipation W_1 can be represented as a function related to time t:

$$W_1 = f(P_t, L, D, d, T, t) \tag{1}$$

In the deformation energy dissipation phase, the steel tube experiences bending and straightening deformation. The primary factors influencing this process are the wall thickness T and the diameter d of the steel tube. Consequently, the deformation energy dissipation W_2 can be described as a function of time t:

$$W_2 = g(T, d, t) \tag{2}$$

In conclusion, the total energy dissipation W of the brake ring can be expressed as:

$$W = W_1 + W_2 = f(P_t, L, D, d, T, t) + g(T, d, t) \tag{3}$$

From the above equation, the primary factors influencing the protective performance of the brake ring, considering its structural dimensions, are the ring diameter D, tube diameter d, steel tube wall thickness T, and length of the aluminum sleeve L.

2.2. Calibration of numerical models

The elongation process of the brake ring exhibits large deformation effects and involves complex forces, addressing issues of geometric and material nonlinearity. This paper employs the numerical simulation method for brake rings using LS-DYNA, as applied in several studies[24-26].

In the numerical simulation, the aluminum sleeve is modeled using solid elements with the default single-point integration algorithm. The steel tube is modeled using shell elements with the default Belytschko-Tsay single-point integration algorithm. The wire rope, subjected only to axial loads during tension and not to bending moment loads, is modeled using beam elements with the truss integration algorithm.

During the deformation of the brake ring, there is a complex contact relationship between the steel tube, aluminum sleeve, and wire rope. In LS-DYNA software, automatic surface-to-surface contact is used to account for all possible contact surfaces between different parts. This approach significantly aids in calculating the large deformations of the brake ring and enhances computational accuracy. The static and dynamic friction coefficients between steel tubes and wire ropes are 0.15 and 0.1, respectively, while those between steel tubes and aluminum sleeves are 0.18 and 0.15, respectively.

In selecting material models, an elastic material model is used for the wire rope, which often remains in the elastic stage. In contrast, elastoplastic material models are applied for the aluminum sleeve and steel tube, which undergo significant plastic strain during deformation. During the calculation process, the effects of the material hardening stage are not considered. The tangent modulus for both the steel tube and aluminum sleeve is assumed to be zero.

When the brake ring stretches at a lower speed, numerical calculations closely match the mechanical test results[11]. Considering the relevant brake ring experiments and computation time, a loading speed of 5 m/s is adopted to simulate the mechanical testing process.

Table 1 shows the material model parameters used in the calibration model for the numerical simulation. The geometric dimensions of the brake ring used in the numerical simulation calibration are: ring diameter 450 mm, tube diameter 25 mm, tube wall thickness 2.5 mm, aluminum sleeve length 60 mm, and sleeve thickness 15 mm.

Fig. 6 compares the load-displacement curves between the numerical simulation and test results. The errors for the three mechanical properties of the brake ring between the numerical simulation and test results were 9.0%, 3.7%, and 2.6%, respectively, all within the acceptable range for engineering applications. Table 2 presents the error analysis of the numerical simulation and experimental results. Following the calibration of the numerical model, parameter analysis is performed based on four influencing factors of the brake ring's structural dimensions: ring diameter D, tube diameter d, wall thickness T, and aluminum sleeve length L. Based on the calibrated model, sixteen different analysis models numbered E1 to E16 are established, with their specific parameters and performances summarized in Table 3.

Table 1
Parameters of material mechanical properties

Component	Elastic modulus (GPa)	Density (kg·m^{-3})	Yield strength (MPa)	Poisson's ratio	limit strain
Steel tube	210	7850	300	0.3	0.38
Aluminum sleeve	70	2700	235	0.3	--
wire rope	112	7850	1082	0.3	--

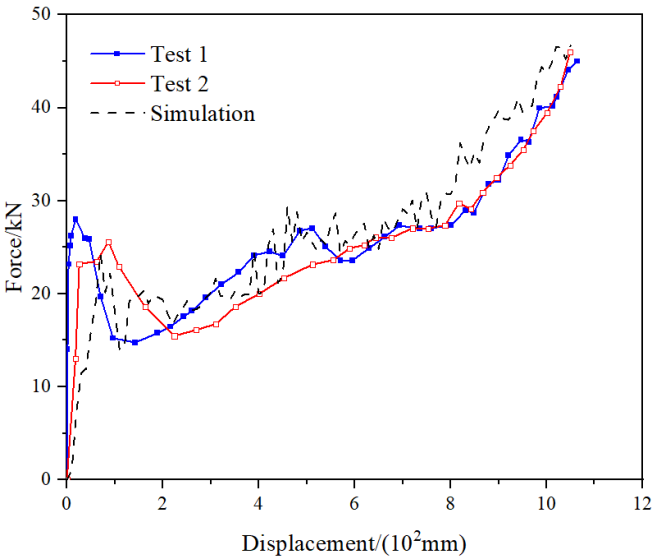

Fig. 6 Load-displacement curves from mechanical tests and numerical simulation of brake ring[24]

Table 2
Analysis of mechanical test and numerical simulation results of brake ring

Item	Starting load F_1	Maximum load F_3	Energy dissipation E
Test 1	28.0	27.3	45.0
Test 2	25.4	26.0	46.0
Test Average	26.7	26.7	45.5
Simulation	24.3	27.7	46.7
error	-9.0%	3.7%	2.6%

2.3. Effect of ring diameter on the performance of brake ring

The ring diameter *D* determines the the maximum displacement stroke of the brake ring and influences the friction and deformation energy consumption of the steel tube. Fig. 7 illustrates the load-displacement curves for four different steel tube diameter models, E1 to E4.

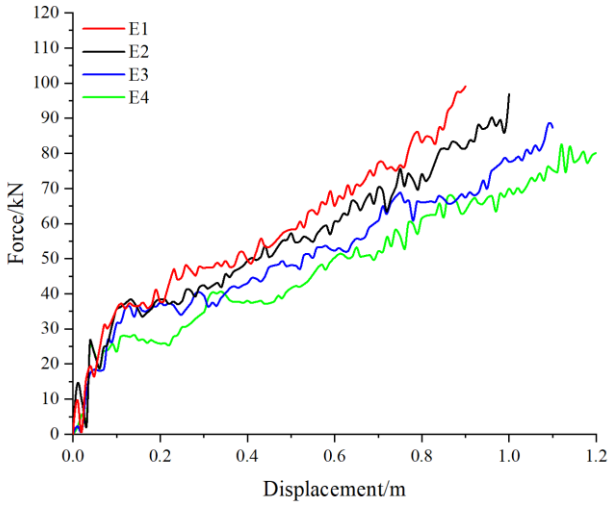

Fig. 7 Load-displacement curves of brake ring with different ring diameters

As shown in Fig. 7, within the effective displacement range, brake rings with smaller diameters *D* exhibit a more distinct three-phase trend in the load-displacement curve. For the two larger ring diameters, the third-phase trend is less distinct and resembles the slope of the second phase. Table 3 indicates that as the ring diameter increases, the starting load and maximum load decrease, while the energy dissipation slightly increases. These results suggest that increasing the diameter of the brake ring increases the effective displacement stroke but reduces the stiffness, leading to a reduction in load. Since the effective displacement is 0.7 times the circumference, larger ring diameters result in more redundant displacement, leading to less pronounced constraints in the third phase and a less evident rapid load increase.

2.4. Effect of tube diameter on the performance of brake ring

The tube diameter *d* of the steel pipe determines the contact area with the aluminum sleeve and the stiffness of the cross-section, impacting friction and deformation energy dissipation. Fig. 8 illustrates the load-displacement curves for six models with different tube diameters: E2 and E5-E9.

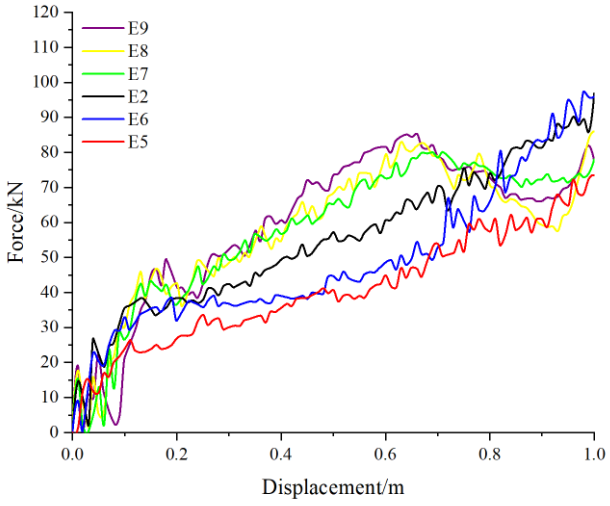

Fig. 8 Load-displacement curves of brake ring with different tube diameters

As shown in Fig. 8, within the effective displacement range, smaller tube diameters display a clear three-phase characteristic in the load-displacement curve. With increasing tube diameter, the load-displacement curve's second phase exhibits a 'bulging' phenomenon, where the load initially increases and then decreases. As shown in Table 3, with an increase in the steel tube's diameter, the contact area with the aluminum sleeve expands, the starting load rises, and energy dissipation increases from 40.8kJ to 59.4kJ, marking a 45.6% rise. For larger tube diameters, the steel tube is more severely flattened in the second phase, leading to a greater reduction in stiffness. Consequently, the load decreases, forming a convex curve. These results indicate that while increasing the tube diameter significantly enhances the brake ring's starting load and energy dissipation capacity, an excessively large diameter causes the convex curve phenomenon, lacking a distinct three-phase characteristic.

2.5. Effect of wall thickness on the performance of brake ring

The wall thickness of the steel tube influences its cross-sectional stiffness and the amount of energy dissipated through deformation. Fig. 9 illustrates the load-displacement curves of four models with different steel tube wall thicknesses, E2 and E10-E12.

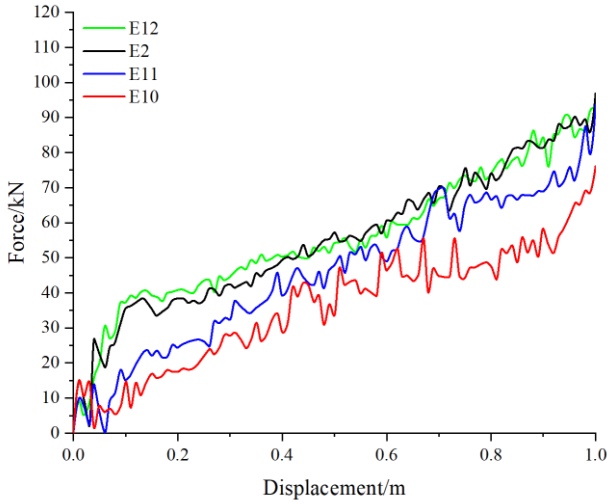

Fig. 9 Load-displacement curves of brake ring with different wall thickness

As shown in Fig. 9, the load-displacement curves of the two models with thinner walls clearly exhibit three distinct phases. For models with thicker steel tube walls, the increased sectional stiffness results in more pronounced aluminum sleeve deformation in the later stages. This reduces the aluminum sleeve's ability to restrain the steel tube during the third phase, leading to the absence of a clear third phase in the load-displacement curve. Results in Table 3 indicate that increasing the wall thickness of the steel tube significantly raises the starting load, maximum load, and energy dissipation. When the wall thickness increases from 2mm to 5mm, the starting load, maximum load, and energy dissipation rise by 140.2%, 20.9%, and 53.7%, respectively. These results demonstrate that increasing the wall thickness of the steel tube significantly enhances the brake ring's energy dissipation capacity.

2.6. Effect of aluminum sleeve length on the performance of brake ring

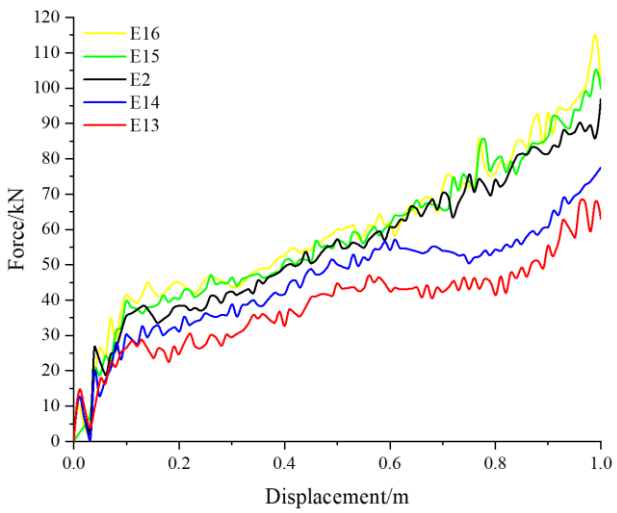

Fig. 10 Load-displacement curves of brake ring with different aluminum sleeve lengths

The length of the aluminum sleeve determines the contact area between the

steel tube and the aluminum sleeve and its ability to constrain the steel tube, thereby influencing the brake ring's friction and energy dissipation. The load-displacement curves for five models with varying aluminum sleeve lengths (E2, E13-E16) are shown in Fig. 10.

Fig. 10 shows that the load-displacement curve of the brake ring generally follows a three-phase change pattern. Longer aluminum sleeves exert stronger constraints on the steel tube, enabling earlier restraint during displacement compared to shorter sleeves. Therefore, the three models with longer aluminum sleeves exhibit weaker third-phase characteristics compared to the two models with shorter sleeves. Table 3 shows that the starting load, maximum load, and energy dissipation significantly increase with the length of the aluminum sleeve. However, for aluminum sleeve lengths within the range of 50-80mm, changes in the brake ring's starting load, maximum load, and energy dissipation are more pronounced. Beyond 80mm, the performance of the brake ring shows little change.

Table 3
Partial data set input and output parameters

Model	Variables	Brake ring dimensions				Mechanical properties		
		D(mm)	d(mm)	T(mm)	L(mm)	F_1(kN)	F_3(kN)	E(kJ)
E1	Ring diameter D	400	36	4	80	37.2	99.1	50.7
E2		450	36	4	80	38.3	96.8	55.0
E3		500	36	4	80	36.4	88.3	56.7
E4		550	36	4	80	28.0	82.5	58.3
E5	Tube diameter d	450	30	4	80	26.3	73.4	40.8
E6		450	33	4	80	33.0	97.4	49.0
E2		450	36	4	80	38.3	96.8	55.0
E7		450	44	4	80	43.3	80.1	57.8
E8		450	47	4	80	45.9	85.9	57.5
E9		450	50	4	80	46.7	85.3	59.4
E10	Wall thickness T	450	36	2	80	16.9	76.1	36.1
E11		450	36	3	80	23.7	59.7	45.7
E2		450	36	4	80	38.3	96.8	55.0
E12		450	36	5	80	40.6	92	55.5
E13	Aluminum sleeve length L	450	36	4	50	28.7	67.9	38.3
E14		450	36	4	65	32.6	77.5	45.4
E2		450	36	4	80	38.3	96.8	55.0
E15		450	36	4	90	39.8	105.1	57.5
E16		450	36	4	100	42.7	115	59.5

3. Data set creation

3.1. Combination of parameters

As analyzed in the previous section, the four structural dimension parameters of the brake ring each impact its performance differently. However, discerning the actual trends based solely on single-parameter analysis is challenging. For example, the significant impact range of the aluminum sleeve length on the brake ring's performance may vary with changes in the steel tube's diameter and wall thickness. Single-parameter analysis fails to describe the variation patterns when multiple parameters are coupled. Therefore, establishing a dataset with extensive parameter variations is more helpful for studying the patterns of how the brake ring's structural dimensions affect its performance.

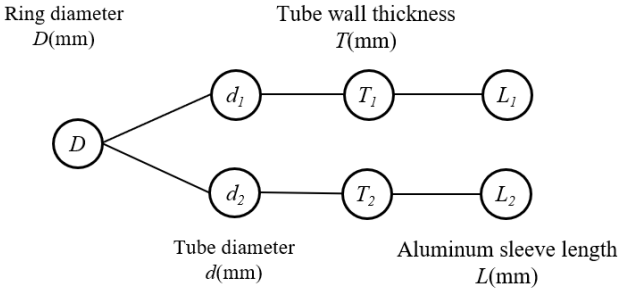

Fig. 11 Brake ring structure size combination of the numerical simulation data set

In establishing the brake ring dataset, commonly used engineering specifications were thoroughly considered. Among the structural dimensions, increasing the tube diameter decreases cross-sectional stiffness. Therefore, for larger tube diameters of 44mm, 47mm, and 50mm, greater wall thickness and longer aluminum sleeves are used to enhance sectional stiffness and constraining ability. Based on this, combinations of the four structural dimension parameters are illustrated in Fig. 11 and Table 4. After combining various structural dimensions, a total of 576 calculation conditions were obtained.

Table 4
Brake ring structure dimension parameters of numerical simulation

D(mm)	d(mm)		T(mm)		L(mm)	
	d_1	d_2	T_1	T_2	L_1	L_2
400	30		2		50	
450	33		3	3	65	65
500	36		4	4	70	80
550		44	5	5	80	90
		47		6	90	100
		50			100	110
						120

After completing the numerical calculations, extract the load-displacement curve results for all calculated conditions and fit the tri-linear load-displacement curve within the effective sliding distance[6]. Here, F_1 represents the starting load to activate the brake ring; F_3 is the maximum load within the effective sliding distance; the energy dissipation E is derived from the area under the load-displacement curve. For F_2, it must ensure that the area enclosed by the

three linear segments and the load-displacement curve equals the area above the displacement axis. Finally, the starting load F_1, maximum load F_3, and energy dissipation E are selected as the mechanical performance indicators. The curve fitting results of the numerical simulation are shown in Fig. 12.

3.2. Normalization of data sets

Considering the significant variation in the magnitudes of parameters in the dataset, it is a common practice to normalize the data before training the neural network. This study employs the Min-Max Scaling method to normalize features to the [0-1] range. This normalization simplifies the complexity of model training, enables rapid and stable training of the neural network, prevents gradient issues, and enhances the model's generalizability and interpretability.

$$x_{norm} = \frac{x - x_{\min}}{x_{\max} - x_{\min}} \tag{4}$$

where, x_{norm} is the normalized feature value; x is the actual feature value; x_{max} and x_{min} are the maximum and minimum values of the feature, respectively.

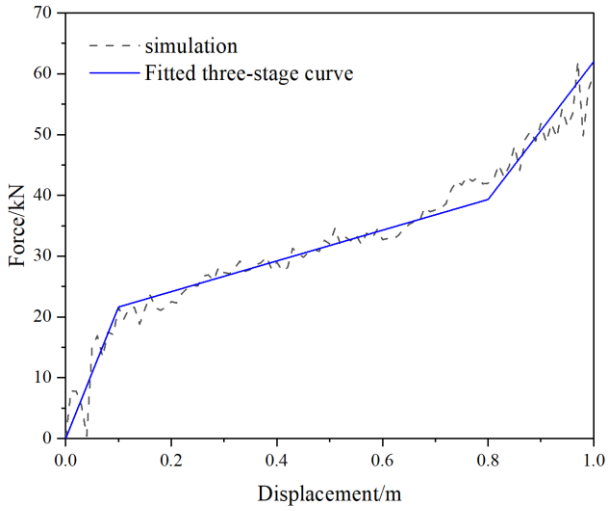

Fig. 12 Trilinear load-displacement curve within effective displacement of brake ring

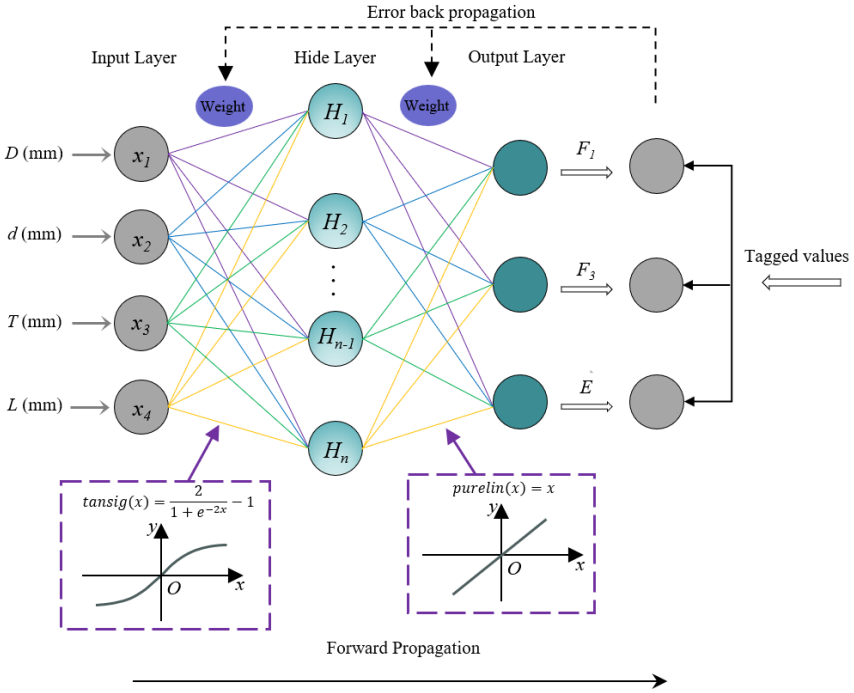

(a) BP neural network structure

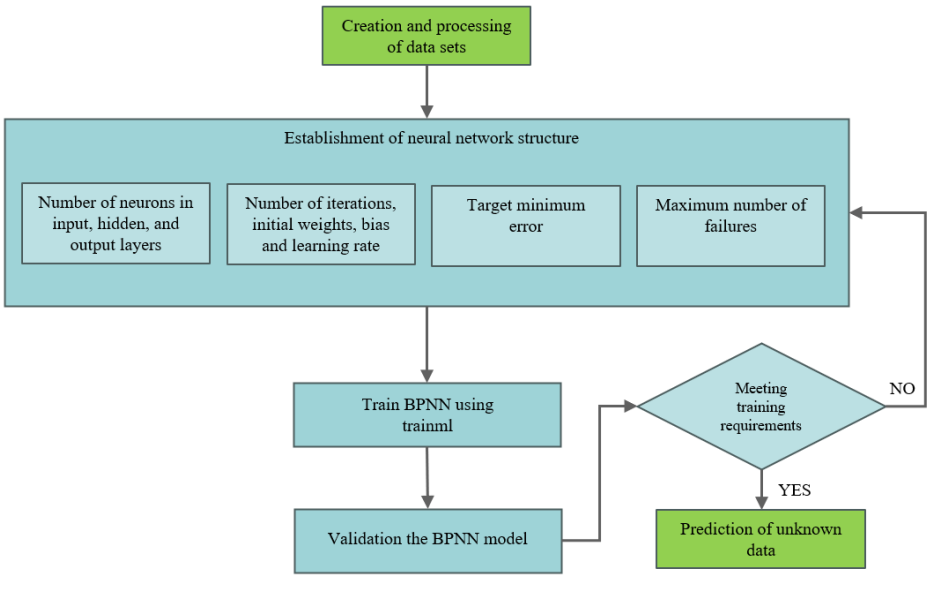

(b) BPNN Flowchart

Fig. 13 Network structure and flow chart of BPNN

4. BP neural network prediction modeling

4.1. BP neural network

The Backpropagation (BP) algorithm is a fundamental training method in deep learning, especially used in Multilayer Perceptrons (MLP). Its fundamental principle relies on supervised learning, calculating the error between the network's output and the actual target, and then adjusting the network's weights layer by layer from the output back to the input layer based on this error. This process uses the chain rule to differentiate the error, determining the direction for weight updates.

The BP neural network is composed of three types of layers: input, hidden, and output layers (see Fig. 13). Each iteration of the BP algorithm involves two main phases: forward propagation and backward propagation.

During forward propagation, sample data passes from the input layer, through the hidden layer, to the output layer (Equations 5 and 7). Activation functions (Equations 6 and 8) are then applied to generate predictions.

$$z_h = W_h \cdot x + b_h \tag{5}$$

$$a_h = \sigma(z_h) \tag{6}$$

$$z_o = W_o \cdot a_h + b_o \tag{7}$$

$$a_o = \sigma(z_o) \tag{8}$$

where, z_h is the weighted input for the hidden layer; W_h is the weight matrix from the input layer to the hidden layer; x is the input vector; b_h is the bias vector for the hidden layer; a_h is the activation output of the hidden layer, and σ is the activation function; z_o is the weighted input for the output layer; W_o is the weight matrix from the hidden layer to the output layer; b_o is the bias vector for the output layer, and a_o is the final output of the network.

During backward propagation, the error between the predicted values for sample x and the actual labels is calculated based on the current network weights (Equations 9 and 10). The weights and biases of each layer are then updated in reverse to adapt to changes in the external environment (Equations 11 and 12). Training is considered complete after multiple cycles, ensuring that the final output closely matches the target value.

$$\delta_o = (a_o - y) \times \sigma'(z_o) \tag{9}$$

$$\delta_h = (W_o^T \cdot \delta_o) \times \sigma'(z_h) \tag{10}$$

$$W_o = W_o - \eta \cdot \delta_o \cdot a_h^T \tag{11}$$

$$W_h = W_h - \eta \cdot \delta_h \cdot x^T \tag{12}$$

where, δ_o is the error of the output layer; y is the actual label; σ' is the derivative of the activation function of the output layer; δ_h is the error of the hidden layer; W_o^T is the transpose of the weights from the output layer to the hidden layer; η is the learning rate.

The neural network models presented in this study were developed and tested using the MATLAB 2022a software (MathWorks, Natick, MA, USA) environment.[27]

4.2. BP neural network structure selection

Hecht-Nielsen laid a robust theoretical foundation for single-hidden-layer feedforward neural networks. He posits that such networks can approximate any continuous function on a finite closed set with arbitrary accuracy, given a sufficient number of hidden layer neurons and an appropriate activation function. To mitigate model complexity and prevent overfitting, this study employs a single hidden layer. Insufficient neurons in the hidden layer can cause underfitting, whereas an excessive number may lead to overfitting. The hidden layer neuron count was determined using the empirical formula (13) [28].

$$n_l = \sqrt{m+n} + a \tag{13}$$

where, n_l is the number of neurons in the hidden layer; m is the number of neurons in the input layer of the network; n is the number of neurons in the output layer of the network; a is an integer between [1-10].

To improve the network's capability in managing nonlinear expressions and to enhance its generalization, this study employs the tansig function as the activation function for the hidden layer and the pureline function for the output layer[29,30].

$$\text{tansig}(x) = \frac{2}{1+e^{-2x}} - 1 \tag{14}$$

$$\text{purelin}(x) = x \tag{15}$$

The BP neural network prediction model presented in this paper takes four structural dimension parameters that influence the mechanical performance of the brake ring as input values: ring diameter D, tube diameter d, tube wall thickness T, and aluminum sleeve length L. The model outputs three mechanical performance indicators derived from the trilinear load-displacement curve within the effective displacement range of the brake ring: starting load F_1, maximum load F_3, and energy dissipation E.

Given the simple data structure in this project, the dataset is divided into 85% for training and 15% for testing, based on random selection. The training set includes the training sample set X1 and the training label set Y1. The test set comprises the test sample set X2 and test label set Y2. X1 and Y1 contain 489 pairs of samples and labels, while X2 and Y2 contain 87 pairs of samples and labels. The number of training iterations is set to 1000, and the learning rate is set to 0.01.

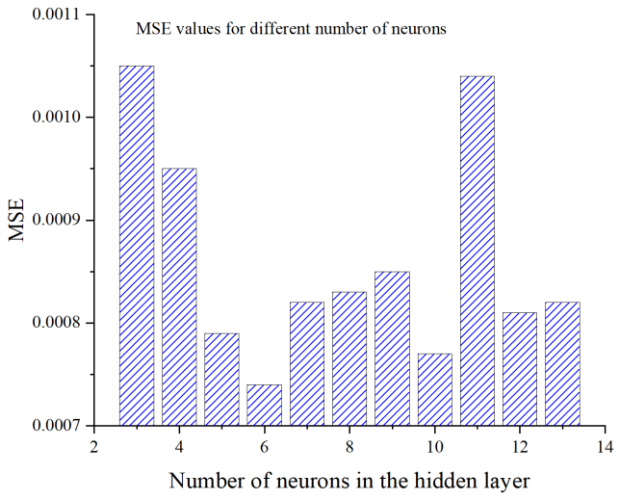

Fig. 14 MSE under different number of hidden layer neurons

To determine the optimal number of neurons within the range determined by empirical formulas, the Mean Squared Error (MSE) values (Formula 16) for multi-output with different neuron counts, ranging from 3 to 15, were plotted in Fig. 14. Based on the experimental data, the minimum multi-output Mean Squared Error occurs when the hidden layer contains six neurons. Therefore, the optimal number of neurons for the hidden layer is determined to be $n_l = 6$, at which the MSE is minimized. The BP neural network model structure in this paper is 4-6-3.

$$MSE = \frac{1}{S}\sum_{k=1}^{S}\left(\frac{1}{N}\sum_{i=1}^{N}\left(y_{ki} - y_{ki}^{'}\right)^2\right) \tag{16}$$

where, N is the number of samples; y_{ki} is the kth predicted output parameter in the ith sample; $y_{ki}^{'}$ is the kth actual output parameter in the ith sample; S is the number of neurons in the output layer, and S is 3 in this paper.

5. Validation of the model for predicting mechanical properties of the brake ring

5.1. Indicators for the assessment of the model

The evaluation metrics for the BP neural network model primarily involve the measurement of prediction accuracy and the model's generalization ability. This paper uses the Root Mean Square Error (RMSE) and the Coefficient of Determination (R^2) as the performance evaluation indicators for the BP neural

network model. The calculation formulas for RMSE and R^2 are:

$$RMSE = \sqrt{\frac{1}{N}\sum_{i=1}^{N}\left(y_i - y_i^{'}\right)^2} \tag{17}$$

$$R^2 = 1 - \frac{\sum_{i=1}^{N}\left(y_i - y_i^{'}\right)^2}{\sum_{i=1}^{N}\left(y_i - \bar{y}\right)^2} \tag{18}$$

where, N is the number of samples; y_i is the predicted value by the model; $y_i^{'}$ is the actual target value of the sample; $\bar{y}$ is the average actual target value of the samples.

5.2. Validation of the model

The accuracy of the BP neural network prediction model is crucial for subsequent reverse structural dimension design based on target mechanical performance. To precisely design brake ring dimensions, it is necessary to adjust neural network parameters multiple times and select the prediction model with the highest accuracy. The training results shown in Fig. 15 indicate that the coefficient of determination (R^2) for all samples reached 0.991, demonstrating high model fidelity. The predicted output values can be approximately considered as the actual outputs of a nonlinear function, meeting the accuracy requirements of the training.

Fig. 16 shows the test set prediction results for various mechanical performance parameters. In the test set, the Root Mean Square Errors (RMSE) for the starting load F_1, maximum load F_3, and energy dissipation E were 1.76 kN, 3.23 kN, and 1.57 kJ, respectively, with prediction accuracies of 97.6%, 96.5%, and 98.8%.

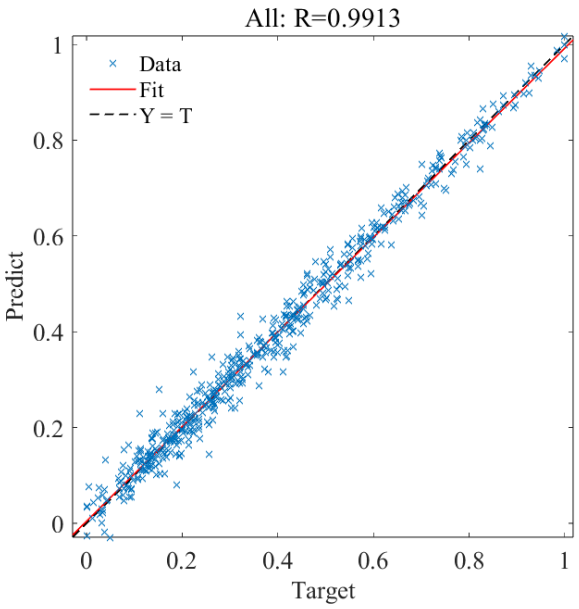

Fig. 15 BP neural network all sample regression results

In the final stages of stretching, the brake ring undergoes significant deformation, with most materials entering the plastic phase. Once the steel tube's diameter reduces to a certain extent, torsional deformation increases component stiffness, significantly increasing the maximum load. Significant deformation in the final calculation stages leads to instability issues, causing variability in the maximum load and greater errors compared to the starting load. However, the energy dissipation of the brake ring is mainly due to the sliding deformation before the load reaches F_2. Therefore, the error from the abrupt change in maximum load has little impact on energy dissipation.

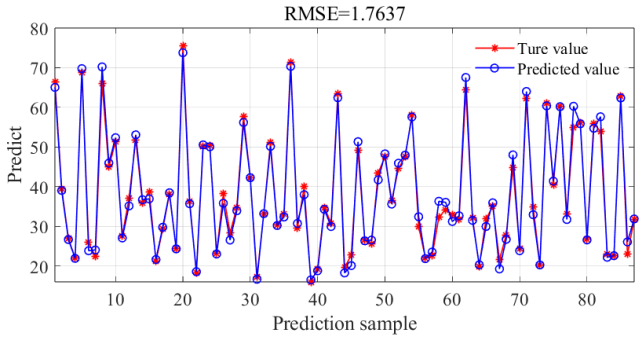

(a) Starting load F_1

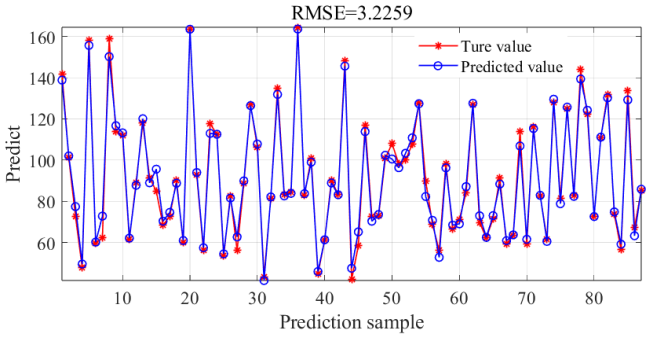

(b) Maximum load F_3

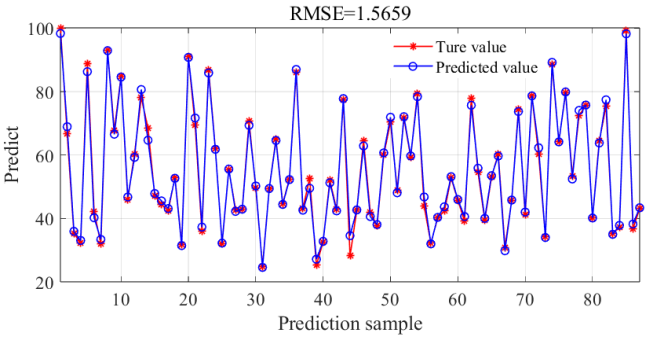

(c) Energy dissipation E

Fig. 16 BP neural network prediction and label comparison

6. Reverse design of brake ring based on PSO algorithm

6.1. Particle Swarm Algorithm

Particle Swarm Optimization (PSO) is a heuristic global optimization technique inspired by the foraging behavior of bird flocks[31,32]. In the PSO algorithm, each "bird" is termed a "particle," and a certain number of particles are randomly generated initially to form a population. Each particle in the population is a vector with multiple spatial dimensions, each having a position and velocity within the search space. Each particle in the population is a vector with multiple spatial dimensions, each having a position and velocity within the search space. The detailed process is illustrated in Fig. 17.

$$\begin{aligned} v_i(t+1) = {} & w \times v_i(t) + c_1 \times rand_1 \times (pbest_i - x_i(t)) + \\ & c_2 \times rand_2 \times (gbest - x_i(t)) \end{aligned} \tag{19}$$

$$x_i(t+1) = x_i(t) + v_i(t+1) \tag{20}$$

where, $v_i(t)$ represents the velocity of particle x_i at time t; $x_i(t)$ represents the position of particle i at time t; ω is the inertia weight; c_1 and c_2 are learning factors; $rand$ is a random number within the interval [0,1]; $pbest_i$ and $gbest$ respectively represent the best position encountered so far by particle i and the best position encountered by all particles to date.

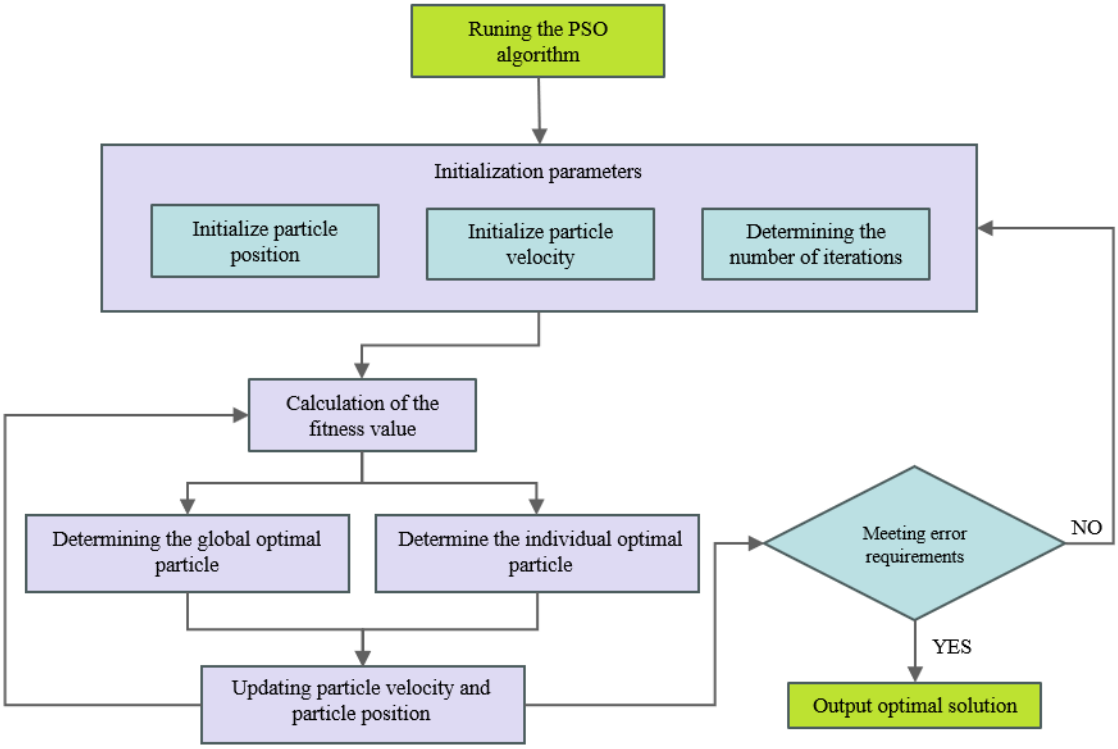

Fig. 17 Flowchart of PSO algorithm

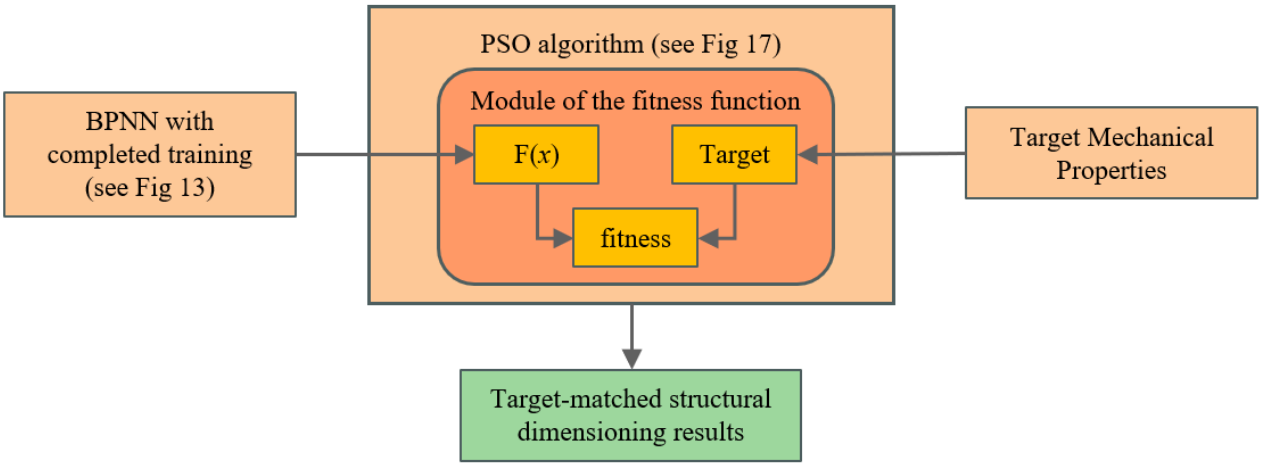

Fig. 18 Flowchart of BPNN-PSO Reverse Design

The fitness value represents the quality of each particle as the best structural dimension design result that matches the target mechanical performance. This paper employs Eq. (21) as the fitness function. A lower fitness value indicates that the particle is closer to the optimal solution. Through multiple iterations of updates, the particle closest to the target is identified.

$$fit(x) = \frac{1}{S}\sum_{k=1}^{S}(y(x)_k - y_k^{'})^2 \tag{21}$$

where, x is the input parameter vector; S represents the number of neurons in the output layer, which in this paper is set to 3; $y(x)_k$ is the *kth* predicted output value for the input parameter x ; $y_k^{'}$ is the *kth* value of the target mechanical performance parameters.

6.2. PSO parameters selection

In the forward prediction model, inputting four structural dimension features allows the prediction of three mechanical performance indicators of the brake ring. In the reverse design problem, which targets optimal structural dimensions based on desired mechanical performance, a population of structural dimension parameters is randomly generated using the forward prediction model. The individual and global optimal particles are determined based on each particle's fitness value within the population. Finally, through continuous iterations and optimization, the structural dimension parameters that best match the target mechanical performance are obtained.

From the input parameters of the BP neural network prediction model, the spatial dimension number M for the PSO algorithm's particle swarm is determined to be four dimensions. This means the position vector of particle individuals can be represented as $x_i = (x_1, x_2, x_3, x_4)_i$, and the velocity vector as $v_i = (v_1, v_2, v_3, v_4)_i$. Both the individual learning factor and the social learning factor are set to 2. The inertia weight is set to a constant value of 1. The particle swarm size is set to 5, and the number of iterations to 100[33].

6.3. Structural dimension design of brake ring based on target mechanical performance

The ring diameter of the brake ring determines its effective sliding distance during stretching process. To systematically categorize brake rings with different effective sliding distances, the reverse design model discretizes the

ring diameter, fixing the values at 400mm, 450mm, 500mm, and 550mm, corresponding to effective sliding distances of 900mm, 1000mm, 1100mm, and 1200mm, respectively. Typically, brake rings with different structural size combinations can have similar mechanical properties. This means that for specific mechanical performance, there is no unique optimal solution for the brake ring; multiple local optima can exist.

In the reverse design model, the basic process is: ① Specify the mechanical performance indicators of the brake ring, including the required starting load, maximum load, and energy dissipation; ② Import the forward mechanical performance prediction model of the brake ring, randomly generating a population of potential optimal structural dimensions; ③ Set up a fitness function, calculate the fitness value of each particle, and use the Particle Swarm Optimization algorithm to iteratively update to the optimal solution; ④ Repeat the above process to output multiple design dimensions. The key step in this process is introducing the trained neural network as the fitness calculation function in the PSO optimization algorithm, as shown in Fig. 18.

For a specific target mechanical performance, such as a starting load of 40kN, a maximum load of 85kN, and energy dissipation of 54kJ, the reverse design model outputs four different structural dimension combinations, as shown in Table 5. The fitness iteration curve of the design process is shown in Fig. 19.

Table 5
Design of brake ring structure size

Number	*D*/mm	*d*/mm	*T*/mm	*l*/mm
1	450	41.96	3.49	80.25
2	450	41.73	4.40	66.67
3	500	36.23	2.58	120.00
4	550	30.00	4.07	120.00

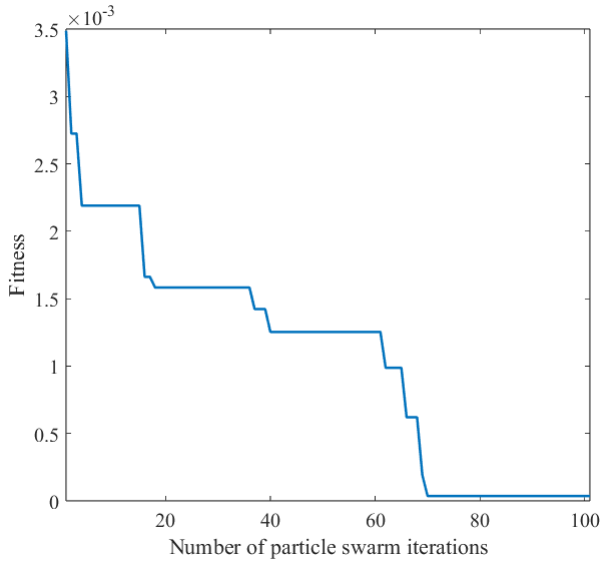

Fig. 19 Fitness value iteration curve

6.4. Mechanical Testing and Numerical Simulation Validation of the Brake Ring Design Model

To verify the effectiveness of the reverse design model, two sets of mechanical tests and numerical simulations were conducted using the structural dimension combination with serial number 1 as an example. The designs of the remaining serial numbers were verified for validity using numerical simulations.

During the mechanical testing process, the actual structural dimensions of the brake ring were: ring diameter of 450 mm, tube diameter of 42 mm, tube wall thickness of 3.5 mm, and aluminum sleeve length of 80 mm. The testing equipment utilized a vertical tensile testing machine with a capacity of 150 tons and a hydraulic cylinder travel of 2500 mm. It was equipped with force and displacement sensors, as shown in Fig. 20. The lower end of the brake ring's wire rope was attached to a shackle fixed to a steel beam anchored to the ground, while the upper end was connected to a shackle fixed to the tensile arm of the testing machine. During the stretching process, force and displacement data were recorded every 0.2 seconds, resulting in the force-displacement curve shown in Fig. 21. Concurrently, a numerical model was established using the designed structural dimensions to perform a numerical simulation analysis of the brake ring, comparing and verifying the reliability of the reverse design model.

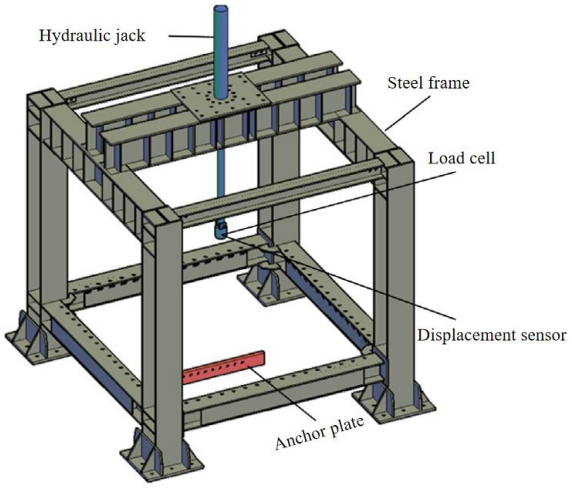

Fig. 20 Quasi-static tensile testing machine

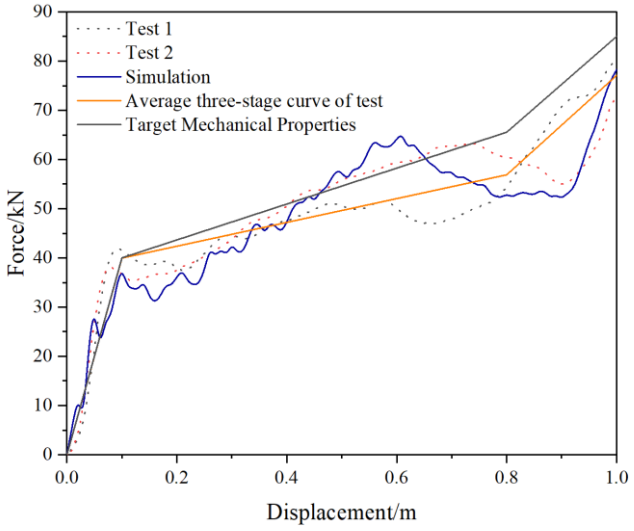

Fig. 21 Comparison of the target, mechanical tests, and simulation results of brake ring

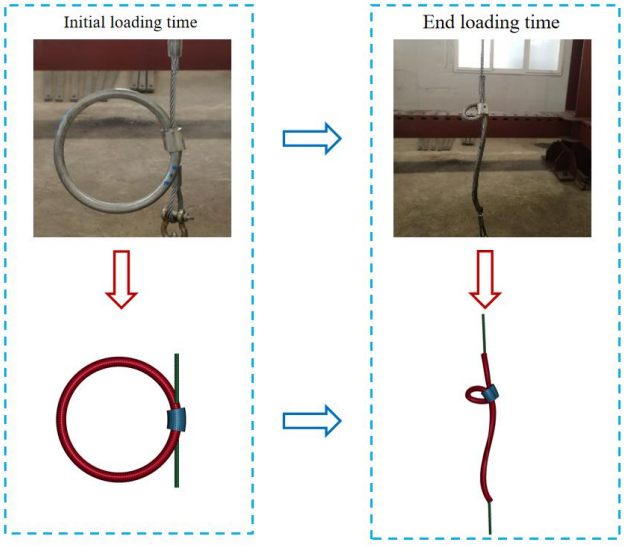

Fig. 22 Comparison of test and simulation deformation for brake ring No. 1

As shown in Table 6, the errors between the experimental results and the target performance for the three mechanical indicators in Design 1 are -0.25%, -9.29%, and -8.89%, respectively, based on both experimental and numerical simulation analysis. Additionally, the numerical simulation aligns with the experimental results, further validating the effectiveness of the design method. For Designs 2, 3, and 4, only numerical simulation validation was conducted. The comparisons of their load-displacement curves with the target performance are shown in Fig. 23, and the result analysis is provided in Table 7.

In summary, the structural dimensions of the brake ring designed according to specific mechanical performance criteria result in actual products whose mechanical performance indicators and numerical simulation results have errors within 10% of the required targets, all within an acceptable engineering range. This achieves a high-precision design, ensuring that the actual structural dimensions of the brake ring meet the required mechanical performance targets.

Table 6
Mechanical test, numerical simulation and target performance analysis of the designed brake ring

Case	F_1(Kn)	F_3(kN)	E(kJ)
Test 1	41.8	80.8	50.2
Test 2	38.1	73.4	48.3
Test Average	39.9	77.1	49.2
Simulation	38.0	78.3	49.2
Target	40.0	85.0	54.0
Test results and target error	-0.25%	-9.29%	-8.89%

Table 7
The numerical simulation results analysis of other designs

Case	F_1(mm)	F_3(mm)	E(mm)	Error F_1	Error F_3	Error E
Design 2	39.0	87.1	55.5	-2.50%	2.47%	2.78%
Design 3	37.3	88.6	58.2	-6.75%	4.23%	7.78%
Design 4	37.7	87.8	58.0	-5.75%	3.29%	7.41%
Target	40.0	85.0	54.0	--	--	--

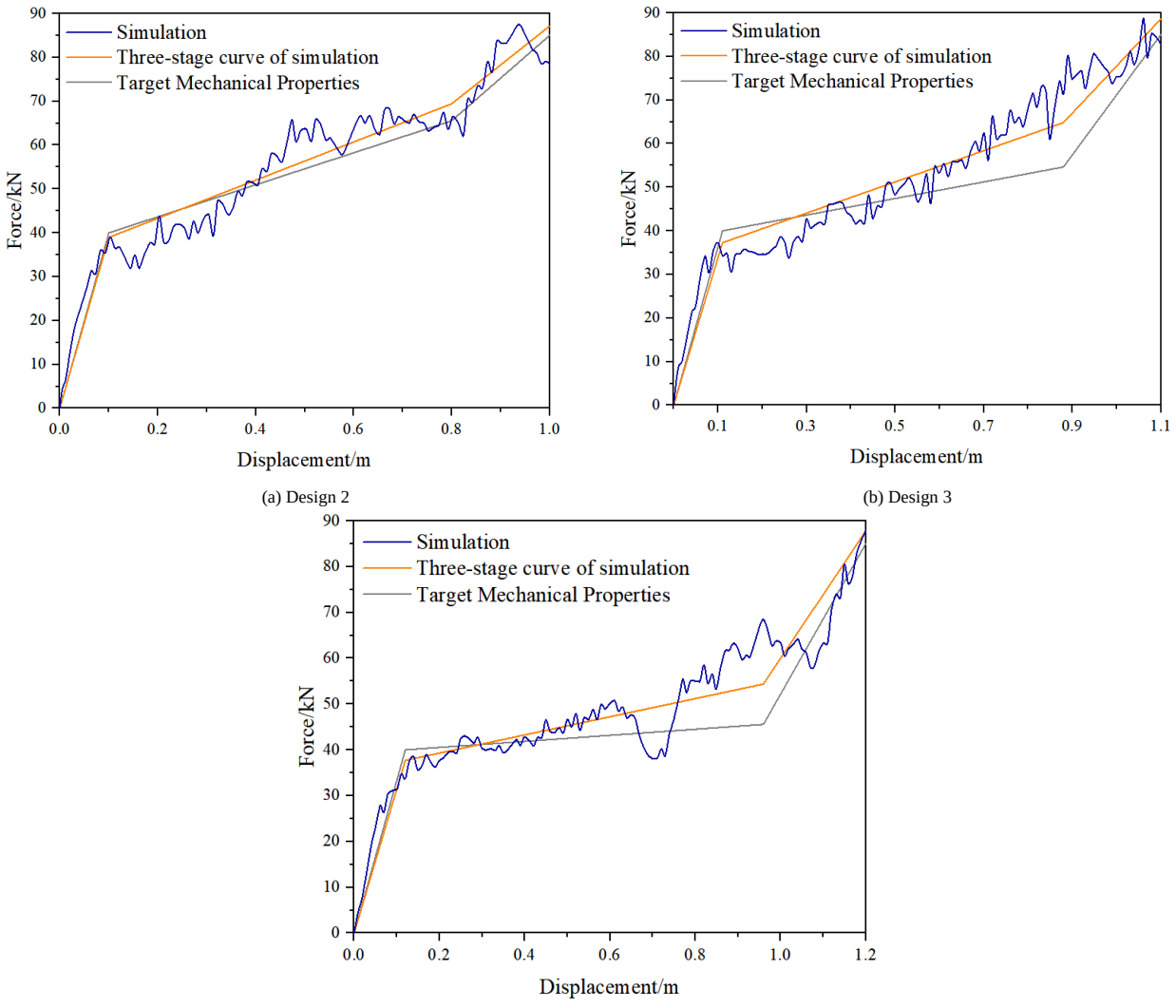

(a) Design 2

(b) Design 3

(c) Design 4

Fig. 23 Numerical simulation results of remaining designs compared to target performance.

7. Conclusions

This paper establishes a brake ring mechanical performance prediction model and a reverse design model based on target mechanical performance using the BP neural network and PSO optimization algorithm, leading to the following important conclusions:

(1) The mechanical performance of the brake ring is mainly influenced by its structural dimensions, including ring diameter, tube diameter, tube wall thickness, and aluminum sleeve length. The BP neural network designed in this study, with an input layer of 4 nodes, a hidden layer of 6 nodes, and an output

layer of 3 nodes, effectively reflects the nonlinear mapping relationship between the brake ring's structural dimensions and mechanical performance.

(2) Through comparison and verification between actual product tests and numerical simulation results of the brake ring, the BP neural network-based prediction model and the PSO algorithm-based reverse design model proposed in this paper can design brake rings that meet specific mechanical performance requirements for engineering projects, offering a practical method for selecting energy dissipators in flexible protection systems.

(3) The successful application of the automated design method for energy dissipators in flexible protection systems proposed in this paper can be extended to other components. Future research will focus on the automated design of both individual components and the overall structure of flexible protection systems.

Acknowledgements

This study is supported by the Sichuan Science and Technology Program (Grant No. MZGC20240052).

References

[1] Yang J, Duan S, Li Q, et al. A review of flexible protection in rockfall protection. Natural Hazards, 2019, 99: 71-89.
[2] JIN Yuntao, YU Zhixiang, LUO Liru, et al. A study on energy dissipation mechanism of a guided flexible protection system under rockfall impact. Journal of Vibration and Shock, 2021, 40 (20): 177-185+192.(in Chinese)
[3] LIU Zhanhui, LU Zhimou, LI Yongle, et al. Study on Impact Resistance of Flexible Shed Tunnel for Bridges in Mountainous Areas. Journal of The China Railway Society,2023,45(03):129-136. (in Chinese)
[4] Muraishi H, Samizo M, Sugiyama T. Development of a flexible low-energy rockfall protection fence. Quarterly Report of RTRI, 2005, 46(3): 161-166.
[5] Castro-Fresno D, Del Coz Díaz J J, Nieto P J G, et al. Comparative analysis of mechanical tensile tests and the explicit simulation of a brake energy dissipater by FEM. International Journal of Nonlinear Sciences and Numerical Simulation, 2009, 10(8): 1059-1085.
[6] Lambert S, Nicot F. Multi-scale analysis of an innovative flexible rockfall barrier. 2013.
[7] del Coz Díaz J J, Nieto P J G, Castro-Fresno D, et al. Nonlinear explicit analysis and study of the behaviour of a new ring-type brake energy dissipator by FEM and experimental comparison. Applied Mathematics and Computation, 2010, 216(5): 1571-1582.
[8] Castanon-Jano L, Blanco-Fernandez E, Castro-Fresno D, et al. Energy dissipating devices in falling rock protection barriers. Rock Mechanics and Rock Engineering, 2017, 50: 603-619.
[9] QI Xin, XU Hu, YU Zhixiang, et al. Dynamic mechanical property study of break rings in Flexible Protective System. Engineering Mechanics, 2018, 35(9):9. (in Chinese)
[10] Lu XZ, Liao WJ, Zhang Y, Huang YL, Intelligent structural design of shear wall residence using physics-enhanced generative adversarial networks, Earthquake Engineering & Structural Dynamics, 2022, 51(7): 1657-1676.
[11] Zhao PJ, Liao WJ, Huang YL, Lu XZ, Intelligent beam layout design for frame structure based on graph neural networks, Journal of Building Engineering, 2023, 63, Part A: 105499.
[12] Bao Yuequan, Li Hui. Artificial Intelligence for Civil Engineering. China Civil Engineering Journal, 2019, 52(5): 1-11. (in Chinese)
[13] Joshi D A, Menon R, Jain R K, et al. Deep learning-based concrete compressive strength prediction model with hybrid meta-heuristic approach. Expert Systems with Applications, 2023, 233: 120925.
[14] Yi Peng, Xinyi Yu, Yixin Huang, et al. Asphalt pavement raveling recognition based on deep learning algorithms, Intelligent Transportation Infrastructure, 2024.
[15] Yongding Tian, Junhao Zhang, et al. Comprehensive review of noncontact sensing Technologies for Bridge Condition Monitoring and Assessment, Intelligent Transportation Infrastructure, 2024.
[16] Chen W, Xu J, Dong M, et al. Data-driven analysis on ultimate axial strain of FRP-confined concrete cylinders based on explicit and implicit algorithms. Composite Structures, 2021, 268: 113904.
[17] Xu J, Chen Y, Xie T, et al. Prediction of triaxial behavior of recycled aggregate concrete using multivariable regression and artificial neural network techniques. Construction and Building Materials, 2019, 226: 534-554.
[18] Pham T M, Hadi M N S. Predicting stress and strain of FRP-confined square/rectangular columns using artificial neural networks[J]. Journal of Composites for Construction, 2014, 18(6): 04014019.
[19] MA Gao, LIU Kang. Prediction of Compressive Strength of CFRP-confined Concrete Columns Based on BP Neural Network. Journal of Hunan University(Natural Sciences) ,2021,48(09):88-97.
[20] ZHOU Zhong, ZHANG Junjie, et al. Prediction model of sewage treatment in tunnel green construction based on PSO-BP neural network. Journal of Railway Science and Engineering, 2022, 19(5): 1450-1458. (in Chinese)
[21] Liao L, Yu Z, Yang X, et al. An automated computation method for flexible protection systems based on neural networks. Computers and Geotechnics, 2024, 165: 105932.
[22] Cascardi A, Micelli F, Aiello MA. An Artificial Neural Networks model for the prediction of the compressive strength of FRP-confined concrete circular columns. Eng Struct 2017;140:199–208.
[23] Jiang K, Han Q, Bai Y, Du X. Data-driven ultimate conditions prediction and stress-strain model for FRP-confined concrete. Compos Struct 2020;112094.
[24] WANG Min, SHI Saoqing, YANG Youkiu. Static tensile test and FEM dynamic simulation for a ring-brake energy dissipater. Journal of Vibration and Shock,2011,30(04):188-193. (in Chinese)
[25] TIAN Zhenhua, SHI Shaoqing, et al. Mechanical Testing on the Ring-brake Energy Dissipater and Influence of Thickness on Its Energy Dissipation Performance. Journal of Logistical Engineering University, 2014, 30(3): 8-12. (in Chinese)
[26] LIU Chengqing, CHEN Linya, CHENG Chi, et al. Full scale test and FEM simulation to ring-type brake energy dissipater in falling rock protection. Chinese Journal of Rock Mechanics and Engineering, 2016, 35(6): 1245-1254. (in Chinese)
[27] The MathWorks. <http://www.mathworks.com/products/matlab/>; 2007.
[28] DAI Yimin, LI Yixin, XU Ying, et al. Prediction of hail impact force induced by Wind-Hail coupling based on GA-BP Neural Network. Engineering Mechanics, 2024. 1-10. (in Chinese)
[29] CHENG Qing, MA Rui, JIANG Zhengwu, et al. Compressive Strength Prediction and Mix Proportion Design of UHPC Based on GA-BP Neural Network. Journal of Building Materials, 2020, 23(1): 176-183+191.(in Chinese)
[30] CHEN W, XU J, DONG M, et al. Data-driven analysis on ultimate axial strain of FRP-confined concrete cylinders based on explicit and implicit algorithms. Composite Structures, 2021, 268: 113904.
[31] POLI R, KENNEDY J, BLACKWELL T. Particle swarm optimization: An overview. Swarm Intelligence, 2007, 1(1): 33-57.
[32] LI Guangbao, GAO Dong, LU Yong, et al. Internal surface treatment of gas-liquid-solid technology based on PSO-BP algorithm and FLUENT. Journal of Jilin University (Engineering and Technology Edition), 2024, 1-12. (in Chinese)
[33] YANG Junqi, FAN Xiaojun, ZHAO Yuehua, et al. Prediction of carbon emissions in Shanxi Province based on PSO-BP neural network. Journal of Environmental Engineering Technology: 1-15. (in Chinese)

Advanced Steel Construction – Vol. 20 No. 4 (2024) 397–405
DOI:10.18057/IJASC.2024.20.4.7

NUMERICAL INVESTIGATION ON SEISMIC PERFORMANCE OF PREFABRICATED STEEL BEAM-TO-COLUMN CONNECTION WITH REPLACEABLE U-SHAPED PLATE

Xun Zhang [1], Bin Zhou [1], Jun-Dong Gao [1,*], Hui Qian [1], Lian-Zhi Song [2] and Li-Ming Cai [3]

[1] *Xun Zhang, Bin Zhou, Jundong Gao and Hui Qian, School of Civil Engineering, Zhengzhou University, Zhengzhou 450001, PR China*

[2] *Lianzhi Song, Henan Xinya Steel Structure Engineering Co., Ltd, Zhengzhou 452470, RP China*

[3] *Liming Cai, Henan Architectural Design and Research Inst. Co., Ltd., Zhengzhou 450099, PR China*

** (Corresponding author: E-mail: gaojundong@zzu.edu.cn)*

ABSTRACT

This paper presents a novel prefabricated steel beam-to-column connection with a replaceable U-shaped plate (PSCU) aimed at enhancing the seismic resilience of steel structures and enabling expedited assembly, disassembly, and post-earthquake recovery. The structural design of the PSCU is delineated, along with the articulation of seismic design objectives and methodologies. A sophisticated finite element (FE) model for PSCU is constructed utilizing solid elements, and the fidelity of this modeling paradigm is validated against documented experimental findings. Quasi-static numerical simulations are conducted for 11 connection patterns with varying U-shaped plate thickness, T-shaped plate thickness and bolt quantity. Comparative investigations into hysteresis curves, failure modes, skeleton curves, and ductility coefficients affirm the precision of the seismic design objectives and methodologies. The findings underscore a pronounced ductile failure in this connection, characterized by a discernible four-stage failure progression: elastic, slip, elastic-plastic, and plastic stages. The post-earthquake recovery method for PSCU was proposed and verified, and recommendations for the design of PSCU were put forward. This research offers a robust scientific basis for the expeditious post-earthquake functional recovery in steel frame structures.

ARTICLE HISTORY

Received: 5 March 2024
Revised: 19 September 2024
Accepted: 20 September 2024

KEYWORDS

Prefabricated steel beam-to-column connection;
Replaceable U-shaped plates;
Post-earthquake functional recovery;
Seismic performance;
Numerical investigations

1. Introduction

The prefabricated steel structure, regarded as a sustainable building with a complete lifecycle, offers advantages such as standardized production, a short construction period, flexible space layout, and substantial economic benefits. It has evolved into a pivotal structural form in developed nations such as Europe, America, and Japan [1,2]. To circumvent brittle failure at the root weld of beam-column connections and adhere to seismic design criteria emphasizing "strong column and weak beam, strong connection and weak connected members," traditional steel frame beam-column connections have historically employed two primary methods to shift the plastic hinge outward. One approach involves weakening the beam section, for example, by utilizing a dog bone section to ensure the appearance of plastic hinges at the weakened segment [3-5]. The alternative strategy is to reinforce the connection at the beam root [6,7]. However, in experimental investigations, the primary components of these connections often sustain severe damage upon connection failure, rendering conventional steel frame structures challenging to repair and restore to functional capacity post-earthquakes [8,9].

In pursuit of enhanced damage control and expeditious post-earthquake recovery for steel beam-column connections, scholars have proposed an earthquake-resilient structure [10]. This innovation aims to minimize earthquake disaster losses and reduce post-earthquake recovery time, with specific applications to beam-column connections [11-15]. However, early-stage earthquake-resilient connections introduced by scholars were generally intricate, involving cumbersome and costly replacement processes after earthquakes. Consequently, domestic scholars proposed simplified forms of connections [16,17]. For example, Zhang and Jiang et al. [18-24] devised a series of earthquake-resilient prefabricated beam-column connections, ensuring the primary structure remains in the elastic stage during earthquakes and can be restored post-earthquake by replacing the flange cover plate. In summary, earthquake-resilient beam-column connections can be effectively repaired by substituting energy-dissipating members or dampers with concentrated deformation. Nevertheless, these connections exhibit notable drawbacks. Firstly, the installation of energy-consuming components is intricate, demanding extensive disassembly and temporary support during replacement. Secondly, the larger connection area raises the complexity and cost of repair. Furthermore, other components of the connection may suffer some degree of damage, resulting in a decline in connection performance [25,26].

Addressing the limitations of existing research, this paper introduces a novel prefabricated steel beam-to-column connection with a replaceable U-shaped plate (PSCU) aimed at enhancing both seismic and post-earthquake recovery performance. The components of this connection include frame columns, H-shaped frame beams, T-shaped plates, and U-shaped plates. In comparison to traditional beam-column connections, the incorporation of the U-shaped plate in this connection enables yielding first and facilitates plastic damage control. Following an earthquake, only the U-shaped plate and high-strength bolts require replacement to achieve rapid functional recovery of PSCU. The paper delves into the theoretical design methodology, numerical simulation, and parametric analysis of PSCU, offering a dependable and cost-effective option to further realize swift assembly, high ductility, and prompt recovery of steel structures post-earthquakes.

2. Structure design and seismic design method of PSCU

2.1. Structure design for PSCU

The PSCU comprises four primary components: frame columns, frame beams, T-shaped plates, and U-shaped plates, as illustrated in Fig.1(a). Within the column, two vertical internal partitions are pre-welded at the level aligned with the T-shaped plate, ensuring even load transfer from the end of beam to the column and preventing stress concentration on the column wall. The frame beam adopts a configuration that widens the flange width at the beam end, causing the plastic hinge to manifest away from the end of beam and ensuring ample ductility for the connection. During the factory prefabrication process, two T-shaped plates are symmetrically welded on one side of the column. The U-shaped plate, fabricated from three perforated steel plates with a Q235 steel grade (lower than that of other components), undergoes yielding first and concentrates connection deformation under seismic actions. This guarantees that the main components remain free from plastic deformation. Following an earthquake, the post-earthquake recovery of this connection is easily achieved by replacing the U-shaped plate and reseting the bolt connections.

All fabrication and welding of components for this connection are executed in the factory. The contact surfaces of the bolt connections undergo sandblasting to augment the frictional energy dissipation capacity of the connection. No special treatment is applied between the frame column and the U-shaped plate or frame beam, thereby enhancing the rotational capacity and post-earthquake recovery performance of the connection. Furthermore, in comparison to other prefabricated beam-column connections, this design incorporates a finite connection area set at the root of the beam. This feature facilitates rapid recovery after an earthquake without compromising the overall structural strength.

On-site assembly involves solely bolt connections for each component, ensuring swift and efficient installation and replacement. The assembly process of PSCU is shown in Fig.1(b). The on-site assembly process of the connection can be delineated into three steps: Initially, lift the frame beam to the

predetermined position of the T-shaped plate and secure the beam to the T-shaped plate using lower flange bolts. Subsequently, place the U-shaped plate onto the upper flange of the beam and the outer side of the T-shaped plate. Sequentially connect the U-shaped plate to the beam and the U-shaped plate to the T-shaped plate using bolts. Finally, apply pretension to all bolts.

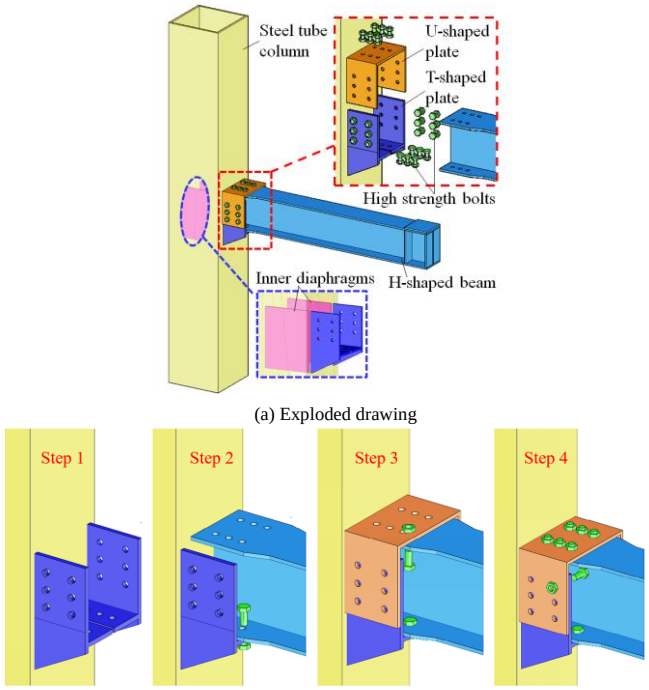

(a) Exploded drawing

(b) Assembly process diagram

Fig. 1 PSCU construction diagram

Owing to the absence of a direct connection between beams and columns in this configuration, intricate stress transmission is circumvented, and the force transmission path is illustrated in Fig.2. The vertical load (F) acted at the beam end is initially conveyed along the beam to the connecting area. As a consequence of the two bolted connections at the widened end of the beam, a part of the beam end load is successively transmitted to the U-shaped plate and T-shaped plate along the blue arrow, while the remaining load is directly transmitted to the T-shaped plate along the orange arrow. Both segments of the load traverse through the frictional force between the plates. Ultimately, the load transmitted via these two paths to the T-shaped plate is directly conveyed to the column.

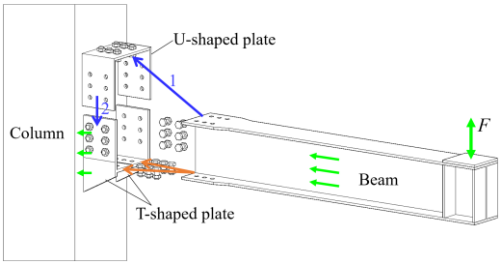

Fig. 2 Load transmission path of PSCU

2.2. Seismic design method of PSCU

The Fig.3 illustrates the connection recover measures required to achieve seismic fortification goals under different seismic actions: Under frequent earthquakes, since the connection is no slip and all components are in the elastic stage, the seismic performance of connection can be completely recovered without repair after earthquake. Under fortification earthquakes, the connection begins to dissipate energy through the friction between bolted plates and all the structural components are still in elastic stage. The seismic performance of connection can be restored by only adjusting the bolts after earthquakes. Under rare earthquakes, the U-shaped plate yields initially and the structure dissipates seismic energy through the friction between contact plates and the plastic deformation of U-shaped plates. At this moment, the performance of the connection can be restored by replacing the U-shaped plates and reseting bolts. Under extremely rare earthquakes, the flange of beam begins to yield and plastic hinge appears at the variable cross-section of beam. The seismic performance of connection can be restored by replacing the U-shaped plate, deformed beam and bolts after earthquakes. To ensure post-earthquake recovery performance of the connection, it is essential to prevent or delay the plastic deformation of T-shaped plates and columns until the latest stage.

The seismic design of PSCU is oriented towards ensuring that seismic energy is predominantly dissipated through slip between contact plates and plastic deformation of the U-shaped plate and beam. In accordance with strength calculations, section 1-1 in Fig.4 represents the section where the beam end first yields, with S_1 and S_2 denoting the connection area and the transition section of the beam, respectively.

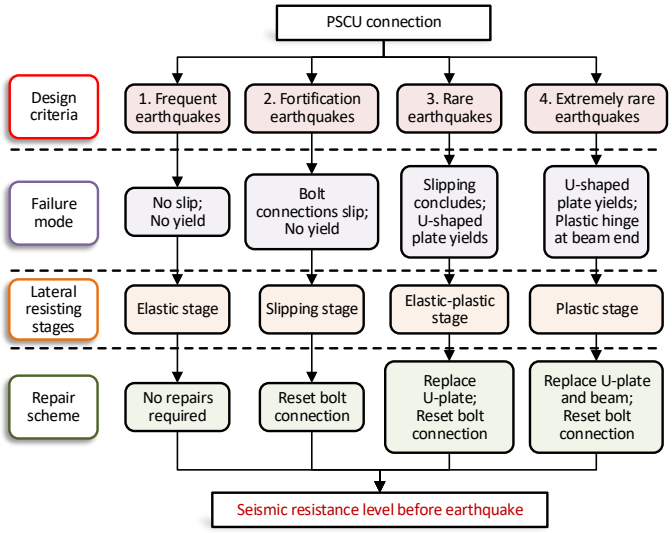

Fig. 3 Flow chart of seismic design

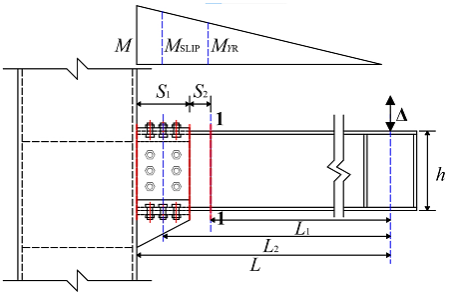

Fig. 4 Bending moment diagram of beam segment

In seismic design, the design formula for bending moment at different stages corresponds to the seismic fortification goal under various seismic actions. The PSCU should adhere to the requirements of no slip between plates during frequent earthquakes, implying that the moment satisfies Eq. (1). Under fortification earthquakes, the connection initiates slipping but does not enter the yield stage, meaning the moment satisfies Eq. (2). In the event of rare earthquakes, the bolts fully slip, the U-shaped plates yield, and the flange of the beam section 1-1 undergoes successive yielding before connection damage, signifying that the moment satisfies Eq. (3).

$$M \le M_{\mathrm{s,t}} = \frac{L}{L_2}\left(\frac{I}{I_{\mathrm{f}}} n_{\mathrm{bf}} P \mu h\right) \tag{1}$$

$$M_{\mathrm{s,t}} < M \le M_{\mathrm{y,t}} = \min\left\{\frac{L}{L_2} M_{\mathrm{y1}}, \frac{L}{L_2} M_{\mathrm{y2}}, \frac{L}{L_1} M_{\mathrm{yr}}\right\} \tag{2}$$

$$M_{\mathrm{y,t}} < M \le M_{\mathrm{u,t}} = \min\left\{\frac{L}{L_2} M_{\mathrm{u1}}, \frac{L}{L_2} M_{\mathrm{u2}}\right\} \tag{3}$$

Where:

M	Design bending moment value of the beam root
$M_{\mathrm{s,t}}$	Slip bending moment value

$M_{y,t}$	Yield moment value of the beam root
$M_{u,t}$	Ultimate moment value of the beam root
L_1, L_2, L	Distances from the loading point to section 1-1, to the center of the connection area, and to the edge of the column, respectively
I, I_f	Inertia moment of the total section of the beam and the inertia moment of the beam flange, respectively
M_{yr}	Yield moment value of the beam section 1-1
n_{bf}	Number of bolts on one side of the splicing center line
P	Pre-tension of high-strength bolt
μ	Anti-slip coefficient
h	Depth of the beam

In Eq. (2), the yield load of the bolt rod M_{y1} and the yield load of the hole wall M_{y2} shall be calculated first, with the calculation methods as presented in Eq. (4) and Eq. (5), respectively. In Eq. (3), the ultimate load of the bolt rod (M_{u1}) and the ultimate load of the hole wall (M_{u2}) shall be calculated first, with the calculation methods outlined in Eq. (6) and Eq. (7), respectively.

$$M_{y1}=\frac{I}{I_f}n_{bf}h\left(0.58A_e^b f_y^{bo}+P\alpha_1\mu\right) \tag{4}$$

$$M_{y2}=\frac{I}{I_f}n_{bf}h\left(t_f D f_y^b+P\alpha_1\mu\right) \tag{5}$$

$$M_{u1}=\frac{I}{I_f}n_{bf}h\left(0.58A_e^b f_u^{bo}+P\alpha_1\mu\right) \tag{6}$$

$$M_{u2}=\frac{I}{I_f}n_{bf}h\left(t_f D f_u^b+P\alpha_1\mu\right) \tag{7}$$

Where:

A_e^b	Effective sectional area at the bolt thread
f_y^{bo}, f_u^{bo}	Yield strength and ultimate strength of bolt steel, respectively
f_y^b, f_u^b	Yield strength and ultimate strength of steel beam, respectively
α_1	Flange friction reduction coefficient
t_f	Flange thickness
D	Diameter of the screw hole

3. The establishment and validation of the FE model for PSCU

3.1. The establishment of the FE model for PSCU

Fig.5 shows the geometric details of PSCU model. The lengths of the column and beam are 3000mm and 1835mm, respectively. The steel column adopts the tube column of 400mm×350 mm×16 mm. The common section and widen flange section of H-shaped beam adopt 300mm×200mm×12mm×8mm and 300mm×250mm×12mm×8mm, respectively. All bolts are 10.9 grade high-strength bolts with a diameter of 20mm, and standard size 22mm diameter holes are provided on all components.

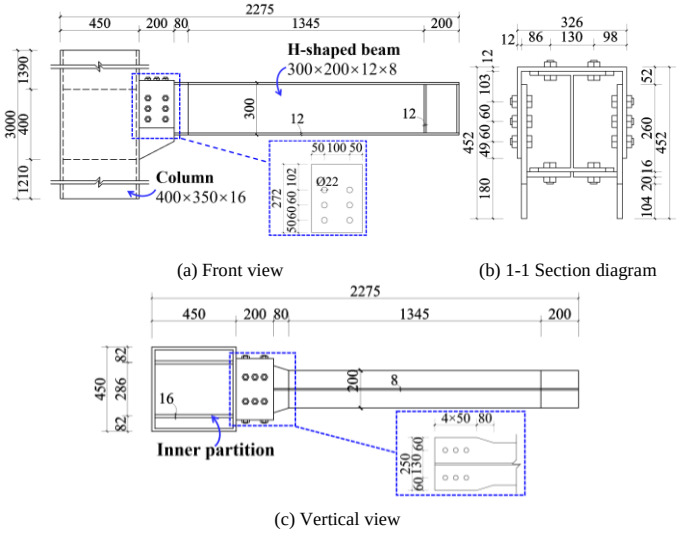

Fig. 5 Geometric dimensions of PSCU

The developed FE model of PSCU is depicted in Fig.6. The three-dimensional eight-node reduced integration solid element (C3D8R) was utilized for each component of the connection. Mesh sizes, particularly in critical areas such as bolt holes and the U-shaped plate, were refined. Contact relationships were established among the U-shaped plate, T-shaped plate, beam, and bolts. The contact property included tangential behavior with a "Penalty" friction formulation and normal behavior with "Hard Contact." The tangential friction coefficient between the contact plates was taken as 0.35, while the friction coefficients for the bolt-related contact surfaces were all set to 0.05. The material properties are shown in Table 1. The value of the ultimate strain is the strain measurement recorded when the material reaches its ultimate strength.

Table 1
Material properties of the steel and bolt

Materials	Q235	Q355	High-strength bolt
Density ρ (10^{-9}t/mm^3)	7.85	7.85	7.85
E (10^5MPa)	2.06	2.06	2.06
Poisson's ratio v	0.3	0.3	0.3
Yeild strength f_y (MPa)	235	355	940
Ultimate strength f_u (MPa)	375	470	1140
Yield strain (%)	0.145	0.184	0.470
Ultimate strain (%)	2.500	2.233	1.470

Hinge constraints were applied to the top and bottom of the column, and axial pressure with an axial pressure ratio of 0.3 was applied at one end of the column. Additionally, to prevent out-of-plane instability of the beam, lateral restraints were implemented at the free end. A rigid plate was introduced at the loading point of the beam free end to mitigate stress concentration. The positive direction was considered upward, while the opposite direction was deemed negative.

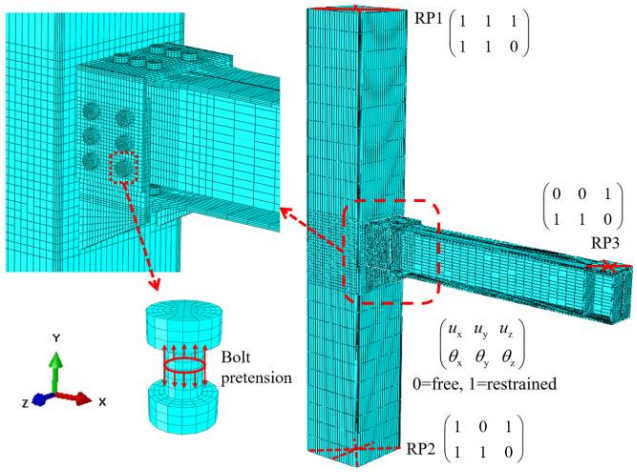

Fig. 6 FE model of PSCU

The loading process for PSCU was conducted in three sequential steps: 1) Applying pretension to the high-strength bolts; 2) Applying axial pressure at the top end of column; 3) Applying low-cycle reciprocating load at the center point of the top surface of the rigid plate. The loading system for PSCU, as per the seismic code of ANSI/AISC 341-16 [27], is illustrated in Fig.7. The cyclic displacement loading was controlled by the inter-story drift angle(θ), representing the ratio of the beam end displacement to the distance from the loading point to the centerline of column (1950mm).

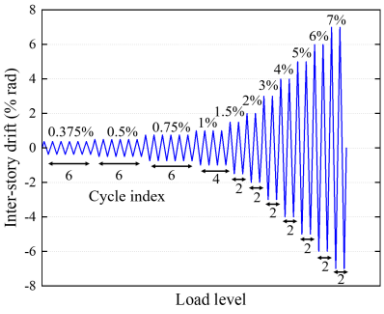

Fig. 7 Loading system

3.2. Verification of the FE model for PSCU

In order to conduct a comprehensive simulation analysis of the seismic performance and post-earthquake reparability of PSCU, it is imperative to pre-validate the established finite element model for PSCU. To achieve this, the same modeling approach employed for PSCU was utilized to model a Z-type cantilever beam splices of the column-tree connection test model (CT-SLIP) [28, 29]. The structural details of CT-SLIP are illustrated in Fig.8. A detailed comparison of the modeling parameters between PSCU and CT-SLIP is presented in Table 2.

Table 2
Model parameters of PSCU and CT-SLIP

Model	Steel tube columns				H-shaped beams				High strength bolt grade	Element type	Contact relation-ships	Friction coeffi-cient
	Length (mm)	Section size (mm)	Steel grade	Boundary	Length (mm)	Section size (mm)	Steel grade	Boundary				
PSCU	3000	200×200×16	Q355	Hinge	1950	300×200×8×12	Q235	Lateral restraints	10.9	C3D8R	Hard contact	0.35
CT-SLIP	3000	400×350×16	Q355	Hinge	1835	300×200×8×12	Q235	Lateral restraints	10.9	C3D8R	Hard contact	0.35

Upon comparison, it was observed that CT-SLIP differs from PSCU in only two aspects: differences in column cross-sectional dimensions and the location of the beam-end loading. From the experimental results of CT-SLIP, it is noted that the column in CT-SLIP did not undergo plastic deformation throughout the entire test. Simultaneously, during result analysis, the numerical values of beam-end loading were transformed into moments, serving as the indicator for subsequent analyses. Consequently, these two differences do not compromise the validation of the finite element modeling approach. All other model parameters for both types of connections remain identical. The developed FE model of CT-SLIP is depicted in Fig.9.

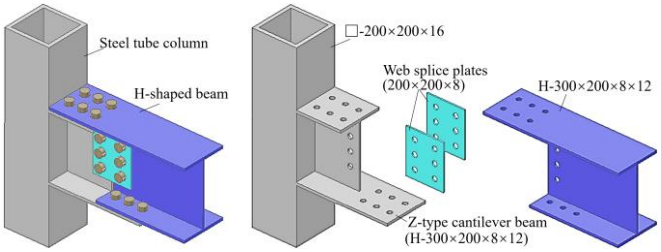

(a) Construction of CT-SLIP (b) Details of CT-SLIP

Fig. 8 The CT-SLIP connection

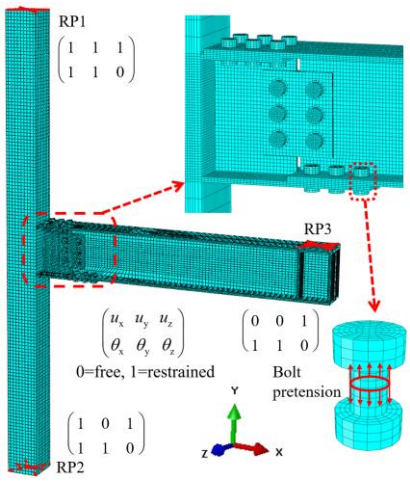

Fig. 9 FE model of CT-SLIP

The low-cycle reciprocating load, which was shown in Fig.7, was applied to the CT-SLIP model, and the finite element results were compared with the experimental results in Reference [30]. As depicted in Fig.10, the failure mode of the CT-SLIP connection obtained through FE analysis is consistent with the experimental failure mode, demonstrating local buckling of the lower flange of the cantilever beam. The stress diagram obtained from the finite element simulation clearly indicate that the stress levels on the cross-section of the column in CT-SLIP consistently remain below the yield strength of the steel. The entire cross-section of the column remains in the elastic phase. This validates the correctness of the earlier assumptions.

Comparing the hysteresis curves from tests and FE analysis reveals that the FE model accurately predicts the ultimate bearing capacity, initial stiffness, and unloading stiffness of CT-SLIP, with only little discrepancies observed in the pinching behavior of the hysteresis curve. This is attributed to the finite element model neglecting initial defects in geometric, material, and contact relationships, along with relatively idealized boundary conditions and uncertainties in material and component properties. As a result, the initial slip moment obtained from the finite element analysis is slightly larger than the experimental value, and the pinching behavior in the finite element curve is slightly less pronounced. Nonetheless, both exhibit a good overall consistency, indicating that the main characteristics of the finite element curve align well with experimental values, affirming the correctness and reliability of the finite element modeling approach adopted in this study.

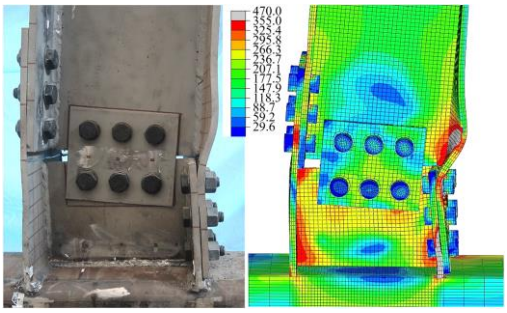

(a) Failure models

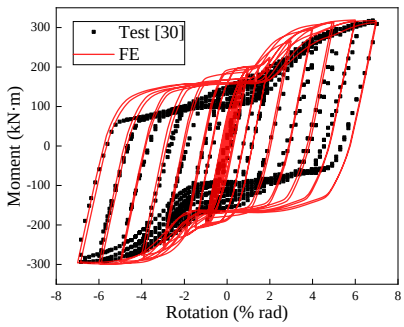

(b) Moment-Rotation curve under cyclic load

Fig. 10 Comparison of test results and FE results for CT-SLIP

4. Numerical analysis of PSCU

4.1. Failure mode of PSCU

The finite element model of PSCU was simulated, and the hysteresis curve and skeleton curve of the connection were extracted, as shown in Fig.11. Stress diagrams of PSCU, relative displacement diagrams of bolt holes, and PEEQ plastic strain diagrams are shown in Fig.12. The analysis reveals the following: 1) When the connection rotation (θ) is less than 0.004rad, both positive and negative skeleton curves exhibit linear variations. The stress in each component of the connection area does not reach the yield strength, and there is no relative slipping, as shown in Fig.12(a) and (b). Thus, it can be defined as: "When $\theta <$ 0.004rad, PSCU is in the elastic stage." 2) When θ reaches 0.004rad, noticeable inflection points appear in both positive and negative skeleton curves, causing a sudden drop in connection stiffness. The stress in each component of the connection area still does not reach the yield strength, but significant relative

slipping occurs between the plates, as shown in Fig.12(c) and (d). Since the slipping stage stops at θ = 0.01rad under positive loading, the bearing capacity of the connection continues to increase. During negative loading, the slipping stage continues until θ = 0.02rad, after which the bearing capacity continues to rise. Thus, it can be defined as: "When 0.004 ≤ θ < 0.01rad (under positive loading) or 0.004 ≤ θ < 0.02rad (under negative loading), PSCU is in the slipping stage." 3) After the slipping stage, the positive and negative load-carrying capacities of the connection significantly increase. At this point, only the maximum stress on the U-shaped plate exceeds its yield strength, and the U-shaped plate starts to yield, as shown in Fig.12(e) and (f). Until θ = 0.04rad, a small yielded area appears at the variable cross-section of the beam end, as shown in Fig.12(g) and (h). In this stage, the maximum bearing capacity of PSCU has not reached its ultimate bearing capacity, but the difference is small. Thus, it can be defined as: "When 0.01 ≤ θ < 0.04 rad (under positive loading) or 0.02 ≤ θ < 0.04 rad (under negative loading), PSCU is in the elastic-plastic stage." 4) With continued loading, the bearing capacity still slightly increases, but the connection rotation significantly increases. Plastic hinges appear at the variable cross-section of the beam end and continue developing. Thus, it can be defined as: "When θ > 0.04 rad, PSCU is in the plastic stage." The loading simulation terminates at θ = 0.07rad due to extremely low efficiency in subsequent calculations.

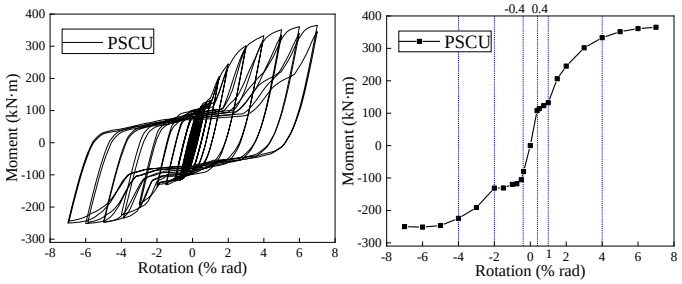

(a) Hysteresis curve (b) Skeleton curve

Fig. 11 FE result curves of PSCU

In light of the foregoing, the entire lateral resistance process of the connection can be delineated into four distinct stages: elastic stage, slipping stage, elastic-plastic stage, and plastic stage, each corresponding to one of the four design criteria depicted in Fig.3. Specifically, under frequent earthquakes, it is imperative for PSCU to maintain an elastic state, with a prescribed inter-story drift angle limit of 0.004rad, a criterion consistent with the stipulations outlined in specifications [31]. In the context of seismic design actions, PSCU is permitted to transition into the slipping stage, wherein none of the constituents within the connection area undergo yield. The connection can exploit frictional energy dissipation, necessitating post-earthquake recovery solely for bolted connections. Under fortification earthquakes, PSCU can harness the yielding behavior of the U-shaped plate for energy dissipation, affording protection to other structural elements. Consequently, the connection enters the elastic-plastic stage, with post-earthquake recovery limited to the U-shaped plate and its corresponding bolted connections. The inter-story drift angle limit at this juncture is set at 0.04, manifesting a conspicuous surplus in contrast to the elastic-plastic inter-story drift angle limit delineated in specifications [31]. In instances of extremely rare earthquakes, the plastic hinge can be formed at the variable cross-section of the frame beam, thereby augmenting the structural capacity for energy dissipation. Subsequent to seismic occurrences, restorative measures might necessitate the replacement of the beam. These deductions substantiate the accuracy of the seismic design objectives and post-earthquake recovery methodologies expounded in Section 2.2 of this discourse.

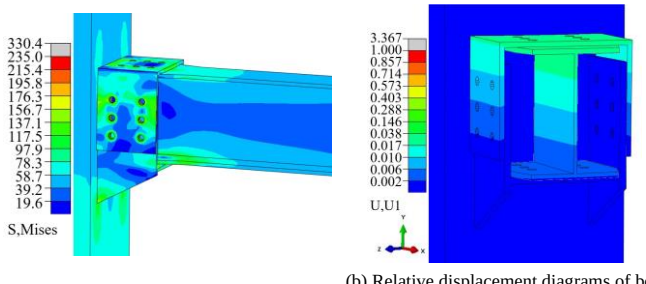

(a) Stress diagrams (θ=0.004rad) (b) Relative displacement diagrams of bolt holes (θ=0.004rad)

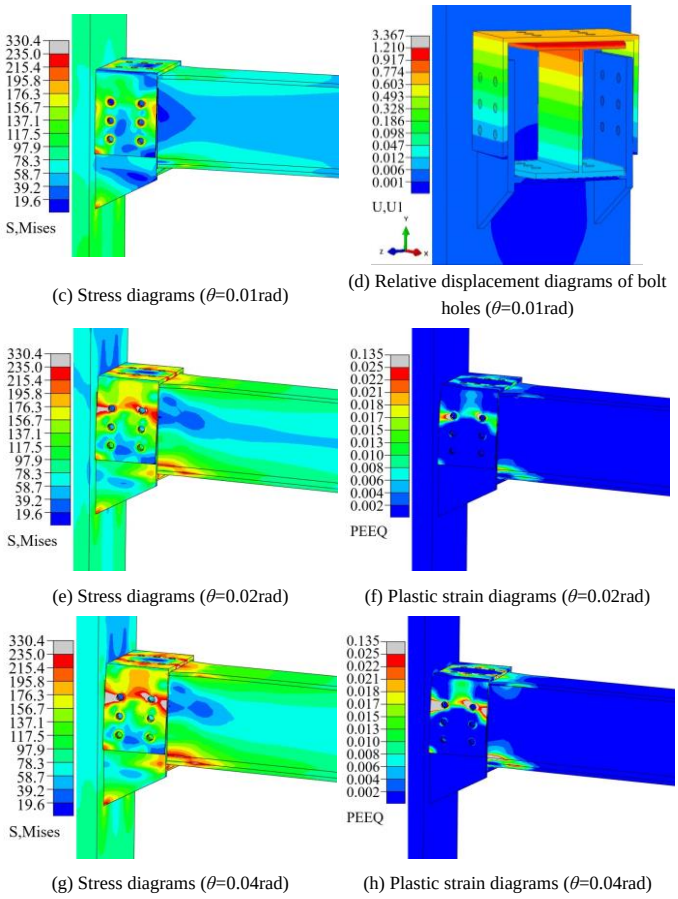

(c) Stress diagrams (θ=0.01rad) (d) Relative displacement diagrams of bolt holes (θ=0.01rad)

(e) Stress diagrams (θ=0.02rad) (f) Plastic strain diagrams (θ=0.02rad)

(g) Stress diagrams (θ=0.04rad) (h) Plastic strain diagrams (θ=0.04rad)

Fig. 12 FE result diagrams of PSCU

4.2. Seismic performance evaluation of PSCU

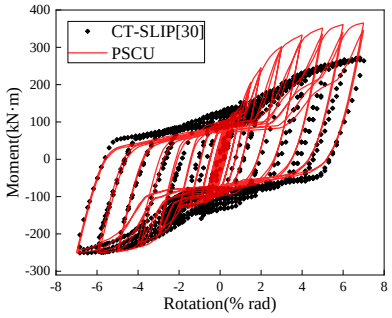

Fig. 13 Comparison of the hysteretic curves between PSCU and CT-SLIP

Comparing the key performance indicators of PSCU and CT-SLIP as presented in Table 3 reveals that the two models differ only in the construction at the connection area. Analyzing the hysteresis curves of both models provides an effective preliminary assessment of the seismic performance of PSCU. A comparison of the hysteresis curves of PSCU and CT-SLIP, as shown in Fig. 13, yields the following insights:

1) The hysteresis curve of PSCU exhibits asymmetry in both positive and negative directions, attributed to the structural asymmetry of the upper and lower parts of the connection area of PSCU. Under positive loading conditions, the PSCU undergoes slipping, culminating in the top of the U-shaped plate making contact with the column. Subsequently, a substantial portion of anticlockwise bending moment is directly transmitted to the column through the U-shaped plate. Under negative loading, the PSCU has limited bending moment transmission capacity, as only the bottom corners of the U-shaped plate contact the column after slipping. Additionally, the longer duration of slipping under negative loading results in a noticeably smaller negative ultimate bearing capacity compared to the positive one.

2) The more pronounced pinching effect in the hysteresis curve of PSCU indicates a smaller residual displacement after seismic shaking compared to CT-SLIP. This is advantageous for the post-earthquake recoverability of the connection.

Table 3 provides the key performance indicators for PSCU and CT-SLIP.

Among them, the ultimate moment (M_u) represents the moment corresponding to the maximum rotation (θ_u), and the ductility coefficient (μ) is the ratio of the maximum rotation to the slipping rotation (θ_s) [30]. Due to the absence of a significant reduction in load-bearing capacity throughout the loading process, the actual ductility coefficient of PSCU should be greater than the calculated value in the table. A comparison with CT-SLIP reveals that under positive loading, PSCU exhibits a significantly higher initial stiffness (K_0), and under negative loading, its initial stiffness is comparable to that of CT-SLIP. PSCU has a smaller slipping moment, indicating a greater tendency for relative slipping between its components. Moreover, PSCU demonstrates higher ultimate bearing capacity, superior ductility, and comparable energy dissipation capacity (E) to CT-SLIP.

Table 3
Key performance indicators of CT-SLIP and PSCU

Connection	Direction	K_0 (kN/mm)	θ_s (% rad)	M_s (kN·m)	θ_u (% rad)	M_u (kN·m)	μ	E (kJ)
CT-SLIP	Positive	5.65	0.74	149.75	6.88	277.41	9.33	249.02
	Negative	5.76	0.73	152.65	6.85	252.64	9.32	
PSCU	Positive	7.56	0.43	107.79	7.00	365.15	>16.27	252.39
	Negative	5.62	0.50	105.44	6.01	251.46	>12.02	

Combining the analysis of the failure mode of PSCU, it is evident that PSCU not only effectively fulfills the initial seismic design objectives, meeting current standards, but also enhances the ultimate bearing capacity, ductility, and post-earthquake repairability of prefabricated steel frame beam-column connections while ensuring overall energy dissipation performance.

5. Parametric analysis of PSCU

Utilizing the PSCU as the foundational model (BASE), this study systematically examines the influence patterns of distinct parameters on the seismic resistance and post-earthquake functional recovery of this connection. The investigated parameters encompass variations in the U-shaped plate thickness (t_U), T-shaped plate thickness (t_T) and the quantity of connecting bolts in different orientations. Model designations and their respective parameter metrics are delineated in Table 4.

Table 4
Parameters of FE models

Model	t_U (mm)	t_T (mm)	n_u	n_s	n_b
BASE	12	16	6	6	6
U-10	10	16	6	6	6
U-16	16	16	6	6	6
T-12	12	12	6	6	6
T-18	12	18	6	6	6
TP-4	12	16	4	6	6
TP-8	12	16	8	6	6
WB-4	12	16	6	4	6
WB-8	12	16	6	8	6
BT-4	12	16	6	6	4
BT-8	12	16	6	6	8

Notes: n_u, n_s and n_b are the number of the upper flange bolts, number of bolts on one side and number of the lower flange bolts, respectively.

5.1. U-shaped plate thickness

Through finite element analysis and theoretical calculations on the 11 models presented in Table 4, key performance indicators for each model were obtained, as detailed in Table 5. Failure modes, hysteresis curves, and skeleton curves were extracted for the U-10, BASE, and U-16 models, as illustrated in Fig.14. Comparative analysis of the finite element simulation results for these three models reveals the following:

1) As the thickness of the U-shaped plate increases, the stress at both the T-shaped plate and the beam end significantly increases. When the U-plate thickness is 16mm, in the final loading stage, certain regions of the T-shaped plate also undergo plastic deformation, which contradicts the post-earthquake functional recovery requirement;

2) The increase of U-shaped plate thickness has a negligible impact on the initial stiffness (K_0) and slipping moment (M_s) of PSCU, with no significant effect on the slipping angle (θ_s);

3) The ultimate bearing capacity (M_u) of the connection correlates positively with the increase in U-shaped plate thickness, especially in the negative direction of connection bearing capacity. Enlarging U-shaped plate thickness significantly diminishes the discrepancy in positive and negative ultimate bearing capacities of PSCU.

4) A comparative analysis of finite element results and theoretical results indicates an error margin generally within 7%, with theoretical results consistently undershooting finite element results. This underscores the scientific and accurate nature of the theoretical model established in Section 2.2.

Table 5
Key performance indicators of FE models

Model	Direction	K_0 (kN/mm)	θ_s (% rad)	M_s (kN·m)	θ_u (% rad)	M_u (kN·m)	μ	E (kJ)	$M_{s,t}$ (kN·m)	$M_{u,t}$ (kN·m)
BASE	Positive	7.56	0.43	107.79	7.00	365.15	>18.7	204.4	102.5	360.7
	Negative	5.62	0.50	105.44	6.01	251.46	>12.0		100.6	238.8
U-10	P	7.49	0.42	106.83	6.99	357.69	>18.7	189.2	101.9	355.3
	N	5.45	0.50	102.68	5.02	214.54	>10.0		100.3	199.6
U-16	P	7.69	0.42	109.65	7.01	378.07	>18.7	225.0	102.9	370.2
	N	5.88	0.50	108.87	7.00	318.59	>14.0		100.9	308.4
T-12	P	6.69	0.43	95.33	7.00	324.99	>18.7	175.3	100.6	336.3
	N	5.64	0.50	103.31	7.00	247.36	>14.0		99.1	238.8
T-18	P	7.91	0.44	112.34	7.00	365.28	>18.7	210.6	103.8	369.1
	N	6.03	0.50	109.08	6.02	258.46	>12.0		102.8	238.8
TP-4	P	7.45	0.41	106.28	7.00	361.40	>18.7	194.7	102.5	360.7
	N	5.49	0.44	78.32	5.03	249.64	>13.3		84.8	238.8
TP-8	P	7.57	0.42	107.94	7.00	370.21	>18.7	195.5	102.5	360.7
	N	5.54	0.50	72.02	6.00	245.31	>16.0		80.5	238.8
WB-4	P	7.48	0.43	106.62	6.99	363.54	>18.7	183.4	102.5	360.7
	N	4.99	0.42	68.09	7.02	245.94	>18.7		67.1	216.9
WB-8	P	7.57	0.44	107.82	6.02	363.15	>16.0	220.8	102.5	360.7
	N	5.94	0.50	113.62	6.00	262.92	>12.0		119.2	272.6
BT-4	P	5.60	0.42	79.82	6.01	327.80	>18.7	187.4	74.6	300.6
	N	5.56	0.50	102.26	7.01	248.95	>14.0		100.6	238.8
BT-8	P	8.71	0.44	124.21	7.03	397.13	>18.7	221.2	122.7	412.3
	N	5.72	0.50	106.98	6.02	260.21	>12.0		100.6	238.8

Notes: $M_{s,t}$ and $M_{u,t}$ are the theoretical results of slip moment and ultimate moment, respectively, which were calculated by Eq.(1)-(3).

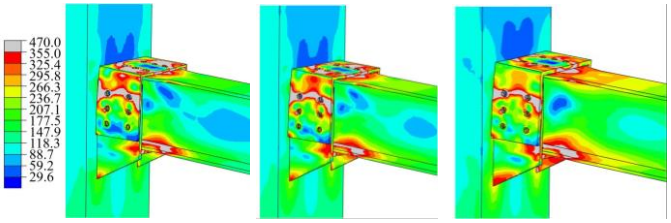

(a) U-10 (b) BASE (c) U-16

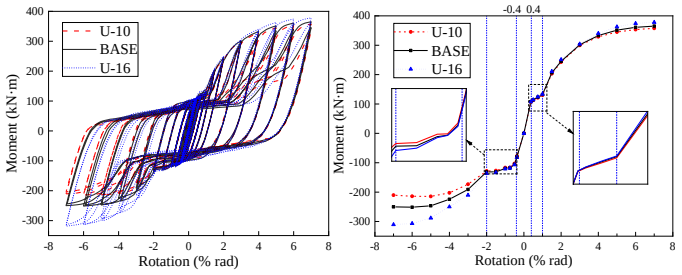

(d) Hysteretic curves (e) Skeleton curves

Fig. 14 Failure modes and result curves of FE models

5.2. T-shaped plate thickness

The failure modes, hysteresis curves, and skeleton curves of the models of T-12, BASE, and T-18 are extracted, as shown in Fig.15. Combining the key performance indicators of these 3 models in Table 5, the analysis indicates that:

1) As the thickness of the T-shaped plate increases, the stress within the plate decreases markedly, the yielding zone in the U-shaped plate remains essentially unchanged, and there is a slight decrease in stress at the variable cross-section of the beam end;

2) When the thickness of the T-shaped plate is 12mm, PSCU only exhibits a significant decrease in slip load and ultimate bearing capacity under positive loading, with the initial stiffness of the overall connection decreasing by 12% compared to the BASE model, and a 14.2% decrease in cumulative energy dissipation. This indicates that in the design of PSCU, priority should be given to ensuring that the T-shaped plate does not yield, thereby ensuring that the connection has good seismic performance, which is also an important condition for achieving the post-earthquake functional recovery of PSCU;

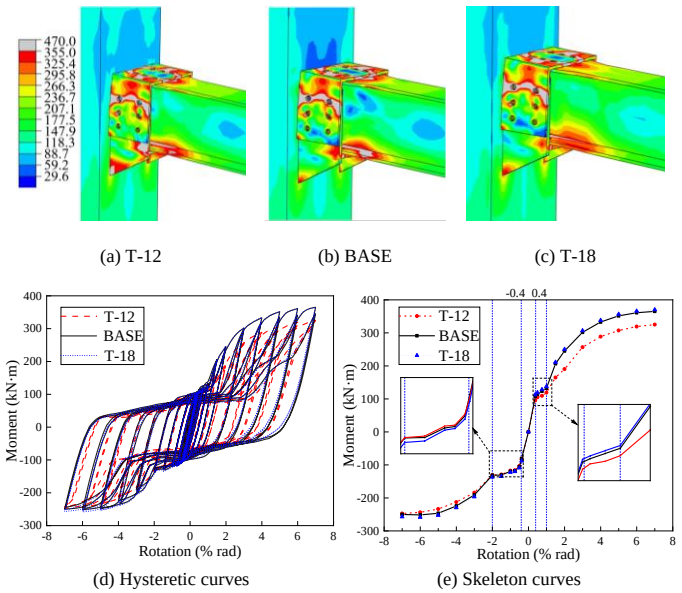

(a) T-12 (b) BASE (c) T-18

(d) Hysteretic curves (e) Skeleton curves

Fig. 15 Failure modes and result curves of FE models

3) When the thickness of the T-shaped plate is 18mm, PSCU only has a slight increase in initial stiffness (4.6% increase in positive direction, 7.3% increase in negative direction), and the improvement in other performance indicators does not exceed 3%. This indicates that once the T-shaped plate does not yield during loading, increasing its thickness does not significantly affect the seismic performance of the PSCU;

4) The error between the finite element results and the theoretical results can still be controlled within 10%, indicating that the accuracy of the theoretical model can still be ensured after changing the thickness of the T-shaped plate.

5.3. Number of bolts connecting between U-shaped plate and upper flange of beam

The failure modes, hysteresis curves, and skeleton curves of the models of TP-4, BASE, and TP-8 are extracted, as shown in Fig.16. Combining the key performance indicators of these 3 models in Table 5, the analysis indicates that:

1) The number of connecting bolts on the upper flange of the beam has a negligible impact on the initial stiffness and ultimate bearing capacity of the PSCU;

2) Reducing the number of connecting bolts on the beam upper flange has a minor effect on the load-bearing capacity of the PSCU under positive loading conditions, but it significantly influences the negative slipping process. This occurs because a reduction in the number of connecting bolts decreases the maximum static friction between the U-shaped plate and the beam upper flange. When the external load reaches this maximum static friction force, the U-shaped plate slides first between the upper flange of the beam until the bolt rod contacts the hole wall, and then the remaining bolt connections begin to slide, forming a two-stage slipping phenomenon, as shown by the red curve in Fig.16 (e);

3) Increasing the number of connecting bolts on the upper flange of the beam only does not enhance the slipping load of the PSCU. This is because while adding more bolts significantly raises the maximum static friction force between the U-shaped plate and the beam upper flange, it also makes sliding at that specific connection more difficult. Consequently, other bolt connections may experience premature slipping, resulting in minimal overall slipping of the beam upper flange throughout the loading process;

4) Comparing the cumulative energy dissipation, it can be obtained that regardless of whether the number of bolts is increased or decreased, the cumulative energy dissipation of the connection is reduced (compared to the BASE model, TP-4 is reduced by 4.7%, and TP-8 is reduced by 4.4%), indicating that appropriate slipping between the components contributes to the energy dissipation of PSCU.

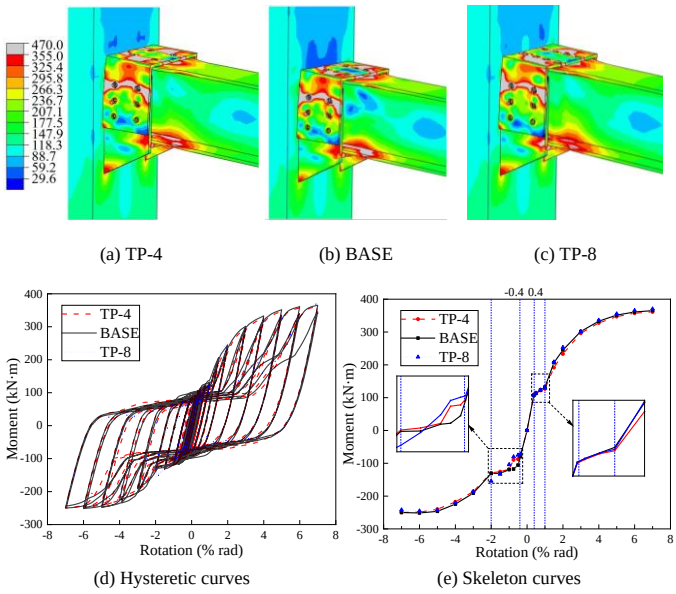

(a) TP-4 (b) BASE (c) TP-8

(d) Hysteretic curves (e) Skeleton curves

Fig. 16 Failure modes and result curves of FE models

5.4. Number of bolts connecting between U-shaped plate and T-shaped plate on one side

The failure modes, hysteresis curves, and skeleton curves of the models of WB-4, BASE, and WB-8 are extracted, as shown in Fig.17. Combining the key performance indicators of these 3 models in Table 5, the analysis indicates that:

1) The influence of increasing the number of bolts connecting the U-shaped plate and T-shaped plate on the ultimate bearing capacity, initial stiffness, and positive slip load of PSCU remains inconspicuous;

2) The reduction in the number of bolts connecting the U-shaped plate and T-shaped plate has a significant impact on the negative slipping process of PSCU. This occurs because a reduction in the number of bolts connecting the U-shaped plate and the T-shaped plate directly results in a decrease in the maximum static friction force between the two components. When the external load reaches this maximum static friction force, slip occurs first between the U-shaped plate and the T-shaped plate, until the bolt shank contacts the hole wall at this point, after which the remaining bolted connections start to slip, thereby forming a two-stage slip phenomenon, as shown by the red curve in Fig.17(e);

3) Only increasing the number of bolts connecting the U-shaped plate and T-shaped plate can increase the negative slip load of PSCU, but its effect is minimal. The sequence of slipping is characterized by the initial slipping of the bolted connections at the upper and lower flanges of the beam, followed by the subsequent slipping of the bolted connections between the U-shaped plate and the T-shaped plate. This results in a two-stage slip phenomenon, as illustrated by the blue curve in Fig. 17(e);

4) Comparing the cumulative energy dissipation, it can be seen that the cumulative energy dissipation of the connection is increased with the increasing

of the number of bolts (compared to the BASE model, WB-4 is reduced by 10.3%, and WB-8 is increased by 8.1%). An observation of the hysteresis curve in Fig. 17(d) reveals that the hysteresis curve for WB-4 exhibits significant pinching. This phenomenon is attributable to the relatively small number of bolts connecting the U-shaped plate and the T-shaped plate in WB-4. With the increase of cyclic loading, the loss of bolt pre-tension force and friction coefficient is severe, and the slip energy dissipation mechanism basically disappears. Therefore, ensuring the reliability of the bolted connection between the U-shaped plate and T-shaped plate is beneficial for improving the energy dissipation performance of PSCU.

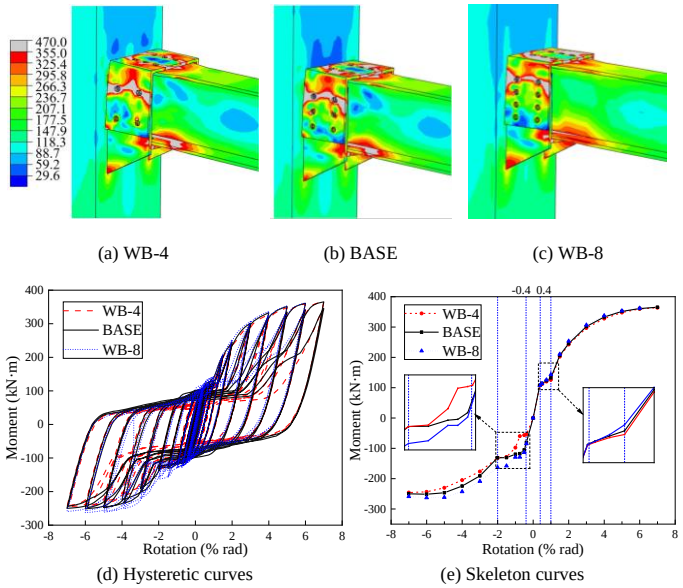

(a) WB-4 (b) BASE (c) WB-8

(d) Hysteretic curves (e) Skeleton curves

Fig. 17 Failure modes and result curves of FE models

5.5. Number of bolts connecting between T-shaped plate and lower flange of beam

The failure modes, hysteresis curves, and skeleton curves of the models of BT-4, BASE, and BT-8 are extracted, as shown in Fig.18. Combining the key performance indicators of these 3 models in Table 5, the analysis indicates that:

1) As the number of connecting bolts between the lower flange of the beam increases, the stress on both the T-shaped plate and the variable cross-section at the beam end rises significantly, and the T-shaped plate of BT-8 has already yielded after loading, which does not meet the requirement for the post-earthquake functional recovery of PSCU;

2) Increasing the number of connecting bolts in the lower flange of the beam has little influence on the negative ultimate bearing capacity, negative initial stiffness, and negative slip load of PSCU;

3) Strengthening the connection strength of the lower flange of the beam will significantly increase the positive stiffness and slip load of PSCU, and at the same time, the positive ultimate bearing capacity of PSCU will also be significantly improved, but this will also make the difference in positive and negative bearing capacities of PSCU more apparent;

4) The cumulative energy dissipation capacity of PSCU significantly improves with the increase in the number of connecting bolts in the lower flange of the beam. This enhancement is attributed not only to the improved positive bearing capacity but also to the reduction in hysteresis curve pinching, which is effectively mitigated by the greater number of bolts.

Considering the analysis results of Sections 5.3, 5.4, and 5.5, and taking into account the seismic performance and the requirement for post-earthquake functional recovery of PSCU, the following design recommendations can be made: To prevent yielding of the T-shaped plate, it is recommended that the number of connecting bolts on the upper flange, lower flange of the beam, and between the U-shaped plate and the T-shaped plate on each side should be kept consistent.

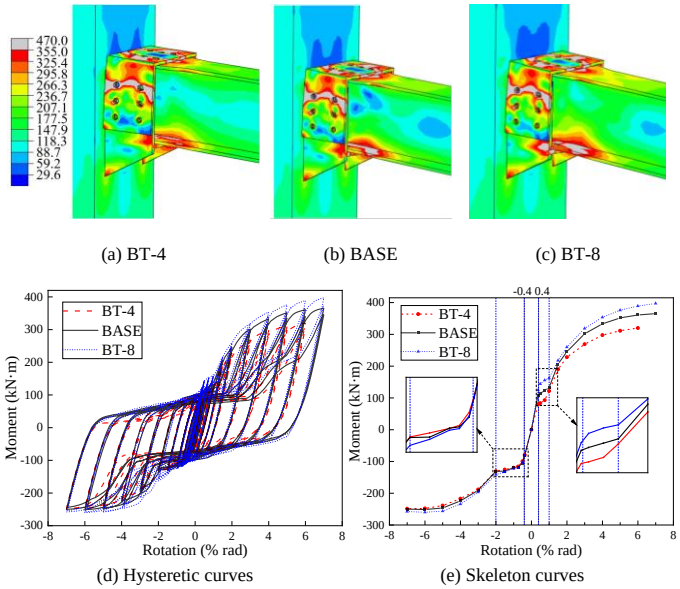

(a) BT-4 (b) BASE (c) BT-8

(d) Hysteretic curves (e) Skeleton curves

Fig. 18 Failure modes and result curves of FE models

6. Conclusion

To investigate the seismic performance and post-earthquake recovery of PSCU, this study employed theoretical methods to establish design criteria and post-earthquake recovery methods for PSCU, and derived design equations for PSCU. Additionally, a refined finite element (FE) model of PSCU was developed and validated, and parameterized numerical analysis of PSCU was conducted. The main conclusions are as follows:

(1) The failure mode of PSCU belongs to typical ductile failure, and even when the rotation angle reaches 0.07rad, PSCU can still ensure the integrity of non-replaceable components, thereby ensuring its good post-earthquake recovery performance.

(2) The entire lateral resistance process of PSCU can be delineated into four distinct stages: elastic stage (the connection rotation angle θ < 0.004rad), slipping stage ($0.004 \le \theta < 0.01$rad under positive loading or $0.004 \le \theta < 0.02$rad under negative loading), elastic-plastic stage ($0.01 \le \theta < 0.04$ rad under positive loading or $0.02 \le \theta < 0.04$ rad under negative loading), and plastic stage ($\theta >$ 0.04 rad).

(3) PSCU can meet the post-earthquake functional recovery requirements through the following measures, namely “no repair is needed in the elastic stage, only bolted connection repair is needed in the slip stage, only U-shaped plate replacement is needed in the elastic-plastic stage, and U-shaped plate and beam replacements are needed in the plastic stage”.

(4) When designing PSCU, the thickness of the U-shaped plate should not exceed that of the T-shaped plate to ensure that the T-shaped plate does not yield throughout the entire lateral resistance process. Bolted connections can be designed based on the elastic limit of the PSCU, and the number of bolts on each connected surface should be as uniform as possible.

(5) By comparing the finite element (FE) results with the theoretical results of all models, it can be obtained that the maximum error is 12%, with an average error of less than 3%. The high level of agreement between the FE results and the theoretical results indicates that theoretical design equations of PSCU established in this paper is relatively scientific and accurate.

Acknowledgement

This research was funded by the Key Research and Promotion Project (Scientific and Technological Project) of Henan Province (No. 242102321013), Postdoctoral research grant in Henan Province (No. 202103010), China Postdoctoral Science Foundation (No. 2023M733248), Scientific and Technological Innovation Leaders in Central Plains of Henan Province (No. 234200510022), and the Support Program for Innovative Research Team (in Science and Technology) in University of Henan Province (No. 23IRTSTHN006).

References

[1] X.C. Liu, S.H. Pu, A.L. Zhang, et al, Performance analysis and design of bolted connections in modularized prefabricated steel structures, Journal of Constructional Steel Research, 2017, 133, 360-373.

[2] Zhang A L, Shangguan G H, Zhang Y X, et al. Experimental study of resilient prefabricated steel frame with all-bolted beam-to-column connections. Advanced Steel Construction, 2020,

16(3): 255-271.
[3] K. Oh, R. Li, L.Y. Chen, et al, Cyclic Testing of steel column-tree moment connections with weakened beam splices, International Journal of Steel Structures, 2014, 14, 471-478.
[4] Koken A, Hatipoglu E T. Investigation of the behavior of weakened and strengthened steel column-beam connections under seismic effects. Advanced Steel Construction, 2014, 10: 1-13.
[5] Guo Y, Yao X. Seismic performance and design of reduced steel beam section with concrete filled square tubular column. Advanced Steel Construction, 2013, 9(3): 173-189.
[6] X.H. Zhang, S.S. Zheng, X.R. Zhao, Seismic performance of steel beam-to-column moment connections with different structural forms, Journal of Constructional Steel Research, 2019, 158, 130-142.
[7] H.B. Liu, J. Lan, Z.H. Chen, et al, Study on the seismic behavior of connection via welding strengthening under load, Journal of Constructional Steel Research, 2022, 196, 107387.
[8] Y.Z. Tian, M. Liu, Z.H. Jia, et al, Study on mechanical behavior and optimization of prefabricated square column H-beam outer-shell joint, Mechanics of Advanced Materials and Structures, 2019, 19, 1-8.
[9] X.C. Liu, X.X. Zhan, S.H. Pu, et al, Seismic performance study on slipping bolted truss-to-column connections in modularized prefabricated steel structures, Engineering Structures, 2018, 163, 241-254.
[10] X.L. Lv, Y. Chen, Y.J. Mao, New concept of structural seismic design: earthquake resilient structures, J Tongji Univ, 2011, 39, 941-948(in Chinese).
[11] X.L. Lv, Y. Chen, H.J. Jiang, Research progress in structural systems with replaceable members, Earthquake Engineering Structural Dynamics, 2014, 34, 27-36 (in Chinese).
[12] Zhao L Y, Guo D, Yang Y Q, et al.Seismic Performance and Replaceability of Steel Frame Structures with Replaceable Beam Segments. Advanced Steel Construction,2024, 20(1): 69-80.
[13] Zhang Y, Wang Z, Zhao W, et al. A pseudo-dynamic test study on a self-centering prefabricated steel frame with a column base connected by semi-rigid joints. Advanced Steel Construction, 2016, 12(3): 296-315.
[14] Y.Z. Chen, L.W. Tong, Y.Y. Chen, Experimental study on cyclic behavior of cast steel connectors for beam-to-column joints, Journal of Structural Engineering, 2016, 19, 1677-1695.
[15] M. Rui, L. Válter, P. Stefano, Development of steel angles as energy dissipation devices for rocking connections, Structural Concrete, 2018, 25, 1-15.
[16] M. Wang, P. Bi, Study on seismic behavior and design method of dissipative bolted joint for steel frame with replaceable low yield point steel connected components, Construction and Building Materials, 2019, 198, 677-695.
[17] M. Wang, X.G. Ke, Seismic design of widening flange connection with fuses based on energy dissipation, Journal of Constructional Steel Research, 2020, 170, 106076.
[18] A.L. Zhang, Q. Wang, Z.Q. Jiang, et al, Experimental study of earthquake-resilient prefabricated steel beam-column joints with different connection forms, Engineering Structures, 2019, 187, 299-313.
[19] Z.Q. Jiang, X.F. Yang, C. Dou, et al, Cyclic testing of replaceable damper: earthquake-resilient prefabricated column-flange beam-column joint, Engineering Structures, 2019, 183, 922-936.
[20] Z.Q. Jiang, T. Lan, C. Dou, et al, Cyclic loading tests of earthquake-resilient prefabricated cross joint with single flange cover plate, Journal of Constructional Steel Research, 2020, 164, 105752.
[21] Z.Q. Jiang, S.H. Lin, X.C. Liu, et al, Influence of bolts on seismic performance of earthquake-resilient prefabricated sinusoidal corrugated web steel beam-column joints, Journal of Constructional Steel Research, 2020, 172, 106214.
[22] A.L. Zhang, H. Zhang, Z.Q. Jiang, et al, Low cycle reciprocating tests of earthquake-resilient prefabricated column-flange beam-column joints with different connection forms, Journal of Constructional Steel Research, 2020, 164, 105771.
[23] Z.Q. Jiang, C. Dou, H. Zhang, et al, Experimental study of earthquake-resilient prefabricated beam-column steel joint with L-shaped plate, Journal of Constructional Steel Research, 2020, 166, 105928.
[24] Z.Q. Jiang, Z.Y. Niu, K.K. Cheng, et al, Experimental study of earthquake-resilient high ductility prefabricated opening-web steel channel beam-column joint, Journal of Building Engineering, 2022, 49, 104041.
[25] Z.X. Bai, C.J. Shen, Z.Q. Jiang, et al, Cyclic loading tests of an earthquake-resilient prefabricated steel frame with open-web steel channel beams, Journal of Constructional Steel Research, 2021, 177, 106477.
[26] X.W. Zhang, X. Rong, X.N. Shi, et al, Experimental evaluation on the seismic performance of high-strength reinforcement beam-column joints with different parameters, Structures, 2023, 51, 1591-1608.
[27] ANSI/AISC 341-16. Seismic Provisions for Structural Steel Buildings. Chicago, USA, American Institute of Steel Construction, 2016.
[28] A.L. Zhang, Z.P. Guo, X.C. Liu, Seismic performance of Z-type cantilever beam splices of column–tree connection, Journal of Constructional Steel Research, 2017, 133, 97-111.
[29] Z.P. Guo, A.L. Zhang, X.C. Liu, et al, Seismic behavior of prefabricated steel frame connection with Z-shaped cantilever beam and reduced beam section, Journal of Building Structures, 2017, 38, 43-52 (in Chinese).
[30] A.L. Zhang, Z.P. Guo, X.C. Liu, et al, Experimental study on seismic performance of prefabricated steel frame joints with Z-shaped cantilever beam segment splicing, Engineering Mechanics, 2017, 34, 31-41(in Chinese).
[31] GB50017-2017. Code for Design of Steel Structures. Beijing, China, 2017.Chan S.L. and Chui P.T., Non-Linear Static and Cyclic Analysis of Steel Frames with Semi-Rigid Connections, Elsevier, New York, 2000.

Advanced Steel Construction – Vol. 20 No. 4 (2024) 406–412
DOI:10.18057/IJASC.2024.20.4.8

EXPERIMENTAL AND NUMERICAL ANALYSIS ON THE MECHANICAL BEHAVIOR OF A GLULAM SUSPENDOME

Chen-Rui Zhang [1], Jian-Xiong Zhao [2, *], Hong-Bo Liu [2, 3], Shi-Xing Zhao [4], Jing-Xian Zhao [2], Shu-Heng Yang [4] and Ting Zhou [2]

[1] *School of Civil Engineering, The University of Sydney, Sydney, Australia*
[2] *Department of Civil Engineering, Tianjin University, Tianjin 300072, China*
[3] *Department of Civil Engineering, Hebei University of Engineering, Handan 056000, China*
[4] *Sichuan Provincial Architectural Design and Research Institute Co., Ltd., Chengdu, Sichuan 610000, China*
** (Corresponding author: E-mail: zhao_jx@tju.edu.cn)*

ABSTRACT

To enhance the overall stability of the glulam reticulated shell, an innovative structural solution, the glulam suspendome, is introduced by integrating a cable-strut system. A destructive test utilizing 13 hydraulic jacks was carried out to assess the overall stability. This study primarily encompassed analyses of load-displacement curves for nodes, load-strain characteristics of structural members, load-cable force assessments of hoop cables, and an investigation into failure mode. The failure mode of the structure involved instability around the weak axis of the member near the mid-span node, along with member fracture. The structure sustained an ultimate load of 1094.21kN (84.17kN×13). Based on the parameter analysis of the finite element model (FEM) of more than 200 cases of glulam suspendome, the ultimate bearing capacity improvement coefficient (k) of the suspendome structure compared with single-layer reticulated shell was given. The experimental and numerical analysis on the mechanical properties of glulam suspendome serves as a dependable point of reference for the design of other glulam suspendome.

ARTICLE HISTORY

Received: 6 January 2024
Revised: 27 June 2024
Accepted: 30 August 2024

KEYWORDS

Glulam suspendome;
Mechanical behavior;
Experimental investigation;
Numerical analysis;
Overall stability

1. Introduction

Nowadays, spatial structures employing steel, aluminum alloy, and glulam as primary materials, notably single-layer reticulated shells, have gained extensive utilization in contemporary public buildings. Ensuring the static stability of spatial structures constitutes an important aspect of structural design. To achieve a more comprehensive understanding of the static stability of single-layer reticulated shells, extensive investigations have been conducted through physical model testing. Ma et al. [1] conducted an experimental inquiry into a reticulated shell made of steel featuring bolt-ball joints, revealing that under the load of 22.43kN, instability occurred at the mid-span joint. Xiong et al. [2, 3] performed an experimental investigation on a reticulated shell connected by aluminum alloy gusset joints. Failure was observed in the rods near the mid-span node when subjected to a load of 99.7kN. For glulam reticulated shell, Lu et al. [4] carried out tests employing various rise-span ratios and bolt arrangement configurations. The structure exhibited an ultimate bearing capacity of approximately 5.50kN, with the failure mode primarily characterized by parallel-to-grain cracking in the compression zone of the glulam members.

Numerous studies have consistently demonstrated the inherent weaknesses in joint stiffness and overall stability within single-layer reticulated shells. To enhance the stability of reticulated shells, a novel structural form known as the suspendome structure has been developed [5]. The suspendome structure achieves higher stiffness and reduces structural deformation under similar loads by increasing cable-strut system within the single-layer reticulated shell. Many experts and scholars have conducted the static properties of the suspendome in detail through model tests, encompassing assessments of structural deformation under both design load and excessive load, as well as evaluating the impact of asymmetric loading on the structure [5-11]. However, there has been a scarcity of experiments conducted to investigate the stability of the suspendome structure. Zhang et al. [12] conducted tests on a suspendome structure, which experienced overall instability leading to pronounced collapse of the structure. The ultimate bearing capacity of the structure was determined to be 327.34kN. The basic profiles of experimental tests are shown in Table 1.

Table 1
Destructive tests of reticulated shells and suspendome

Structural form	Material	Dimension	Loading point	Ultimate load
Single-layer cylindrical reticulated shell [1]	Steel	Span: 5m×6m; Height: 1.25m	Single-point	22.4kN
Single-layer spherical reticulated shell [2, 3]	Aluminum alloy	Span: 8m; Height: 0.5m	Single-point	99.7kN
Single-layer spherical reticulated shell [4]	Glulam	Span: 4m; Height: 0.8m/0.4m	7-points	5.50kN
Suspendome [12]	Steel	Span: 9.3m;Height: 0.93m	442-points	327.34kN

To date, research on suspendome utilizing steel and aluminum alloy had indicated that the upper members of the structure predominantly experience compression. Taking into account the exceptional compressive capabilities of glulam, this paper innovatively applied it to the upper reticulated shell, thereby introducing a novel type of structure termed as the glulam suspendome. However, regarding the static properties and the overall stability of glulam suspendome, no experimental investigations have been conducted thus far.

In this study, the ultimate bearing capacity and the overall stability of glulam suspendome were studied through the destructive test of 13 hydraulic jacks. Based on the theoretical analysis of the instability of the glulam members, the failure mode of glulam suspendome was investigated. Using finite element software, the numerical model of the structure was established, while the parameter analysis of the structures was analyzed. Based on the ultimate bearing capacity of single-layer glulam reticulated shells, the ultimate bearing capacity improvement coefficient (k) of glulam suspendome was given. The test and numerical analysis results of the glulam suspendome have yielded satisfactory outcomes, providing valuable assistance to the structural design.

2. Experimental methods

2.1. Material test

As depicted in Fig. 1, tests were conducted to ascertain the parallel-to-grain compressive strength of the glulam material utilized in this study. TCT24 grade Douglas Fir glulam conforming to GB/T 50708-2012 [13] standard was used in the material test. The specimen was determined in accordance with ASTM

D143[14], while testing was conducted using a 100kN-capacity electronic universal testing machine. The test loading speed was controlled by displacement, with a specific speed of 0.3mm/min. The test results are shown in Table 2.

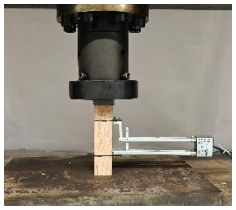

Fig. 1 Parallel-to-grain compressive test

Table 2
Test results of glulam material properties

Material properties (MPa)	Number of specimens	Average value $\bar{X}$	Standard deviation S	Coefficient of variation v
Parallel-to-grain elastic modulus	16	12254	1769	14.44%
Parallel-to-grain compressive strength		43.89	3.87	8.81%

2.2. Specimen design

Serving as the upper structure of the glulam suspendome, the single-layer glulam reticulated shell adopts the Kiewitt-6 structural configuration [15]. In accordance with the suggestions provided in technical specification [16] and relevant literature [17, 18], the design of glulam suspendome in this research entailed a span of 6m and a height of 1.2m, resulting a rise-span ratio of 0.2. The specimen was characterized by a strut height of 0.6 m, while the sag-span ratio was 1/400. The section size and material of each component were shown in Fig. 2.

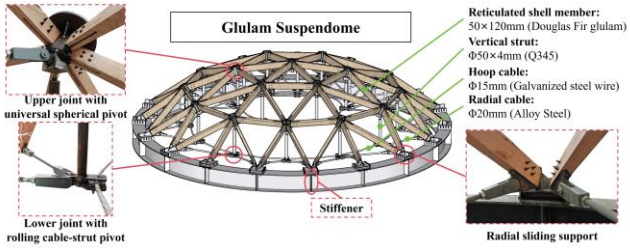

Fig. 2 Diagram and dimension of the glulam suspendome

2.3. Measurement layout

To investigate the mechanical properties of the glulam suspendome, it was essential to accurately measure the displacement of typical nodes, the strain of the members, and the tension of hoop cables. The specific measurement scheme followed the same approach as outlined in the reference [15].

2.4. Prestressed tension and loading scheme

In this research, the prestress ratio was 1:2[19]. LC1 was 4.5kN, while LC2 was 2.25kN. As depicted in Fig. 3, 13 hydraulic jacks were employed for synchronous loading in the destructive test.

The destructive test adopted the same loading method as the full-span loading, utilizing 13 hydraulic jacks to execute synchronous loading. At the beginning of the formal loading, the load was set to 0.1 times the predicted ultimate load (P_u) until the load reached 0.7 times P_u. When the load is 0.7 to 0.8 times Pu, the load for each stage was adjusted to 0.05 times Pu. Once the load reached 0.8 times P_u, a displacement-controlled loading method was adopted. According to ASTM D1761-12 [20], the loading speed was set at 0.9mm/min.

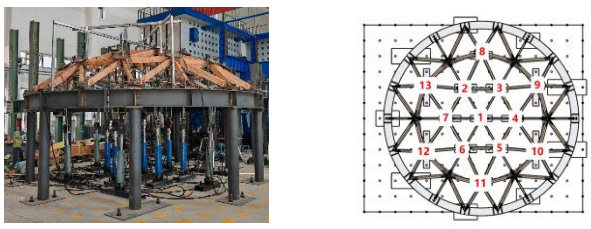

Fig. 3 Diagram of the formal loading in destructive loading

3. Destructive loading

3.1. Failure mode

The load-displacement curve of the 1st node is depicted in Fig. 4, along with the corresponding failure modes of the relevant members during the loading process. When the load reached 26kN, the first crack appeared in the first circumferential member, with the failure location observed in the 4th member. When loading to 52kN, the 55th member of the second main rib exhibited cracking near the bolts. Subsequently, when the load reached 72kN, the 58th member within the same circle sustained damage. The structural damage occurred in the upper reticulated shell of the glulam suspendome, while the cable-strut system remained undamaged.

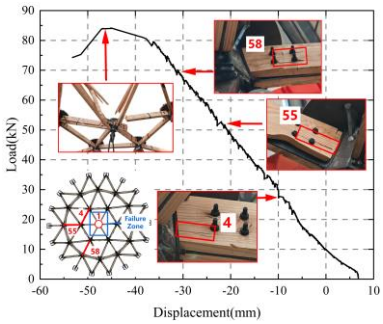

Fig. 4 Load-displacement curve

The ultimate load capacity of the structure was determined to be 84.17kN, with a total load reaching 1094.21kN (84.17kN×13). The displacement recorded at the 1st node reached -45.10mm. Upon reaching the ultimate load, the sound of crack within the glulam material became apparent. Parallel-to-grain cracking was observed in some of the main rib members adjacent to the 1st node. Concurrently, the 37th member experienced a fracture, roughly attributed to the member buckling. Meanwhile, other members adjacent to the 1st node exhibited instability along the weak axis. Members from the 37th to the 42nd rotated around the mid-span node. The structural failure mode was depicted in Fig. 5. Detailed buckling analysis was presented in Section 3.5.

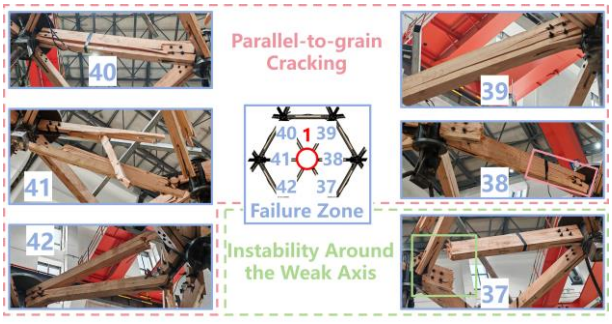

Fig. 5 Failure mode of glulam suspendome

3.2. Load-displacement curves

(1) Node displacement

As shown in Fig. 6a, the displacement of the 2nd, 3rd, 5th and 6th node were recorded as -42.9mm, -38.66mm, -31.65mm, and -35.95mm, respectively. The displacement of the nodes on the first ring exhibited a smaller magnitude compared to that of the 1st node, with a consistent change trend observed across these nodes. This observation suggested that the 13-point synchronous loading scheme effectively ensured symmetrical deformation of the structure.

As depicted in Fig. 6b, among the outer ring nodes of the glulam suspendome, the 15th node exhibited the largest displacement, measuring -24.55 mm. Since the main rib node of the second circle was not the loading point, its displacement was minimal. The displacement of the 8th, 10th, 14th and 16th node were recorded as -2.04mm, -13.14mm, -7.99mm, and -10.12mm, respectively.

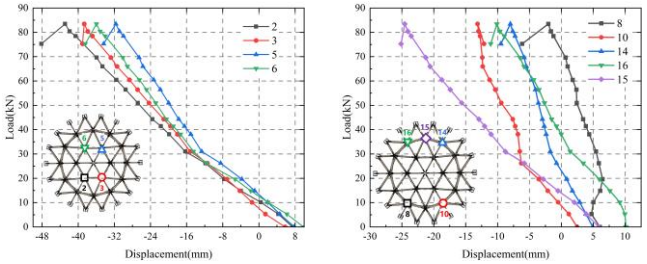

(a) 2, 3, 5, 6 (b) 8, 10, 14, 16, 15

Fig. 6 Node displacement

(2) Support displacement

As depicted in Fig. 7, all support displacements were observed to be radial outward. The displacement of the 35th support was the smallest, measuring 3.16mm. The displacements of 21st and 22nd supports were relatively close, measuring 7.91mm and 8.38mm, respectively.

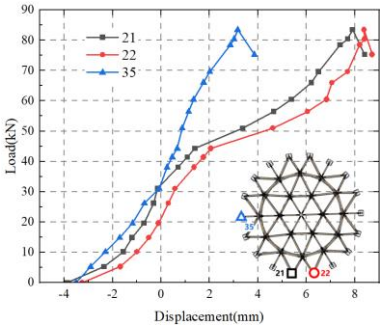

Fig. 7 Load-displacement curves in support

3.3. Cable tension curves

As shown in Fig. 8, the cable force of hoop cables exhibited a positive linear growth relationship with the load. When the structure experienced failure, LC1 measured 97.12kN, while LC2 was recorded as 24.69kN. LC1 was significantly larger than LC2 because nodes in the second circle transferred a greater load to the cable-strut system.

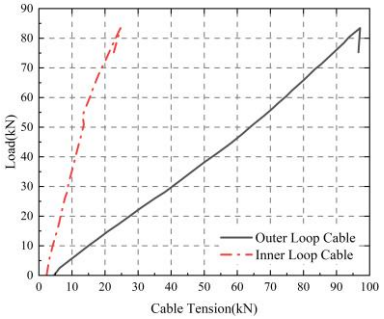

Fig. 8 Cable tension

3.4. Strain distribution curves

To further investigate the mechanical behavior of the glulam suspendome, representative members are selected to analyze.

(1) Reticulated shell member

The main rib members of reticulated shell were analyzed, and their load-strain curves were presented in Fig. 9. Throughout the loading process, the main rib members primarily experienced compression. As illustrated in Fig. 9b and d, the strain of the 39th and 37th member was recorded as -1388.95με and -2186.53με, respectively. The 39th and 37th members of the first circle exhibit the highest force, followed by the members of the second circle, and finally, the outermost ring members displayed the least force.

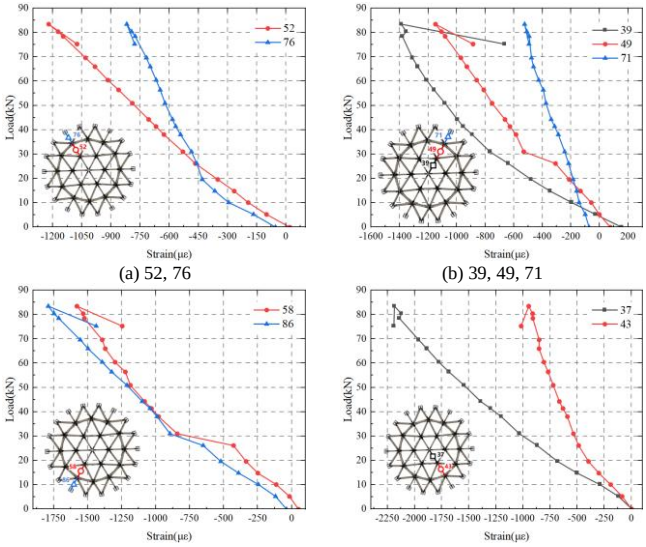

(a) 52, 76 (b) 39, 49, 71

(c) 58, 86 (d) 37, 43

Fig. 9 Load-strain curves in radial members

As depicted in Fig. 10, an analysis of the circumferential members of the reticulated shell was conducted. The members of the first ring experienced compression, while members of the second ring underwent strain. The strain of the 6th and 18th member at failure state was recorded as -930.64με, 189.57με, respectively.

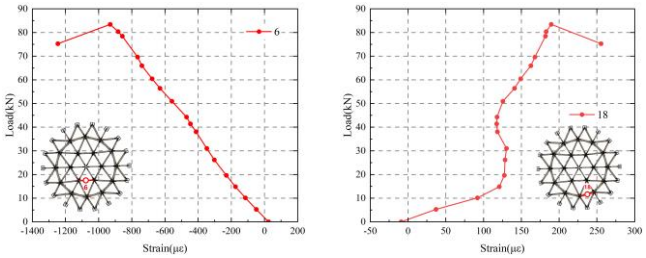

(a) 6 (b) 18

Fig. 10 Load-strain curves in circumferential members

As depicted in Fig. 11, an analysis of the diagonal members of the reticulated shell was conducted. Obviously, all diagonal members were subjected to compression, with the pressure trend of symmetric members exhibiting consistency. As shown in Fig. 11a, the strain of the 60th and 59th member was recorded as -1106.38με and -584.26με. As depicted in Fig. 11b, the strain of the 87th and 90th member approached -1800με, while the strain of the 88th and 89th member was close to -850με. The compressive strain of the 90th member was the largest, measured at -1865.93με.

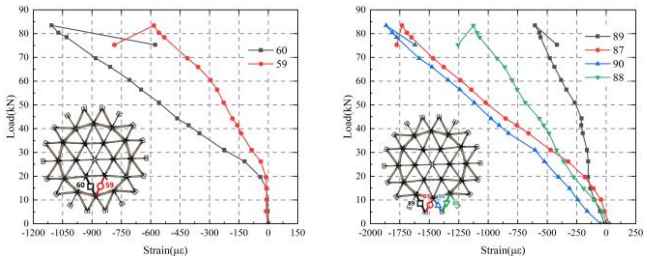

(a) 59, 60 (b) 89, 87, 90, 88

Fig. 11 Load-strain curves in diagonal members

(2) Vertical strut

As illustrated in Fig. 12, the struts of the glulam suspendome experienced compression during loading. The force on the 91st and 92nd struts was nearly identical, with their strain measuring close to -190με. Among the struts corresponding to the third circle nodes, the 97th strut exhibited the largest force, while the 98th strut had the smallest force. The maximum compressive strain was recorded at -242.23με.

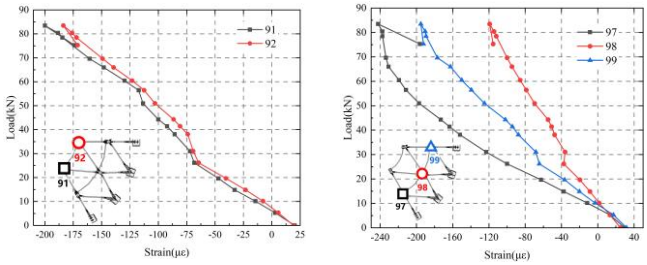

(a) 91, 92 (b) 97, 98, 99

Fig. 12 Load-strain curves in vertical struts

(3) Radial cable

The radial rods corresponding to the main rib members of the reticulated shell were analyzed, as shown in Fig. 13a. The strain of the 127th and 128th member was recorded as 408.35μεand 497.82με, respectively.

As shown in Fig. 13b, radial cables in the third circle were all tensioned, with a relatively consistent changing trend. Among them, the strain of the 151st rod was the largest, measuring 838.26με. The strain of the 161st and 164th rods was approximately 400με, while the strain of the 163rd rod was the smallest, measured at 85.62με.

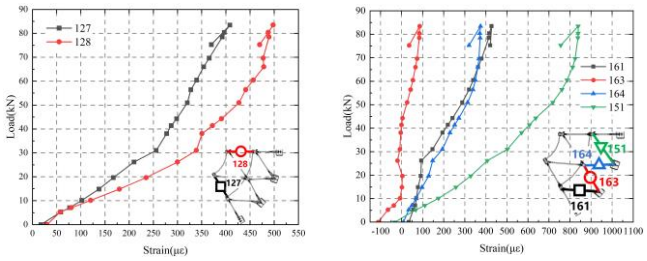

(a) 127, 128 (b) 161, 163, 164, 151

Fig. 13 Load-strain curves in radial cables

3.5. Analysis of the member buckling

As depicted in Fig. 14, an assessment was conducted to ascertain whether any glulam member became buckled by calculating the axial force of the main rib member. The approach to determining member instability is as follows: the axial force of the member should exceed the stable bearing capacity of a single member, calculated under standard hinged conditions at both ends, yet remain below the stable bearing capacity calculated assuming fixed joints at both ends. Additionally, the load-axial force curve of the member must exhibit a decreasing section after reaching its maximum value.

The stability bearing capacity can be calculated using the following formula [13]:

$$N = \varphi f_c A_0 \tag{1}$$

$$\varphi = \frac{1+(f_{cE}/f_c)}{1.8} - \sqrt{\left[\frac{1+(f_{cE}/f_c)}{1.8}\right]^2 - \frac{f_{cE}/f_c}{0.9}} \tag{2}$$

$$f_{cE} = \frac{0.47E}{(l_0/b)^2} \tag{3}$$

$$l_0 = k_l l \tag{4}$$

Where, f_c is the parallel-to-grain compressive strength of the glulam; A_0 is the area of the cross section of the member; φ is the stability reduction coefficient of axially loaded compression; E is the parallel-to-grain elastic modulus of the glulam; b is the width of the cross section; l_0 is the calculation length; k_l is the effective length factor, which is valued as 1.0 for the member which has hinge joint at both ends and is valued as 0.65 for the member which has fixed joint at both ends.

In this study, under conditions where both ends are hinged, the ultimate bearing capacity of the axial compression member is determined to be 109.14kN. Conversely, when both ends are fixed, the ultimate bearing capacity of the axial compression member is calculated to be 204.86kN. As illustrated in Fig. 14c and d, the axial forces acting on the 37th, 58th, and 86th members all adhere to the initial criterion of the judgment principle. Compared with the axial force of the 58th and 86th members, the axial force of the 37th member was greater. Therefore, it can be concluded that the 37th member experienced instability first, consequently leading to structural damage.

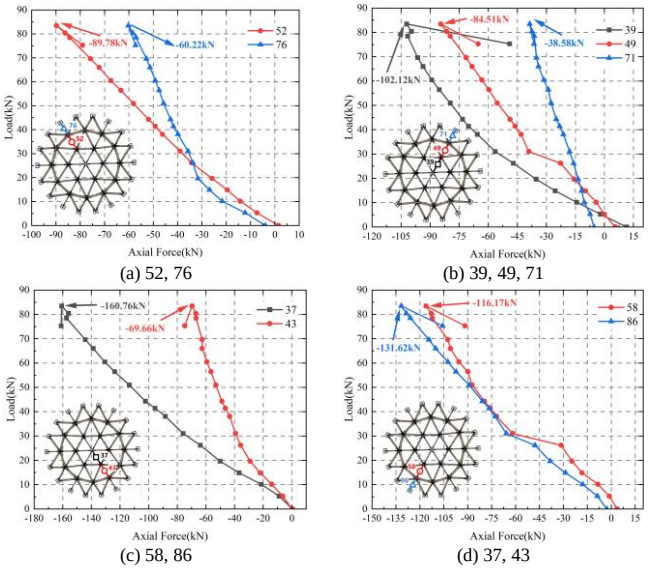

(a) 52, 76 (b) 39, 49, 71

(c) 58, 86 (d) 37, 43

Fig. 14 Load-Axial Force curves in radial members

In Fig. 15a, the failure mode of the aluminum reticulated shell depicted members near the loading point buckling around the weak axis, leading to the inclined failure of the structure [21]. As shown in Fig. 15b, it is evident from the literature [12] that the failure of the steel suspendome was attributed to the buckling of the local member. This phenomenon further highlights the importance of considering member stability and selecting appropriate slenderness ratios in the design of suspendome.

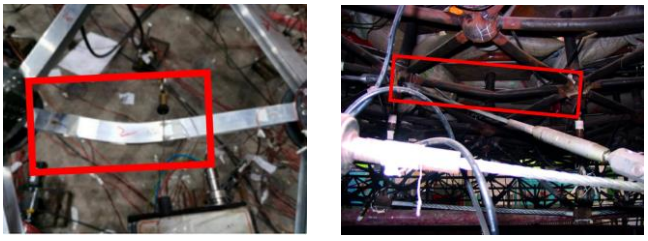

(a) Aluminum reticulated shell (b) Steel suspendome

Fig. 15 Failure mode of the members in the reticulated shell and suspendome

4. Parameter analysis

4.1. Validation of the FEM

The numerical model of the glulam suspendome was constructed using the ANSYS software. The glulam members were represented using BEAM188 elements. The vertical struts and radial cables were modeled using Link180 elements. Additionally, the hoop cables were represented using Link10 elements. The constraints applied to the finite element model included circumferential and vertical constraints on the outermost node. Prestress was applied to the structure by setting the initial strain of hoop cables.

As depicted in Fig. 16, the analysis focused on the 1st node to compare the test results with the results obtained from FEM. The structural deformation observed in the finite element model closely matched the experimental findings. The relative error of ultimate bearing capacity calculated by the FEM was 9.16%, compared with the experimental results.

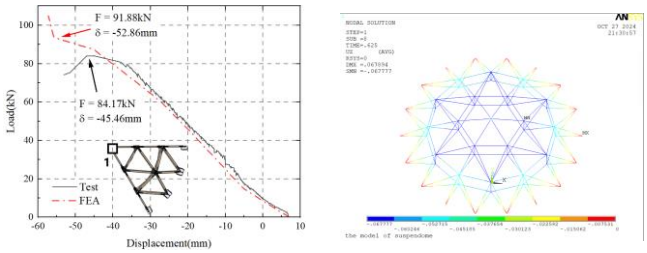

(a) Load-Displacement Curve (b) Node Displacement

Fig. 16 Comparison between FEM and test

4.2. Parameter analysis

In the parameter analysis, this paper selected the structural prestress, span and span-ratio, height of vertical struts, initial defections to analyze the overall stability of glulam suspendome. Table 3 showed the structural size and the section size of glulam member. The upper structure of glulam suspendome adopted K6-type reticulated shell, while each ring was built with a hoop cable. The prestress of the structure was applied by adjusting the cable force of hoop cables. Refer to relevant practical projects, the constraints were typically defined as radial sliding and circumferential constraints to reflect this design approach in FEM. Only the parallel-to-grain compressive strength is considered in this analysis, reflecting the primary loading condition of the glulam members.

The key parameters include the prestress ratio (the ratio of the cable force of each ring) and the prestress amplitude (the prestress of the outermost hoop cable). Fig. 17a showed the naming rules of the finite element model (FEM), while Fig. 17b showed the diagram of the FEM. The selection of parameters was as follows:

Span: 30m, 45m, 60m, 75m, 90m, 105m, 120m;

Span-Ratio (f/L): 1/5, 1/6, 1/8, 1/10, 1/12, 1/15;

Length of vertical struts(m): 2.0, 2.5, 3.0, 3.5, 4.0, 5.5, 6.0, 6.5, 7.0, 7.5;

Prestress Ratio: Ratio of the number of nodes corresponding to each loop cable;

Amplitude of prestress (kN): 90 (30m, 45m, 60m), 120 (75m, 90m, 105m, 120m);

Section of member: Vertical strut (φ219×7), Radial cable (φ80), Hoop cable (φ7×73).

Table 3
Structural parameters

Span (m)	30	45, 60	75, 90	105, 120
Section of glulam members (mm)	180×540	240×720	300×900	360×1080
Rings	5	7	9	11

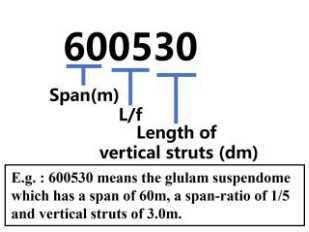

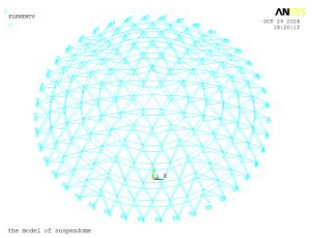

(a) Naming rules of FEM (b) Diagram of FEM (600530)

Fig. 17 Finite element model (FEM)

4.2.1. Prestress Amplitude and Initial Defection

Based on the glulam suspendome named "600530", the initial prestress of the structure was changed to explore the influence of different prestresses on the overall stability of the structures. Concurrently, the influence of initial defects on the overall stability of glulam suspendome was studied by setting the initial defection values of different sizes.

As shown in Fig. 18a, different prestress amplitude had little effect on the ultimate bearing capacity of glulam suspendome. When the cable force of the outermost ring cable was 90kN (A), the ultimate bearing capacity of the structure was the maximum, which was 11.46kN/m^2. When the cable force of the outermost ring cable was increased to 1.4A, the ultimate bearing capacity of the structure was the smallest, which was 11.00kN/m^2. The ultimate bearing capacity of the structure was reduced by about 4.18%.

Damage to the upper reticulated shell occurred prior to the full activation of the load-bearing capacity of the lower cable-strut system. With greater prestress amplitude, the structural stiffness is enhanced, leading to reduced deformation under identical loading conditions. However, variations in prestress amplitude exert little influence on the stress distribution within the upper glulam members. As structural failures predominantly occur in the glulam components, often due to premature instability, the ultimate bearing capacity of the glulam suspendome is relatively insensitive to changes in prestress amplitude.

As depicted in Fig. 18b, different initial defections also had little influence on the ultimate bearing capacity of glulam suspendome. When the structure had no initial defection, the ultimate bearing capacity was 11.46kN/m^2. When the structural defection was L/100, the ultimate bearing capacity was 11.00kN/m^2, which was reduced by about 4.18%.

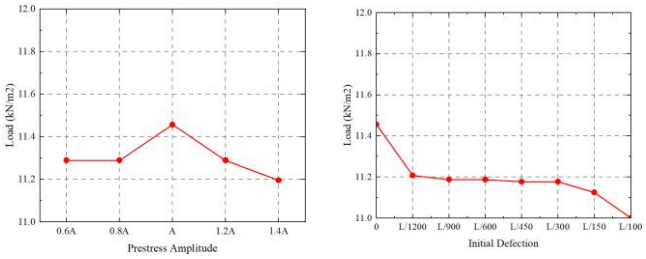

(a) Prestress Amplitude (b) Initial Defection

Fig. 18 Results of parameter analysis

4.2.2. Span, Span-ratio and Height of vertical struts

As shown in Fig. 19a, more than 200 cases of glulam suspendome with different span, span-ratio and length of struts were analyzed in order to explore the influence of structural span and span-ratio on structural stability bearing capacity. As shown in Fig. 19b, the ultimate bearing capacity of the structure decreased with the reduction of the span-ratio. Taking span-75m as an example, the ultimate bearing capacity of the structure was 125.31kN/m^2 when the span-ratio was 1/5. When the span-ratio is 1/15, the ultimate bearing capacity of the structure was 39.03kN/m^2, which decreased by 72.05%. With the decrease of the span-ratio, the force of the upper reticulated shell was more, which leaded to the easy destruction of glulam material.

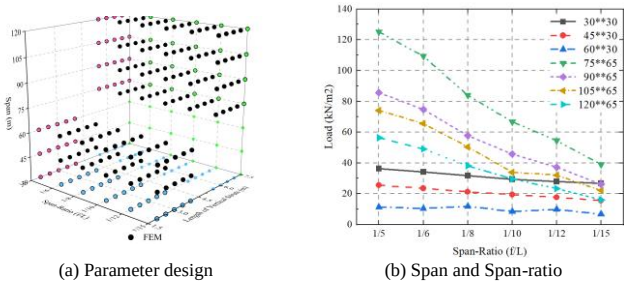

(a) Parameter design (b) Span and Span-ratio

Fig. 19 Span, Span-ratio and Height of vertical struts

As shown in Fig. 20a, as the length of the struts increased, the ultimate bearing capacity of the structure gradually increased. For example, when the length of the strut was 2.0m, the ultimate bearing capacity of the structure is the lowest, which was 22.78kN/m^2. When the strut length was 4.0m, the ultimate bearing capacity of the structure was the highest, which was 28.33kN/m^2, an increase of 24.36%. As shown in Fig. 20b, the ultimate bearing capacity of the

glulam suspendome with a span of more than 75m did not increase significantly with the increase of the length of the struts. This indicated that the overall stability of glulam suspendome with small span can be effectively improved by increasing the length of struts. However, for the structure with large span, it is necessary to increase the section size of the glulam members to improve the overall stability of the structure.

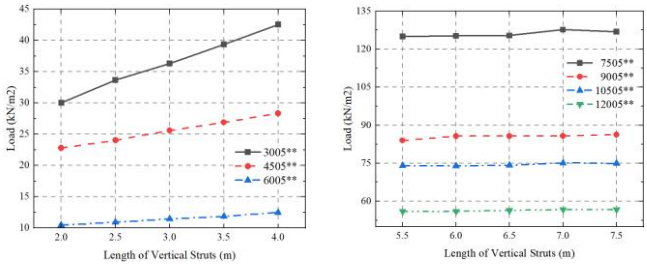

(a) 30m, 45m, 60m (b) 75m, 90m, 105m, 120m

Fig. 20 The length of vertical struts

4.3. Estimation of ultimate bearing capacity of glulam suspendome

At present, there were few theoretical studies on the overall stability performance of suspendome structure, and there was no corresponding calculation formula of ultimate bearing capacity. Based on the calculation of ultimate bearing capacity of single-layer glulam reticulated shells, the reinforcement factor "*k*" was proposed to estimate the ultimate bearing capacity of K6-type glulam suspendome. It is worth noting that the ultimate bearing capacity of K6 single-layer glulam reticulated shell was also calculated by FEM in Section 4.1.

$$k = \frac{\Lambda_{\text{suspendome}}}{\Lambda_{\text{shell}}} \tag{5}$$

$\Lambda_{suspendome}$ is the ultimate bearing capacity of glulam suspendome, kN/m^2; Λ_{shell} is the ultimate bearing capacity of the single-layer glulam reticulated shell corresponding to the suspendome, kN/m^2.

According to the parameter analysis in Section 4.2, the prestress and initial defection had little influence on the ultimate bearing capacity, while the span, span-ratio and strut length had great influence on the ultimate bearing capacity. Therefore, this paper carried out numerical simulation analysis on several groups of glulam suspendome with different spans, span-ratios and strut lengths, and put forward the growth coefficient table of K6-type structures (Table 4-10). The enhancement coefficient which was not given in the table can be calculated by interpolation. It can be inferred from the data that the smaller of the span-ratio and the longer the length of struts, the more obvious tension system can improve the overall stability of the structure.

Table 4
k- (Span= 30m)

Length of vertical struts (m)	Span-Ratio					
	1/5	1/6	1/8	1/10	1/12	1/15
2	1.75	1.82	1.91	2.03	2.24	2.83
2.5	1.97	2.01	2.15	2.29	2.57	3.29
3	2.12	2.20	2.38	2.54	2.84	3.66
3.5	2.30	2.40	2.58	2.78	3.12	4.06
4	2.48	2.59	2.79	3.03	3.39	4.45

Table 5
k- (Span= 45m)

Length of vertical struts (m)	Span-Ratio					
	1/5	1/6	1/8	1/10	1/12	1/15
2	1.27	1.27	1.30	1.38	1.45	1.67
2.5	1.34	1.34	1.37	1.46	1.55	1.81
3	1.42	1.41	1.44	1.53	1.64	1.94
3.5	1.50	1.49	1.50	1.60	1.73	2.06
4	1.57	1.55	1.57	1.66	1.82	2.20

Table 6
k- (Span= 60m)

Length of vertical struts (m)	Span-Ratio					
	1/5	1/6	1/8	1/10	1/12	1/15
2	1.24	1.23	1.28	1.31	1.43	1.52
2.5	1.29	1.28	1.34	1.38	1.52	1.64
3	1.35	1.34	1.41	1.45	1.61	1.76
3.5	1.40	1.40	1.47	1.52	1.70	1.87
4	1.48	1.46	1.52	1.59	1.78	1.99

Table 7
k- (Span= 75m)

Length of vertical struts (m)	Span-Ratio					
	1/5	1/6	1/8	1/10	1/12	1/15
5.5	1.10	1.09	1.18	1.23	1.29	1.33
6	1.10	1.11	1.18	1.24	1.30	1.34
6.5	1.10	1.10	1.17	1.24	1.30	1.34
7	1.12	1.11	1.18	1.24	1.31	1.35
7.5	1.12	1.12	1.19	1.25	1.31	1.36

Table 8
k- (Span= 90m)

Length of vertical struts (m)	Span-Ratio					
	1/5	1/6	1/8	1/10	1/12	1/15
5.5	1.12	1.13	1.23	1.34	1.41	1.45
6	1.14	1.14	1.24	1.33	1.41	1.46
6.5	1.14	1.14	1.24	1.33	1.42	1.46
7	1.14	1.14	1.25	1.34	1.42	1.47
7.5	1.15	1.16	1.25	1.34	1.42	1.49

Table 9
k- (Span= 105m)

Length of vertical struts (m)	Span-Ratio					
	1/5	1/6	1/8	1/10	1/12	1/15
5.5	1.15	1.18	1.27	1.40	1.52	1.51
6	1.15	1.18	1.33	1.42	1.54	1.51
6.5	1.16	1.19	1.33	1.42	1.55	1.52
7	1.17	1.19	1.34	1.46	1.56	1.52
7.5	1.17	1.20	1.34	1.47	1.56	1.52

Table 10
k- (Span= 120m)

Length of vertical struts (m)	Span-Ratio					
	1/5	1/6	1/8	1/10	1/12	1/15
5.5	1.17	1.20	1.42	1.56	1.64	1.64
6	1.17	1.20	1.42	1.57	1.68	1.65
6.5	1.18	1.20	1.42	1.58	1.69	1.65
7	1.18	1.20	1.42	1.60	1.71	1.66
7.5	1.18	1.22	1.43	1.61	1.73	1.67

5. Conclusions

In this study, a novel type of glulam suspendome is proposed. A destructive test with 13-point synchronous loading is conducted on a structural model with a span of 6m and a height of 1.2m. Based on the analysis of structural failure mode, load-displacement curves and load-strain curves, the mechanical properties of glulam suspendome are investigated. Based on the analysis of structural parameters, the method of estimating the ultimate bearing capacity of the structure and the improvement coefficient (k) are proposed. The following conclusions are drawn:

(1) In the destructive test, the failure load recorded at each loading point is 84.17kN, resulting in a total load received by the glulam suspendome of 1094.21kN (84.17kN×13). The failure mode of the structure involved instability around the weak axis of the member near the mid-span node, along with member fracture. The displacement of the mid-span node is the largest, measuring -47.10mm. The compressive strain of the main rib member of the first layer is the largest, measured at -2186.53με (-160.76kN). This suggests that the importance of considering member stability and selecting appropriate slenderness ratios in the design of the glulam suspendome.

(2) In the destructive test, the second ring members in the reticulated shell are subjected to tension. Consequently, the corresponding position of the vertical struts experiences greater pressure, resulting in higher tension in the outer ring radial rods. This observation indicates that the load of the glulam suspendome is primarily transmitted downwards to the cable-strut system through the outer ring nodes. In the design of the glulam suspendome, the load dispersion effect of the outer cable-strut system should be taken into consideration.

(3) The parameter analysis of more than 200 finite element models showed that prestress and initial defections had little influence on the overall stability of glulam suspendome. The geometrical dimensions of the structure, such as the span-ratio and the length of vertical struts, had a great influence on the overall stability of glulam suspendome. It is worth noting that when the span of the structure is greater than 75m, the ultimate bearing capacity of the structure cannot be effectively improved by increasing the length of the struts.

(4) By comparing the ultimate bearing capacity of single-layer glulam reticulated shell and glulam suspendome of the same size, the reinforcement factor "k" of glulam suspendome was given. The results showed that the smaller of the span-ratio and the longer the length of the strut, the more obvious tension system can improve the overall stability of the structure.

Acknowledgements

This work was supported by the Hebei Natural Science Foundation (No. E2020402074).

References

[1] Ma H, Fan F, Wen P, Zhang H, Shen S. Experimental and numerical studies on a single-layer cylindrical reticulated shell with semi-rigid joints. Thin-Walled Structures. 2015;86:1-9.
[2] Xiong Z, Guo X, Luo Y, Zhu S. Elasto-plastic stability of single-layer reticulated shells with aluminium alloy gusset joints. Thin-Walled Structures. 2017;115:163-75.
[3] Xiong Z, Guo X, Luo Y, Zhu S, Liu Y. Experimental and numerical studies on single-layer reticulated shells with aluminium alloy gusset joints. Thin-Walled Structures. 2017;118:124-36.
[4] Lu B, Ye Y, Ji Y, Lu W, Pan X, Huang Y et al. Investigations on the critical load of mid-span Kiewitt-type single-layer timber reticulated shells considering the effect of joint stiffness. Structures. 2024;63:106423.
[5] Kawaguchi M, Abe M, Tatemichi IJJ-IAfS, Structures S. Design, tests and realization of suspen-dome system. 1999;40:179-92.
[6] Guo J, Dong S, Yuan X. Research on static property of suspen-dome structure under heap load. Advanced Steel Construction. 2012;8:137-52.
[7] Nie G, Zhi X, Fan F, Shen S. Study of the tension formation and static test of a suspendome for Dalian Gymnasium. China civil engineering journal. 2012;45:1-10.
[8] Chen ZH, Yan RZ, Wang XD, Liu HB, Xiao X. EXPERIMENTAL RESEARCHES OF A SUSPEN-DOME STRUCTURE WITH ROLLING CABLE-STRUT JOINTS. ADVANCED STEEL CONSTRUCTION. 2015;11:15-38.
[9] Xue S, Lu Z, Li X, Liu R, Zhao Z, Jing H et al. Experimental and numerical investigations on the influence of center-hung scoreboard on dynamic characteristics of suspend-dome structure. Journal of Building Engineering. 2022;57:104787.
[10] Xue S, Wang Z, Li X, Liu R, Lu Z, Jing H et al. Model test study on static performance of rib-patterned small rise-span ratio suspend-dome structure. Structures. 2022;43:1615-28.
[11] Yan RZ, Zhu MH, Liu T, Liu JQ, Chen ZH. EFFECT OF RANDOM PRE-STRESSED FRICTION LOSS ON THE PERFORMANCE OF A SUSPEN-DOME STRUCTURE. ADVANCED STEEL CONSTRUCTION. 2022;18:465-78.
[12] Zhang A, Liu X, Wang D, Wei W, Huang D, Wu L et al. Static experimental study on the model of the suspend-dome of the badminton gymnasium for 2008 Olympic Games. Journal of Building Structures. 2007;28:58-67.
[13] GB/T 50708-2012. Technical code of glued laminated timber structures. China Architecture and Building Press. Beijing; 2012
[14] ASTM D143-2014. Standard test methods for small clear specimens of timber. United States; 2014
[15] Liu H, Zhao J, Zhao J, Chen Z, Zhao S, Yang S. Experimental study on the mechanical behavior of glulam suspendome considering the influence of prestressing. Journal of Building Engineering. 2024;95:110180.
[16] JGJ7-2010. Technical specification for space frame structures. China Building Industry Press. Beijing; 2010
[17] Pan DH, Girhammar UA. Influence of Geometrical Parameters on Behaviour of Reticulated Timber Domes. International Journal of Space Structures. 2003;18:105-21.
[18] Pan D, Girhammar UA. Effect of Ring Beam Stiffness on Behaviour of Reticulated Timber Domes. International Journal of Space Structures. 2005;20:143-60.
[19] Kang W, Chen Z, Lam H-F, Zuo C. Analysis and design of the general and outmost-ring stiffened suspen-dome structures. Engineering Structures. 2003;25:1685-95.
[20] ASTM D1761-12. Test Methods for Mechanical Fasteners in Wood. United States; 2012
[21] Sun GJ, Xiao S, Wu JZ, Yu SF, Wei MY, Qin J et al. Study on the static stability of aluminum alloy single-layer spherical reticulated shell. JOURNAL OF BUILDING ENGINEERING. 2024;84.

Advanced Steel Construction – Vol. 20 No. 4 (2024) 413–423
DOI:10.18057/IJASC.2024.20.4.9

WEB CRIPPLING BEHAVIOUR OF COLD-FORMED STEEL CHANNELS WEB HOLES UNDER END TWO FLANGE (ETF) LOADING

Yakup Bölükbaş *

Civil Engineering Dept., School of Engineering, Aksaray University, Aksaray, 68100, Türkiye
** (Corresponding author: E-mail: ybolukbas@aksaray.edu.tr)*

ABSTRACT

The design of the web-crippling behavior of cold-formed steel elements (CFS), which have been widely used in recent years, is essential. The concentrated loads acting on CFS members cause the section's web to crush and buckle. For this reason, it is necessary to calculate the web crippling strength correctly in the design of CFS sections. In order to observe the web-crippling behavior of CFS channel sections with holes drilled in the webs, this paper presents experimental and numerical experiments. Seven sections of the real-world system intended for End Two Flange (ETF) loading scenarios underwent testing. The tested cells were simulated by the finite element method with ABAQUS software. As a result of the numerical studies, 150 different model finite element analysis results are presented in the parametric study. In addition, the equations proposed by AISI and Eurocode 3 for the web-crippling design of CFS channel sections without web holes are analyzed. The findings of parametric investigations are compared with the design equation for sections with web holes presented by Uzzaman et al., and new coefficients are suggested for this equation. As a result of the study, the distance from the hole to the loading plate of CFS channel sections affects the section bearing capacity. Increasing the hole diameter drilled into the section web reduces the bearing capacity of the section. It is seen that h/t and N/t are more effective than R/t in the equation proposed by AISI for predicting the web-crippling strength of CFS channel sections.

ARTICLE HISTORY

Received: 7 May 2024
Revised: 14 October 2024
Accepted: 7 November 2024

KEYWORDS

Cold-formed steel;
Web crippling;
Finite element analysis;
End two-flange loading;
Web hole

1. Introduction

In recent years, there has been a significant increase in the use of Cold-Formed Steel (CFS) elements as load-bearing and supplementary structural components. These elements are favored due to their superior strength-to-weight ratio compared to conventional structural steel and advantages such as flexibility in cross-sectional design and ease of assembly. When concentrated loads or support responses are applied to Cold-Formed Steel (CFS) sections, a failure condition known as "web crippling" can occur (see Fig. 1). The effect of such concentrated loads results in the crushing and buckling of the section's web. Therefore, accurate calculation of web crippling strength is crucial in the design of CFS sections [1].

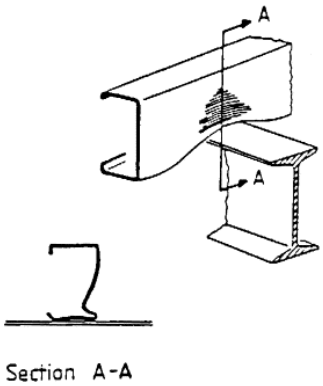

Fig. 1 Web crushing at a support point [2]

A theoretical model for predicting the web crippling capacity of Cold-Formed Steel (CFS) sections has proven challenging due to factors such as non-uniform stress distribution across the section, local yielding, significant deformations, plastic behavior in the section webs, and initial imperfections. In order to better understand this phenomenon, research has been conducted since the 1940s that have experimentally examined the web-crippling behavior of different CFS section forms [3–12]. In order to forecast the web-crippling strength of CFS sections, researchers' empirically based formulae have been integrated into the AISI [13] and AS/NZS [14] standards. While the North American standard offers a more simplified design methodology than Eurocode 3 [15], both standards' approaches are limited to specific section types and material properties.

In the following years, researchers conducted studies examining the web-crippling behavior of Cold-Formed Steel (CFS) sections for each loading condition (see Fig. 2), based on the AISI S909 [16] standard web crippling test methods [17-21].

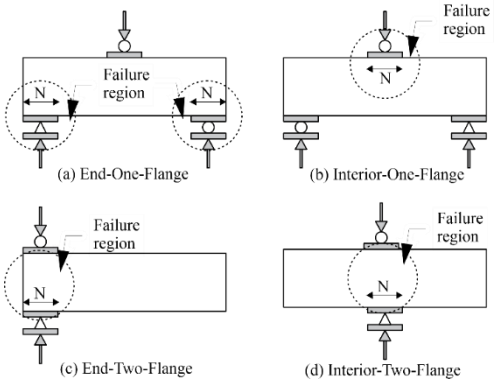

Fig. 2 Four alternative loading types for web buckling analysis [16]

In buildings composed of CFS sections, it is often necessary to create openings in the section web to install electrical or plumbing services easily. This effort is aimed at facilitating the assembly of structures. Cold-formed steel sections typically have web holes that are drilled or punched before being unstiffened. However, the portions become more vulnerable to web crippling when concentrated loads are applied close to the sites where openings are made [22].

For channel sections with holes in the web under through interior one flange (IOF) and end one flange (EOF) loading situations, Uzzaman et al. offered design ideas for web crippling strength reduction factor equations. [23-26] and Lian et al [27-30]. Furthermore, a great deal of research has been done to examine the web-crippling behavior of CFS sections that include web holes [31-36]. While the holes drilled on CFS sections are mostly drilled straight, nowadays, holes with an edge-stiffened can also be drilled. The combination of experimental and numerical investigation conducted by Uzzaman et al. on the web crippling capacity of CFS channels with edge-stiffened web holes was only documented in the literature [37–40]. They discovered that a CFS channel with edge-stiffened web holes has about the same improved web-crippling capability as a plain channel. The study by Elilarasi et al. investigates the effects of circular web openings shifted in centre or off-axis on the capacity reduction of freestanding supported lipless channels subjected to web crushing in two-end flange loading cases. Based on the results obtained from the numerical study, suitable reduction factor equations are proposed for circular web openings of lipless channels located directly under and away from the bearing plate [41]. Finally, Gunalan and Mahendran investigated the suitability of existing design rules for lipless channels subjected to web-crippling single flange loading cases and suggested appropriate adjustments where necessary [42]. In a recent study, researchers investigated the web buckling behavior of CFS channel sections

under ETF loading conditions, considering the influence of reinforced holes. Utilizing a finite element model derived from prior research, they further developed and conducted a comprehensive parametric study with this model [43]. Another finite element-based study aimed to investigate the web crippling behaviour of Sigma sections under ETF load condition. After successfully validating the numerical approach, a comprehensive numerical study was carried out on Sigma sections made of aluminium, carbon steel and stainless steel by creating 1512 numerical models. The results obtained from the numerical study were compared using parameters such as section depth, thickness, yield strength, bearing length and radius. The numerical results are also compared with the existing design equations and modified design provisions are proposed considering their inaccuracy in predicting the web crippling capacity of Sigma sections made of CF carbon steel, stainless steel and aluminium under ETF load case [44].

The CFS channel sections with web holes and their web-crippling behavior with End Two Flange (ETF) loading were investigated in this study through a battery of tests. 7 specimens were prepared with the same cross-sectional shape but with different hole sizes and locations. In addition, a finite element model of the tested specimens was created using Abaqus software [45]. The FE model was verified by comparing it with the test results. After obtaining a satisfactory FE model verification, parametric studies were carried out on 150 different models including different cross-sectional dimensions and variations of hole diameters. The equation proposed by Uzzaman et al. [24, 25] and the predictions made using the current AISI [13] and Eurocode 3 [15] standards were compared with the web crippling capacity estimates derived from the experimental and numerical research. As a result, the coefficients in the equation proposed by Uzzaman et al. [24, 25] were updated by regression analysis, and an alternative equation was proposed for the estimation of the web crippling capacity of CFS sections with web holes under ETF loading conditions.

2. Experimental study

2.1. Test specimens

This study tested 7 CFS channel sections under ETF loading conditions. While one specimen without holes in the web was tested as a reference (see Fig. 3a), six specimens were tested with web holes (see Fig. 3b). In accordance with AISI S909 [16], the length of each specimen was adjusted to be 1.5 times the web height in addition to the loading plate width for the ETF loading scenario.

The holes in the web of the specimens were drilled in two different diameters (a), 50 mm and 100 mm. The holes drilled in the web of the sections were drilled straight without any stiffening. In addition, the distances (x) of the web holes to the loading plate were adjusted as 0, 50 mm, and 150 mm. In the study, the width of the loading plate was kept constant at 50 mm. The loading plates were fixed to the top and bottom flange of the section with the help of 8 mm diameter bolts.

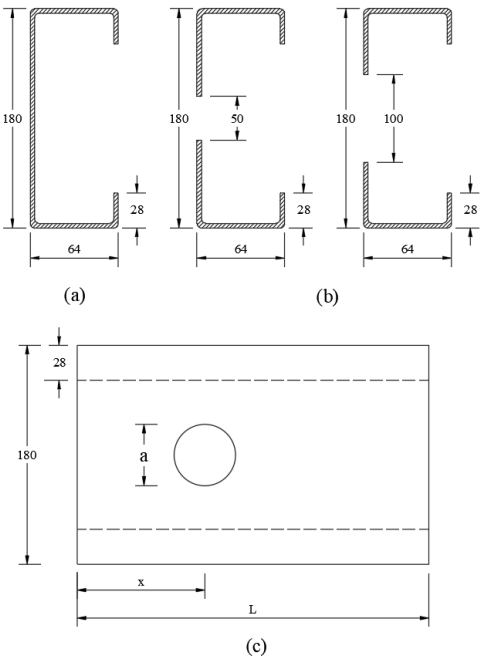

Fig. 3 Dimensions of CFS sections to be used in the study, a) reference, b) web hole specimens, c) side view of specimens (all dimensions in mm)

2.2. Specimens labelling

The labels of the test specimens are shown in Fig. 4. For example, the "ETF_Ref" identifies the reference specimen with the end of two flange loadings and no hole in the cross-sectional web. The "ETF_CIRC_50_0" indicates the model loaded with end-two flanges with a 50 mm circular hole on the web and 0 mm from the loading plate.

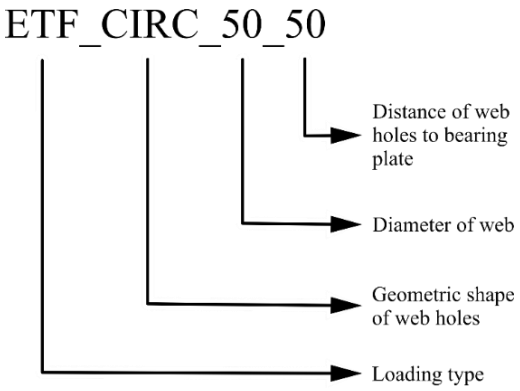

Fig. 4 Specimens labeling.

2.3. Material properties

To ascertain the mechanical characteristics of the specimens under examination, tensile tests were performed. Four coupons were prepared from flat sections of both the web and flange of the channel sections (see Fig. 5). These coupon specimens were subjected to tensile tests following EN 10002-1 [46].

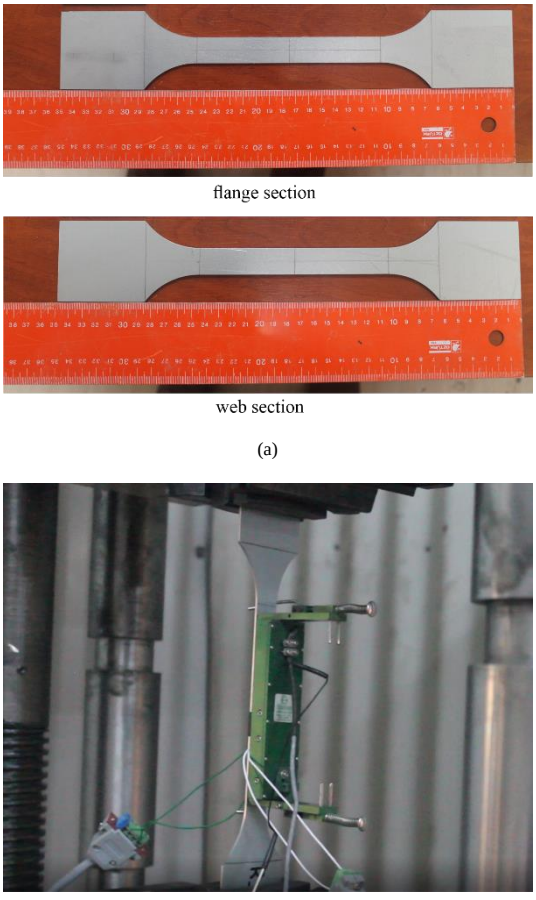

Fig. 5 Tensile test (a) Coupon specimens and (b) test setup tensile coupon test.

The engineering stress-strain curves derived from the specimens following the tensile tests are illustrated in Fig. 6. The yield strength (0.2% offset yield stress) and tensile strength of the specimens obtained from the tensile tests are presented in Table 1.

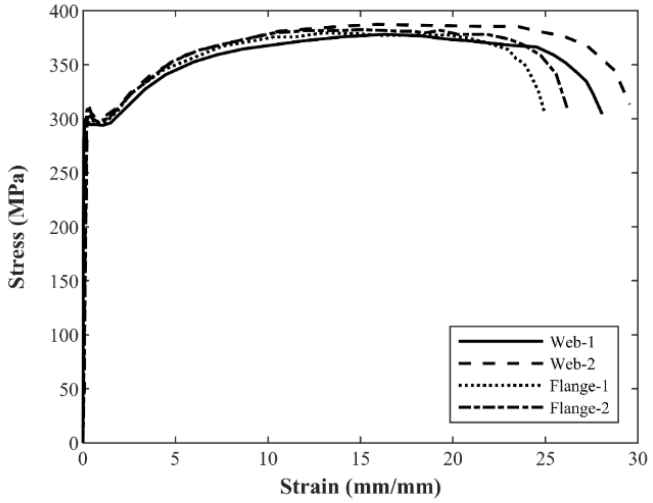

Fig. 6 Stress-strain curves

Table 1
Material properties of specimens

Specimens	σy (MPa)	σu (MPa)	εf (%)	E (MPa)
Web-1	299.75	378.13	28.066	202027
Web-2	311.78	387.33	29.55	203250
Flange-1	302.68	379.41	24.49	201768
Flange-2	308.62	380.98	26.17	205746
Mean	305.70	381.41	27.07	203197

2.4. Test rig and procedure

The prepared specimens were loaded under the ETF conditions as described in AISI S909 [16]. The loading plates were held to the top and bottom flange of the section with 8 mm diameter bolts. Semicircular joints were placed on the top of the loading plate to provide the bearing condition. Loading was applied to these semicircular joints (see Fig. 7).

A servo-controlled testing machine applied the loading to the specimen at 0.05 mm/min speed. Displacement transducers (LVDT) were used to measure displacements in the horizontal and vertical directions. Measurements were taken from the top flange to determine the vertical displacements. For horizontal displacements, measurements were taken at the center of the section under the loading plate (see Fig. 7).

During the experiment, load and displacement measurements were transferred to the data acquisition unit in such a way that 4 data can be taken per second. During the experiment, a video recording of the experiment was taken with a high-resolution camera.

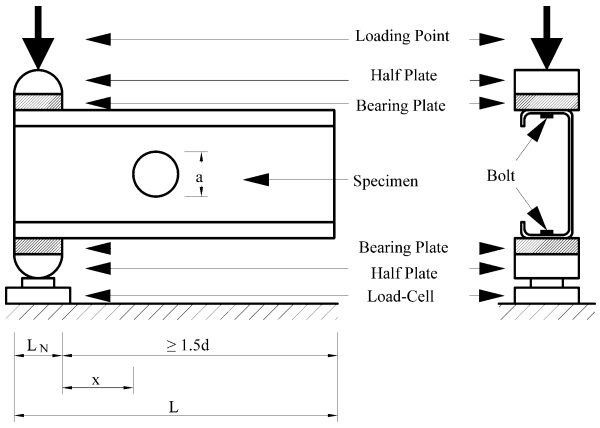

Fig. 7 Test rig

2.5. Test results

The web crippling failure loads (P_{EXP}) obtained from the experimental studies are given in Table 2. In addition, the effect of the change of the distance (x) of the holes drilled on the section web to the loading plate on the capacity is shown in Fig. 8-9. The specimens' experimental setup and failure modes are shown in Fig. 10-12.

Table 2
Web crippling capacity of specimens with circle and square web holes

Specimens	Bearing length L_N (mm)	Web hole size (mm)	Distance of web holes to the bearing plate x (mm)	Web crippling capacity P_{EXP} (kN)
ETF_REF	50	-	-	9.81
ETF_CIRC_50_0	50	50	0	9.32
ETF_CIRC_50_50	50	50	50	9.30
ETF_CIRC_50_150	50	50	150	9.93
ETF_CIRC_100_0	50	100	0	7.14
ETF_CIRC_100_50	50	100	50	8.27
ETF_CIRC_100_150	50	100	150	9.71

An analysis of Table 3 reveals that, as anticipated, the bearing capacity diminishes as the proximity of the drilled hole in the web to the bearing plate decreases. Furthermore, an increase in hole size also results in a reduction in bearing capacity. These findings are consistent with the results reported by Uzzaman et al. [24,25].

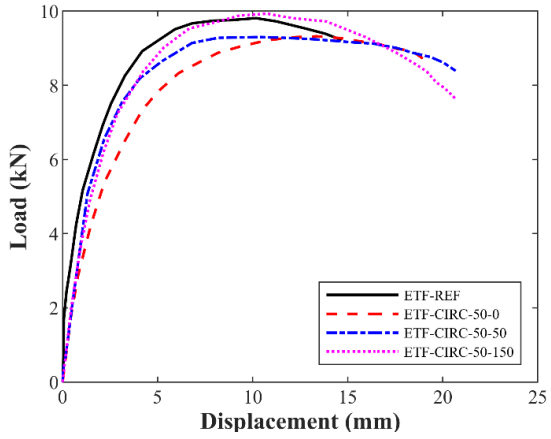

Fig. 8 The effect of hole location on web crippling capacity for 50 mm size circle hole

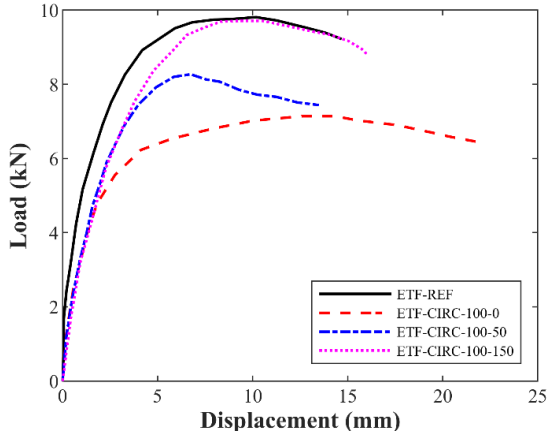

Fig. 9 The effect of hole location on web crippling capacity for 100 mm size circle hole

The bearing capacity of a CFS channel section with holes measuring 50 mm in diameter is dependent on the distance between the hole and the loading plate. The bearing capacity of the members with the hole next to the loading plate was 5% less. When the hole diameter was 100 mm, the section bearing

capacity decreased by 27%. Increasing the hole diameter reduces the capacity of the section.

Fig. 10 ETF_CIRC_50_0 specimen test setup and failure mode

Fig. 11 ETF_CIRC_50_50 specimen test setup and failure mode

Fig. 12 ETF_CIRC_50_150 specimen test setup and failure mode

3. Numerical investigation

3.1. General

In this study, a finite element (FE) model was established using ABAQUS software [41] to simulate the web-crippling behavior of Cold-Formed steel (CFS) sections under End-Two-Flange (ETF) loading conditions. The CFS channel section was meticulously transferred to the FE model to ensure precise replication of the test case, strictly following the actual dimensions. Additionally, the FE model incorporates the connections between the loading plates and the CFS section to enhance simulation fidelity.

3.2. Geometry and material properties

The cross-sectional dimensions prepared for the finite element model are shown in Fig. 3. The section dimensions used in the laboratory tests were modeled precisely in the finite element model. The loading plate was designed to be 50 mm x 80 mm.

The FE model incorporated the mechanical characteristics discovered during the tensile test. Considering the studies in the literature [24-30], the mechanical properties obtained are included in the model for the whole section, while the stress increases occurring at the corner bends and the residual stresses in the section are neglected. Engineering stress-strain behavior of the test specimens to the model, the true stress-strain curve was transferred to the model as described in the ABAQUS manual [42]. To convert the stress-strain curve obtained from the experiments to the true stress-strain curve, Eq.1 and Eq. 2.

$$\sigma_{true} = \sigma_{eng}\left(1 + \varepsilon_{eng}\right) \tag{1}$$

$$\varepsilon_{true(pl)} = \ln\left(1 + \varepsilon_{eng}\right) - \frac{\sigma_{true}}{E} \tag{2}$$

Where E is the Young's modulus, σ_{true} and ε_{true} are the true stress and strain, σ_{eng} and ε_{eng} are the engineering stress and strain.

3.3. Element type and mesh size

S4R shell element was selected in the finite element model of CFS channel sections. The S4R is a four-node double, curved, thin, or thick shell element with reduced integration and finite membrane strains. It is mentioned in the ABAQUS Manual [45] that the S4R element is suitable for complex buckling behavior. The S4R has six degrees of freedom per node and provides accurate solutions to most applications. The loading plates were modeled with the C3D8R element, which is suitable for the three-dimensional modeling of structures with plasticity, stress reinforcement, large deflection, and significant strain characteristics [45].

All sections designed in the finite element model were prepared as a 5 mm x 5 mm mesh. In the sections with web holes, it was controlled so that the dimensions of the meshes around the hole did not change too much. The mesh layout used in the finite element model is given in Fig. 13.

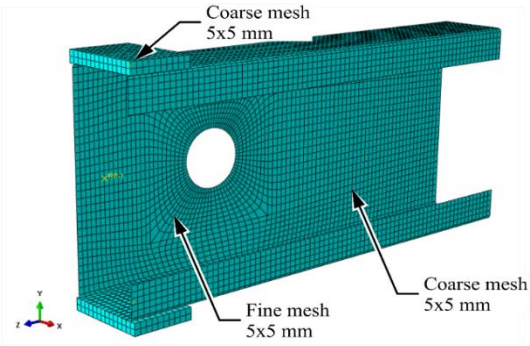

Fig. 13 Mesh type

3.4. Loading and boundary condition

The experimental study tested the CFS section in displacement with ETF loading mode. In the finite element model, loading was performed by defining a displacement of 20 mm in the y-axis perpendicular to the section flange from the loading plate connected to the CFS section top flange. Displacement in the x and z directions and rotation around the y and z axis of the upper loading flange were prevented. The displacements in the x, y, and z directions of the loading plate on the lower flange of the section were restricted, as were the rotations around the y and z axes (see Fig 14).

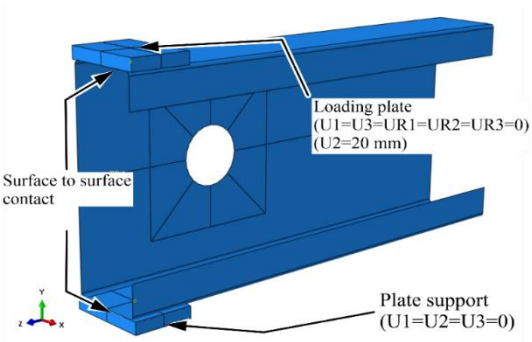

Fig. 14 Boundary conditions and contact modeling

Hard contact with friction (0.3 coefficient) is defined between the CFS section and the loading plate. This contact model describes the CFS section as slave and the loading plate as master. The CFS section head and the loading plate were fixed in laboratory experiments with 8 mm diameter bolts. This connection was simulated in the finite element model by defining a fastener element with connector properties.

3.5. Initial imperfection and residual stress

Initial geometrical imperfections and residual stresses on the section are neglected in FE models of CFS channel sections under the web crippling effect. In many studies in literature, there are analyses in which these effects are neglected [46-53]. Therefore, the initial geometrical imperfections and residual stresses on the cross-section are not considered in the FE model.

3.6. Finite element analysis performance

Finite element analysis was performed for all section types tested in laboratory studies. To demonstrate the performance of the prepared finite element model, the bearing load values (P_{FEA}) obtained as a result of the finite element analysis were compared with the load values (P_{EXP}) measured in the experimental studies. The results of this comparison are given in Table 3. The experimental load value (P_{EXP}) to the finite element analysis results (P_{FEA}) was calculated as 97%. Also, the coefficient of variation was calculated as 0.02. The comparison of the load-displacement behavior of the sections between experimental and finite element analysis is given in Fig. 15-16

Table 3
Comparison of web crippling capacity predicted from experiments and FEA

Specimens	Web crippling capacity from test P_{EXP} (kN)	Web crippling capacity from FEA P_{FEA} (kN)	Comparison P_{EXP}/P_{FEA}
ETF_REF	9.81	10.15	0.96
ETF_CIRC_50_0	9.32	9.13	1.02
ETF_CIRC_50_50	9.30	9.60	0.96
ETF_CIRC_50_150	9.93	10.17	0.97
ETF_CIRC_100_0	7.14	7.57	0.94
ETF_CIRC_100_50	8.27	8.41	0.98
ETF_CIRC_100_150	9.71	9.72	0.99
Mean			0.97
COV			0.02

As a result of the finite element analysis, the model prepared approached the experimental results by 97%. On the other hand, the COV ratio was obtained as 0.02.

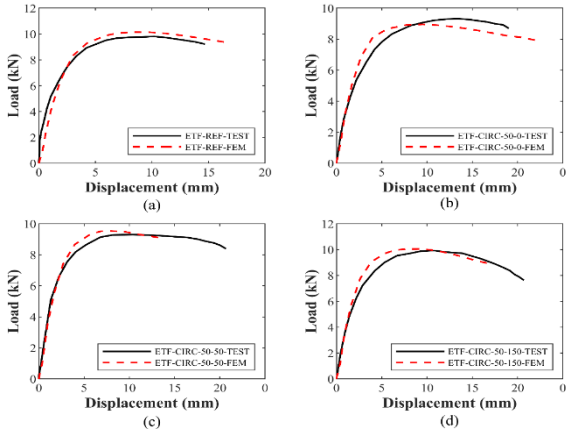

Fig. 15 Comparison between the web crippling capacity of test and FEA model

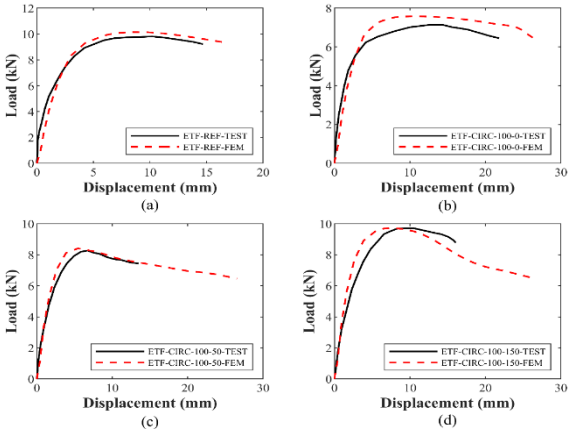

Fig. 16 Comparison between the web crippling capacity of test and FEA model

The comparison of the failure modes on the model as a result of the finite element analysis with the experimental failures is given in Fig. 17. When the pictures are examined; it is seen that in almost all sections, the failure mode result of the finite element model is consistent with the experimental collapse mode.

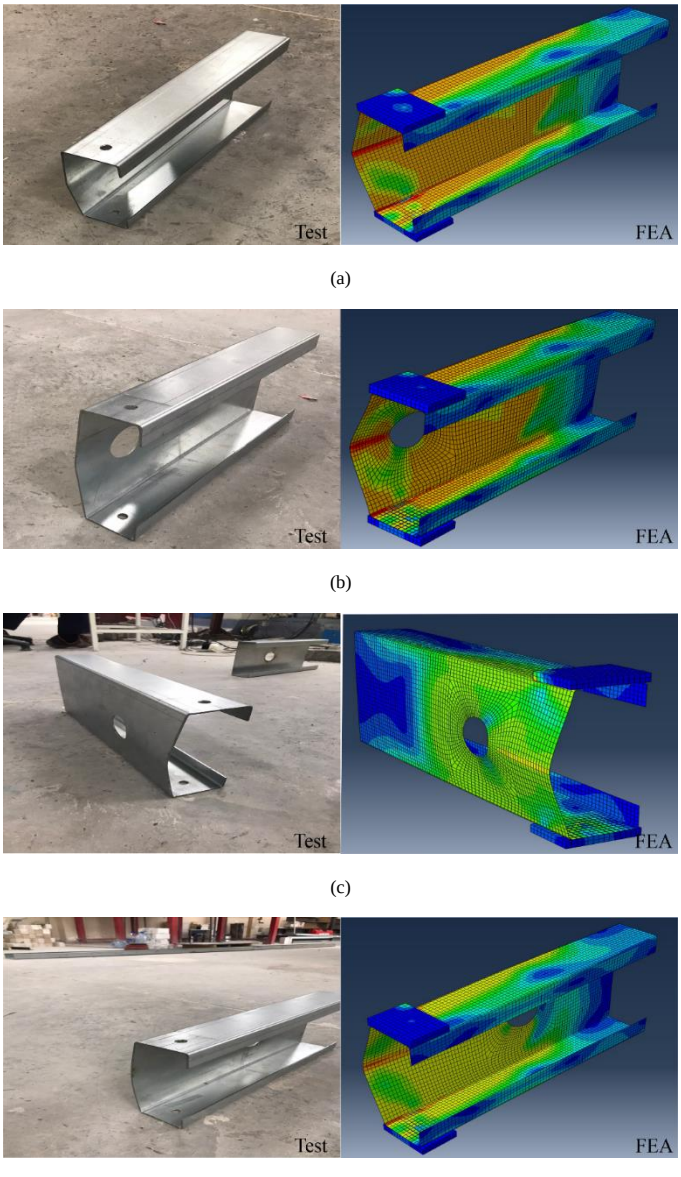

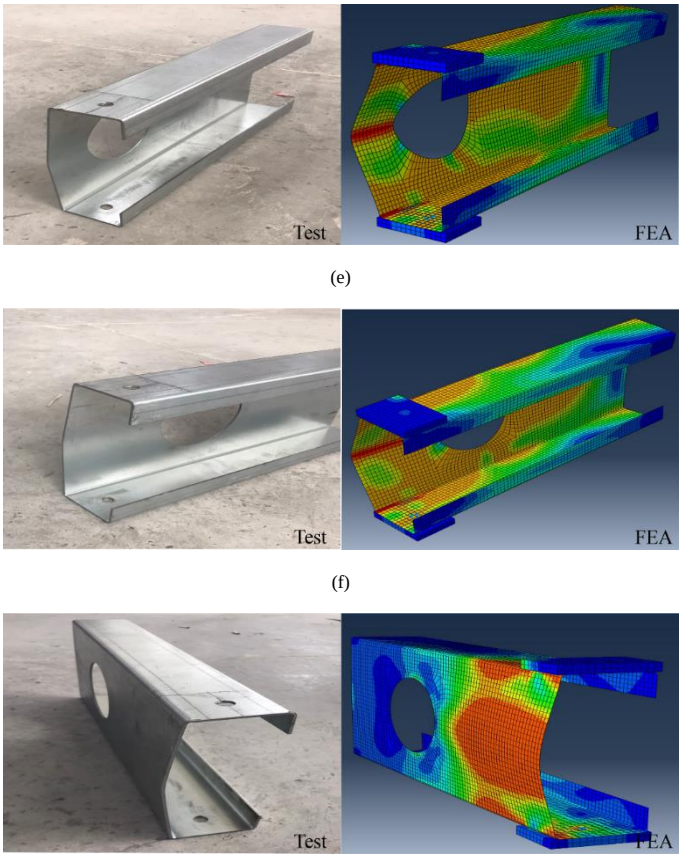

Fig. 17 Comparison between the failure modes of the test and FEA model. a) ETF_REF, b) ETF_CIRC_50_0, c) ETF_CIRC_50_50, d) ETF_CIRC_50_150, e) ETF_CIRC_100_0, f) ETF_CIRC_100_50, g) ETF_CIRC_100_150

4. Parametric study

4.1. General

After validating the FE models, a parametric study was conducted on the variation of some section parameters affecting the web-crippling capacity of these sections. In the parametric study, models without web holes were prepared, and the FE model was created to estimate the web crippling capacity. The web crippling capacity was calculated and compared with the calculation made according to the current standard AISI [13]. Similar parametric work has been done in elements with web hole. Here, according to the varying web, crippling capacities were determined by FEA and Uzzaman et al. compared with the inequality they proposed [24,25]. In all parametric studies, 150 models were created, and the section parameters affecting the web-crippling behavior of CFS channel sections were examined.

4.2. Variation of web crippling strength without holes

To investigate the web-crippling behavior of CFS channel sections, a parametric research using the finite element model with sections without web holes and with ETF loading was conducted. Considering the equation proposed in the AISI S100-16 [13] standard for the prediction of web crippling strength, the web crippling behavior is influenced by the ratio of section bend radius to thickness (R/t), web height to thickness (h/t), and loading plate width to thickness (N/t). The parametric study focuses on the effect of the variation of these three section properties on web-crippling behavior.

First, the change in web crippling capacity was analyzed by varying the web height of the CFS channel section between 50 mm and 400 mm. In comparison, the section thickness was kept constant at 2 mm, the bend diameter at 3 mm, and the loading plate width at 50 mm. The web crippling bearing capacity load obtained as a result of the parametric study is given in Table 4. In addition, the bearing capacity graph corresponding to varying web height-to-thickness (h/t) ratio is shown in Fig. 18.

Table 4
Web crippling bearing capacity load of changing h/t

Specimens	Web flat heigh (h)	Sectio thickness (t)	Section bending ra-dius (R)	Loading plate width (N)	h/t	Bearing Load (kN) (Parametric)
P1-H50	50	2	3	50	25	16.18
P1-H60	60	2	3	50	30	15.63
P1-H70	70	2	3	50	35	15.1
P1-H80	80	2	3	50	40	14.56
P1-H90	90	2	3	50	45	14.04
P1-H100	100	2	3	50	50	13.55
P1-H110	110	2	3	50	55	13.06
P1-H120	120	2	3	50	60	12.6
P1-H130	130	2	3	50	65	12.19
P1-H140	140	2	3	50	70	11.8
P1-H150	150	2	3	50	75	11.4
P1-H160	160	2	3	50	80	11.09
P1-H170	170	2	3	50	85	10.76
P1-H180	180	2	3	50	90	10.61
P1-H190	190	2	3	50	95	10.35
P1-H200	200	2	3	50	100	10.12
P1-H210	210	2	3	50	105	9.89
P1-H220	220	2	3	50	110	9.66
P1-H230	230	2	3	50	115	9.43
P1-H240	240	2	3	50	120	9.2
P1-H250	250	2	3	50	125	8.95
P1-H260	260	2	3	50	130	8.7
P1-H270	270	2	3	50	135	8.44
P1-H280	280	2	3	50	140	8.18
P1-H290	290	2	3	50	145	7.9
P1-H300	300	2	3	50	150	7.65
P1-H310	310	2	3	50	155	7.4
P1-H320	320	2	3	50	160	7.15
P1-H330	330	2	3	50	165	6.9
P1-H340	340	2	3	50	170	6.67
P1-H350	350	2	3	50	175	6.45
P1-H360	360	2	3	50	180	6.23
P1-H370	370	2	3	50	185	6.01
P1-H380	380	2	3	50	190	5.8
P1-H390	390	2	3	50	195	5.62
P1-H400	400	2	3	50	200	5.44

When Fig. 18a is examined, the h/t ratio dramatically affects the bearing capacity. The h/t increases from 25 to 200, the cross-sectional web crippling load decreases from 16 kN to 5.4 kN.

The change in capacity by changing the section height with constant section thickness, bending radius, and loading plate width on 36 different sections without holes in the web was investigated. The bearing capacity decreased by 57% with the change in section height from 50 mm to 400 mm.

In the analysis carried out to examine the effect of the width of the loading plate on the cross-sectional web crippling bearing capacity, sections with loading plate widths ranging from 20 mm to 300 mm were modeled. The thickness of the CFS channel section was kept constant at 2 mm, height 150 mm, and bend diameter 3 mm. The section length was increased for sections with large loading plate widths to meet the ETF loading case conditions. The bearing capacity obtained from the parametric study is given in Table 5. Also, the web

crippling bearing load corresponding to changing N/t is shown in Fig. 18.

Table 5
Web crippling bearing capacity load of changing N/t

Specimens	Web flat heigh (h)	Sectio thickness (t)	Section bending ra-dius (R)	Loading plate width (N)	h/t	Bearing Load (kN) (Parametric)
P2-N20	150	2	3	20	10	8.87
P2-N30	150	2	3	30	15	9.48
P2-N40	150	2	3	40	20	10.5
P2-N50	150	2	3	50	25	11.4
P2-N60	150	2	3	60	30	12.48
P2-N70	150	2	3	70	35	13.53
P2-N80	150	2	3	80	40	14.62
P2-N90	150	2	3	90	45	15.7
P2-N100	150	2	3	100	50	16.76
P2-N110	150	2	3	110	55	17.8
P2-N120	150	2	3	120	60	18.77
P2-N130	150	2	3	130	65	19.77
P2-N140	150	2	3	140	70	20.67
P2-N150	150	2	3	150	75	21.56
P2-N160	150	2	3	160	80	22.41
P2-N170	150	2	3	170	85	23.4
P2-N180	150	2	3	180	90	24.03
P2-N190	150	2	3	190	95	25.12
P2-N200	150	2	3	200	100	25.6
P2-N210	150	2	3	210	105	26.59
P2-N220	150	2	3	220	110	27.27
P2-N230	150	2	3	230	115	27.91
P2-N240	150	2	3	240	120	28.54
P2-N250	150	2	3	250	125	28.8
P2-N260	150	2	3	260	130	29.39
P2-N270	150	2	3	270	135	29.98
P2-N280	150	2	3	280	140	30.56
P2-N290	150	2	3	290	145	31.46
P2-N300	150	2	3	300	150	31.97

As the N/t increased from 10 to 150, the web crippling load increased from 8 to 32 kN. The cross-section of the loading plate width significantly affects the web's crippling strength. To determine the effect of the width of the loading plate on the bearing capacity, the parametric study examined the change in bearing capacity by varying the width of the loading plate from 20 mm to 300 mm for a section with constant web height, section thickness, and bending radius. As a result of the study, the bearing capacity increases as the loading plate width increases.

Thirty-six models were designed by varying the bending radius from 0.5mm to 5mm to investigate the effect of twist diameter-thickness (R/t) ratio on web crippling strength. Web height was kept constant at 150 mm, loading plate at 50 mm, and section thickness at 2 mm. The payloads obtained from the analysis are given in Table 6. The web crippling bearing load graph for varying R/t is shown in Fig. 18. When the graph is analyzed, the increase in the R/t caused a decrease in the section-bearing capacity.

The effect of the change of twist radius on the bearing capacity was found to be relatively less effective. Increasing the twist radius from 0.5 mm to 4 mm decreased the bearing capacity by 7%.

Table 6
Web crippling bearing capacity load of changing R/t

Specimens	Web flat heigh (h)	Sectio thickness (t)	Section bending ra-dius (R)	Loading plate width (N)	h/t	Bearing Load (kN) (Parametric)
P3-R05	150	2	0.5	50	0.25	16.28
P3-R06	150	2	0.6	50	0.3	16.13
P3-R07	150	2	0.7	50	0.35	16.04
P3-R08	150	2	0.8	50	0.4	15.82
P3-R09	150	2	0.9	50	0.45	15.76
P3-R10	150	2	1	50	0.5	15.67
P3-R11	150	2	1.1	50	0.55	15.52
P3-R12	150	2	1.2	50	0.6	15.34
P3-R13	150	2	1.3	50	0.65	15.16
P3-R14	150	2	1.4	50	0.7	14.94
P3-R15	150	2	1.5	50	0.75	14.73
P3-R16	150	2	1.6	50	0.8	14.44
P3-R17	150	2	1.7	50	0.85	14.25
P3-R18	150	2	1.8	50	0.9	14.01
P3-R19	150	2	1.9	50	0.95	13.75
P3-R20	150	2	2	50	1	13.48
P3-R21	150	2	2.1	50	1.05	13.2
P3-R22	150	2	2.2	50	1.1	12.98
P3-R23	150	2	2.3	50	1.15	12.73
P3-R24	150	2	2.4	50	1.2	12.52
P3-R25	150	2	2.5	50	1.25	12.3
P3-R26	150	2	2.6	50	1.3	12.13
P3-R27	150	2	2.7	50	1.35	11.94
P3-R28	150	2	2.8	50	1.4	11.76
P3-R29	150	2	2.9	50	1.45	11.59
P3-R30	150	2	3	50	1.5	11.43
P3-R31	150	2	3.1	50	1.55	11.29
P3-R32	150	2	3.2	50	1.6	11.13
P3-R33	150	2	3.3	50	1.65	10.95
P3-R34	150	2	3.4	50	1.7	10.83
P3-R35	150	2	3.5	50	1.75	10.7
P3-R36	150	2	3.6	50	1.8	10.57
P3-R37	150	2	3.7	50	1.85	10.44
P3-R38	150	2	3.8	50	1.9	10.32
P3-R39	150	2	3.9	50	1.95	10.23
P3-R40	150	2	4	50	2	10.15

4.3. Variation of web crippling strength with holes

An equation that computes the reduction coefficient only for the single flange loading situation has been proposed by the AISI S100-16 standard [13] for the prediction of web crippling strength of CFS channel sections with drilled holes in the web. In addition, the Eurocode standard has not made any approach in this regard. However, Uzzaman et al. [24,25], in their 2012 study, proposed an equation that calculates the web crippling strength for two flange loading cases. This equation is based on two parameters: the ratio of diameter of the web holes to the section web height (a/h) and the ratio of the loading plate to the section web height (N/h).

In this part of the parametric studies, the web crippling behavior of CFS channel sections with varying hole diameter to web height ratio (a/h) was investigated, focusing on the attenuation coefficient formula proposed by Uzzaman et al. [24,25]. The web height of the section was kept constant at 150 mm, thickness at 2 mm, bend diameter at 3 mm, and loading plate width at 50

mm. Twenty-three models were prepared by varying the hole diameter (a) between 10 mm and 120 mm. As a result of the finite element analysis, the web crippling bearing load depending on the changing a/h is given in Table 7. The comparison graph obtained from parametric study is shown in Fig. 18.

Table 7
Web crippling capacity load of changing a/h

Specimens	Web flat heigh (h)	Sectio thick-ness (t)	Section bending radius (R)	Loading plate width (N)	Hole diameter (a)	a/h	Bearing Load (kN) (Para-metric)
P4-a10	150	2	3	75	10	0.07	13.98
P4-a15	150	2	3	75	15	0.10	13.7
P4-a20	150	2	3	75	20	0.13	13.36
P4-a25	150	2	3	75	25	0.17	13.05
P4-a30	150	2	3	75	30	0.20	12.76
P4-a35	150	2	3	75	35	0.23	12.4
P4-a40	150	2	3	75	40	0.27	12.08
P4-a45	150	2	3	75	45	0.30	11.75
P4-a50	150	2	3	75	50	0.33	11.44
P4-a55	150	2	3	75	55	0.37	11.14
P4-a60	150	2	3	75	60	0.40	10.84
P4-a65	150	2	3	75	65	0.43	10.59
P4-a70	150	2	3	75	70	0.47	10.39
P4-a75	150	2	3	75	75	0.50	10.18
P4-a80	150	2	3	75	80	0.53	9.98
P4-a85	150	2	3	75	85	0.57	9.8
P4-a90	150	2	3	75	90	0.60	9.61
P4-a95	150	2	3	75	95	0.63	9.42
P4-a100	150	2	3	75	100	0.67	9.07
P4-a105	150	2	3	75	105	0.70	8.7
P4-a110	150	2	3	75	110	0.73	8.25
P4-a115	150	2	3	75	115	0.77	7.71
P4-a120	150	2	3	75	120	0.80	6.98

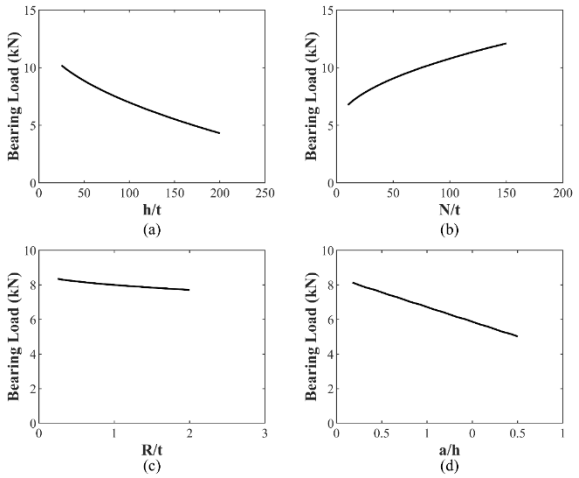

Fig. 18 Web crippling bearing the capacity load of changing parameters

When the graph is analyzed, it is seen that increasing the a/h decreases the web crippling bearing load of the CFS channel section. Although the effect of the web holes with a/h ratio of 0.2 and less is acceptable, the bearing capacity decreases significantly at higher a/h. In the parametric study on the sections with web holes, the hole diameter was varied between 10 mm and 120 mm in sections where the web height, section thickness, bending radius, and loading plate width were kept constant. The increase in hole diameter decreased the bearing capacity by 38%. In sections with web holes, the hole diameter was varied between 10 mm and 120 mm in sections where the web height, section thickness, bending radius, and loading plate width were kept constant. The increase in hole diameter decreased the bearing capacity by 38%. The Uzzaman et al. equation [24,25] uses the a/h to determine the web crippling strength of perforated CFS channel sections.

5. Current design rules

5.1. Design equations for web crippling strength of CFSS channel sections without web holes

Eurocode [15] and AISI [13] design standards are very popular for the calculation of web crippling strength of CFS sections.

5.1.1. AISI S100-16 [13]

The design equation with different coefficients according to the section shape, loading condition, and support condition can be obtained from AISI S100-16 [13]. The nominal web crippling strength ($P_{n(AISI)}$) is given in Equation 3:

$$P_{n(AISI)} = Ct^2 F_y \sin\theta \left(1 - C_R\sqrt{\frac{R}{t}}\right)\left(1 + C_N\sqrt{\frac{N}{t}}\right)\left(1 - C_h\sqrt{\frac{h}{t}}\right) \quad (3)$$

Where is the bearing length, N is the web thickness, t is the web thickness, h is the depth of the flat part of the webs, and is the inside bent radius. Fy denotes the yield stress, the angle between the web's plane and the bearing surface is represented by θ, and the coefficients of inside bent radius, bearing length, and web slenderness are represented by C_R, C_N, and C_h, respectively. Note that sections with higher r_i/t ratios are not covered by these design formulae.

5.1.2. Eurocode 3 [15]

Eurocode 3 [15] design standard provides an equation for the calculation of web crippling strength of CFS sections in ETF loading case. Unlike the AISI standard, this design, which ignores whether the flange is retained in the support state, presents a different design equation for each loading case. The following formula, based on Eurocode 3, determines the web crippling strength (Pn(EC3)) of the CFS channel segment under the ETF loading scenario.

$$P_{n(EC3)} = \frac{k_1 k_2 k_3 \left[6.66 - \frac{h_w/t}{64}\right]\left[1 + 0.01\frac{s_s}{t}\right] t^2 f_{yb}}{\gamma_{M1}} \quad (4)$$

Where, k_1, k_2, and k_3 are the coefficients from Eurocode 3; hw is the web height; t is the web thickness; ss is the nominal length of stiff bearing; f_{yb} is the basic yield stress.

5.2. Design equations for web crippling strength of CFSS channel sections with web holes

The AISI S100-16 [13] and Uzzaman et al. [24, 25] strength reduction equations were utilized to determine the web crippling strength of CFS channel sections that have web holes. The equations presented in the AISI S100-16 standard are proposed only for EOF and IOF loading cases. In Eurocode 3, there is no recommendation for the calculation of the web-crippling strength of CFS sections with holes drilled in the web.

5.2.1. AISI S100-16 [13]

To determine the web crippling strength of CFS channel sections for EOF and IOF loading drums AISI S100-16 [13] the following equations were proposed.

$$R_{c(AISI)} = 1.01 - 0.325\frac{d_h}{h} + 0.083\frac{x}{h} \leq 1.0 \quad (5)$$

$$R_{c(AISI)} = 0.90 - 0.047\frac{d_h}{h} + 0.053\frac{x}{h} \leq 1.0 \quad (6)$$

Where, d_h is the diameter of web hole; h is the depth of flat portion of web measured along the plane of web; x is the nearest distance between web hole and edge of bearing.

5.2.2. Uzzaman et al. [24,25]

Using bivariate linear regression analysis, design equations were proposed to calculate the strength reduction factor (R_p) for CFS channel sections under ITF and ETF loading. Equation 7 is proposed for unfastened flange sections in ITF loading case and Equation 8 is proposed for fastened flange. Equation 9 is proposed for unfastened flange sections in ETF loading case and Equation 10 is proposed for the fastened flange.

$$R_{p(AISI)} = 1.05 - 0.54\frac{a}{h} + 0.01\frac{N}{h} \leq 1.0 \quad (7)$$

$$R_{p(AISI)} = 1.01 - 0.051\frac{a}{h} + 0.06\frac{N}{h} \leq 1.0 \quad (8)$$

$$R_{p(AISI)} = 0.95 - 0.49\frac{a}{h} + 0.17\frac{x}{h} \leq 1.0 \quad (9)$$

$$R_{p(AISI)} = 0.96 - 0.36\frac{a}{h} + 0.14\frac{x}{h} \leq 1.0 \quad (10)$$

Where, a is the diameter of web hole; h is the depth of flat portion of web measured along the plane of web; N is the bearing length; x is the nearest distance between web hole and edge of bearing.

5.3. Proposed strength reduction factors

As shown in Table 8, the web crippling strength decreases as the size of the web holes increases. Evaluation of the experimental and numerical results shows that the a/h ratio is the primary parameter affecting the web-crippling behavior of perforated sections. Therefore, based on parametric results obtained in this study, a strength reduction factor (Rp) is proposed for the ETF loading condition using linear regression analysis.

$$R_{p(AISI)} = 0.99 - 0.58\frac{a}{h} + 0.14\frac{x}{h} \leq 1.0 \quad (11)$$

The limits for the reduction factor, given by Equation 11 are as follows: h/t ⩽156h/t⩽156, N/t⩽84N/t⩽84, N/h⩽0.63N/h⩽0.63, a/h⩽0.8a/h⩽0.8, and θ=90∘θ=90∘.

Comparison graphs were created to observe the performance of the reduction factor developed for the prediction of web buckling strength of CFS channel sections with web holes. Fig. 19 shows the variation graph of the web crippling bearing strength values predicted by the parametric study and the bearing strength values obtained by the reduction equation proposed by Uzzaman et al. [24,25] according to the a/h. In Fig. 20, the web crippling bearing strength values obtained from the parametric study are compared with the bearing strength values obtained with the reduction coefficient (Equation 11) proposed in this study.

When Fig. 19 is analyzed, the difference between the bearing capacity obtained with the reduction coefficient proposed by Uzzaman et al. [24,25] and the bearing capacity obtained in the parametric study is 8%, while the difference between the bearing capacity obtained with the reduction coefficient proposed in Equation 11 and the parametric study results is 1%.

5.4. Comparison of test results with the design strength

The results of the tests performed to determine the web crippling strength, and the prediction results of the design standards are given in Table 8. In the table, test results are compared with AISI [13], Eurocode 3 [16] and Uzzaman [24,25] predictions.

When the table is analyzed, the difference between the bearing strength values calculated according to AISI and Eurocode 3 with the reference specimen without web holes is 34% and 48%, respectively. It is seen that the design standards are more conservative in predicting the web-crippling strength of CFS channel sections without holes in the web. On the other hand, only a small number of test specimens for web portions without holes were used in this investigation. No reduction coefficient equation is advised in both AISI [13] and Eurocode 3 [16] for the prediction of the web crippling strength of CFS channel sections with web holes and ETF loading. For this reason, the reduction coefficient proposed in the studies of Uzzaman et al. [24,25] and the equations proposed in the study were used. When Table 8 is examined, it is seen that the difference between the bearing strength obtained with the reduction coefficient proposed by Uzzaman et al. [24,25] is around 4% when compared with the test results. The difference between the web crippling bearing strength values obtained with the equation proposed in the study and the results obtained in the experimental studies was 1%.

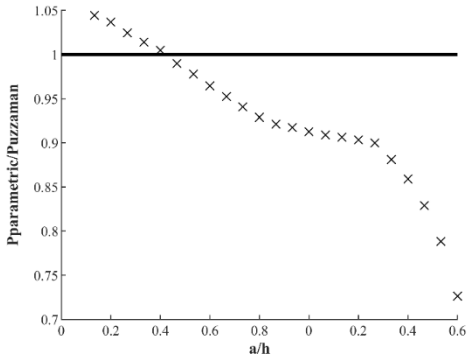

Fig. 19 Comparison between the web crippling capacity of parametric study and Uzzaman et al model

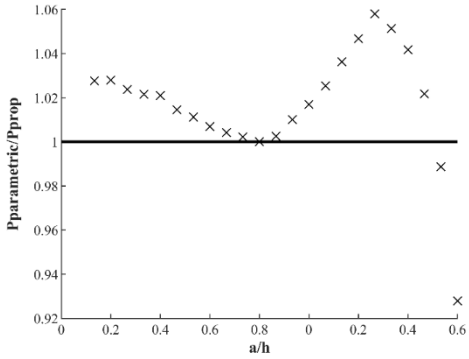

webweb

Fig. 20 Comparison between the web crippling capacity of parametric and Proposed equation model

6. Conclusions

In this study, a series of experimental and numerical studies were carried out to investigate the web-crippling behavior of CFS channel section's web holes under ETF loading. Experimental studies were carried out under ETF loading of two sections with different hole diameters. FE analysis of the test specimens was carried out with the prepared FE model. The model's performance was verified by comparing the finite element analysis with the experimental results. The web crippling strength of 150 different CFS channel sections with different cross-sectional dimensions and hole diameters was determined by the parametric study. The strengths obtained from the parametric study are compared with the equations proposed by the current AISI [13] and Eurocode [15] design standards and the equations proposed by Uzzaman et al. for the calculation of the web-crippling strength of CFS sections with cavities in the web. Finally, the coefficients of the equation proposed by Uzzaman et al. [24,25] are updated for the present problem using the linear regression method and proposed as a new equation.

- As a result of the experimental studies, it was observed that when the web holes were 50 mm in diameter, the bearing capacity decreased by about 5%, while when the hole diameter was 100 mm, the bearing capacity decreased more than expected and reached 27%.
- The variance between the bearing capacity outcomes derived from the finite element analysis and the experimental test results averaged at 3%. This discrepancy is deemed within an acceptable range for estimation.
- In the parametric study, h/t and N/t were observed as the most influential variables on the web crippling strength of CFS channel sections without holes in the web. It is seen that the a/h is an important variable in the load-carrying capacity of CFS canal sections with web holes.
- Upon comparing the bearing capacity computations derived from the prevailing design standards with the experimental test outcomes, it is evident that the AISI [13] and Eurocode 3 [15] standards exhibit conservative tendencies, showcasing differences of 34% and 48%, respectively. Additionally, an average deviation of 4% was noted between the web crippling bearing strength equation proposed by Uzzaman et al. [24,25] for sections featuring perforations in the web and the corresponding test results.
- In the context of a parametric study, the analysis of results employing the proposed equation revealed commendable predictive accuracy, with a minimal discrepancy of 1%.

Table 8
Comparison of web crippling capacity predicted from experiments, FEA and design

Specimen	Web crippling capacity (kN)						Comparison				
	P_{EXP}	P_{FEA}	P_{AISI}	P_{EC3}	$P_{Uz.}$	$P_{Prop.}$	P_{EXP}/P_{FEA}	P_{EXP}/P_{AISI}	P_{EXP}/P_{EC3}	$P_{EXP}/P_{Uz.}$	$P_{EXP}/P_{prop.}$
ETF_REF	9.81	10.15	7.31	6.63	-	-	0.96	1.34	1.48	-	-
ETF_CIRC_50_0	9.32	9.13	-	-	8.73	9.05	1.02	-	-	1.06	1.03
ETF_CIRC_50_50	9.30	9.60	-	-	9.12	9.39	0.96	-	-	1.02	0.99
ETF_CIRC_50_150	9.93	10.17	-	-	9.52	9.79	0.97	-	-	1.05	1.01
ETF_CIRC_100_0	7.14	7.57	-	-	7.71	8.05	0.94	-	-	0.93	0.89
ETF_CIRC_100_50	8.27	8.41	-	-	8.11	8.55	0.98	-	-	1.02	0.96
ETF_CIRC_100_150	9.71	9.72	-	-	8.50	8.94	0.99	-	-	1.14	1.08
Mean							**0.97**	**1.34**	**1.48**	**1.04**	**0.99**

Declaration of competing interest

The author declares that no known competing financial interests or personal relationships could have appeared to influence the work reported in this paper.

Acknowledgments

The author would like to thank Obial Silo company for supporting the CFS elements and material testing used in the studies and BABÜR DELİKTAŞ, faculty member of Bursa Uludağ University, Faculty of Engineering, Department of Civil Engineering, for his help in the finite element analysis used in the study.

References

[1] Prabakaran K. and Schuster., Web Crippling of Cold-Formed Steel Members, 14th International Specialty Conference on Cold-Formed Steel Structures (1998), 151–164.
[2] Rhodes J. and Nash D., An investigation of web crushing behavior in thin-walled beams, Thin-Walled Structures, 32, 207-230, 1998. https://doi.org/10.1016/S0263-8231(98)00035-4
[3] Winter G. and Pian R.H.J., Crushing strength of thin steel webs, Cornell Bulletin 35, Cornell University, Ithaca, N.Y., 1946.
[4] Yu W.W. and Hetrakul N., Webs for cold formed steel flexural members structural behavior of beam webs subjected to web crippling and a combination of web crippling and bending, Missouri University of Science and Technology, 1978.
[5] Bhakta B.H., LaBoube R.A. and Yu W.W., The effect of flange restraint on web crippling strength, Final Report, Civil Engineering Study, University of Missouri- Rolla, Rolla, Missouri, USA, 1992.
[6] Cain D.E, LaBoube R.A. and Yu W.W., The effect of flange restraint on web crippling strength of Cold-Formed Steel Z-and I-sections, Final Report, Civil Engineering Study, University of Missouri-Rolla, Rolla, Missouri, USA, 1995.
[7] Prabakaran K., Web Crippling of Cold-Formed Steel Sections, Project Report Department of Civil Engineering, University of Waterloo, Ontario, Canada, 1993.
[8] Prabakaran K. and Schuster B., Web crippling of cold-formed steel sections, Proc. Of 14th International Speciality Conference on Cold-Formed Steel Structures, St. Louis, Missouri, USA, 1998.
[9] Beshara B. and Schuster R.M., Web crippling of cold-formed steel C and Z sections, Proc. Of 15th International Speciality Conference on Cold-Formed Steel Structures, St.Louis, Missouri, USA, 2000.
[10] Young B. and Hancock G., Design of cold-formed channels subjected to web crippling, J. Struct. Eng., 127, 1137–1144, 2001. https://doi.org/10.1061/(ASCE)0733-9445(2001)127:10(1137)
[11] Macdonald M., Heiyantuduwa M.A., Kotelko M. and Rhodes J., Web crippling behaviour of thin-walled lipped channel beams, Thin-Walled Struct., 49, 682–690, 2011. https://doi.org/10.1016/j.tws.2010.09.010
[12] Macdonald M. and Heiyantuduwa M.A., A Design rule for web crippling of cold-formed steel lipped channel beams based on nonlinear FEA, Thin-Walled Struct., 53,123–130, 2012. https://doi.org/10.1016/j.tws.2012.01.003
[13] AISI S100-16, Specifications for the cold-formed steel structural members, cold-formed steel design manual, American Iron and Steel Institute (AISI), 2012.
[14] Standards Australia/Standards New Zealand, Australia/New Zealand Standard AS/NZS 4600 Cold-Formed Steel Structures, 2018.
[15] Eurocode. Eurocode 3: Design of steel structures - Part 1-3: General rules - Supplementary rules for cold-formed members and sheeting. European Committee for Standardization, 2007.
[16] AISI S909-17, Test Standard for Determining the Web Crippling Strength of Cold-Formed Steel Flexural Members, American Iron and Steel Institute (AISI), 2017.
[17] Sundararajah L., Mahendran M. and Keerthan P., Experimental studies of lipped channel beams subject to web crippling under two flange load cases, ASCE J. of Structural Engineering, 142(9), 04016058, 2016. https://doi.org/10.1061/(ASCE)ST.1943-541X.0001523
[18] Sundararajah L, Mahendran M. and Keerthan P., Web crippling experiments of high strength lipped channel beams under one-flange loading, J. Constr. Steel Res., 138, 851–866, 2017. https://doi.org/10.1016/j.jcsr.2017.06.011
[19] Janarthanan B., Mahendran M. and Gunalan S., Bearing capacity of cold-formed unlipped channel with restrained flanges under EOF and IOF load cases, Steel Construction Design and Research, 8 (3),146–154, 2015. https://doi.org/10.1002/stco.201510027
[20] Lian Y., Uzzaman A., Lim B.P.J., Abdelal G., Nash D. and Young B., Effect of web holes on web crippling strength of cold-formed steel channel sections under end-one-flange loading condition – Part I: tests and finite element analysis, Thin-Walled Struct., 107, 443–452, 2016. https://doi.org/10.1016/j.tws.2016.06.025
[21] Gunalan S. and Mahendran M., Web crippling tests of cold-formed steel channels under two flange load cases, J. Constr. Steel Res., 110, 1–15, 2015. https://doi.org/10.1016/j.jcsr.2015.01.018
[22] Uzzaman A., Lim B.P.J., Nash D. and Young B., Effects of edge-stiffened circular web openings on the web crippling strength of cold-formed steel channel sections under one-flange loading conditions, Eng. Struct., 139, 96–107, 2017. https://doi.org/10.1016/j.engstruct.2017.02.042
[23] Uzzaman A., Lim B.P.J., Nash D., Rhodes J. and Young B., Web crippling behaviour of cold-formed steel channel sections with offset web holes subjected to interior two-flange loading, Thin-Walled Struct., 50, 76–86, 2012. https://doi.org/10.1016/j.tws.2011.09.009
[24] Uzzaman A., Lim B.P.J., Nash D., Rhodes J. and Young B., Cold-formed steel sections with web openings subjected to web crippling under two-flange loading conditions - Part I: tests and finite element analysis, Thin-Walled Struct., 56, 38–48, 2012. https://doi.org/10.1016/j.tws.2012.03.010
[25] Uzzaman A., Lim B.P.J., Nash D., Rhodes J. and Young B., Cold-formed steel sections with web openings subjected to web crippling under two-flange loading conditions - Part II: parametric study and proposed design equations, Thin- Walled Struct., 56, 79–87, 2012. https://doi.org/10.1016/j.tws.2012.03.009
[26] Uzzaman A., Lim B.P.J., Nash D., Rhodes J. and Young B., Effect of offset web holes on web crippling strength of cold-formed steel channel sections under end-two flange loading condition, Thin-Walled Struct., 65, 34–48, 2013. https://doi.org/10.1016/j.tws.2012.12.003
[27] Lian Y., Uzzaman A., Lim J.B.P., Abdelal G., Nash D. and Young B., Effect of web holes on web crippling strength of cold-formed steel channel sections under end-one-flange loading condition - Part I: tests and finite element analysis, Thin-Walled Struct., 107, 443-452, 2016. https://doi.org/10.1016/j.tws.2016.06.025
[28] Lian Y., Uzzaman A., Lim J.B.P., Abdelal G., Nash D. and Young B., Effect of web holes on web crippling strength of cold-formed steel channel sections under end-one- flange loading condition - Part II: parametric study and proposed design equations, Thin-Walled Struct., 107, 489–501, 2016. https://doi.org/10.1016/j.tws.2016.06.026
[29] Lian Y., Uzzaman A., Lim J.B.P., Abdelal G., Nash D. and Young B., Web crippling behaviour of cold-formed steel channel sections with web holes subjected to interior-one-flange loading condition-part I: experimental and numerical investigation, Thin-Walled Struct., 111, 103–112 2017. https://doi.org/10.1016/j.tws.2016.10.024
[30] Lian Y., Uzzaman A., Lim J.B.P., Abdelal G., Nash D. and Young B., Web crippling behaviour of cold-formed steel channel sections with web holes subjected to interior-one-flange loading condition – part II: parametric study and proposed design equations, Thin-Walled Struct., 114, 92–106, 2017. https://doi.org/10.1016/j.tws.2016.10.018
[31] Yu W.W. and Davis C.S., Cold-formed steel members with perforated elements, J Struct Div 99, 2061–2077, 1973. https://doi.org/10.1061/JSDEAG.0003620
[32] Sivakumaran K.S. and Zielonka K.M., Web crippling strength of thin-walled steel members with web opening, Thin-Walled Struct., 8, 295–319, 1989. https://doi.org/10.1016/0263-8231(89)90035-9
[33] LaBoube R.A., Yu W.W., Deshmukh S.U. and Uphoff C.A., Crippling Capacity of Web Elements with Openings, J Struct Eng., 125, 137–141, 1999. https://doi.org/10.1061/(ASCE)0733-9445(1999)125:2(137)
[34] LaBoube R.A., Yu W.W. and Langan J.E., Cold-formed steel web with openings: summary report, Thin-Walled Struct., 28, 355–372, 1997. https://doi.org/10.1016/0263-8231(96)00021-3
[35] Chung K.F., Structural performance of cold formed sections with single and multiple web openings. Part-1: experimental investigation, Struct Eng., 73(9), 141-149, 1995.
[36] Chung K.F., Structural performance of cold formed sections with single and multiple web openings. Part-2: design rules. Struct Eng., 73(14), 223-228, 1995.
[37] Uzzaman A., Lim B.P.J., Nash D. and Young B., Effects of edge-stiffened circular web openings on the web crippling strength of cold-formed steel channel beams under one-flange loading conditions, Eng. Struct., 139, 96–107, 2017. https://doi.org/10.1016/j.tws.2019.106307
[38] Uzzaman A., Lim B.P.J., Nash D., Young B. and Toy K., Cold-formed steel channel beams under end-two-flange loading condition: Design for edge-stiffened holes, unstiffened holes and plain webs, Thin-Walled Struct., 147, 106532, 2020. https://doi.org/10.1016/j.tws.2019.106532
[39] Uzzaman A., Lim B.P.J., Nash D., Young B. and Toy K., Web crippling behaviour of cold-formed steel channel sections with edge-stiffened and unstiffened circular holes under interior-two-flange loading condition, Thin-Walled Struct., 154, 106813, 2020. https://doi.org/10.1016/j.tws.2020.106813.
[40] Chen B., Roy K., Fang Z., Uzzaman A., Chi Y. and Lim J.B.P., Web crippling capacity of fastened cold-formed steel channels with edge-stiffened web holes, un-stiffened web holes and plain webs under two-flange loading, Thin-Walled Struct., 163, 107666, 2021. https://doi.org/10.1016/j.tws.2021.107666
[41] Elilarasi, K., Kasthuri, S., and Janarthanan, B., Effect of circular openings on web crippling of unlipped channel sections under end-two-flange load case, Advanced Steel Construction, 16 (4), 310-320, 2020. https://doi.org/10.18057/IJASC.2020.16.4.3

[42] Gunalan, S., and Mahendran, M., Experimental study of unlipped channel beams subject to web crippling under one flange load cases, Advanced Steel Construction, 15 (2), 165-172, 2020. https://doi.org/10.18057/IJASC.2019.15.2.6

[43] Wang, W., Roy, K., Fang, Z., Ananthi, G. B. G., and Lim, J. B.., Web crippling behaviour of cold-formed steel channels with elongated un-stiffened and edge-stiffened web holes under end-two-flange loading condition, Thin-Walled Struct., 195, 111398, 2024. https://doi.org/10.1016/j.tws.2023.11139

[44] Thirunavukkarasu, K., Alsanat, H., Pologanathan, K., Gunalan, S., Gatheeshgar, P., Kanthasamy, E., and Higgins, C., Web crippling behaviour of sigma sections under end two flange loading–Numerical investigation, Structures, 59, 105765, 2024. https://doi.org/10.1016/j.istruc.2023.105765

[45] ABAQUS Analysis User's Manual-Version 6.14-2. USA: ABAQUS Inc.; 2018.

[46] TS EN ISO 6892-1. Metallic materials - Tensile testing - Part 1: Method of test at room temperature (ISO 6892-1:2019). Turkish Standards Institution; 2020.

[47] Yousefi A.M., Lim J.B.P. and Charles C.G., Cold-formed ferritic stainless steel unlipped channels with web openings subjected to web crippling under interior two-flange loading condition – Part I: Tests and finite element model validation, Thin-Walled Struct., 116, 333–341, 2017.

[48] Yousefi A.M., Lim J.B.P. and Charles C.G., Web Crippling Behavior of Unlipped Cold-Formed Ferritic Stainless Steel Channels Subject to One-Flange Loadings, J Struct Eng., 144 (8), 04018105, 2018. https://doi.org/10.1061/(ASCE)ST.1943-541X.0002118

[49] Yousefi A.M., Lim J.B.P. and Charles C.G., Web crippling strength of perforated cold-formed ferritic stainless steel unlipped channels with restrained flanges under one- flange loadings, Thin-Walled Struct., 137, 94–105, 2019. https://doi.org/10.1016/j.tws.2019.01.002

[50] Yousefi A.M., Lim J.B.P., Uzzaman, A., Uzzaman Y., Charles C.G., and Young B., Web crippling strength of cold-formed stainless steel lipped channel-sections with web openings subjected to interior-one-flange loading condition, Steel Compos Struct., 21, 629–59, 2016. https://doi.org/10.12989/scs.2016.21.3.629

[51] Fang Z., Roy K., Ma Q., Uzzaman A. and Lim J.B.P., Application of deep learning method in web crippling strength prediction of cold-formed stainless steel channel sections under end-two-flange loading, Struct., 33, 2903–2942, 2021. https://doi.org/10.1016/j.istruc.2021.05.097

[52] Fang Z., Roy K., Chi Y., Chen B. and Lim J.B.P., Finite element analysis and proposed design rules for cold-formed stainless steel channels with web holes under end-one-flange loading, Struct., 34, 2876–2899, 2021. https://doi.org/10.1016/j.istruc.2021.09.017

[53] Fang Z., Roy K., Uzzaman A. and Lim J.B.P., Numerical simulation and proposed design rules of cold-formed stainless steel channels with web holes under interior-one-flange loading, Engineering Structures 252, 113566, 2022. https://doi.org/10.1016/j.engstruct.2021.113566

Advanced Steel Construction – Vol. 20 No. 4 (2024) 424–436
DOI:10.18057/IJASC.2024.20.4.10

METAL BEAMS SUSCEPTIBLE TO OUT-OF-PLANE INSTABILITY DUE TO COMBINED COMPRESSION AND BENDING WITH GEOMETRIC IMPERFECTIONS

Antonio Aguero [1,*], Ana Almerich-Chulia [1], Yvona Kolekova [2] and Pedro Martin-Concepcion [1]

[1] *Dept. of Continuous Medium Mechanics and Theory of Structures, Universitat Politècnica de València, c/Camino de Vera s/n, 46022 Valencia, Spain*
[2] *Dept. of Structural Mechanics, Faculty of Civil Engineering, Slovak University of Technology in Bratislava, Bratislava, Slovak Republic*
** (Corresponding author: E-mail: anagra@mes.upv.es)*

ABSTRACT

The parts of the second generation of Eurocodes are continuously published. The full set of the 2nd generation of these new European standards consists of 68 parts of Eurocodes, 15 Technical Specifications and 5 Technical Reports and they will all be available in 2028. The aim of the paper is to bridge the gap concerning one of the newest and the most complex UGLI (Unique Global and Local Initial) imperfection methods. According to EN 1993-1-1:2022, ultimate limit state design checks may be carried out using methods of analysis named hereafter as M0, M1, M2, M3, M4, M5 or EM. Both Eurocodes EN 1993-1-1:2022 and EN 1999-1-1:2023 state, as an alternative that to sway and equivalent bow imperfection the new UGLI imperfection method may be employed for global and member analyses. In previous papers, plane stability was mostly investigated. The method presented in this paper enables the computing of the amplitude of the initial imperfection of elements under compression bending susceptible to out-of-plane buckling, and is a generalization of Eurocode rules, which is valid only for members under compression. This work is a continuation of a previous work by Agüero, in which the way to compute the UGLI imperfection was generalized for flexural torsional buckling due to compression and lateral torsional buckling due to bending. Some examples are presented to show the agreement with GMNIA (Geometrical material nonlinear analysis of imperfect structures), tests and proposals with codes.

ARTICLE HISTORY

Received: 22 April 2024
Revised: 21 October 2024
Accepted: 9 November 2024

KEYWORDS

Out-of-plane instability;
EN 1993-1-1:2005;
EN 1993-1-1:2022;
Equivalent UGLI imperfection;
Imperfection shapes;
Imperfection amplitudes

1. Introduction

EN 1993-1-1 [1] and EN 1999-1-1 [2] outline the design of metal structures with compression elements, and imperfections and their effects must be considered.

1-Indirectly by performing a linear analysis, plus interaction formulae. This method includes nonlinearity using buckling curves to obtain reduction factor χ.

2-Directly by including imperfections in the nonlinear analysis.

This involves geometrical imperfections and residual stresses. The imperfections below must be contemplated: a) global imperfections for bracing systems and frames; b) local imperfections for individual members; c) the structure's elastic critical buckling mode η_{cr} shape in line with clauses 5.3.2(11) of [1] and [2], 7.3.6 of [4] as the geometrical equivalent UGLI (Unique Global and Local Initial) imperfection.

Below are some methods that allow the buckling resistance of sensitive beams to lateral torsional buckling according to [1], [2], [3] and [4] to be obtained:

• The indirect method involves a linear analysis. It includes not only geometrical, but also material nonlinearity and imperfections, by buckling curves to acquire reduction factor χ_{LT} according to clause 6.3 of [1].

• The direct method involves a second-order analysis with equivalent geometric imperfections.

In accordance with clauses 5.3.4(3) in [1,2] and 7.3.4(3) in [4], "Taking account of lateral torsional buckling of a member in bending the imperfections may be adopted as $k \cdot e_0$, where e_0 is the equivalent initial bow imperfection of the weak axis of the profile considered. In general, additional torsional imperfection does not need to be allowed for. The value k = 0.5 is recommended. The National Annex may choose the value of k."

In line with 7.3.3.2 in [3], "For a 2nd-order analysis, by taking into account the lateral torsional buckling of a member in bending, the equivalent imperfection may be determined according to (7.11), where $e_{0,LT}$ is the equivalent bow imperfection about the weak axis of the considered profile. In general, additional torsional imperfection may be neglected".

Here a numerical method permits the equivalent initial imperfection to be obtained for beams with a doubly symmetric section susceptible to lateral torsional buckling.

For the elements that form part of the bending-compression combination, and with out-of-plane instability, clauses 6.3.3 and 6.3.4 in [1,2], or clauses 8.3.3 and 8.3.4 in [4], come into play. Interaction formula or a nonlinear analysis of the imperfect structure may be used.

It is possible to express imperfection in the form of single imperfection, as in the structure's buckling mode $\eta_{cr}(x)$ (clauses 5.3.2 (11) in [1-2], 7.3.6(1) in [3], 7.3.2(11) in [4]). It is known as the geometrical equivalent UGLI (Unique Global and Local Initial) imperfection. See Chladný et al. [5,6,7] for a complete description.

The proposals of [1-4] fall in line with "(1)", with flexural buckling occurring around a strong axis due to compression.

Imperfections are generally expressed as:

$$\{\eta_{init}(x)\} = \eta_0 \{\eta_{cr}(x)\}$$

$$\eta_{init}(x) = \left(\frac{\alpha\left(\bar{\lambda} - \bar{\lambda}_0\right)}{\bar{\lambda}^2} \frac{1 - \frac{\bar{\lambda}^2 \cdot \chi}{\gamma_{M1}}}{1 - \bar{\lambda}^2 \cdot \chi} \frac{f_y}{E\left(\frac{I}{W}\frac{d^2\eta_{cr}}{dx^2}\right)} \right)_{X_{cr}} \tag{1}$$

$$\eta_{cr}(x) = \eta_0 \cdot \eta_{cr}(x)$$

For flexural buckling around a strong axis:

$$\eta_{init,w}(x) = \left(\frac{\alpha\left(\bar{\lambda} - \bar{\lambda}_0\right)}{\bar{\lambda}^2} \frac{1 - \frac{\bar{\lambda}^2 \cdot \chi}{\gamma_{M1}}}{1 - \bar{\lambda}^2 \cdot \chi} \frac{f_y}{E\left(\frac{I_y}{W_y}\frac{d^2\eta_{cr,w}}{dx^2}\right)} \right)_{X_{cr}} \tag{2}$$

$$\eta_{cr,w}(x) = \eta_0 \cdot \eta_{cr,w}(x)$$

For flexural buckling around a weak axis:

$$\eta_{init,v}(x) = \left(\frac{\alpha\left(\bar{\lambda} - \bar{\lambda}_0\right)}{\bar{\lambda}^2} \frac{1 - \frac{\bar{\lambda}^2 \cdot \chi}{\gamma_{M1}}}{1 - \bar{\lambda}^2 \cdot \chi} \frac{f_y}{E\left(\frac{I_z}{W_z}\frac{d^2\eta_{cr,v}}{dx^2}\right)} \right)_{X_{cr}} \tag{3}$$

$$\eta_{cr,v}(x) = \eta_0 \cdot \eta_{cr,v}(x)$$

No iteration is needed for prismatic elements with uniform axial forces. The critical section occurs where the curvature is maximum. Iteration is needed in the majority of practical cases.

See Chladný et al. [5-7] for further generalization. Flexural buckling takes place around both the axes as so "(4)".

$$\begin{Bmatrix}\eta_{init,v}(x)\\ \eta_{init,w}(x)\end{Bmatrix}=\left(\frac{\alpha\left(\bar{\lambda}-\bar{\lambda}_0\right)}{\bar{\lambda}^2}\frac{1-\frac{\bar{\lambda}^2\cdot\chi}{\gamma_{M1}}}{1-\bar{\lambda}^2\cdot\chi}\frac{f_y}{E\left(\frac{I_z}{W_z}\left|\frac{d^2\eta_{cr,v}}{dx^2}\right|+\frac{I_y}{W_y}\left|\frac{d^2\eta_{cr,w}}{dx^2}\right|\right)}\right)_{X_{cr}} \quad (4)$$

$$\begin{Bmatrix}\eta_{cr,v}(x)\\ \eta_{cr,w}(x)\end{Bmatrix}=\eta_0\cdot\begin{Bmatrix}\eta_{cr,v}(x)\\ \eta_{cr,w}(x)\end{Bmatrix}$$

Simplifying "(2)", "(3)" and "(4)" can be done by discarding partial safety factor γ_{M1}.

This is not advisable because it destroys the method's basic feature and the results differ from those obtained for the equivalent member method for $N_{Ed} = N_{b,Rd}$.

The novel methodology has emerged in recent times in some publications, with examples displaying how to achieve flexural buckling resistance for members with arch structures, nonuniform cross-sections and nonuniform axial forces [8-11]. According to [8], the amplitude of such imperfection offers a different way by comparing it to Chladný`s method.

Agüero et al. [9,10] offer a generalization of flexural torsional buckling owing to compression, in which an imperfect structure analysis is done as "(5)".

$$\begin{Bmatrix}\eta_{init,v}(x)\\ \eta_{init,w}(x)\\ \eta_{init,\theta x}(x)\end{Bmatrix}=\left(\frac{\alpha\left(\bar{\lambda}-\bar{\lambda}_0\right)}{\bar{\lambda}^2}\frac{1-\frac{\bar{\lambda}^2\cdot\chi}{\gamma_{M1}}}{1-\bar{\lambda}^2\cdot\chi}\frac{f_y}{E\left(\frac{I_z}{W_z}\frac{d^2\eta_{cr,v}}{dx^2}+\frac{I_y}{W_y}\frac{d^2\eta_{cr,w}}{dx^2}+\frac{I_w}{W_{Bi}}\frac{d^2\eta_{cr,\theta x}}{dx^2}\right)}\right)_{X_{cr}} \quad (5)$$

$$\begin{Bmatrix}\eta_{cr,v}(x)\\ \eta_{cr,w}(x)\\ \eta_{cr,\theta x}(x)\end{Bmatrix}=\eta_0\cdot\begin{Bmatrix}\eta_{cr,v}(x)\\ \eta_{cr,w}(x)\\ \eta_{cr,\theta x}(x)\end{Bmatrix}$$

The next equation can be applied in accordance with clause 8.3.1.4 [3] for doubly symmetric I- and H-sections.

$$\begin{Bmatrix}\eta_{init,v}(x)\\ \eta_{init,w}(x)\\ \eta_{init,\theta x}(x)\end{Bmatrix}=\left(\left(\frac{\bar{\lambda}_{TF}}{\bar{\lambda}_z}\right)^2\frac{\alpha_{TF}\left(\bar{\lambda}_z-\bar{\lambda}_0\right)}{\bar{\lambda}_{TF}^{\,2}}\frac{1-\frac{\bar{\lambda}_{TF}^{\,2}\cdot\chi}{\gamma_{M1}}}{1-\bar{\lambda}_{TF}^{\,2}\cdot\chi}\frac{f_y}{E\left(\frac{I_z}{W_z}\frac{d^2\eta_{cr,v}}{dx^2}+\frac{I_y}{W_y}\frac{d^2\eta_{cr,w}}{dx^2}+\frac{I_w}{W_{Bi}}\frac{d^2\eta_{cr,\theta x}}{dx^2}\right)}\right)_{X_{cr}} \quad (6)$$

$$\begin{Bmatrix}\eta_{cr,v}(x)\\ \eta_{cr,w}(x)\\ \eta_{cr,\theta x}(x)\end{Bmatrix}=\eta_0\cdot\begin{Bmatrix}\eta_{cr,v}(x)\\ \eta_{cr,w}(x)\\ \eta_{cr,\theta x}(x)\end{Bmatrix}$$

Agüero et al. [9,10] (Fig. 4) present another generalization for lateral torsional buckling, which describes the imperfect structure analysis as "(7)".

$$\begin{Bmatrix}\eta_{init,v}(x)\\ \eta_{init,\theta x}(x)\end{Bmatrix}=\left(\frac{\alpha_{LT}\left(\bar{\lambda}_{LT}-\bar{\lambda}_{LT,0}\right)}{\bar{\lambda}_{LT}^{\,2}}\frac{1-\frac{\bar{\lambda}_{LT}^{\,2}\cdot\chi_{LT}}{\gamma_{M1}}}{1-\beta\cdot\bar{\lambda}_{LT}^{\,2}\cdot\chi_{LT}}\frac{f_y}{E\left(\frac{I_z}{W_z}\left|\frac{d^2\eta_{cr,v}}{dx^2}\right|+\frac{I_w}{W_{Bi}}\left|\frac{d^2\eta_{cr,\theta x}}{dx^2}\right|\right)}\right)_{X_{cr}} \quad (7)$$

$$\begin{Bmatrix}\eta_{cr,v}(x)\\ \eta_{cr,\theta x}(x)\end{Bmatrix}=\eta_0\cdot\begin{Bmatrix}\eta_{cr,v}(x)\\ \eta_{cr,\theta x}(x)\end{Bmatrix}$$

The curvatures for doubly symmetric sections are taken as the absolute value.

According to clause 8.3.2.3 in [3] for not only fork supports at both ends, but also doubly symmetric I and H-sections, the next equation may apply, where $f_M = 1$ (Table 8.6 of [3]):

$$\begin{Bmatrix}\eta_{init,v}(x)\\ \eta_{init,\theta x}(x)\end{Bmatrix}=\left(\left(\frac{\bar{\lambda}_{LT}}{\bar{\lambda}_z}\right)^2\frac{\alpha_{LT}\left(\bar{\lambda}_z-\bar{\lambda}_{LT,0}\right)}{\bar{\lambda}_{LT}^{\,2}}\frac{1-\frac{\bar{\lambda}_{LT}^{\,2}\cdot\chi_{LT}}{\gamma_{M1}}}{1-\bar{\lambda}_{LT}^{\,2}\cdot\chi_{LT}}\frac{f_y}{E\left(\frac{I_z}{W_z}\left|\frac{d^2\eta_{cr,v}}{dx^2}\right|+\frac{I_w}{W_{Bi}}\left|\frac{d^2\eta_{cr,\theta x}}{dx^2}\right|\right)}\right)_{X_{cr}} \quad (8)$$

$$\begin{Bmatrix}\eta_{cr,v}(x)\\ \eta_{cr,\theta x}(x)\end{Bmatrix}=\eta_0\cdot\begin{Bmatrix}\eta_{cr,v}(x)\\ \eta_{cr,\theta x}(x)\end{Bmatrix}$$

Bijlaard et al. [11] and Wieschollek et al. [12] generalize the equation found in Eurocodes [1,3] for lateral torsional buckling cases, when cross-section flanges are taken as sensitive members to flexural buckling and under compression by applying Chladný's method. Papp [13] solves buckling under bending and compression, and Trahair [14] contemplates beam column behavior.

In the event of out-of-plane instability caused by compression and bending in line with clause 6.3.4 in [1], the most recent proposals can be generalized by applying exactly the same method as that depicted in [9,10]. A similar equation to former ones is obtained:

$$\begin{Bmatrix}\eta_{init,v}(x)\\ \eta_{init,\theta x}(x)\end{Bmatrix}=\left(\frac{\alpha^*\left(\bar{\lambda}_{op}-\bar{\lambda}_{op,0}\right)}{\bar{\lambda}_{op}^{\,2}}\frac{1-\frac{\bar{\lambda}_{op}^{\,2}\cdot\chi_{op}}{\gamma_{M1}}}{1-\bar{\lambda}_{op}^{\,2}\cdot\chi_{op}}\frac{f_y}{E\left(\frac{I_z}{W_z}\left|\frac{d^2\eta_{cr,v}}{dx^2}\right|+\frac{I_w}{W_{Bi}}\left|\frac{d^2\eta_{cr,\theta x}}{dx^2}\right|\right)}\right)_{X_{cr}} \quad (9)$$

$$\begin{Bmatrix}\eta_{cr,v}(x)\\ \eta_{cr,\theta x}(x)\end{Bmatrix}=\eta_0\cdot\begin{Bmatrix}\eta_{cr,v}(x)\\ \eta_{cr,\theta x}(x)\end{Bmatrix}$$

where:

$$\bar{\lambda}_{op}=\sqrt{\frac{\alpha_{ult,k}}{\alpha_{cr,op}}} \quad (10)$$

$$\frac{1}{\alpha_{ult,k}}=\left(\frac{N_{Ed}}{N_{Rk}}+\frac{M_{y,Ed}}{M_{y,Rk}}\right)_{x_{cr}} \quad (11)$$

The critical section is accomplished as in Agüero [9,10].

2. Research significance

This article reports innovation by accomplishing imperfection for beam columns with out-of-plane instability that form part of the bending-compression combination when only bending "(9)" exists and is the equivalent to "(7)". The means to do so is coherent with the authors' former proposals.

The inclusions of the equivalent geometric imperfections in nonlinear analyses offer these advantages:

- At the section level, buckling appears as further internal forces and displacements. Equilibrium and compatibility equations are checked rather than stability checks, which are carried out on members and diminish their strength.
- A global issue is the buckling problem. It is analyzed by bearing in mind structures' members interaction, and not only that of members under compression. Here secondary internal forces emerge on either tension members or stabilizing beams.

3. The method followed to know the amplitude of imperfection

Buckling shape is scaled with a maximum value of 1.0; e.g. $\max[\eta_{cr,v}(x)] = 1.0$. η_0, which means the amplitude of imperfection in the shear center.

$$\begin{aligned}\eta_0&=\eta_{init,v}(x_{\max,v})=\max\left(\eta_{init,v}(x)\right)=\max\left(\eta_0\eta_{cr,v}(x)\right)\\ \eta_{init,\theta x}(x_{\max,\theta x})&=\max\left(\eta_{init,\theta x}(x)\right)=\max\left(\eta_0\eta_{cr,\theta x}(x)\right)\end{aligned} \quad (12)$$

To know imperfection, the next four steps are taken:

Step 1: compute buckling load αcr and buckling shape $\eta_{cr}(x)$, both of which can be calculated by the FEM (Finite Element Method).

Step 2: compute not only the bending moments around weak axes z, but also the bi-moments associated with the buckling mode. Internal bending/torsion forces are accomplished as so:

$$M_{z\eta}(x) = EI_z \frac{d^2\eta_{cr,v}}{dx^2}$$
$$B_{\eta}(x) = EI_w \frac{d^2\eta_{cr,\theta x}}{dx^2} \tag{13}$$

Relevant stresses are computed from this equation:

$$\sigma_{Mz}(x) + \sigma_B(x) = \frac{EI_z}{W_z}\frac{d^2\eta_{cr,v}}{dx^2} + \frac{EI_w}{W_B}\frac{d^2\eta_{cr,\theta x}}{dx^2} \tag{14}$$

Step 3: The first calculation iteration applies the initial guess:

$$\alpha_{ult,1} = \min\left(\frac{1}{\frac{N}{A\cdot f_y} + \frac{M_y}{W_y \cdot f_y}}\right)$$
$$\bar{\lambda}_{op,1} = \sqrt{\frac{\alpha_{ult,1}}{\alpha_{cr}}} \rightarrow \chi_{op,1} \rightarrow \alpha_{b,1} = \frac{\alpha_{ult,1}\cdot\chi_{op,1}}{\gamma_{M1}} \tag{15}$$

To acquire the maximum in"(14)", a better initial guess can be contemplated. To reach cross-section resistance $\alpha_{b,1}$ at the moment when the buckling load level is achieved, imperfection (scale factor $\Omega_1(x)$) needs to be computed in all the sections.

$$\frac{f_y}{\gamma_{M0}} = \frac{N_{Ed}\cdot\alpha_{b,1}}{A} + \frac{M_{y,Ed}\cdot\alpha_{b,1}}{W_y} + \frac{\Omega_1(x)}{\left(\frac{\alpha_{cr}}{\alpha_{b,1}}-1\right)}\left(E\left(\frac{I_z}{W_z}\frac{d^2\eta_{cr,v}}{dx^2} + \frac{I_w}{W_B}\frac{d^2\eta_{cr,\theta x}}{dx^2}\right)\right) \tag{16}$$

$$\Omega_1(x) = \frac{\left(\frac{f_y}{\gamma_{M0}} - \frac{N_{Ed}\cdot\alpha_{b,1}}{A} - \frac{M_{y,Ed}\cdot\alpha_{b,1}}{W_y}\right)\left(\frac{\alpha_{cr}}{\alpha_{b,1}}-1\right)}{E\left(\frac{I_z}{W_z}\frac{d^2\eta_{cr,v}}{dx^2} + \frac{I_w}{W_B}\frac{d^2\eta_{cr,\theta x}}{dx^2}\right)} \tag{17}$$

The purpose of the first iteration is to obtain the minimum of these scale factors; e.g., $\eta_{0,1}$ occurs at critical section $x_{cr,1}$.

$$\eta_{0,1} = \min(\Omega_1(x)) = \Omega_1\left(x_{cr,1}\right) \tag{18}$$

Step 4: For the second iteration:

$$\alpha_{ult,2} = \left(\frac{1}{\frac{N}{A\cdot f_y} + \frac{M_y}{W_y \cdot f_y}}\right)\cdot x_{cr} \rightarrow \bar{\lambda}_{op,2} = \sqrt{\frac{\alpha_{ult,2}}{\alpha_{cr}}} \rightarrow \chi_{op,2} \rightarrow$$
$$\alpha_{b,1} = \frac{\alpha_{ult,1}\cdot\chi_{op,2}}{\gamma_{M1}} \tag{19}$$

Then calculate utilization factor U(x) along the beam:

$$U_{N+My+Mz+Bi}(x) =$$
$$= \left(\frac{N_{Ed}\cdot\alpha_{b,2}}{A\frac{f_y}{\gamma_{M0}}}\right) + \left(\frac{M_{y,Ed}\cdot\alpha_{b,2}}{W_y\frac{f_y}{\gamma_{M0}}}\right) + \tag{20}$$
$$+ \left[\frac{\eta_{0,1}}{\left(\frac{\alpha_{cr}}{\alpha_{b,2}}-1\right)}\frac{EI_z\left|\frac{d^2\eta_{cr,v}}{dx^2}\right|}{W_z\frac{f_y}{\gamma_{M0}}}\right] + \left[\frac{\eta_{0,1}}{\left(\frac{\alpha_{cr}}{\alpha_{b,2}}-1\right)}\frac{EI_w\left|\frac{d^2\eta_{cr,\theta x}}{dx^2}\right|}{W_B\frac{f_y}{\gamma_{M0}}}\right]$$

The maximum utilization for doubly symmetric sections is acquired as the sum of the absolute values of the partial utilizations.

Compute the next critical section $x_{cr,2}$. Utilization factor U is the maximum:

$$\max(U_{N+M_y+M_z+B}(x)) = U_{N+M_y+M_z+B}(x_{cr,2}) \tag{21}$$

Let's assume that the critical section is the same as in the previous iteration event. In this case, critical section xcr is found and, as a consequence, it also takes the initial imperfection amplitude η0 value toward initial imperfection.

$$\{\eta_{init}\} = \eta_0(\eta_{cr}) \tag{22}$$

If the critical section's location is different from the one before, another iteration is necessary in Step 4 until the critical section's position is known:

$$\eta_{0,2} = \left(\frac{\left(\frac{f_y}{\gamma_{M0}} - \frac{N_{Ed}\cdot\alpha_{b,2}}{A} + \frac{M_{y,Ed}\cdot\alpha_{b,2}}{W_y}\right)\left(\frac{\alpha_{cr}}{\alpha_{b,2}}-1\right)}{E\left(\frac{I_z}{W_z}\frac{d^2\eta_{cr,v}}{dx^2} + \frac{I_w}{W_B}\frac{d^2\eta_{cr,\theta x}}{dx^2}\right)}\right)_{x_{cr,2}} \tag{23}$$

4. Examples

Comparing the presented out-of-plane instability proposal to the geometric equivalent imperfection for bending and compression can solve four examples. Current Eurocode, GMNIA (geometric and material nonlinear analysis of the imperfect structure) and the test results can be compared by discussing the factors that influence differences.

Applying the Beamcolumnimperfection software by Agüero [15] provides the plots below:

Plot 1: ν (lateral displacement), θ_x (torsional rotation), M_z (bending moment around a weak axis), B (Bimoment).

Plot 2: Utilization M_z, B, My (bending moment around a strong axis), N (axial force) and a linear interaction formula.

Plot 3: T_t (Saint-Venant Torsional moment), T_w (Warping torsional moment), V_y (shear force that parallels axis y), V_z (Shear force that parallels axis z).

Plasticity is considered concentrated by means of a simplified linear interaction equation or with exact curves obtained by linear programming (simplex).

The number of elements used for beams and columns is 20.

In the portal frame, warping is considered continuous in the beam-column connection.

4.1. Example 1

The beam with IPE 200, S235 (Figs. 1-3) is studied with fork supports (3.78 m long), compression force and concentrated force at the midspan. The impact of the midspan load application on the shear center and top flange is examined, and the obtained results are compared to GMNIA Papp [13].

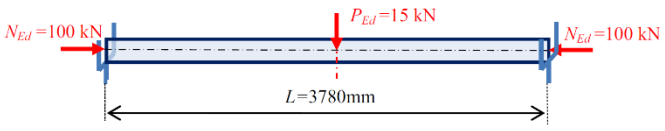

Fig. 1 Example of a figure

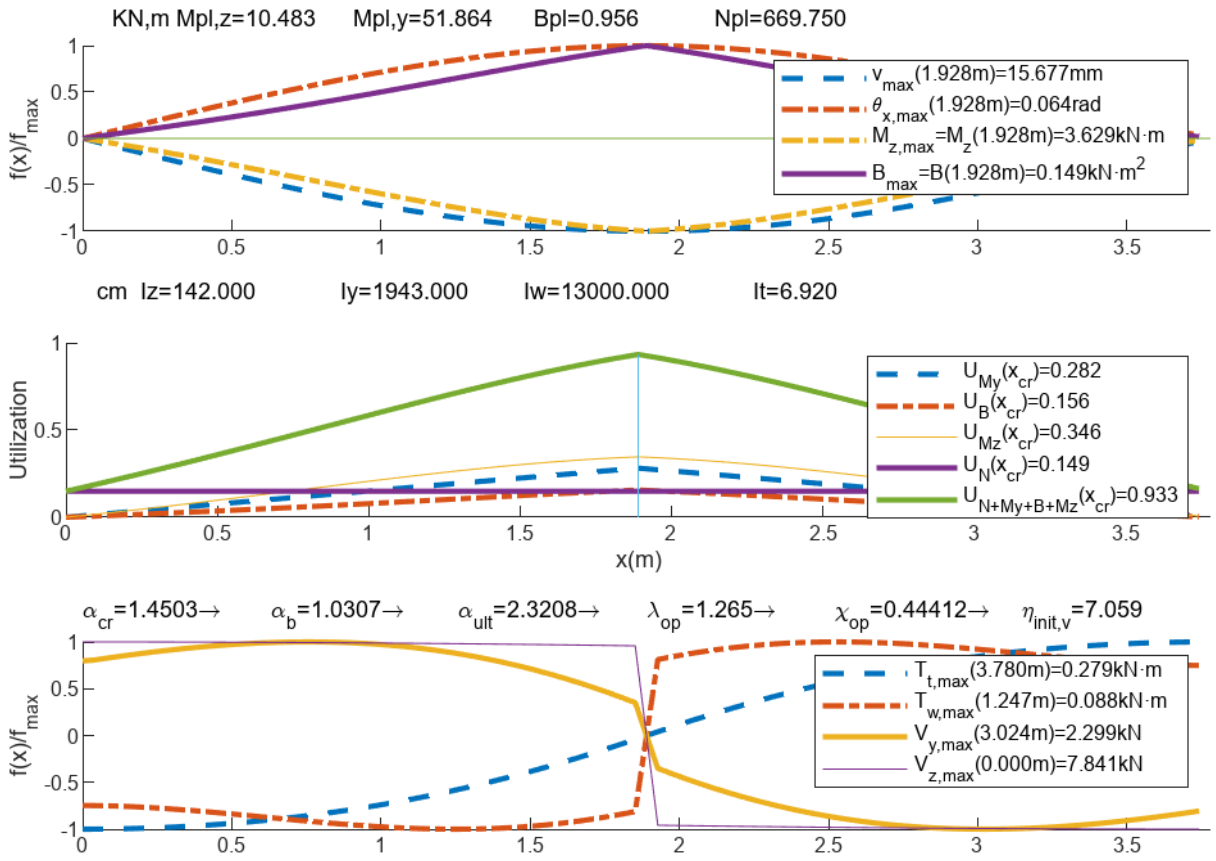

Fig. 2 Example 1: P_{Ed} is applied to the top flange of IPE 200, S235

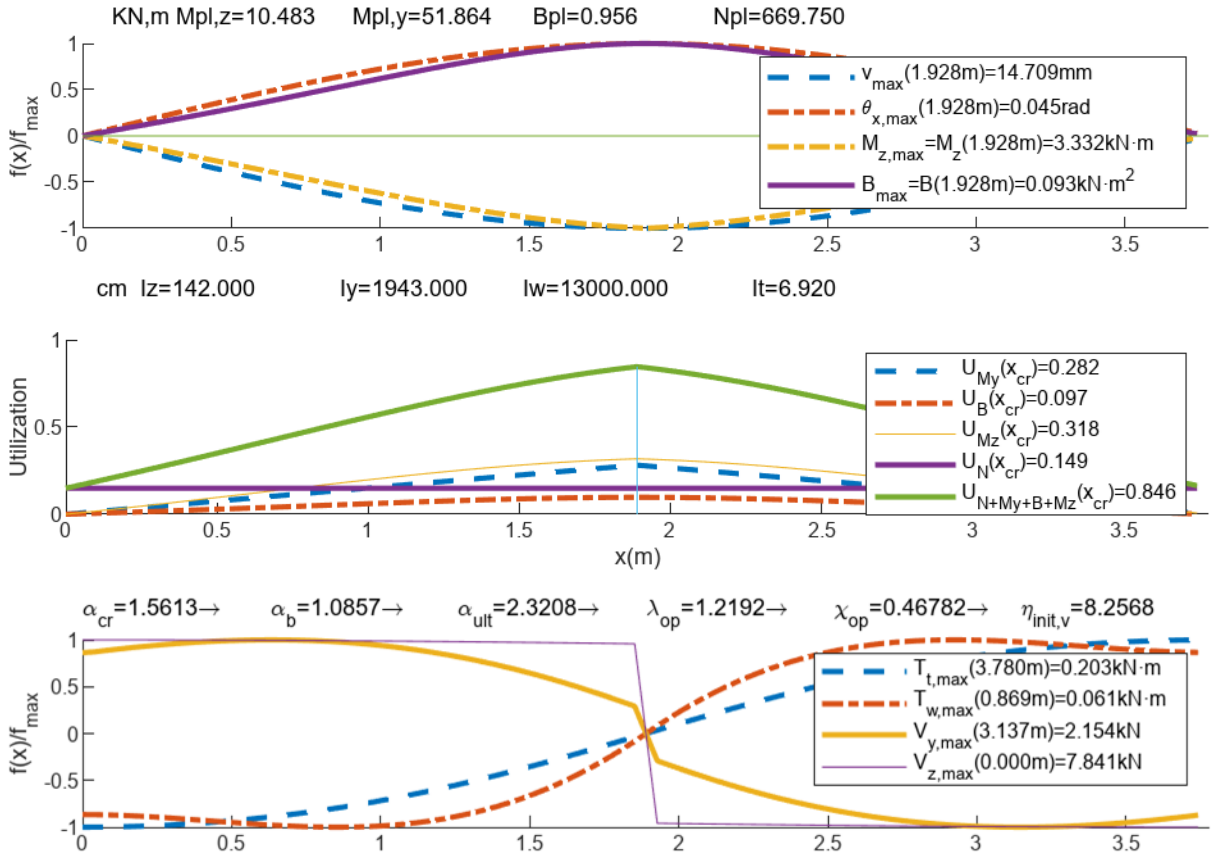

Fig. 3 Example 1: P_{Ed} is applied to the shear center of IPE 200, S235

4.2. Example 2

The beam with IPE 500, S235 (Figs. 4 to 10) is examined with not only fork supports (8.097 m long), but also the lateral support on the top flange at the midspan. A moment is applied to one support and compression force. The compression and bending moment combination is studied, and leads to failure in this example. The GMNIA results and those in Papp [13] are compared.

In example 2, the lateral support at the midspan is located on the top flange. The compression-bending moment combination fails.

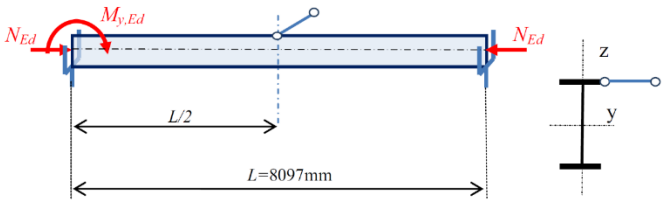

Fig. 4 Example 2: geometry and loadings IPE 500, S235

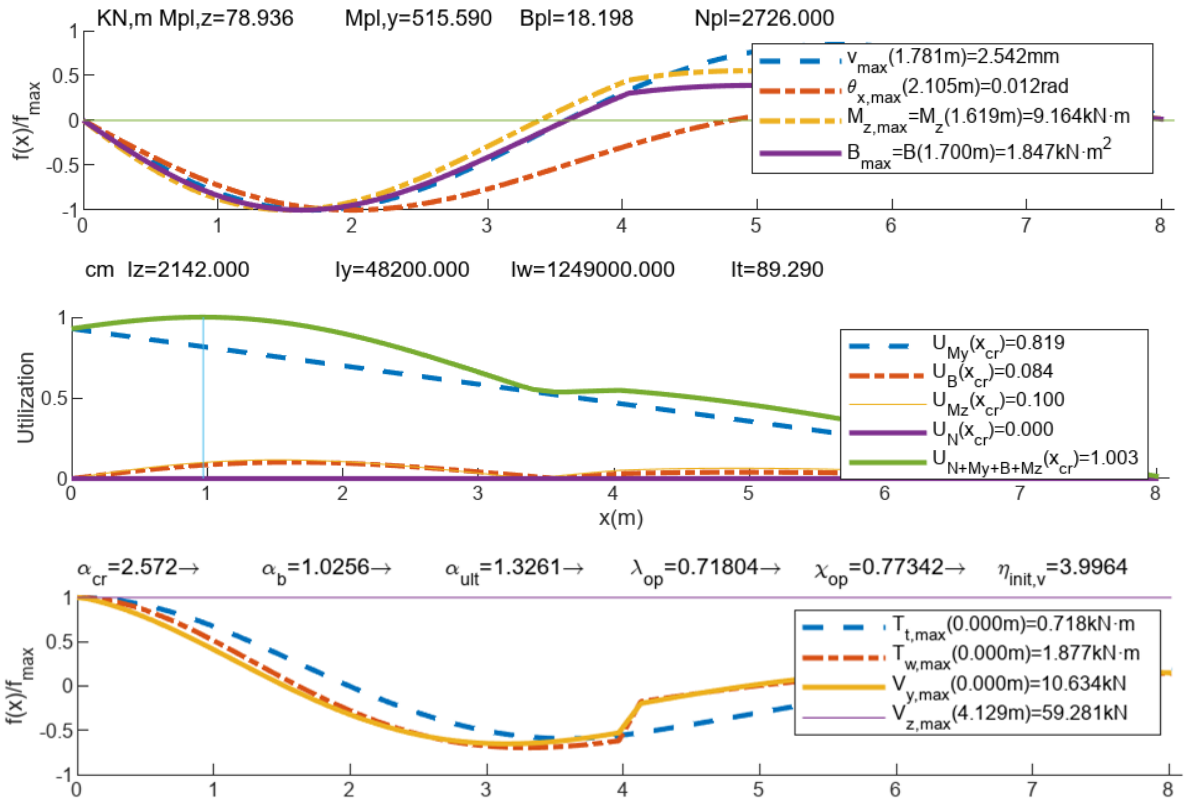

Fig. 5 Example 2a: Combination of N = 0 kN, My = 480 kNm

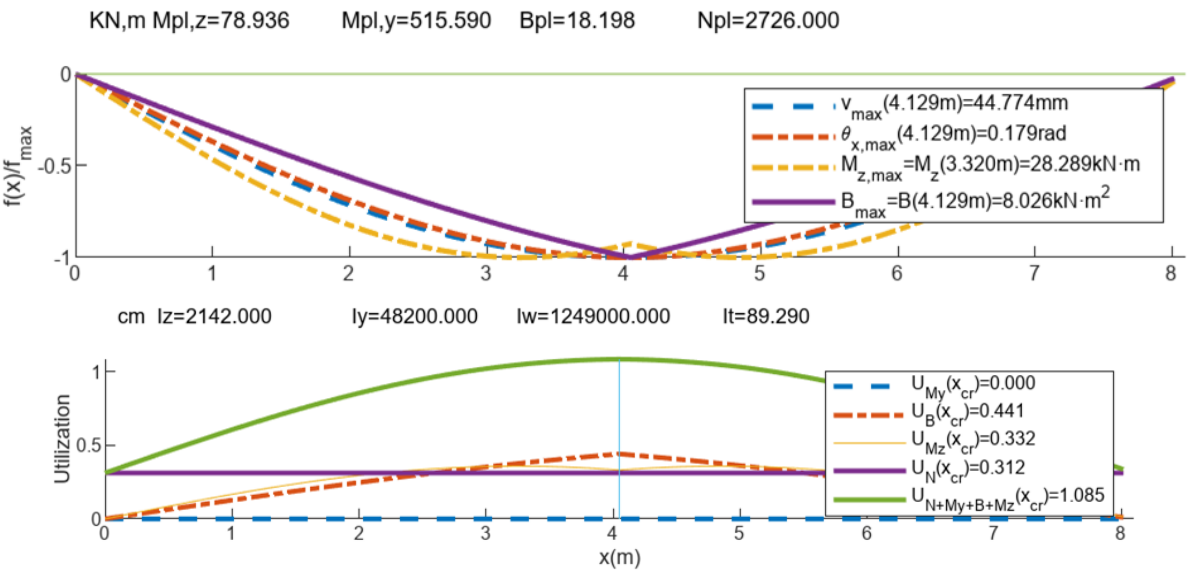

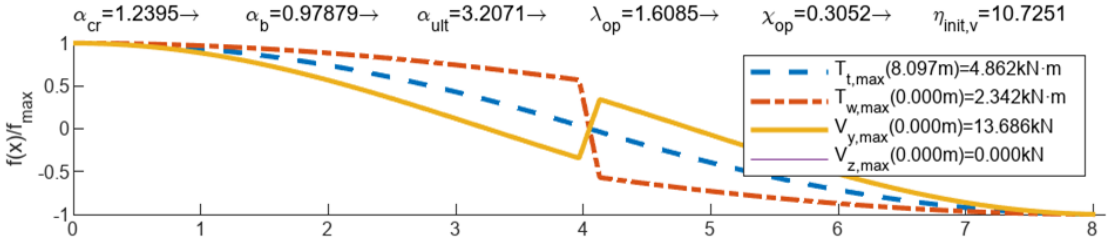

Fig. 6 Example 2b: Combination of N = 850 kN, My = 0 kNm

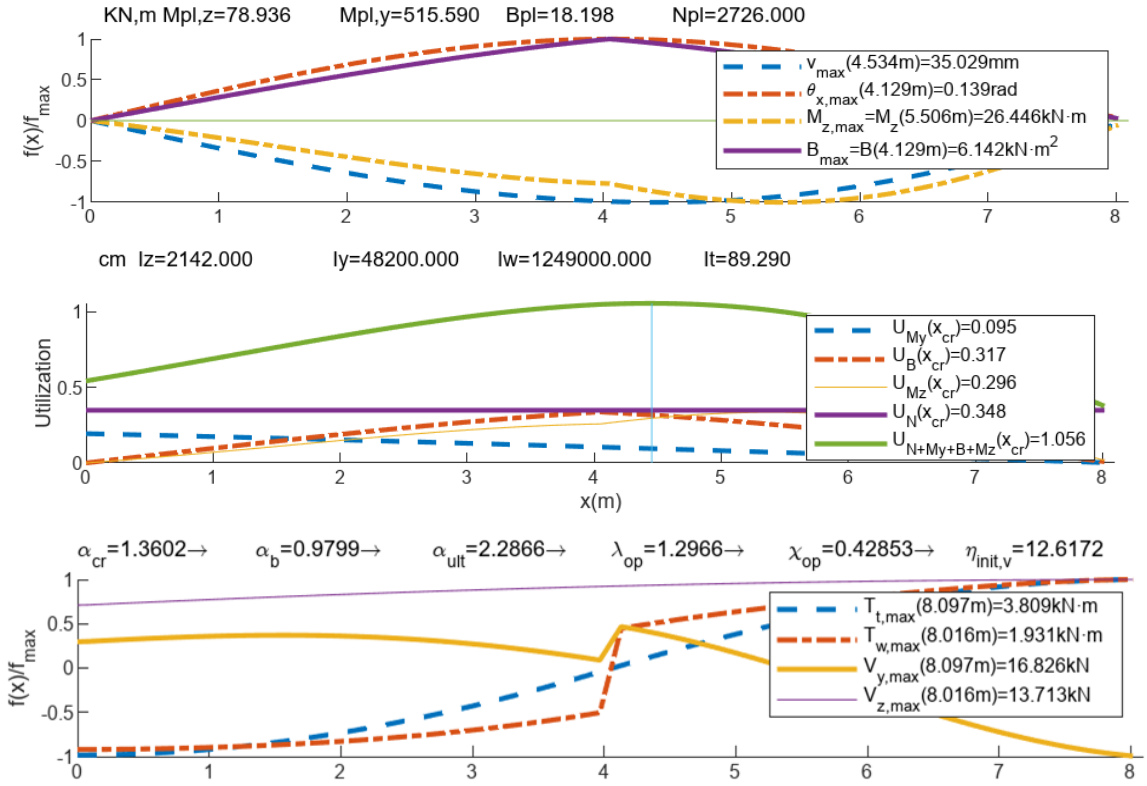

Fig. 7 Example 2c: Combination of N = 950 kN, My = 100 kNm

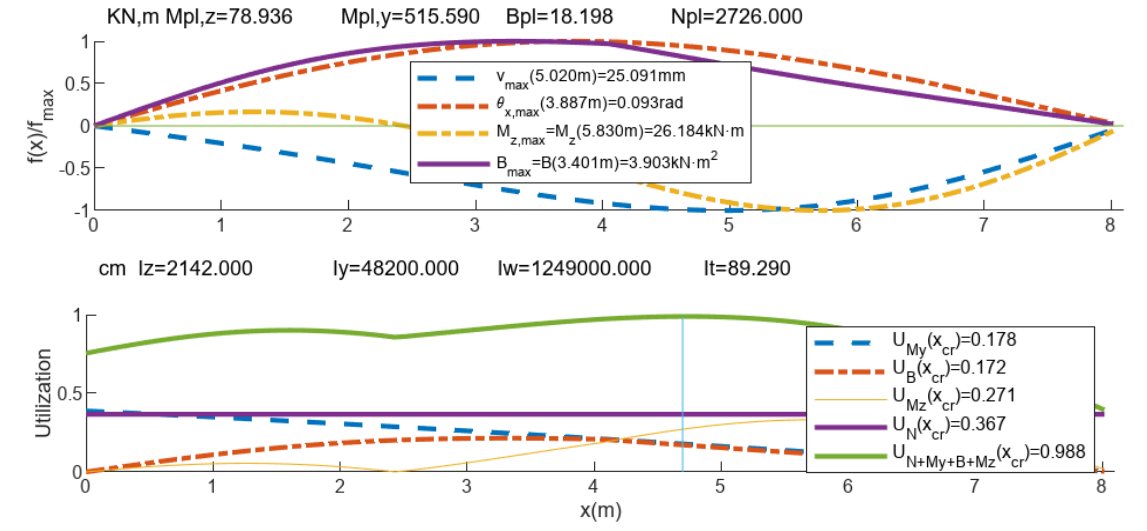

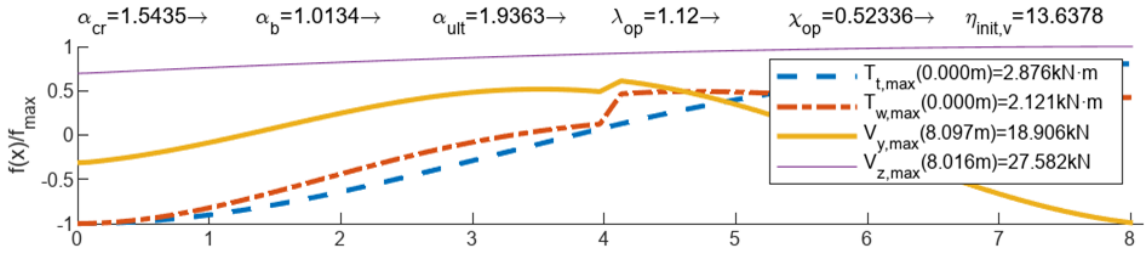

Fig. 8 Example 2d: Combination of N = 10000 kN, M y = 200 kNm

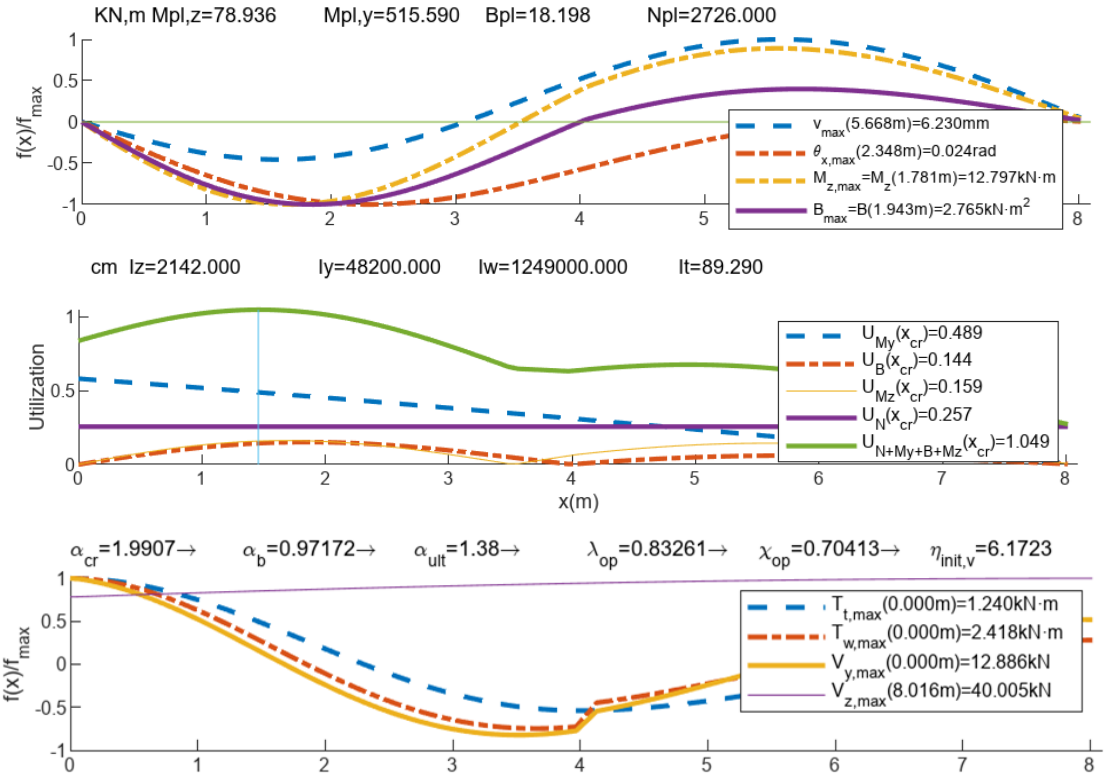

Fig. 9 Example 2e: Combination of N = 700 kN, My = 300 kNm

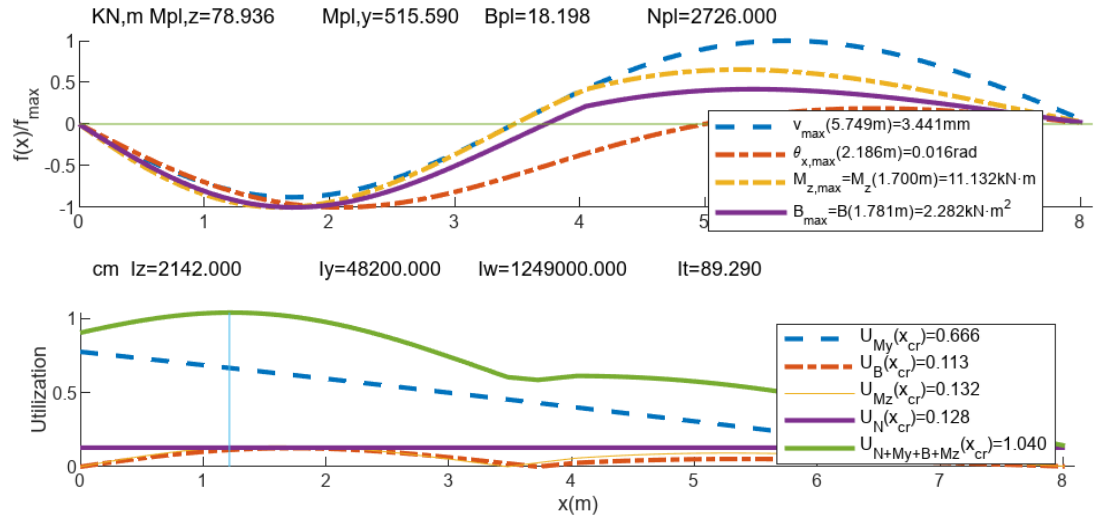

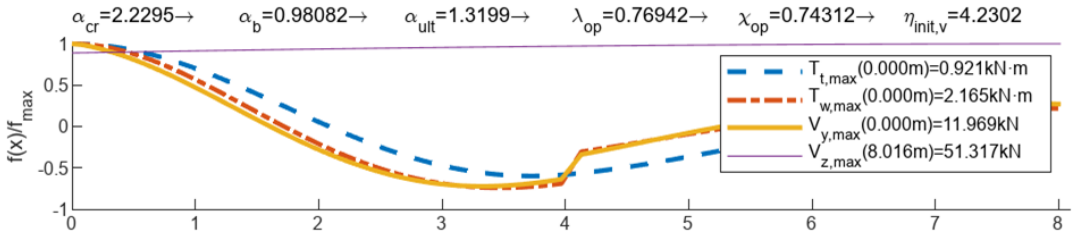

Fig. 10 Example 2f: Combination of N = 350 kN, My = 400 kNm

4.3. Example 3

Work is done with the beam by applying HEB 200, fy = 378 MPa (Figs. 11-15) and fork supports (7.8 m beam column length). Compression force + eccentric load applied at the midspan. Eccentricity is e_y=100 mm, e_z=-150 mm. The obtained results and the experimental ones reported in Winkler et al. [16] are compared. Two assumptions apply to solve this example with: warping-free on supports; restrained warping.

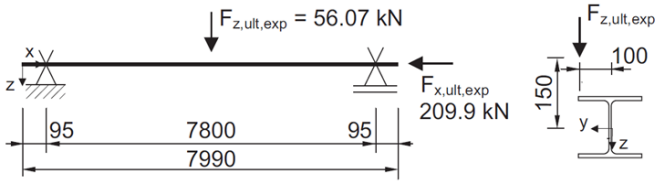

Fig. 11 Example 3: geometry and loadings. HEB 200, f_y = 378 Mpa

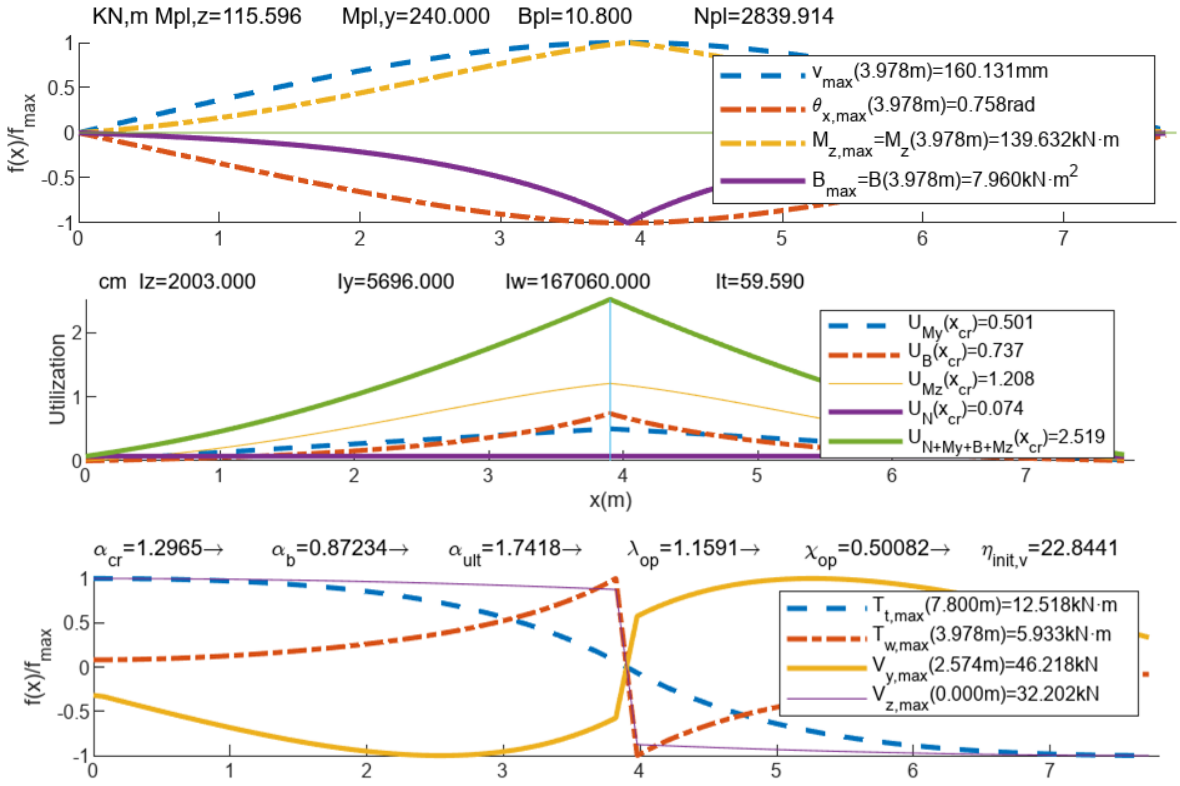

Fig. 12 Example 3: it considers the maximum experimental load and a linear interaction formula

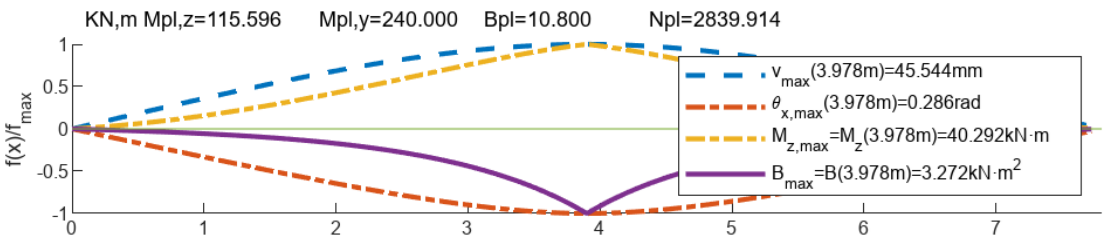

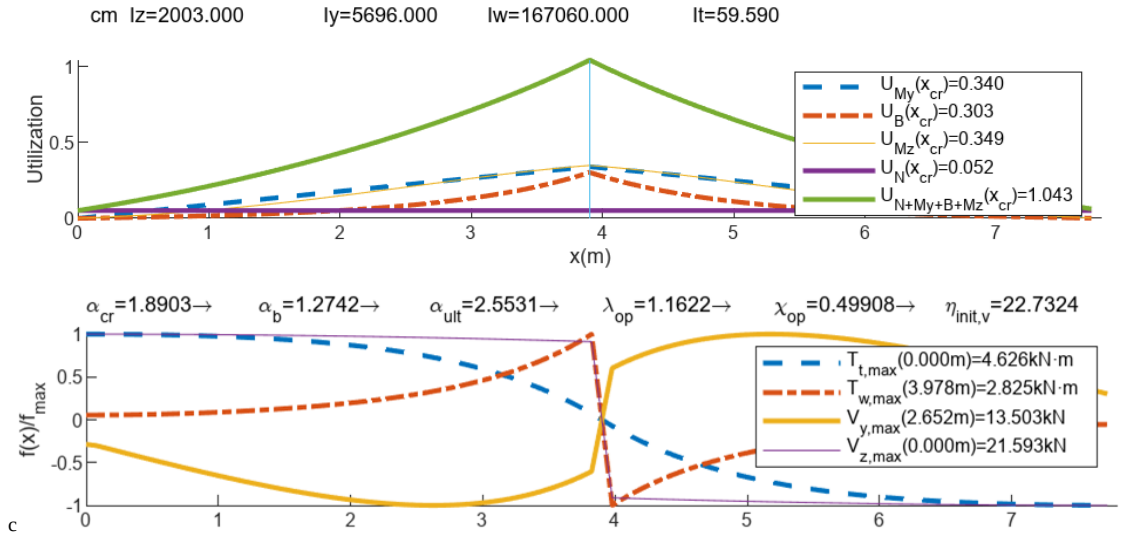

c

Fig. 13 Example 3: it considers a 70% maximum experimental load and a linear interaction formula

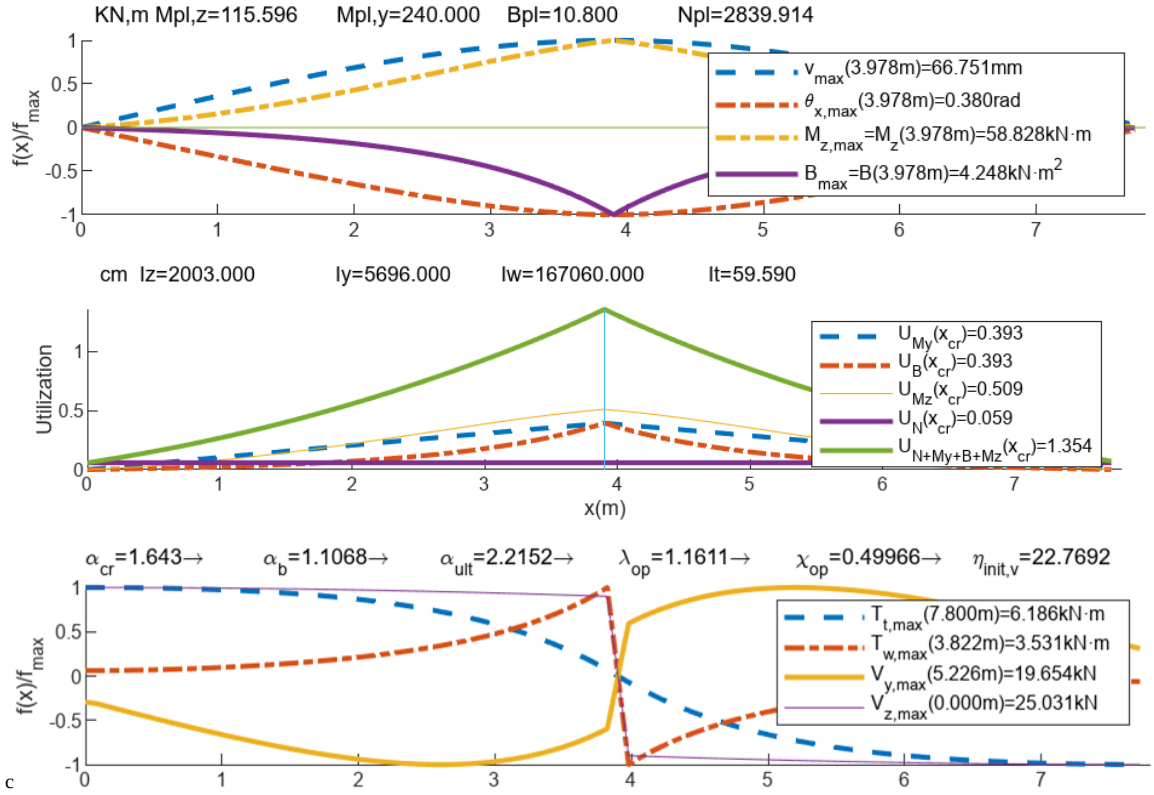

c

Fig. 14 Example 3: it considers an 80% maximum experimental load and a linear interaction formula with the linear interaction formula utilization factor U = 1.354 with the Thinwallsectiongeneral software by Agüero [16][1]

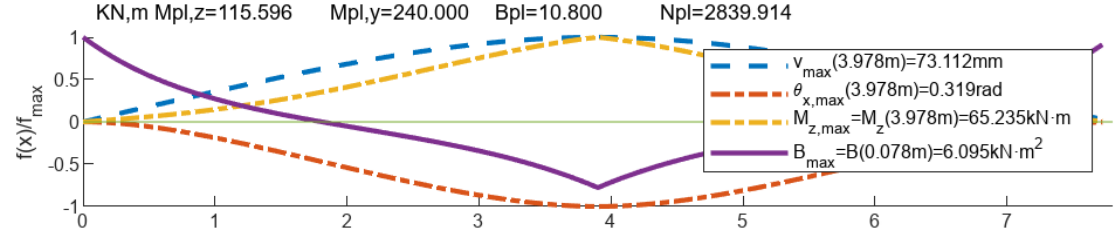

[1] A real interaction formula results in utilization factor U = 1/1.052 = 0.95. By including out-of-plane imperfection, the ultimate load exceeds the 80% load achieved with the experimental results, and material hardening is also taken into account

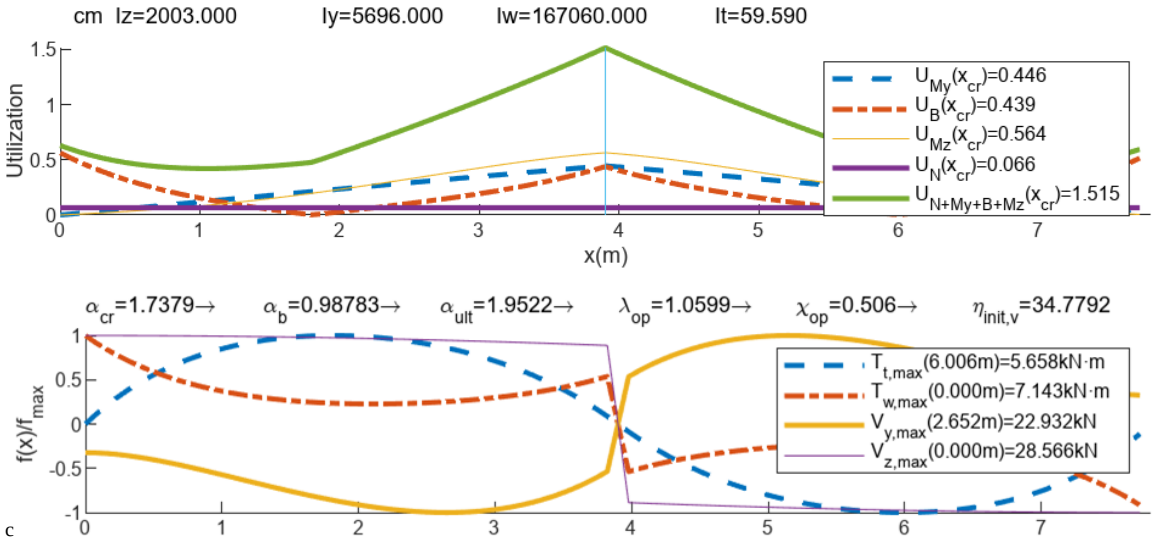

Fig. 15 Example 3: it applies a 90% ultimate load and warping is taken as restrained. The utilization factor with a linear interaction formula is U = 1.515, but is 1.06 ≈ 1.0 when the real interaction is taken into account with the Thinwallsectiongeneral software [16].

4.4. Portal frame components

The portal frame (Figs. 16-19) is computed by Chladný's UGLI imperfection method. During calculations, safety factor γ_{M1} = 1.1 in quantity $e_{0,m}$ is employed. This is set out in EN 1999-1-1:2023, EN 1999-1-1:2007 and EN 1993-1-1:2005. Safety factor γ_{M1} in EN 1993-1-1:2022 lacks $e_{0,m}$. Fig.17a and Fig.17b contain the obtained outcomes.

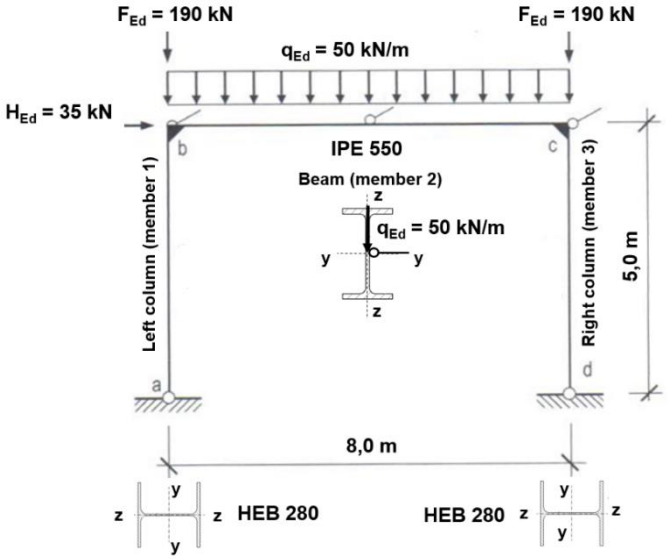

Fig. 16 Investigated portal frame

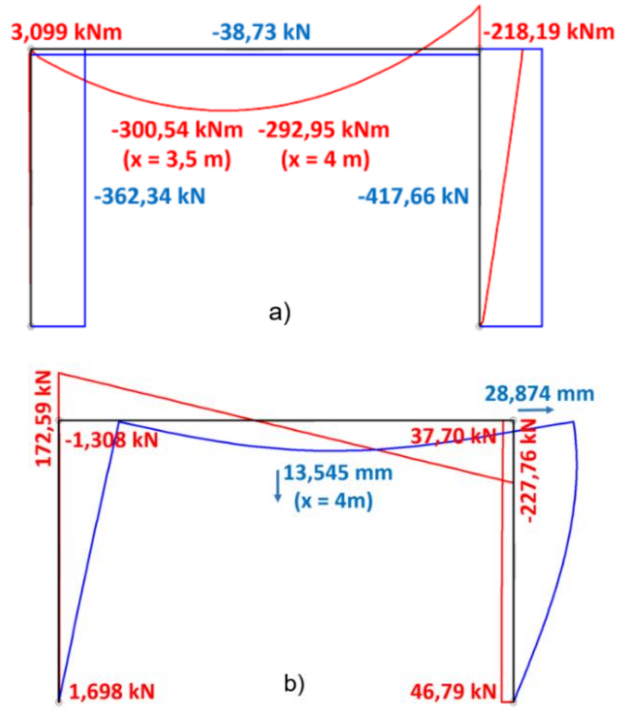

Fig. 17 (a) Distribution of bending moments and normal force; (b) distribution of shear forces and deformation of the investigated portal frame due to UGLI imperfection

Applying clause 8.3.3 "Uniform members in bending and axial compression" of EN 1993-1-1:2022, which include interaction formulae (8.88) and (8.89), results in the internal forces that appear in Fig. 17, as well as these utilization factors: a) U = 0.850 for the right column; b) U = 0.653 for the left beam part (Fig. 16).

Examples 4.4a and 4.4b investigate the beam and right column as individual members that are loaded by normal forces, end moments and uniform loading q to generate exactly the same internal forces as those found in Fig. 17. The impact that the out-of-plane UGLI imperfection of both the column (example 4.4a) and beam (example 4.4b) has on this portal frame components' behavior and their utilization factors is studied. A comparison is made of the utilization factors to the above values of 0.850 and 0.653, respectively, for the column and beam.

4.4.a. Portal frame column

If the column resistance verification is carried out in line with clause 8.3.3 of EN 1993-1-1:2022, it should be substituted for the calculation in Fig. 18. Hence the utilization factor would be 0.817 rather than 0.850. Indeed these differing procedures are not completely comparable.

4.4.b. Portal frame beam

If column resistance verification is performed as in clause 8.3.3 of EN 1993-1-1:2022, it would be substituted for the calculation in Fig. 19. The utilization factor would be 0.596 rather than 0.653. Indeed these differing procedures are not completely comparable.

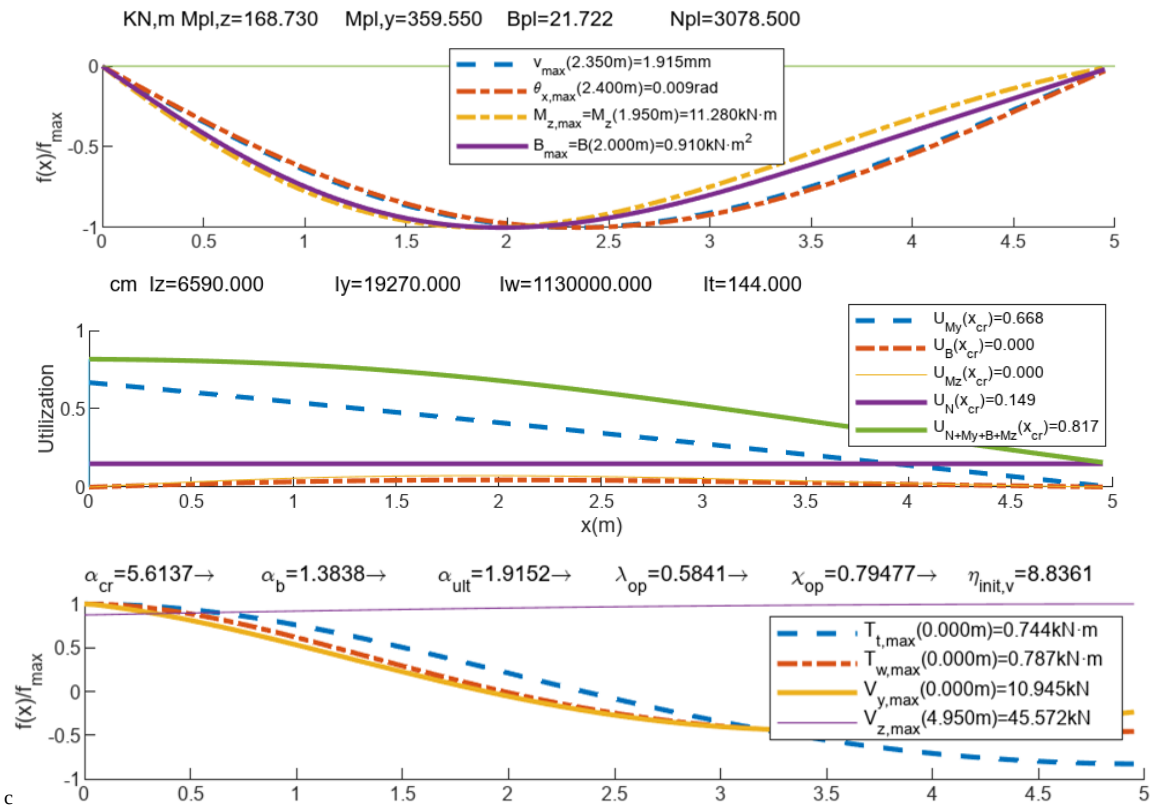

Fig. 18 Example 4.4a: Column. HEB 280. Safety factor γ_{M1} = 1.1 and imperfection factor α = 0.49. The utilization factor is U = 0.817

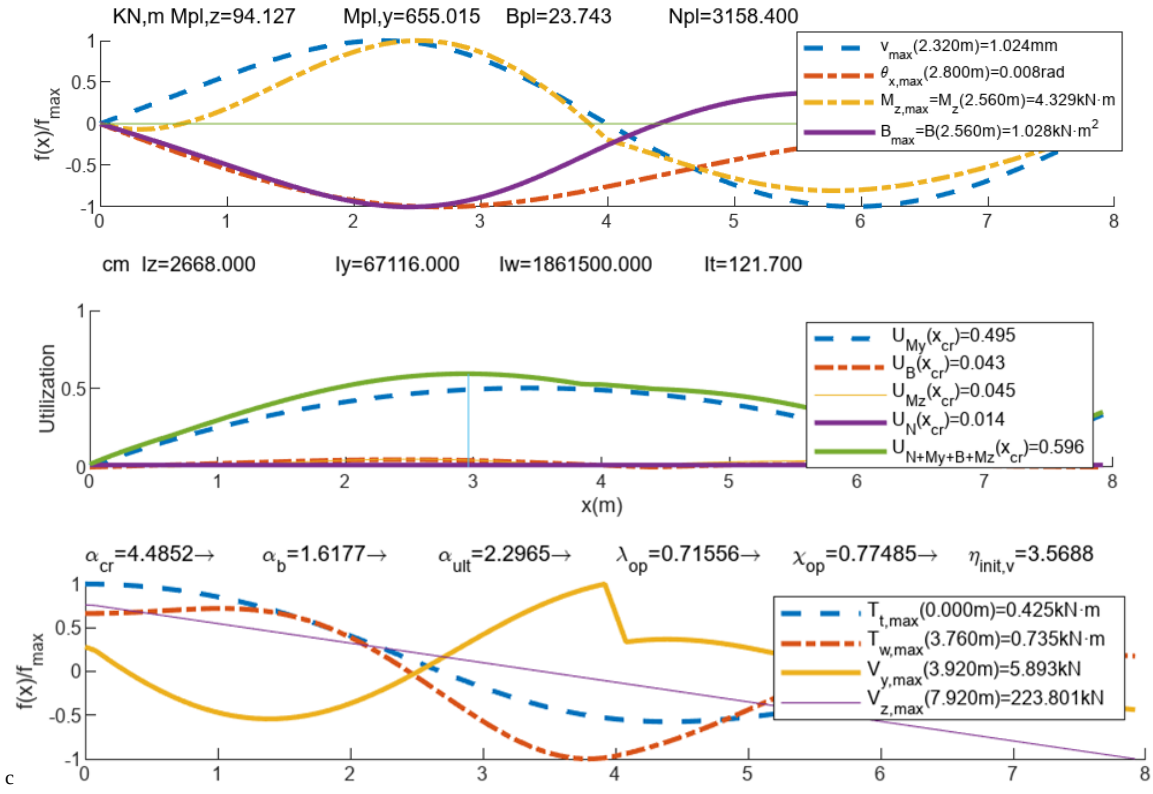

Fig. 19 Example 4.4b: Beam. IPE 550. Safety factor γ_{M1} = 1.1 and imperfection factor α = 0.34. The utilization factor is U = 0.596

5. Comparisons to other authors and GMNIA

Example 1 (Figs. 1 to 3) and Example 2 (Figs. 4 to 10) show results that compare to those in Papp [13].

Example 1 indicates that the utilization factor in accordance with GMNIA is U = 0.89, and is U = 0.933 in accordance with this proposal when the load application point is on the top flange surface, and U = 0.846 when load acts in the shear center. Further information can be found in Papp's article in Example 6, Table 6.

Example 2 shows how our results are on the safe side by 10% vs. those indicated by GMNIA. Further information can be found in Papp's article in Example 7, Fig. 11.

Example 3 (Figs. 11 to 15) contains results that are comparable to Winkler et al. [17]. Our results are on the safe side vs. the experimental results.

If the beam end cross-sections on supports are warping-free, our results are on the safe side by 20% vs. the test results. If warping is constrained at beam ends, our results are also on the safe side by 10% vs. the test results.

Example 4 is compared to the Eurocode method [18] for designing beam-columns after investigating portal frame components: beam (Example 4.4a); column (Example 4.4b). Comparisons appear in relation to the: (i) results in line with interaction formulae (8.88) and (8.89) in [3]; (ii) results acquired according to the herein proposed procedure.

6. Conclusions

A generalization of Chladný's method is proposed to explain buckling resistance in sensitive structures to flexural buckling. This method falls in line with the former generalizations to lateral torsion owing to bending and flexural torsional buckling given compression. In the present work, the proposed imperfection is utilized in out-of-plane owing to compression-bending with the reference clause 6.3.4 in [1,2] or 8.3.4 in [3].

Five examples are employed to compare the method. It offers good agreements with the GMNIA, test and Eurocode 3 design proposals.

Our method is also applied in four examples: example 1 (Figs. 1-3); example 2 (Figs. 4-10); example 3 (Figs. 11-15); example 4 (Figs. 16-20). Comparisons are made to Papp [13] by employing GMNIA (examples 1 and 2), the test of Winkler et al. [17] (example 3) and the Eurocode procedure [18] (example 4), and all with acceptable agreements.

Appendix. Nomenclature

α denotes the imperfection factor related to the flexural buckling curve (Tables 6.1 and 6.2 in EN 1993-1-1 [1]; Tables 3.2 and 6.6 of EN 1999-1-1 [2])

α_{LT} represents the imperfection factor for lateral torsional buckling related to the buckling curve (Tables 6.3, 6.4 and 6.5 of EN 1993-1-1 [1]; 6.3.2.2 of EN 1999-1-1 [2])

α_{cr} depicts the minimum load amplifier for axial force configurations in members to achieve elastic critical buckling loads (5.2.1(3) of [1]; 5.2.1(3) of [2])

α_{ult} refers to the amplifier for members' load to accomplish critical cross-section resistance (6.3.4(2) in [1]. A more convenient symbol αult,k is utilized; [2] is unaware of this quantity/symbol)

α_b relates to relative lateral torsional buckling resistance (Eq. 12); [1] and [2] do not employ the symbol)

γ_{M0} indicates the partial safety factor for cross-section resistance when the Class cross-section is (6.1 in [1]; [2] is unaware of such quantity/symbol)

γ_{M1} refers to the partial safety factor for members that resist instability, evaluated by member checks (6.1 of [1] and 6.1.3; Table 6.1 of [2])

χ denotes the reduction factor for the relevant buckling curve (6.3.1.2 of [1]; 6.3.1.2 of [2]

χ_{LT} depicts the reduction factor for lateral torsional buckling in relation to relative slenderness (6.3.1.2 of [1]; 6.3.1.2 of [2])

$\bar{\lambda}$ indicates the plateau length of buckling curves (for steel [1]: 0.2; for aluminum alloy [2]: 0.1 for Buckling Class A, 0.0 for Buckling Class B)

$\bar{\lambda}_0$ denotes relative slenderness for lateral torsional buckling (6.3.2.2 and 6.3.2.3 of [1]; 6.3.2.2 of [2])

$\bar{\lambda}_{LT}$ represents the plateau length for lateral torsional buckling curves (for steel [1]: 0.2 of 6.3.2.2 and 0.2-0.4 of 6.3.2.3; for aluminum alloy [2]: 0.6 for Class 1 and 2 cross-sections; 0.4 for Class 3 and 4 cross-sections of 6.3.2.2)

$\bar{\lambda}_{op}$ refers to the relative slenderness for out-of-plane buckling (6.3.4 of [1] and [2])

β denotes the correction factor for lateral torsional buckling curves (6.3.2.3 in [1]; [2] is unaware of this quantity/symbol)

$\{\eta_{init}\}$ indicates UGLI imperfection in the elastic critical buckling mode shape

$\{\eta_{cr}\}$ identifies the elastic critical buckling mode shape

$\eta_{cr,w}$ depicts buckling shape component displacement perpendicularly to axis y

$\eta_{cr,v}$ depicts buckling shape component displacement perpendicularly to axis z

$\eta_{cr,\theta x}$ is related to the torsional rotation of the buckling shape component around the shear center axis

A means the cross-sectional area

η_0 denotes UGLI imperfection amplitude

E stands for the modulus of elasticity (210 000 MPa for steel [1]; 70 000 MPa for aluminum alloy [2])

I_y, I_z respectively reflect the second moments of the area in relation to axes y and z

I_w denotes the warping constant

N_{cr} implies the elastic critical force of the relevant buckling mode in accordance with gross cross-section properties

$M_{y,Ed}$ represents the design value for the bending moment around axis y

N_{Rk} reflects the characteristic resistance of normal force on critical section x_{cr}

M_{Rk} denotes the characteristic resistance of the bending moment on critical section x_{cr}

$U_{N+My+Mz+B}$ respectively indicate the utilization factor given by N_{Ed}, $M_{y,Ed}$, $M_{z,Ed}$, and B_{Ed}

W_z represents the section modulus around axis z

W_y represents the section modulus around axis y

W_B means the warping section modulus

x_{cr} depicts the critical section; the utilization factor is higher than the factors in all the other sections

Appendix. Background equations to analyze the imperfect structure.

The following equation is used to perform the analysis of the imperfect structure; these equations are implemented in the software ¨Buckling Beam Column N My Mz B T any support & section¨ by Aguero [19,20]. Other software can be found in [21]:

$$\left([K_L]+[K_G]\right)\{d\}=\{f_{ext}\}+[K_G]\{\eta_{init}\} \tag{24}$$

Where:

$$[K_L]\{d\} \leftarrow \frac{1}{2}\int_0^L \left(EA\left(\frac{du}{dx}\right)^2 + GJ\left(\frac{d\theta_x}{dx}\right)^2 + EI_y\left(\frac{d^2w}{dx^2}\right)^2 + EI_z\left(\frac{d^2v}{dx^2}\right)^2 + EI_w\left(\frac{d^2\theta_x}{dx^2}\right)^2 \right) dx \tag{25}$$

$$[K_G]\{d\} \leftarrow \frac{1}{2}\int_0^L \left(\begin{array}{l} N\left[\left(\frac{dv}{dx}\right)^2+\left(\frac{dw}{dx}\right)^2+2z_{sc}\left(\frac{dv}{dx}\right)\left(\frac{d\theta_x}{dx}\right)-2y_{sc}\left(\frac{dw}{dx}\right)\left(\frac{d\theta_x}{dx}\right)+\left(\frac{d\theta_x}{dx}\right)^2 r_0^2\right] \\ +2M_z\left(\frac{d^2w}{dx^2}\right)\left(\frac{d\theta_x}{dx}\right)+2M_y\left(\frac{d^2v}{dx^2}\right)\left(\frac{d\theta_x}{dx}\right)+\left(M_y\beta_z-M_z\beta_y+B\beta_w\right)\left(\frac{d^2\theta_x}{dx^2}\right)^2 \end{array} \right) dx \tag{26}$$

$$\begin{aligned} \beta_z &= \frac{1}{I_y}\iint z\left(y^2+z^2\right)dA - 2z_{sc} \\ \beta_y &= \frac{1}{I_z}\iint y\left(y^2+z^2\right)dA - 2y_{sc} \\ \beta_w &= \frac{1}{I_w}\iint w\left(y^2+z^2\right)dA \\ r_0^2 &= \frac{I_y+I_z}{A}+y_{sc}^2+z_{sc}^2 \end{aligned} \tag{27}$$

Funding

This research project is supported by the Slovak Grant Agency VEGA No.1/0155/23.

References

[1] Eurocode 3: Design of steel structures. Part 1.1: General rules and rules for buildings. EN 1993-1-1, 2005, Corrigendum AC, 2006, Corrigendum AC, 2009, Amendment A1, 2014, CEN Brussels.
[2] Eurocode 9: Design of aluminium structures.Part 1.1: General structural rules. EN 1999-1-1, 2007, Amendment A1, 2009, Amendment A2, 2013, CEN Brussels.
[3] Eurocode 3: Design of steel structures. Part 1.1: General rules and rules for buildings. EN 1993-1-1, 2022, CEN Brussels.
[4] Eurocode 9: Design of aluminium structures. Part 1.1: General structural rules. prEN 1999-1-1, 2020-07-01, CEN Brussels.
[5] E. Chladný and M. Štujberová, Frames with unique global and local imperfection in the shape of the elastic buckling mode (part 1), Stahlbau, 8, pp. 609-617, 2013.
[6] E. Chladný and M. Štujberová, Frames with unique global and local imperfection in the shape of the elastic buckling mode (Part 2), Stahlbau, 9, pp. 684-694, 2013.
[7] E. Chladný and M. Štujberová, Errata: frames with unique global and local imperfection in the shape of the elastic buckling mode. Part 1, Stahlbau, 82:H. 8, S. 609–617, 2013. Part 2. Stahlbau, 83:H. 9, S. 684–694, 2013. Stahlbau, 82:H. 9 S. 684-694, 2013. Stahlbau, 1, 64-64, 2014.
[8] I. Baláž, "Determination of the flexural buckling resistance of frames with members with non-uniform cross-section and non-uniform axial compression forces", Zborník z XXXIV Aktívu pracovníkov odboru OK so zahraničnou účast'ou "Teoretické a konštrukčné problémy ocel'ových a drevených konštruckcií a mostov", 16–17, 10, Pezinok, 17–22, 2008.
[9] A. Agüero, L. Pallarés and F.J. Pallarés, "Equivalent geometric imperfection definition in steel structures sensitive to flexural and/or torsional buckling due to compression", Engineering Structures, 96(1), 160-177, 2015.
[10] A. Agüero, F.J. Pallarés and L. Pallarés, "Equivalent geometric imperfection definition in steel structures sensitive to lateral torsional buckling due to bending moment", Engineering Structures, 96(1), 41-55, 2015.
[11] F. Bijlaard, M. Feldmann, J. Naumes and G. Sedlacek, "The "general method" for assessing the out of plane stability of structural members and frames and the comparison with alternative rules in EN1993 – Eurocode3 – Part 1-1", Steel Construction, 3(1), 19-33, 2010.
[12] M. Wieschollek, N. Schillo, M. Feldmann and G. Sedlacek. "Lateral–torsional buckling checks of steel frames using second-order analysis", Steel Construction, 5(2), 71-86, 2012.
[13] F. Papp, "Buckling assessment of steel members through overall imperfection method", Engineering Structures, 106, 124−136, 2016.
[14] N.S. Trahair, Flexural–torsional buckling of structures, E&Fnspon, 1993.
[15] A. Agüero, "Beamcolumnimperfection" Software, Online available from https://laboratoriosvirtuales.upv.es/webapps/Beamcolumn_imperfection.html, 2023
[16] A. Agüero, "Thinwallsectiongeneral" Software, Online available from https://laboratoriosvirtuales.upv.es/webapps/thinwallsectiongeneral.html, 2023.
[17] R. Winkler, A. Bours, A. Walter and M. Knobloch, "Redistribution of internal torsional moments caused by plastic yielding of structural steel members", Structures, 17, 21-33, 2019.
[18] I. Baláž, Manual to EN 1993-1-1:2022 with numerical examples in MATHCAD, ÚMS SR in Bratislava. In print.
[19] A. Agüero, "Buckling Beam Column N My Mz B T any support & section" Software, Online available from https://labmatlab-was.upv.es/webapps/home/Bucklingresistanceopenclosed_anyBC_N_My_Mz_B_U.html, 2023.
[20] A. Agüero. "Bucklingresistance open + closed" Software online available from: https://labmatlab-was.upv.es/webapps/home/Bucklingresistanceopenclosed.html, 2023
[21] A. Agüero. Software online https://antonioagueroramonllin.blogs.upv.es/, 2003